



Quantitative MRI: towards fast and reliable T_1 , T_2 and proton density mapping at ultra-high field

Lisa Leroi

► To cite this version:

Lisa Leroi. Quantitative MRI: towards fast and reliable T_1 , T_2 and proton density mapping at ultra-high field. Imaging. Université Paris Saclay (COMUE), 2018. English. NNT: 2018SACLS429. tel-01954603

HAL Id: tel-01954603

<https://theses.hal.science/tel-01954603>

Submitted on 13 Dec 2018

HAL is a multi-disciplinary open access archive for the deposit and dissemination of scientific research documents, whether they are published or not. The documents may come from teaching and research institutions in France or abroad, or from public or private research centers.

L'archive ouverte pluridisciplinaire **HAL**, est destinée au dépôt et à la diffusion de documents scientifiques de niveau recherche, publiés ou non, émanant des établissements d'enseignement et de recherche français ou étrangers, des laboratoires publics ou privés.

Quantitative MRI: towards fast and reliable T_1 , T_2 and proton density mapping at ultra-high field

Thèse de doctorat de l'Université Paris-Saclay
préparée à l'Université Paris-Sud,
au sein de Neurospin, CEA Paris-Saclay

École doctorale n°575 : Electrical, optical,
bio-physics and engineering (EOBE)
Spécialité de doctorat: Imagerie et Physique Médicale

Thèse présentée et soutenue à Gif-sur-Yvette, le 23/11/2018, par

Lisa Leroi

Composition du Jury :

Pr. Richard Bowtell Professor, Sir Peter Mansfield Imaging Centre	Rapporteur
Pr. Jean-Michel Franconi Professeur des Universités, Centre de Résonance Magnétique des Systèmes Biologiques	Rapporteur
Pr. Vincent Lebon Professeur des Universités – Praticien Hospitalier, CEA - Service Hospitalier Frédéric Joliot	Président, Examineur
Pr. Jérôme Hodel Professeur des Universités – Praticien Hospitalier, Hôpital Henri Mondor	Examineur
Dr. Maja Musse Chargé de Recherche, Institut national de recherche en sciences et technologies pour l'environnement et l'agriculture	Examineur
Dr. Alexandre Vignaud Ingénieur-Chercheur, CEA - Neurospin	Directeur de thèse
Dr. Ludovic de Rochefort Chargé de Recherche, Centre de Résonance Magnétique Biologique et Médicale	Co-encadrant Invité

Remerciements

Tout a commencé en 2007, dans l'un des plus mauvais lycées du département varois. Monsieur Bardiot, professeur de physique, retraité depuis, me communiquait alors sa passion des sciences et me poussait dans cette voie. Mes premiers remerciements lui sont directement adressés... puisque j'arrive aujourd'hui, plus de 8 années après, en fin de doctorat en sciences physiques au sein de Neurospin, un laboratoire de rang mondial, qui verra bientôt la mise en service de l'IRM clinique le plus puissant au monde. Je tiens à remercier **Denis le Bihan** et **Cyril Poupon**, pour m'avoir accueillie à Neurospin et dans l'équipe UNIRS au sein desquels j'ai pu profiter de conditions de travail hors du commun.

Alexandre, il m'est difficile d'écrire des remerciements à la hauteur de ton encadrement ! Tout d'abord, merci de m'avoir donné l'incroyable chance de travailler avec toi dans cette sinieuse recherche de bourse de thèse. Ta façon de diriger et d'encadrer cette thèse m'a permis de mieux appréhender le monde de la recherche et sa méthodologie rigoureuse. Merci pour tes conseils toujours avisés et clairvoyants dans ce travail, pour ton soutien infaillible et tes encouragements dans chaque étape. Merci pour ces heures d'explications à dessiner des diagrammes de séquence, des spins et des graphs, sur un tableau ou alors un cahier de manip'. Merci pour ton management d'équipe exemplaire, qui te permet de gérer mille et une choses à la fois, tout en accordant de l'importance à chacun. Merci pour ta bienveillance à mon égard jusqu'au bout de cette thèse et pour les multiples opportunités d'échanger en France comme à l'international, qui vont me permettre à présent de partir vers des contrées bien lointaines...

Ludovic, merci pour tous tes conseils sur l'implémentation et l'exploitation de la méthode que tu as brillamment inventée. Ta patience pendant tes explications du brevet et tes idées éclairées m'auront permis de progresser tout au long des 3 ans et d'en apprendre toujours plus. Sans ton savoir et le partage de tout ton travail, rien de tout ça n'aurait vu le jour.

Je tiens à remercier chaleureusement tous les membres du projet « qMRI », qui ont chacun apporté leur pierre à l'édifice. **Mathieu Santin** et **Romain Valabrègue**, merci pour avoir mis à disposition tous vos outils, indispensables à la réussite de ce projet. **Paulo Loureiro de Sousa**, merci pour ces discussions très enrichissantes sur ta vision de l'IRM quantitative, et plus largement de la recherche dans le domaine de la santé. Je garderai un grand souvenir de ce séjour à Obernai ! **Julien Lamy**, merci pour la mise à disposition d'outils de développement partagés de haut vol et pour le financement FLI qui nous a permis de continuer à collaborer tous ensemble. **Geneviève Guillot**, merci pour ces suggestions scientifiques, et pour le coup de pouce de démarrage ! J'espère pouvoir continuer la grande lignée, et m'inscrire dans une nouvelle génération de chercheurs en imagerie médicale.

Franck Mauconduit, merci infiniment pour ton aide quotidienne qui a été indispensable tout au long de ces trois années. Sans tes conseils et ton expertise, mes « functors » seraient perdus dans un océan de lignes de code...

Nicolas Boulant et **Vincent Gras**, merci pour votre aide et vos précieux conseils dans ce travail. Merci pour les fantômes d'agar, outil numéro 1 d'un physicien d'IRM. Merci aussi, et surtout, pour avoir appliqué vos pulses universels à QuICS, pour votre temps dans les manips, et pour vos yeux d'experts dans l'analyse des résultats. Merci à **Fawzi Boumezbeur** et **Cécile Lerman** pour ces discussions autour de la théorie du sodium. Merci aussi à **Alexis Amadon**, **Philippe Ciuciu** et **Benoît Larrat** pour vos questions très constructives tout au long de ce travail.

Merci à l'équipe des manip', **Chantal Ginisty**, **Séverine Desmidt-Becuwe** et **Séverine Roger**, avec qui j'ai partagé beaucoup de temps à la console, avec des images parfois réussies et parfois complètement ratées, mais toujours dans la joie et la bonne humeur !

Merci à tous ceux qui ont rejoint l'équipe des « petits spins », pour quelques mois ou bien quelques années, et avec qui j'ai pu partager l'open-space au quotidien. Merci au Dr(?) **Arthur** pour ces longues discussions à refaire le monde et pour cette superbe collaboration autour du sodium. Merci **Gaël** pour ta bonne humeur communicative et ton accent chantant qui me rappelait le soleil du sud. Merci **Raphaël** pour toutes tes anecdotes et pour tous ces échanges pendant le tunnel partagé de la rédaction. Merci **Emilie** pour ces pauses café, pour tous tes encouragements et pour ces souvenirs ensemble à Singapour et Hawaï. Merci **Carole** aussi, pour ces supers voyages partagés à Montréal et aussi Hawaï. Merci **Loubna** de rire aux

éclats pour toutes nos blagues, y compris les moins bonnes, **Bruno** pour tes magnifiques bobines, **Jacques** pour tes outils de recalage, **Sylvain**, **Hamza**, **Hanaé**, **Noémie**, **Benoit**, **Véra**, **Morgane**, **Robin** et enfin **Zo** pour avoir partagé chaque matin ta bonne humeur légendaire !

Du côté marseillais... **Redha Abdeddaïm**, merci infiniment pour ton énergie et ton soutien tout au long de ces trois années. J'ai adoré réaliser toutes ces manips de méta-matériaux, plus ou moins fructueuses, mais toujours aussi stimulantes ! Merci d'avoir encadré mon stage avec autant de temps et d'intérêt. Encore bravo pour M-CUBE, qui j'espère, ne sera qu'un tremplin pour te permettre d'aller toujours plus loin ! Merci aussi à **Stefan Enoch** pour tes conseils et ton intérêt continu pour tout ce travail. Merci **Marc Dubois** pour ton travail sur la modélisation des méta-matériaux et pour avoir poussé ce papier jusqu'au bout avec une telle persévérance ! Merci à **Pierre Sabouroux** et **Luisa Neves**, pour avoir décoré mon bureau d'une sympathique Léonie en pate de fruit, mais surtout pour votre gentillesse et vos mesures EpsiMu.

Je remercie également tous les membres de mon jury : Professeur **Richard Bowtell** et Professeur **Jean-Michel Franconi** pour avoir accepté d'être rapporteurs de ce travail, ainsi que Professeur **Vincent Lebon**, Professeur **Jérôme Hodel** et Docteur **Maja Musse** pour avoir examiné ce travail.

Je vais clore ces remerciements en remerciant ma petite famille. **Amine**, merci pour m'avoir encouragée, poussée et soutenue tout au long de ce voyage de 3 ans et demi. Merci pour tout ce que tu m'apportes au quotidien. Merci aussi à ta famille d'avoir agrandi le cercle des Kaddache (à une docteure de plus !). Ces trois années auront été riches en joie et en événements, et sont annonciatrices, je l'espère, d'une vie remplie de bonheur et d'aventures ensemble...

Merci à **Sissi**, ma grande sœur, d'avoir ouvert la voie depuis toujours... et surtout de m'avoir donné autant d'exercices de maths quand on jouait à la maîtresse étant petites. Je suis sûre que tout est parti de là ! Merci aussi à **Gautier**, et au petit **César** qui m'émerveille un peu plus de jour en jour. Enfin, merci à mes parents, **Nathalie** et **Jean-François**, pour m'avoir offert une enfance idyllique. Merci aussi de m'avoir poussée à aller toujours plus haut et à m'extraire de ce lycée varois, en me répétant des centaines de fois de « ne pas me reposer sur mes lauriers » et de ne jamais me contenter d'un 18 si le 20 est atteignable. Merci pour votre joie de vivre communicative, vos précieux conseils, votre infaillible confiance en moi et surtout, votre soutien dans tout ce que j'entreprends. Cette thèse, c'est avant tout grâce à vous.

Content

Remerciements.....	i
Introduction.....	5
Chapter 1. Towards ultra-high field quantitative magnetic resonance imaging	9
1.1. Quantitative MRI and clinical interests	11
1.1.1. NMR parameters to investigate	11
1.1.2. Clinical interests of quantitative MRI	19
1.1.3. Conclusion	21
1.2. Enhancing MR signal using ultra-high fields strengths.....	22
1.2.1. The benefits to go towards higher field strengths.....	22
1.2.2. Challenges from ultra-high field MRI.....	23
1.2.3. Solutions.....	27
Chapter 2. Measuring NMR parameters	31
2.1. Measuring NMR parameters of interest.....	33
2.1.1. Spatial encoding.....	33
2.1.2. Spin-Echo sequences.....	34
2.1.3. Steady-State Free Precession (SSFP) sequences	43
2.1.4. Conclusion	54
2.2. Simultaneous multi-parametric mapping methods.....	55
2.2.1. Inversion-Recovery TrueFISP	55
2.2.2. QRAPTEST and QRAPMASTER	56
2.2.3. Double Echo Steady-State (DESS), Diffusion-weighted DESS (DW-DESS) and Triple Echo Steady-State (TESS)	58
2.2.4. Magnetic Resonance Fingerprinting (MRF).....	60
2.2.5. MR-Spin TomogrAphy in Time domain (MR-STAT)	62
2.2.6. Quantitative Imaging using Configuration States (QuICS)	63
2.3. Objectives and challenges.....	70

Chapter 3. Implementation and validation of a multiple contrasts spoiled SSFP sequence for simultaneous multi-parametric extractions at 7T	73
3.1. Materials and methods.....	75
3.1.1. Phantom validation using 1Tx/1Rx.....	75
3.1.2. Phantom validation using 1Tx/32Rx and phase combination	76
3.1.3. Reproducibility of the method.....	79
3.1.4. Accelerating acquisition time	80
3.2. Results.....	82
3.2.1. 1Tx/1Rx application	82
3.2.2. 1Tx/32Rx application	83
3.2.3. Reproducibility of the results	84
3.2.4. Optimized protocol.....	85
3.3. Conclusion.....	86
Chapter 4. In vivo simultaneous multiparametric quantitative MRI under UHF constraints	87
4.1. Introduction	89
4.2. Setup formulation for in vivo acquisitions in optimal conditions.....	89
4.3. Limiting B_1^+ heterogeneities at 7T	92
4.3.1. B_1^+ homogenization using meta-materials	92
4.3.2. Parallel transmission: universal pulses for brain applications	100
4.4. QuICS application in vivo using parallel transmission	101
4.4.1. Materials and methods	101
4.4.2. Results	102
4.4.3. Discussion.....	104
Chapter 5. ^3Na quantitative MRI: an in vitro demonstration	107
5.1. Introduction	109
5.2. Materials and methods.....	110
5.2.1. In-silico experimental setup formulation	110
5.2.2. MRI acquisitions	110

5.2.3. Data analysis	111
5.3. Results	112
5.4. Discussion.....	114
5.5. Conclusion and perspectives.....	117
General conclusion and perspectives	119
Publications.....	123
Abbreviations and acronyms.....	127
Résumé court en Français (French abstract)	129
Appendices: Articles and abstracts submitted as first author.....	137
Appendix 1: Simultaneous multi-parametric mapping of total sodium concentration, T_1 , T_2 and ADC at 7 T using a multi-contrast unbalanced SSFP	139
Appendix 2: Kerker Effect in Ultrahigh-Field Magnetic Resonance Imaging.....	149
Appendix 3: Abstracts accepted in international conferences.....	163
References.....	171

Introduction

Since its discovery in the early 70s, Magnetic Resonance Imaging (MRI) has become the most powerful tool to explore the anatomy non-invasively. Imaging the body in vivo and diagnosing a large range of diseases in almost all parts of the human body has become possible. Standard MRI is based on the detection of protons (^1H) present in water, lipids and macromolecules in the body. It employs a powerful magnet which produces a strong magnetic field of fixed strength (typically 1.5 or 3T) that forces protons in the body to align with that field called B_0 . The application of a radiofrequency field using a dedicated coil will stimulate protons. Their spins will dephase from their natural position from an angle, called the flip angle, and they will strain against the pull of the magnetic field. The time it takes to realign with the magnetic field, as well as the amount of released energy, can change depending on the environment and the chemical nature of the molecules. This spin behavior can be investigated using the spin-lattice relaxation, denoted T_1 , corresponding to the magnetization aligned with the main magnetic field, and the spin-spin relaxation, denoted T_2 , corresponding to the transverse magnetization, in the orthogonal plane to B_0 . Other parameters such as diffusion and proton density can reflect the way the molecules will propagate in their environment and supplement this tissues' characterization.

From these different nuclear magnetic resonance (NMR) properties, a wide range of different contrasts can be generated in MRI, giving different anatomical or structural information on the tissues under investigation (Haacke et al., 2014). Conventional MRI exams performed in clinics are usually qualitative and based on weighted imaging, evaluating the relative contrast from neighboring tissues. The retrieved signal is related to the above tissue properties in a

nonlinear manner, and depends on acquisition conditions and external factors that cannot be reproduced over time. It does not provide direct biochemical information on tissue viability, depends on the clinician expertise to interpret images and cannot be used properly for medical follow-up. Obtaining quantitative information would be of utmost importance for diagnosing and prognosing diseases, or for assessing the effect of treatments and new drug tests as it is more objective, traceable and reliable.

With the aim of continuously improving MRI and associated medical diagnoses, higher main magnetic field strengths have been explored. Indeed, the application of a higher magnetic field strength B_0 increases the available Signal-to-Noise ratio while exacerbating contrasts. Hence, for the same acquisition time, image quality will be improved. The trend to go toward higher magnetic field strengths is a global phenomenon observed not only in research, but also in clinics. Since its FDA approval in the 2000's, the selling of 3T scanner are widely increasing. The very recent FDA approval and CE marking of the Siemens 7T Terra scanner in 2017, during the time-course of this thesis, is another demonstration of this upscaling trend. Currently, the three major vendors of human MRI systems, Siemens, Philips, and General Electric have together installed more than 70 7T scanners around the world (Polimeni and Uludağ, 2018), taking 7T one step closer to becoming a platform for advanced clinical imaging. However, the use of such strong magnets is tainted by heterogeneity in both static magnetic field and radiofrequency (RF) fields. Indeed, when increasing B_0 , the RF wavelength is decreased and human body size becomes non negligible compared to the associated wavelength, ending up in shaded areas and corrupted contrasts on images. Some solutions are being developed and will be discussed in this manuscript.

This PhD thesis aimed at implementing a fast and reliable MR method to retrieve simultaneously 3D quantitative maps of T_1 , T_2 , proton density and flip angle, with the objective to eventually apply it in clinical routine for population imaging at ultra-high field. This manuscript is divided into 5 chapters.

In the first chapter, we will develop how current literature highlights the clinical interests of quantitative MRI, and show how UHF imaging can be a precious tool to obtain images of higher quality.

In the second chapter, we will present the different existing ways to measure parameter of interests using MR sequences: first, in a conventional way using a classic spin-echo sequence, and then using more rapid methods based on steady-state free precession sequences. We will then review some existing simultaneous multi-parametric methods in literature.

In the third chapter, we will implement the method to perform Quantitative Imaging using Configuration States (QuICS). We will optimize it to provide unbiased and accelerated multi-parametric extractions on phantom and ex-vivo tissues at 7T.

In chapter 4, we will examine the sensitivity of QuICS to flip angle heterogeneity encountered at UHF. We will focus on a solution to mitigate the RF field using metamaterials at 7T. QuICS will be applied using the most advanced and efficient solution to obtain an adjusted flip angle, namely the parallel transmission. A protocol validating the quantitative extraction in vivo at 7T in a clinically-relevant time will be presented.

Finally, in the last chapter, we will apply this method to an exotic nucleus of interest for the community, namely the sodium (^{23}Na). Its total concentration, T_1 , T_2 and ADC will be retrieved. This work will be the occasion to show the ability of the method to probe different molecular environments with very short relaxation times. It is also the first time that ^{23}Na MRI of diffusion imaging will be performed.

Chapter 1.

Towards ultra-high field quantitative magnetic resonance imaging

Computed Tomography (CT), Positron Emission Tomography (PET) and Magnetic Resonance Imaging (MRI) are the most well-known three-dimensional imaging techniques used in clinical routine. Although each of them has its merits, CT and PET both involve ionizing radiation and offer either limited soft tissue contrast or a relatively coarse resolution. On the contrary, MRI allows images to be resolved down to a sub-millimeter voxel size, while facilitating multiple contrast mechanisms that can be exploited to differentiate tissues and/or indicate various pathological conditions. Currently, clinical MR imaging diagnoses are mainly based on qualitative weighted images, where the signal is related to tissue properties in a nonlinear manner, and depends on external factors, such as the scanner used for acquisition for example. Quantifying the different physical parameters available in NMR has been demonstrated to have many clinical interests, as will be presented in this chapter. Such a quantification would help to go further in tissue characterization and thus in radiological diagnoses, moving from lesion detection and characterization to a better gradation of pathology, and even the possibility of a proper therapeutic follow-up. Moving towards ultra-high fields ($B_0 > 3T$) would bring an undeniable gain in signal and contrast to noise ratio, that could be profitable to enhance sensitivity and specificity of these measurements. Unfortunately, these benefits are hampered by several challenges that need to be tackled to take maximum advantage of such powerful tools. Some solutions are currently being developed in the MR community to facilitate their use, and will be presented in this chapter.

1.1. Quantitative MRI and clinical interests

1.1.1. NMR parameters to investigate

1.1.1.1. Introducing Bloch equations

Magnetic resonance imaging is based on the exposure of tissues to a uniform static magnetic field, called B_0 . During the exposure to B_0 , the spins of the nuclei of the studied atom, here hydrogen, adopt a precession frequency ω_0 , called the Larmor frequency, defined by the equation:

$$\omega_0 = \gamma B_0 \quad (1.1)$$

Where γ is the gyromagnetic ratio of the considered nucleus ($\frac{\gamma_{1H}}{2\pi}=42,576 \text{ MHz/T}$).

When a set of $1/2$ spin nuclei is immersed in a static magnetic field, it can be perceived as a macroscopic entity where the magnetization is described by the Boltzmann relation:

$$M_0 = N \frac{\gamma^2 \hbar^2}{4 k_B T} B_0 \quad (1.2)$$

Where N is the number of nuclei present in the considered sample, \hbar the Planck constant divided by 2π , and $k_B T$ represents the thermal energy, with k_B the Boltzmann constant.

To obtain a signal, it is necessary to apply an oscillating radiofrequency field, called the B_1 field, lying in the transverse plane, orthogonal to the magnetic field B_0 , lying in the longitudinal axis. This B_1 field results from the radiofrequency (RF) pulse having a precession of ω_0 induced by an electrically resonating circuit integrated in an antenna, also called a coil. This B_1 field will provoke the excitation of the spins of the atoms that will resonate and absorb its energy. The spins then reach a higher energy level which, macroscopically, will flip M_0 by an angle of α , depending on B_1 intensity and application time.

When perturbed by this B_1 field, the energy absorbed by the system makes it unstable, and it immediately starts to move, or “relax”, back to a state of equilibrium, releasing the energy that had been put into it. This energy is dispersed by a number of processes, such as relaxation mechanisms or diffusion. Relaxation mechanisms can be grouped into the ones that transfer energy away from the spins to ‘the lattice’, contributing to spin-lattice relaxation (T_1); and the ones that redistribute it within the spin system, contributing to the spin-spin relaxation (T_2). The temporal evolution of the magnetization vector $\vec{M} = \{M_x(t), M_y(t), M_z(t)\}^T$ can be described by the Bloch-Torrey equations (Bloch, 1946; Wangsness and Bloch, 1953; Torrey, 1956), Eq. (1.3).

$$\frac{\partial \vec{M}}{\partial t} = -\gamma \vec{B} \times \vec{M} + \frac{1}{T_1} (M_0 - M_z) \vec{e}_z - \frac{1}{T_2} \vec{M}_T + D \nabla^2 \vec{M} \quad (1.3)$$

Where $\vec{B} = \{B_x(t), B_y(t), B_z(t)\}^T$ is the magnetic field which may depend on time and whose static main component is oriented along the z-axis, $\vec{M}_T = \vec{M}_x + i\vec{M}_y$ is the transverse magnetization, D is the free diffusion coefficient. The time it takes for the protons to realign with the magnetic field as well as the way they diffuse and the amount of energy released change depending on the environment and the chemical nature of the molecules, leading to different contrasts. These different mechanisms are therefore tissue-specific characteristics and are fundamental to MRI as they affect any NMR experiment.

1.1.1.2. Longitudinal relaxation time (T_1)

Longitudinal relaxation time, T_1 , is an intrinsic biophysical property of the tissue. It is related to the time required for the substance to recover its net equilibrium magnetization on the z-axis. When considering the immersion of the object into the main magnetic field and perturbed by a 90° RF pulse, Bloch equations show:

$$\frac{dM_z}{dt} = \frac{1}{T_1} (M_0 - M_z) \quad (1.4)$$

which has the solution:

$$M_z(t) = M_0 (1 - e^{-\frac{t}{T_1}}) \quad (1.5)$$

Graphically, T_1 can be viewed as the time required for M_z to reach $1 - e^{-1}$ or about 63% of its maximum value, M_0 , after a 90° flip angle, as shown in Figure 1.1. In biological materials, T_1 values ranging from a few tenths of a second to several seconds are typically found.

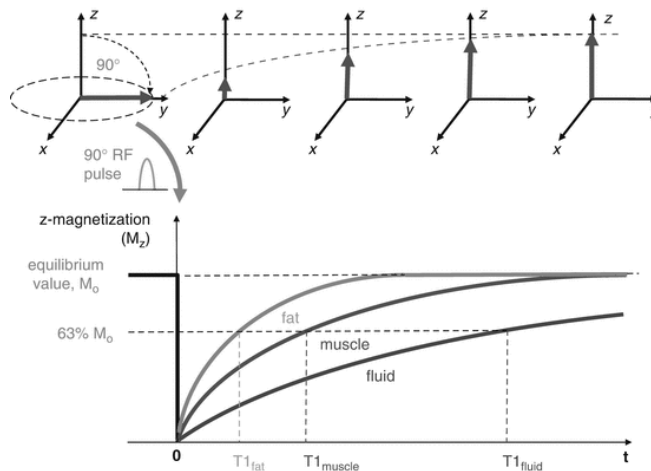


Figure 1.1 : T_1 recovery after the application of a 90° RF pulse. The z -magnetization is shown as a function of time for different tissues such as fat, muscle or fluid, which exhibit different T_1 values. From (Ridgway, 2010)

Longitudinal relaxation is due to energy exchange between the spins and surrounding lattice. Spins go from a high energy state back to a low energy state and RF energy is released back into the surrounding lattice. Therefore, T_1 -relaxation is simply an energy flow between spins and their external environment through collisions or rotations. This energy loss represents a heat transfer, and the system is said to re-establish “thermal equilibrium”. Fluctuating fields are local, random in magnitude, and affect only a few spins. Hence, the amount of energy transferred from the nuclei is very small and goes largely unnoticed at body temperatures.

In 1948, Nicolaas Bloembergen, Edward Mills Purcell, and Robert Pound proposed the so-called Bloembergen-Purcell-Pound theory (BPP theory) (Bloembergen et al., 1948) to explain the relaxation constant of a pure substance in correspondence with its state, taking into account the effect of tumbling motion of molecules on the local magnetic field disturbance. From this theory, one can get (Nelson and Tung, 1987):

$$\frac{1}{T_1} = C \left(\frac{2\tau_c}{1 + \omega_0^2 \tau_c^2} + \frac{8\tau_c}{1 + 4\omega_0^2 \tau_c^2} \right) \quad (1.6)$$

Where C is a constant depending on the gyromagnetic ratio and the inter-nuclear distance for proton, and τ_c represents the correlation time with $\tau_c = \frac{4\eta b^3}{kT}$, where η is the viscosity, b the radius of the molecule treated as a sphere, k is the Boltzman’s constant, and T is the absolute temperature. T_1 evolution as a function of correlation time is displayed in Figure 1.2. It is now evident from Eq. (1.6) and Figure 1.2 that T_1 depends on the molecular environment considered, temperature, but also the magnetic field strength B_0 . If B_0 increases, T_1 values will increase as well, in a non-linear manner.

Much of the relaxation in biological systems takes place at relaxation sites. These are locations where magnetization energy is easily and quickly dissipated. A prime example of a relaxation site is a metal nucleus such as gadolinium (Gd). Often used as a contrast-agent in MRI, it allows for significant shortening of the T_1 by supplying a relaxation site to many spins. Other metals such as iron (in hemoglobin) and zinc (present in many proteins) similarly act as naturally occurring relaxation sites (Tofts, 2005).

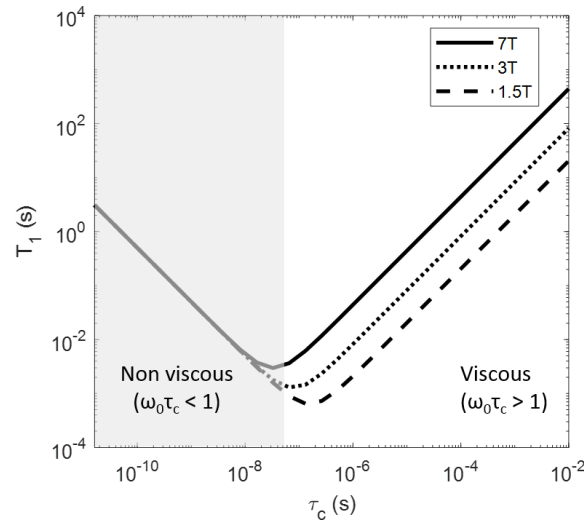


Figure 1.2 : Log-log representation of T_1 depending on correlation time (which is proportional to viscosity and inversely proportional to temperature). Different magnetic field strengths are considered (line: 7T, dotted-line: 3T and dashed line: 1.5T). The T_1 value depends on the molecular environment, reflected by the correlation time, τ_c . The minimum values of the curves corresponds to $\omega_0 \tau_c = 1$. The shaded area corresponds to $\omega_0 \tau_c < 1$ at 7T, where the molecular environment is non-viscous. Therefore, the interactions are restrained and T_1 does not depend on field strength. In viscous environments, T_1 varies with magnetic field strength in a non-linear manner.

Biological basis of T_1

As described above, the T_1 recovery is caused by the fluctuating magnetic fields arising largely from the motion of molecules in the neighborhood of the magnetic moments. Therefore T_1 relaxation is often associated with water mobility and structural density, reflecting binding of water molecules. In the brain, it has been shown to be highly correlated with myelin or macromolecular volume content, both in grey (Stüber et al., 2014) and white matter (Mezer et al., 2013; Yeatman et al., 2014). That is why T_1 contrast is generally used in brain exams: myelin causes white matter to have a shorter T_1 than grey matter, leading to a clear contrast.

T_1 can change due to pathologies. For instance, edema around tumors or inflammatory acute MS lesions leads to an increase in T_1 (Brück et al., 2004). T_1 is also increased in chronic MS lesions, probably as a result of the reduction in myelin and increase in water content. But at the rim of active MS lesions, T_1 is reduced because of the presence of cellular debris which constitute extra-relaxation centers in the fluid. Other changes, such as myelination of developing brain (Paus et al., 2001), or decrease of myelination due to aging (Cho et al., 1997) can benefit from T_1 quantification. An extensive review of T_1 values in normal and pathological tissues across a range of field strengths can be found in (Bottomley P. A. et al., 1998).

1.1.1.3. Transverse relaxation time (T_2)

The transverse relaxation time, T_2 , is related to the magnetization decay on the transverse plane. Considering a simplified model where only the transverse component is considered, the Bloch equations show that after a 90° pulse, it can be expressed as:

$$\frac{dM_T}{dt} = -\frac{M_T}{T_2} \quad (1.7)$$

Therefore, it is found that it takes the form of an exponential decay, described by:

$$M_T(t) = M_T(0) e^{-\frac{t}{T_2}} \quad (1.8)$$

Where $M_T(0)$ is the transverse component at $t = 0$. T_2 is the time required for the transverse magnetization to fall to approximately 37% (e^{-1}) of its initial value, as shown in Figure 1.3.

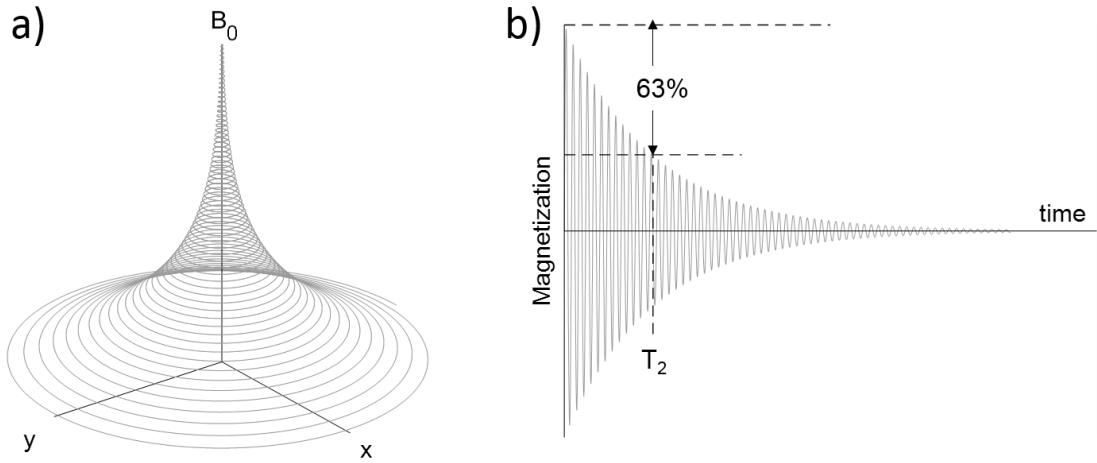


Figure 1.3 : a) Precession of the magnetization vector and b) corresponding signal, showing the T_2 relaxation mechanism.

The resulting decay in transverse magnetization is due to magnetic field interactions occurring between protons (spin-spin interaction), slightly modifying their precession rate. For example, neighboring protons bound to macromolecules locally change the magnetic field sensed by the free protons. These local field non-uniformities cause the free protons to precess at slightly different frequencies. Thus, following an excitation pulse, the protons lose phase coherence and the net transverse magnetization is gradually lost resulting in transverse magnetization decay.

As for T_1 , its expression can be derived from its correlation time, τ_c , and a constant C dependent on the gyromagnetic ratio and the inter-nuclear distance for proton (Nelson and Tung, 1987):

$$\frac{1}{T_2} = C(3\tau_c + \frac{5\tau_c}{1 + \omega_0^2\tau_c^2} + \frac{2\tau_c}{1 + 4\omega_0^2\tau_c^2}) \quad (1.9)$$

Figure 1.4 shows the T_2 sensitivity on the correlation time, which is linked to the viscosity of the environment and temperature. As illustrated, T_2 values will be less sensitive to the field strength than T_1 .

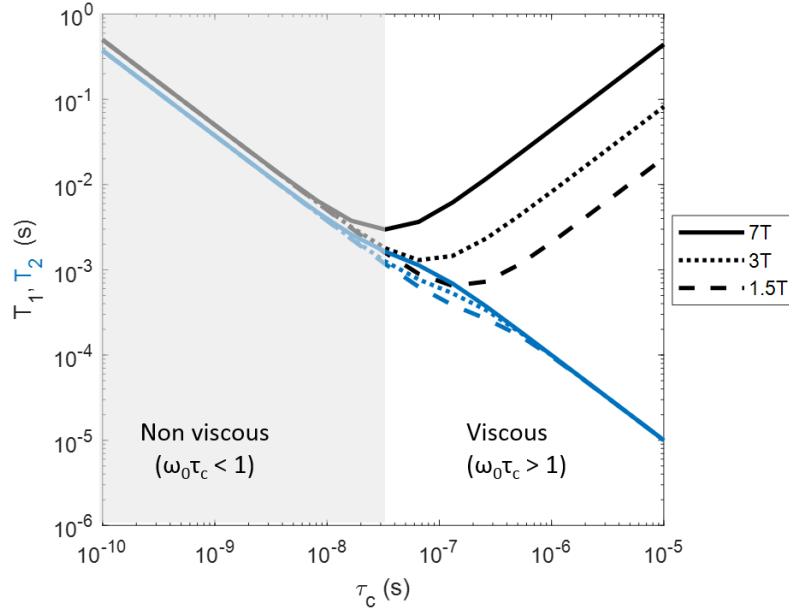


Figure 1.4 : Log-log representation of T_1 (black lines) and T_2 (blue lines) depending on correlation time (which is proportional to viscosity and inversely proportional to temperature) for different magnetic field strength. Here, the dependence of T_2 on magnetic field strength is less important than for T_1 . The molecular environment plays a pivotal role in T_1 and T_2 values, showing their sensitivity to probe such information.

Off-resonance effects such as imperfections in the main magnetic field, susceptibility differences among various tissues or at tissue-air interfaces, and chemical shift lead to an additional dephasing of the spins and thus to a faster decay of the transverse magnetization M_T . The overall transverse relaxation time T_2^* , taking into account this additional reduction in transverse magnetization, is determined by (Chavhan et al., 2009):

$$\frac{1}{T_2^*} = \frac{1}{T_2} + \gamma \Delta B_{inhom} \quad (1.10)$$

Where ΔB_{inhom} is the magnetic field inhomogeneity, sensitive to paramagnetic mesoscopic particles such as iron or amyloid plaques. Even with a perfect B_0 shimming, T_2^* contains external effects (e.g. susceptibility variations within the patient or chemical shift effects). As such, T_2^* is always lesser than T_2 . The dephasing induced by the second term of Eq (1.10) can be eliminated by the application of an appropriate pulse (180° pulse in a spin-echo MR sequence as seen in section 2.1.2.1) which cause a reversal of the initial dephasing. In contrast, the T_2 losses internal in the proton system and characteristic of the tissue are maintained as they are caused by local, random, and time-dependent field variations.

Biological basis of T_2

In the brain, T_2 reflects the degree of binding and water compartmentalization. This was evident in studies on human preterm neonates where T_2 showed a decrease with brain maturation (Ferrie et al., 1999). During brain maturation, tissue water decreases, myelin precursors such as cholesterol and proteins appear, glial cells proliferate and differentiate, and a number of biochemical cell membrane changes occur. These changes increase the proportion of bound to free water and thus shorten the T_2 relaxation time (Dobbing and Sands, 1973). T_1 relaxation times also decrease with cerebral maturation, particularly with the onset of myelination. However, T_2 decreases more rapidly. Therefore, T_2 has been suggested as a particularly interesting biomarker of the developing brain (Tofts, 2005).

A number of studies have shown that GM possesses a longer T_2 relaxation time than WM. This is thought to be due to differences in water compartmentalization, vascularity and iron concentration. The paramagnetic property of iron produces a shortening of the proton relaxation times. (Vymazal et al., 1999) reported shorter T_2 in regions like substantia nigra, in globus pallidus and putamen in Parkinson's patients for example.

1.1.1.4. Proton Density

Proton density (PD) refers to the concentration of protons that resonate and give rise to the NMR signal in the tissue. It is expressed as a percentage of the proton concentration in water, in percentage unit (pu). Thus, CSF is 100pu, WM is about 70pu and GM 80pu (Tofts, 2005; Whittall et al., 1997). All images have intensity proportional to PD. Therefore, all images are PD-weighted, in addition to the influence of any other parameter such as T_1 or T_2 for example. PD is sometimes called 'spin density' and abbreviated ρ .

Since most visible tissue protons are resident in water, it is often seen as a short-hand way of looking at water content. But PD slightly differs from water concentration. Indeed, water content would include protons that have short T_2 , not visible in the usual imaging process. Significant numbers of protons are resident in non-water environments (e.g. lipids or macromolecules), although most of these have short T_2 and are therefore MRI-invisible. But in practice, the effect of these factors seems to be small, especially in the brain, where most mobile protons (with a long T_2) are in water. (Tofts, 2005). Therefore, PD is often approximately the same as the mobile water content of the tissue.

Biological basis

PD is the essence of MR imaging, as it directly reflects water content as discussed above. Yet, we have little experience to measure it, and even less experience of using it clinically. PD measurements can be used to infer water content, its change in disease like inflammation and edema, and its response to treatment (e.g. mannitol to reduce edema). Changes in PD often correlate closely with T_1 changes, and may provide no extra information, if T_1 has already been measured. But PD does have the advantage that its biological interpretation is unambiguous and specific. In contrast, the parameters T_1 and T_2 , although sensitive, produce changes that are harder to interpret. PD maps are also used to aid segmentation and tissue classification schemes, in conjunction with T_1 , T_2 and sometimes diffusion maps (Tofts, 2005).

1.1.1.5. Diffusion

Every fluid has a characteristic intrinsic self-diffusion constant, D , which reflects the mobility of the molecules in their microenvironment. MRI can be made sensitive to dynamic displacements of water molecules between 10^{-8} and 10^{-4} m in a timescale of a few milliseconds to a few seconds. Each molecule within the sample behaves independently from the others. Since these displacements are of the same order of magnitude as cellular dimensions within biological tissues, MRI diffusion measurements can provide a unique insight into tissue structure and organization. Some applications like Diffusion Tensor Imaging can be used to perform fiber tracking, for example, or Intra-Voxel Incoherent Motion (IVIM) to quantitatively assess all the microscopic translational motion that could contribute to the acquired signal. Here, we will consider the mean diffusion signal encountered at the scale of a voxel.

In a free environment such as CSF, water can diffuse isotropically in all directions. In biological tissues, there are barriers, such as cells and nerve fibers, which reduce the ability of water to diffuse. In the adult brain, WM and GM are characterized by structural complexity, which affects the measurements of the water diffusion coefficient in tissues. The collision between molecules provokes a random displacement of each one, with no preferred direction.

When considering the NMR imaging experiment, diffusion adds a random drift to the considered spins between the processes of dephasing and rephasing from gradients. The loss of phase coherence leads to a signal attenuation. The amount of diffusion attenuation depends on two factors. First, the sample structural characteristics determine the motion of the spins. Secondly, sequence parameters, where the diffusion time, t_d , determines the time during which the diffusive motion takes place. Indeed, the measured diffusion depends on the time for molecules to diffuse, t_d , relative to the average time between two successive collisions of a molecule and a boundary, τ . If $t_d \ll \tau$, most of the molecules behave as if no boundaries were present and the molecular motion appears unrestricted with a diffusion coefficient D_{free} .

If the $t_d \gg \tau$, any molecule is likely to encounter a boundary. This will affect the displacement, and a completely restricted diffusion regime is reached. In the intermediate regime, an Apparent Diffusion Coefficient (ADC) can be estimated. Because of the dependency to the diffusion time used t_d , a ‘true absolute’ value of diffusion is not retrieved, but only an apparent coefficient of the system under investigation, for the chosen acquisition parameters.

The contrast of the diffusion-weighted images is specific to the diffusion direction investigated, and can change with patient orientation. To remove these dependences, three diffusion-images can be obtained, each looking at diffusion along one of the three orthogonal directions (Readout, Slice and Phase encoding, respectively denoted x , y and z here). In that case, the anisotropic diffusions D_x , D_y and D_z can be retrieved, and ADC is defined as the geometric mean of these three diffusions (Bernstein et al., 2004):

$$ADC = \frac{D_x + D_y + D_z}{3} \quad (1.11)$$

This ADC value is sometimes called the “trace ADC”, as it can be considered as the trace of a diffusion tensor matrix.

Biological basis

In biological tissues, diffusing molecules are surrounded by a complex microstructural environment, unknown in detail and difficult to model, where elements such as cell membranes create partial barriers or obstacles to the molecular motion. These barriers or obstacles can restrict diffusion. The destruction of such biological barriers in disease is seen by an increase in ADC. Changes due to pathological process can modify the molecular environment and affect ADC, such as inflammation, edema, cell swelling or necrosis, membrane damage, demyelination, and others (Tofts, 2005).

1.1.2. Clinical interests of quantitative MRI

In 1971, Damadian (Damadian, 1971) attracted the attention of the medical community by his work on tumor detection in animals using relaxation time measurements based on NMR. He was the first to report that normal and pathological tissues can be distinguished by means of relaxometry. Ever since, relaxometry has gained paramount importance and proved to fundamentally advance the diagnostic power of MRI. Indeed, abnormalities observed on weighted-imaging can be associated with multiple biological disorders. To attain a greater understanding of the natural history of the disorder, characterize the extent of tissue injury, and monitor the temporal evolution of both individual lesions and the overall disease activity, additional quantification techniques need to be employed (Tofts, 2005).

Better characterization of tissues and pathologies

The intrinsic multiparametric-dependence of MRI signal, reflecting the interactions of water molecules on a cellular level, can provide such in vivo tissue characterization. As discussed in the previous sections, the direct link between the retrieved signal and tissue properties such as PD, T_1 , T_2 and diffusion can reflect tissue composition, allowing a direct characterization of tissues. Hence, tissue alterations can be detected with high specificity and sensitivity. Quantification, being objective and bias-free, has attracted increased interest as a potential biomarker for the detection of even subtle or diffuse pathological changes.

Earlier detection of pathological changes

In several studies, relaxation time measurements have demonstrated potential impact for the early diagnosis and progression monitoring of diseases in the human brain, body, and heart.

Relaxation time variation in the brain has been reported in numerous contexts to improve the detection and staging of various diseases, e.g. in studies concerning autism (Deoni, 2011), dementia (Erkinjuntti et al., 1987), Parkinson's disease (Baudrexel et al., 2010; Vymazal et al., 1999), multiple sclerosis (Larsson et al., 2005; Odrobina et al., 2005), epilepsy (Townsend et al., 2004; Liao et al., 2018), stroke (Bernarding et al., 2000), and tumors (Badve et al., 2016; Just and Thelen, 1988). Quantitative MRI can have considerable clinical value, as intervention or treatment could occur before neurons were irreversibly damaged or lost (Helpert et al., 2004).

In the body, measurements of transverse relaxation times (T_2 and T_2^*) have proven value for the assessment of iron accumulation occurring in many pathologies, e.g. in pancreas, spleen (Schwenzer et al., 2008), kidney (Schein et al., 2008), and the liver, where quantitative T_2 and T_2^* relaxometry has proven to be an accurate noninvasive means to measure absolute iron content and has replaced gold-standard biopsy procedures in many centers (Cheng et al., 2012). T_1 has also been investigated in the lung (Arnold et al., 2004; Jakob et al., 2001). Furthermore, relaxometry is an established method for the evaluation of cartilage disease and has shown ability to detect early biochemical changes before gross morphological alterations occur (Recht and Resnick, 1998). In muscle, diffuse lesions, hardly detectable with weighted imaging become clear with quantitative MRI, comparing with normal tissues references values (de Sousa et al., 2011). In cardiac applications, relaxation time measurements are beneficial for assessing cardiac iron overload (Ghugre et al., 2006), myocardial infarction (Van de Werf et al., 2008), edema (Giri et al., 2009), and hemorrhage (Bradley, 1993). Characterization

of atherosclerotic plaques in the main vessels has been shown to be improved when quantification of T_1 , T_2 and PD replaces qualitative assessment of the vessel walls (Yuan and Kerwin, 2004)

Quantitative MRI has been shown necessary to improve diagnosis or prognosis, and maybe to optimize therapy planning (Higer and Bielke, 2012). Recent studies investigate the possibility of predicting response of tumor to treatment using tissue relaxation times; e.g. the T_1 relaxation time can potentially be an indicator of chemotherapy response (Jamin et al., 2013; Weidensteiner et al., 2014). Several studies have demonstrated the utility of ADC and T_2 mapping in the quantitative evaluation of prostate cancer (Boesen et al., 2015; Hambrock et al., 2011). Currently, ADC mapping is the most widely used quantitative property in the imaging-based diagnosis and characterization of prostate disease (Yu et al., 2017). A comprehensive review of the medical relaxometry applications is given in (Cheng et al., 2012).

Longitudinal follow-up and Multi-centric evaluations

qMRI is a promising tool to isolate particular tissue properties without the confounding influence of other MR parameters. Indeed, accurate and precise measurements are made using careful techniques that take full account of all processes affecting the measurement. Determination of tissue-specific parameters in a quantitative way enables to directly compare MR images across subjects for a proper follow-up. For example, in addition to providing early diagnosis, quantitative relaxometry has been used to follow cartilage repair treatment (Trattin et al., 2011).

The quantitative results can also be compared between scanners for multi-centric evaluations, facilitating group comparisons. A recent example in the literature has shown that using the same sequence on different scanners with the same subject can lead to a variability of 0.8% within the human brain (Voelker et al., 2016).

1.1.3. Conclusion

We now understand the mechanisms that allow an ensemble of spins immersed in a magnetic field and excited by a RF pulse to relax back to equilibrium. These mechanisms reflect tissues properties. PD corresponds to the water content, and varies significantly in disease, although less than other parameters. More knowledge of its behavior may give important insights into biological processes underlying diseases. T_1 and T_2 can vary dramatically depending on pathology. The possibility to perform quantitative MRI opens the possibility of an earlier detection of pathological changes, through a better tissue characterization of tissues. It would also make possible longitudinal intra and inter-individual follow-up, as well as multi-centric

evaluations on different scanners. Retrieving such information with a high resolution would allow a better tissue characterization and would give more insights to the clinicians to pinpoint the exact diagnosis.

1.2. Enhancing MR signal using ultra-high fields strengths

With the aim of continuously improving MR images, higher magnetic field strengths are explored to obtain higher Signal-to-Noise Ratio and Contrast-to-Noise Ratio. Nevertheless, the use of these tools comes with physical constraints. Some solutions are being developed to tackle these limitations and are presented in this section.

1.2.1. The benefits to go towards higher field strengths

Signal-to-Noise Ratio

The signal in a voxel is generated from the total magnetic moment of the spins. There are different ways to enhance this signal, as shown in Equation (1.2). The inverse proportionality of M_0 to the temperature T indicates that sensitivity can be enhanced at lower sample temperatures. Obviously, it is unrealistic for in vivo applications. The other obvious solution comes from the linear dependence of M_0 on the magnetic field strength B_0 . It directly implies that higher magnetic fields improve the signal detected by the MR coil.

In the meantime, no direct relationship exists between noise and magnetic field strength. Therefore, based on Eq.(1.2), the Signal-to-Noise Ratio is expected to increase with B_0 . The theory indicates that it is true in a range of intermediate field, typically around 1.5T, but seems to deviate substantially from this rule with a very high magnetic field, evolving rather supra-linearly as predicted by Ocali (Ocali and Atalar, 1998) and confirmed experimentally by Pohmann in recent works, where $SNR \sim B_0^{1.65}$ (Pohmann et al., 2015).

Contrast-to-Noise Ratio

As important as having a high signal is the possibility to differentiate different neighboring tissues. Going towards more intense fields also influence relaxation times in a non-linear way, as shown in Figure 1.4. The susceptibility effects are exacerbated with magnetic field, leading to an increased sensitivity to T_2^* contrasts. T_1 also increases in tissues with field strength, but remain stable in liquids, as observed in Figure 1.2. Applications such as MR angiography benefits from this property, as the difference between the short T_1 of blood, and the longer T_1 of tissues is increased with field strength.

Physicians have adopted the high-field imaging technology and joined in to actively participate in its progress. Currently, the three major vendors have together installed more than 70 7T around the world (Polimeni and Uludağ, 2018). Siemens obtained the U.S. Food and Drug Administration (FDA) clearance as well as CE marking for a clinical 7T MRI device in October 2017, taking 7T one step closer to becoming a platform for advanced clinical imaging. Their installation and use for research purposes as well as clinical practice are expected to dramatically increase, as observed for 3T in the 2000's. The objectives of such an upmarket move are multiple in radiology, ranging from a better delimitation of lesions to the demonstration of lesions, invisible otherwise (Ge et al., 2008). Unfortunately, alongside the opportunities provided by UHF MRI, several challenges arise.

1.2.2. Challenges from ultra-high field MRI

B_0 heterogeneity

In areas where the difference between tissues' susceptibility is large, such as the air-tissue interface, substantial fluctuations are introduced into the static field observed by the spins, resulting in overall image degradation. Due to the dependence of magnetization M_0 on the external field B_0 , these non-uniformities become more pronounced in UHF MRI, as shown in Figure 1.5. Although these effects can be compensated with the aid of first and second-order shim coils, residual variations typically remain near intracranial cavities. These undesired disparities in the main field not only result in signal loss due to intra-voxel dephasing, but also in geometrical distortions originating from the bias introduced in the frequency encoding.

Different methods are developed to mitigate these undesirable effects, in particular by the use of additional shim coils to homogenize the B_0 up to higher orders. However, these are generally not sufficient. Indeed, at 7T, the slightest respiratory or pulsatile movement can cause large fluctuations in B_0 , going as far as the brain. For this reason, more and more research centers using UHF are moving towards “dynamic shimming” techniques, for example, with field probes that measure and correct these variations in real time. This subject was not in the scope of this work, but more information can be found in literature (Aghaeifar et al., 2018; Vannesjo et al., 2014).

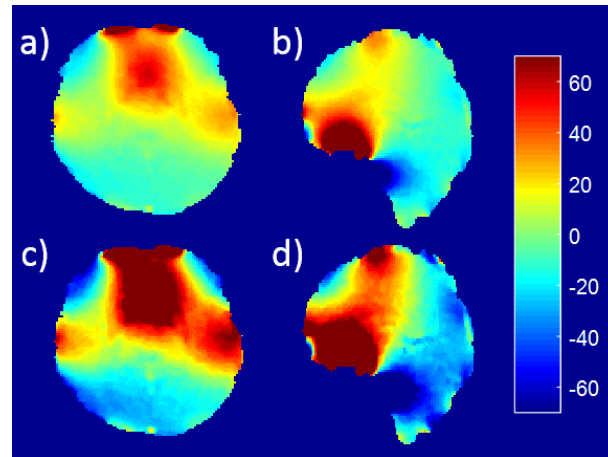


Figure 1.5 : ΔB_0 maps (in Hz) acquired at 3T (a, b) and simulated for 7T (c, d).

B₁ heterogeneity

UHF MRI benefits in terms of SNR and CNR are undermined by the huge disadvantage of the inhomogeneous propagation of the radiofrequency field in the human body at 297MHz. Indeed, the RF excitation of spins should be as uniform as possible to obtain a consistent contrast. The homogeneity of the B₁ field comes from several elements, from which the architecture of the coil constitutes a first factor. In addition, the electromagnetic behavior of tissues constitutes a second factor. It is mainly characterized by two properties. First, the relative permittivity of tissues, ϵ_r , characterizes the ability of atoms to move and orient under the effect of an electric field. Secondly, their conductivity, σ , affects the resulting current density during free charge transport. It defines their ability to let electric charges move under the effect of the electric field. These quantities are related to the magnetic field and the electric field by the Maxwell's equations, governing the laws of electromagnetism (Maxwell, 1865). David Hoult (Hoult, 2000a) has shown that these dielectric properties of the human tissues are modified from 3T and above. This impacts the Maxwell equations and will affect the B₁ excitation field.

Figure 1.6 illustrates the electromagnetic problem encountered at 297 MHz on a sphere as well as on the head. The B₁ fields retrieved from a classic birdcage coil at this frequency in the presence of a human head or a sphere of same permittivity show the B₁ heterogeneity that needs to be tackled.

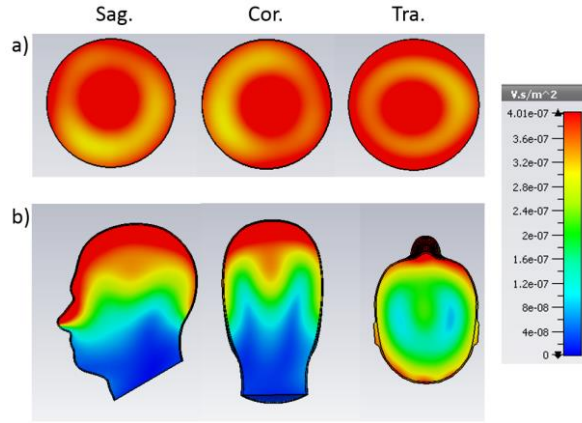


Figure 1.6 : B_1 field resulting from a 16-leg birdcage coil at 297MHz using CST software a) on a sphere b) on a specific anthropomorphic phantom, both filled with same permittivity and conductivity material of $\epsilon_r = 42$ and $\sigma = 0.99$ S/m.

These different factors result in cancellations in certain regions during RF transmission. This leads to dark areas in the image, revealing interference phenomena called “dielectric artifacts” (Hoult, 2000a), even when the desired flip angle α is locally attained in other regions (Van de Moortele et al., 2005) (see Figure 1.7).

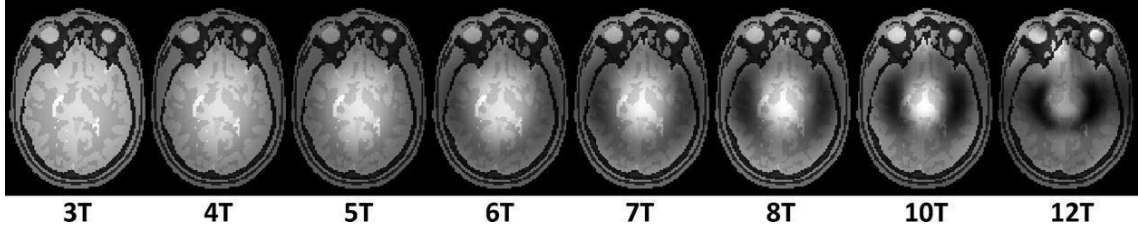


Figure 1.7 : Simulated gradient echo images as a function of the magnetostatic field B_0 using a bird-cage coil with ideal current distributions in the rungs. From (Webb, 2011).

Specific Absorption Rate (SAR)

For a given pulse and flip angle α , an increased energy deposition is encountered at UHF (Bottomley and Andrew, 1978; Hoult, 2000a). For a conducting sphere of radius b and of specific resistance R_S , the power dissipated in a homogeneous way is (Hoult and Lauterbur, 1979):

$$P = \frac{\pi \omega_0^2 B_1^2 b^5}{15 R_S} \quad (1.12)$$

We can observe the quadratic relation of the power dissipated in the object with the magnetostatic field B_0 and with the field B_1 . This has two consequences: first, it is necessary to send more power to obtain a sufficient field B_1 at any point in the region to be imaged. Second, more power is absorbed by the body, resulting in a rise in temperature that could lead to tissue damage.

Since the equipment is not able to directly measure the temperature generated by the coil in the tissues, limitations on the power of the transmitted RF have been established, based on the Specific Absorption Rate (SAR). International standards (IEC 60601-2-33) provide guidelines for the maximum energy deposition in human subjects to provide sufficient safety with respect to the induced temperature. These recommendations are based on the one hand on the measurement of the global SAR, that is to say the SAR induced in all the considered volume (here, the whole head) and on the other hand on the local SAR, induced in 10g of tissue. The recommendations of this standard for SAR for a human head are presented in Table 1.1.

These values are based on various scientific studies (Athey, 1989; Athey and Czerski, 1988; Barber et al., 1990) stating that temperatures of 38 °C located in the head, 39 °C in the trunk and 40 °C in the extremities, are not likely to have harmful effects. Therefore, for the head, these standards are established so that the temperature rise in the eye, an unperfused anatomical part, does not exceed 2°C.

	10s	6min
Local SAR (10g)	20W/kg	10W/kg
Global SAR (whole head)	6,4W/kg	3,2W/kg

Table 1.1 : International SAR standards for acceptable limits for a human head based on two scales (spatial and temporal)

It turns out that, according to Hoult, (Hoult, 2000a), the evolution of the SAR as a function of the frequency and as a function of the distance in the sample is not linear. Figure 1.8 shows that for any fixed distance z , when the frequency increases, the SAR reaches a maximum and then decreases. The same goes for a fixed frequency.

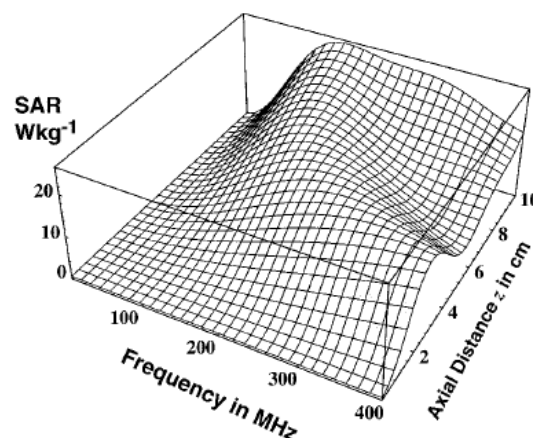


Figure 1.8 : Absolute value of SAR in a sphere of 10cm radius, for a B_1 field applied by a quadrature coil of 5.87uT ($\nu = 250\text{Hz}$), depending on the frequency and depth in the load. (Hoult, 2000a)

Therefore, to obtain images only depending on the relaxation properties of the tissue to be analyzed, it is essential to mitigate the B_1 field locally at 7T, to homogenize the spins' flip angle at every pixels, while taking care to not exceed SAR limitations.

1.2.3. Solutions

1.2.3.1. Dielectric pads and meta-materials

As seen in simulations (Figure 1.6 and Figure 1.7) and confirmed by images obtained on human brain in vivo at 7T, dark areas appear in the temporal lobes and in the cerebellum area when using a standard birdcage. It is necessary to modify the B_1 field locally to homogenize the flip angle at any point in the image.

One way to do this would be to better adapt the coils to the medium to be imaged by adding materials in the coil. The study of the literature shows that this adaptation can be achieved by applying pads composed of a mixture of water and high permittivity materials on the skin of the patient (Brink and Webb, 2014; Yang et al., 2006), near the temporal lobes or in front of the cerebellum. The permittivity of the air is close to that of the vacuum whereas that of the water is much higher (≈ 80 at 20 °C). Replacing the air with a high permittivity material makes it possible to carry out an impedance adaptation, thus avoiding electromagnetic losses.

Quantitative measurements have shown that these high permittivity pads introduced into the coil do not increase global or local SAR (Teeuwisse et al., 2012a), while significantly increasing the quality of the image, particularly in the temporal lobes and the cerebellum, as shown in Figure 1.9.

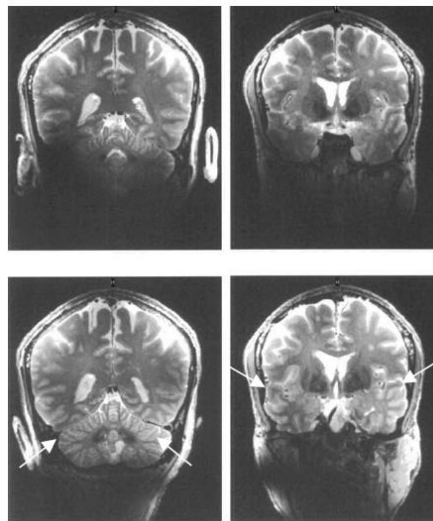


Figure 1.9: Images from a Turbo Spin Echo sequence (T_2 -weighted), without dielectric pads (first line) and with dielectric pads (second line). The white arrows show the areas particularly improved by the dielectric pads, from (Teeuwisse et al., 2012a).

Unfortunately, dielectric pads are not entirely fulfilling the requirements to be used in UHF clinical routine. They represent an important bulk in the coil, they reduce patient's comfort, and they degrade rapidly. Some materials can be expensive and others like barium titanate (BaTiO_3), referenced as toxic. To foster the RF transmission and avoid these inconveniences, a solution based on the use of Meta-Material structures, acting like a magnetic resonators in the RF coil, has been proposed by the Institut Fresnel in collaboration with Neurospin and is currently being studied. It will be discussed in more details in Chapter 4

1.2.3.2. Parallel transmission

RF static shimming

To address the origins of the problem, another solution adopted in the community is the use of parallel transmission (pTx). The coil remains a birdcage, but each rung is powered by separate amplifiers instead of a single one. The interferences of these n_T transmission channels are then optimized to produce a more homogeneous RF field. In RF static shimming, the same RF pulse waveform, $p(t)$, is transmitted on each channel, scaled by a channel-specific complex weight, w_c , so that the sum of the fields is as homogeneous as possible, according to the following equation:

$$B_1^+(r, t) = p(t) \sum_{c=1}^{n_T} w_c S_c(r) \quad (1.13)$$

Where $B_1^+(r, t)$ is the resulting field in position r of the volume at time t , $S_c(r)$ is the spatial transmit sensitivity produced by each channel, and w_c is the complex coefficient (magnitude and phase) applied to each transmitting coil to obtain a $B_1^+(r, t)$ as close as possible from the targeted value in every point of the region of interest.

To estimate the coefficients w_c , a calibration of the system is necessary. It consists in the acquisition of B_1^+ maps from each of the n_T channels separately, to perform an adjustment to optimize the different w_c . This new degree of freedom given by such technology makes possible the correction of a large part of the problems encountered at 3T on large organs. At higher fields, this approach unfortunately only partially solves the problems encountered.

RF dynamic shimming

Another more complex solution is to determine individually the excitation that will be applied in each region of the space. Yip and colleagues have proposed a method to design pulses that satisfy this query (Yip et al., 2005). The counterpart is in very long pulses that are difficult to use in a conventional sequence pattern. Thus Grissom (Grissom et al., 2006) and

Katscher (Katscher and Börnert, 2006) have proposed an extension of this approach by taking advantage of multichannel transmission systems.

In that case, it is not a static complex coefficient w_c that is optimized for each transmission channel but rather a pulse specific to each channel, p_c , taking into account their respective behavior $S_c(r)$. We then speak of a “dynamic B_1^+ shimming”. This can be written:

$$B_1^+(r, t) = \sum_{c=1}^{n_T} p_c(t) S_c(r) \quad (1.14)$$

Like static shimming, it is necessary to make a specific calibration of each of the channels according to the patient placed in the coil. To further reduce the pulses durations, more effective strategies have been proposed in recent years as was able to synthesize Padormo in a review article on the subject (Padormo et al., 2016). These solutions are very elegant but require computing time during the exam and are very complex. More recently, (Gras et al., 2017a) came up with a solution taking advantage of the reproducibility of the brain shape to provide a push-button solution, called “Universal Pulses”. Given a coil and a sequence, this solution provides a pulse applicable to any patient in the scanner, avoiding such loss of time and efficiency in clinical routines for the brain. These solutions will be discussed in more details later on in this manuscript. The application of such techniques allows to make the most of UHF, in order to obtain high-resolution quantitative images, to go further in the quantification of tissues and possible diagnosis. To perform such quantification, different strategies can be adopted, as will be presented in the next chapter.

Chapter 2.

Measuring NMR parameters

Quantitative MRI relies on measurement of NMR parameters of interest listed in Chapter 1 in a robust manner. The measurement must not depend on any external factor, but only reflect tissue properties and environment. Different approaches have been studied to retrieve such information. In this section, we will first describe the Spin-Echo sequence, used for gold-standard measurements, and show how it is used to properly retrieve quantitative measurements. Although some acceleration strategies can be adopted, these spin-echo based solutions are still long and can hardly be applied in clinical routine at UHF. Another strategy is to use Steady-State Free Precession (SSFP) sequences, described later on in this section.

As the correlation of multiple complementary NMR parameters could help in the interpretation of the physio-pathological events, strategies for implementing multi-parametric simultaneous measurements in a single sequence are currently being developed in the literature, usually based on such SSFP sequences. A brief and qualitative overview of these methods will also be presented in this chapter, discussing the feasibility to apply each strategy at 7T. Finally, the objectives and challenges of this PhD thesis will be described.

2.1. Measuring NMR parameters of interest

2.1.1. Spatial encoding

To perform imaging, the vast majority of sequence consists of a train of excitation pulses that are separated by a constant repetition time (TR). A specificity of MRI is that the images are acquired in the Fourier domain, by filling the “k-space”. This k-space encoding is performed between consecutive excitation pulses by means of switched magnetic gradient pulses, oriented along arbitrary X, Y and Z logical directions, called read, phase, and slice-selection directions. Their intensities vary over time in order to spatially encode the signal coming from the spins. Indeed, when considering a cluster of spins that precess with the same frequency (called an isochromat), these gradients will induce local magnetic field variations, leading to a unique precession frequency for each isochromat at a distinct spatial location. This precession frequency, depending on the spatial coordinates of the spins, allows to retrieve their location. Figure 2.1 illustrates a basic chronogram of a sequence and the associated k-space sampling pattern. Different gradient-switching patterns can be used to encode the image. The most widespread sampling strategy is the use of Cartesian encoding, where regularly spaced lines (frequency encoding or readout) are acquired each TR, the orthogonal coordinates corresponding to the incremental phase encoding steps. Other non-Cartesian methods can be applied to reduce acquisition time, but are out of the scope of this manuscript. Information can be found in (Lauterbur, 1973; Ahn et al., 1986; Pipe, 1999).

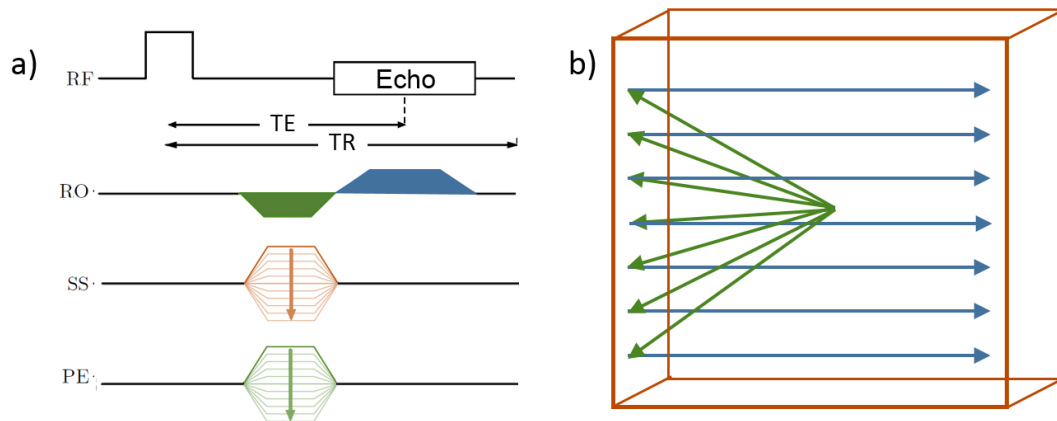


Figure 2.1: a) Chronogram of a 3D Gradient Recalled Echo (GRE) sequence and b) associated schematic sampling pattern in k-space. RF: Radiofrequency emission, RO: Readout gradients, SS: Slice Selection gradients, PE: Phase-Encoding gradients. Colors in the chronogram corresponds to associated displacement in the k-space.

By applying an inverse Fourier transformation, the matrix of NMR signals is reverted into an MR image in the space domain and an image is retrieved, as shown in Figure 2.2.

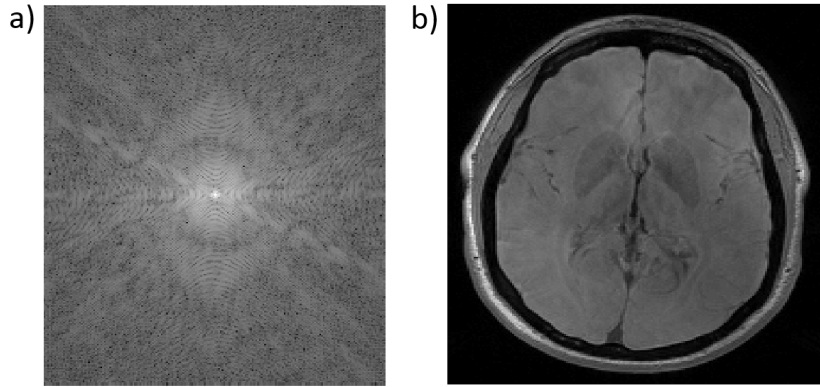


Figure 2.2 : Logarithm of the modulus of complex k -space NMR data (a) and the magnitude of the associated reconstructed image through 2D discrete inverse Fourier transform (b)

We now understand pulse sequence diagrams, and how images can be retrieved using MR. The very basic pulse sequence is called the “Spin-Echo” (SE) experiment, originally discovered by (Hahn, 1950) in spectroscopy. It is now used to perform imaging and has many variations, as described in the following section.

2.1.2. Spin-Echo sequences

2.1.2.1. Spin-echo

In the Spin-Echo experiment, a first flip angle α_1 is applied to the system. Once this excitation has been applied to the system, because of the presence of imaging gradients, these spin isochromats have a range of precession frequencies. Some precess faster than the Larmor frequency, while others precess slower. This produces a phase dispersion among the spin isochromats. The application of a “refocusing RF pulse” of flip angle α_2 will rotate the dispersing spin isochromats about an axis in the transverse plane so that the magnetization vector will rephase (or refocus) at a later time (Haacke et al., 2014). Figure 2.3 presents a simplified picture of the behavior of the individual spins during the experiment.

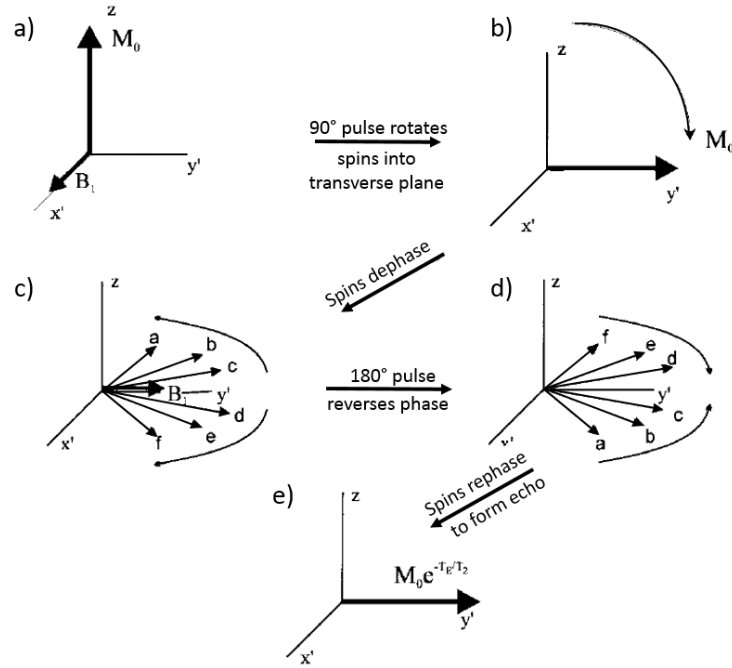


Figure 2.3 : Description of spins behavior during a spin echo experiment. a) Spins are along z-axis, forming M_0 vector. b) A 90° pulse rotates the spins around the x' -axis, into the transverse plane where they begin to precess. c) The spins accumulate extra phase, until d) this accumulation is inverted by the 180° refocusing pulse. The spins continue to collect extra-phase at the same rate and, at a later time, e) all spins return to the positive y' -axis together, forming a spin echo. The echo amplitude is reduced by the intrinsic T_2 decay. From (Haacke et al., 2014)

An expression for the retrieved signal can be derived (Bernstein et al., 2004):

$$S = M_0 \sin \alpha_1 \sin^2\left(\frac{\alpha_2}{2}\right) \frac{1 + (\cos \alpha_2 - 1)e^{-\frac{TR - \frac{TE}{2}}{T_1}} - \cos \alpha_2 e^{-\frac{TR}{T_1}}}{1 - \cos \alpha_1 \cos \alpha_2 e^{-\frac{TR}{T_1}}} \quad (2.1)$$

If $T_1 \ll \left(TR - \frac{TE}{2}\right)$, then the signal in Eq. (2.1) is maximized by setting $\alpha_1 = 90^\circ$ and $\alpha_2 = 180^\circ$, leading to:

$$S \propto M_0 e^{-\frac{TE}{T_2}} \left(1 - 2e^{-\frac{TR - \frac{TE}{2}}{T_1}} + e^{-\frac{TR}{T_1}}\right) \quad (2.2)$$

Therefore, to refocus transverse magnetization optimally, refocusing RF pulses commonly have a flip angle of $\alpha_2 = 180^\circ$. Other values of the flip angles can be used with shorter TR to increase the signal or to maximize the contrast between a particular pair of tissue types. Sometimes, a lower value of the flip angle of the refocusing pulse is used to reduce SAR, particularly at 3.0T and above.

Spin-Echo sequences are usually obtained in 2D mode. Figure 2.4 shows a typical 2D Spin-Echo pulse sequence diagram, with the RF excitation, Readout (RO), Slice-Selection (SS) and Phase-Encoding (PE) gradients used for Fourier encoding.

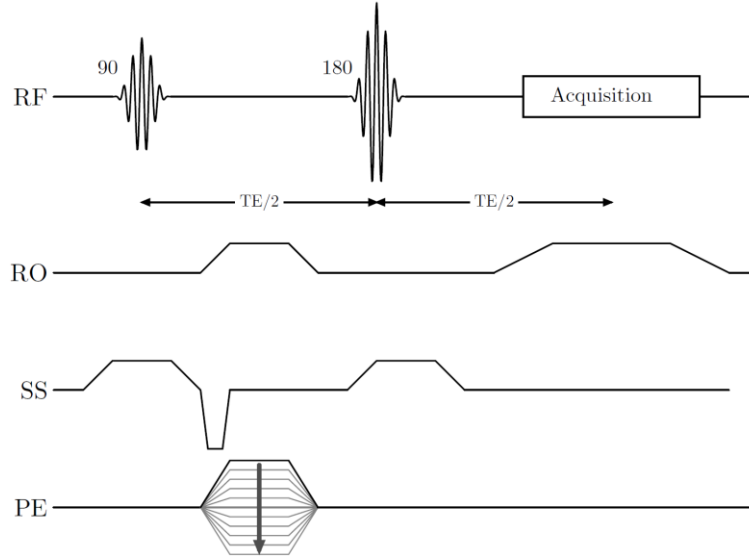


Figure 2.4 : Spin-Echo sequence diagram. The Readout (RO), Slice-Selection (SS) and Phase Encoding (PE) axis contain gradients to encode the k -space from one TR to the other.

As shown in Eq. (2.2), the signal of a SE sequence depends both on T_1 and T_2 . To produce T_1 - or T_2 - weighted contrasts, there are many variants to this basic SE pulse sequence. Mainly, they consist in the addition of a “magnetization preparation” block to the sequence, or in the modification of the applied RF pulse or imaging gradients, or even TE and TR, thus probing the signal differently. Some of the possibilities, used for quantitative MRI, are described here.

2.1.2.2. Spin-Echo Echo-Planar imaging (EPI)

Echo-Planar Imaging (EPI) is a way to encode the k -space in order to accelerate MRI acquisitions. It can be applied in multiple sequences. In a Spin-Echo EPI sequence, the readout gradient encoding is applied, after the combination of 90° and 180° pulses, alternating quickly and therefore probing a spin echo for each oscillation, as shown in Figure 2.5. Each oscillation corresponds to a given line of the k -space. Phase-encoding blips are then applied for each echo, moving from one line to the next. Thus, each k -space line along the phase-encoded direction is acquired at a different TE. The effective TE of the sequence, TE_{eff} , is defined as the TE when the central line is acquired. The TE of the spin echo may or may not correspond to this TE_{eff} . When they both coincide, the image becomes predominantly T_2 -weighted, instead of T_2^* -weighted.

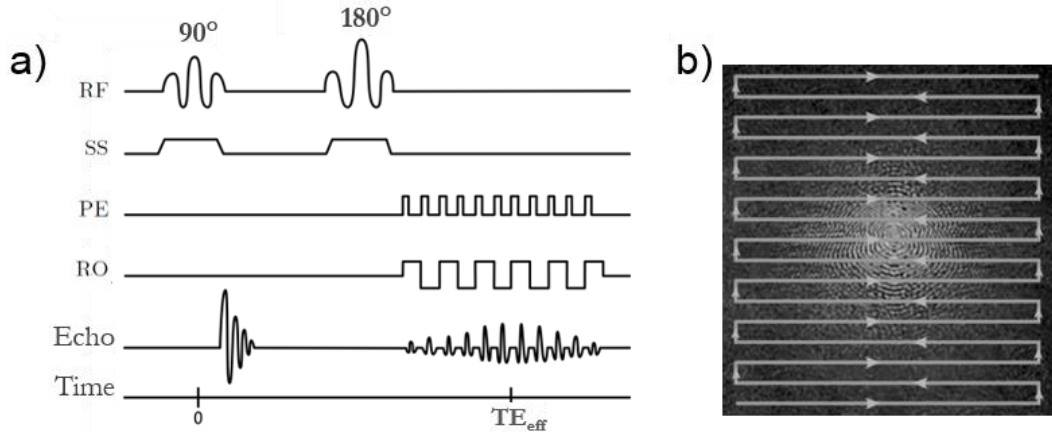


Figure 2.5: a) Spin-echo EPI sequence scheme. b) Illustration of an EPI k-space trajectory. From (Hammer, 2013) and (Elster, 2018)

This sequence scheme is very sensitive to refocusing pulse inaccuracies, but has the advantage to use only one 180° pulse. Therefore, no stimulated echoes are generated. However, the number of useful echoes is limited, to reduce the T_2^* -weighting of the acquisition, as illustrated in Figure 2.5a.

2.1.2.3. Multi-Echo Spin Echo and Carr-Purcell-Meiboom-Gill (CPMG)

In a SE sequence, the transverse magnetization that forms a SE can be repeatedly refocused into subsequent SEs by playing additional 180° RF refocusing pulses. The use of such strategy is called “Multi-Echo Spin Echo”, and allows the acquisition of several echoes with varying TEs. The series of echoes obtained with this process is called an echo train. The series of SE are refocused at times TE_1 , TE_2 , TE_3 , and so on. Each echo number fills its own independent k-space, which is reconstructed with 2D Fourier transform.

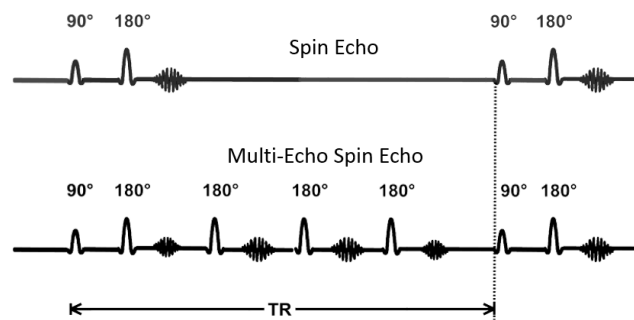


Figure 2.6 : Excitation scheme of conventional Spin Echo and Multi-echo spin echo (adapted from (Elster, 2018))

This strategy seems interesting, but two images produced from echoes with the same TE value may differ, depending on the number of preceding refocusing pulses. Indeed, errors in the 180° pulse are cumulative. Therefore, the magnetization will rotate out of the transverse plane. In addition, the T_2 exponential decay of the signal influences the contrast, but also

limits the number of useful echoes possible to acquire. Finally, contributions from stimulated echoes can introduce unwanted T_1 -weighting variations into the echo-train signals (Bernstein et al., 2004).

The Carr-Purcell-Meiboom-Gill (CPMG) sequence (Carr and Purcell, 1954; Meiboom and Gill, 1958) is an enhancement of this approach in which the phase of the RF pulses is modulated to compensate for small deviations in the refocusing efficiency. In other words, if the 90° -pulse is applied along the x-axis, the 180° -pulses are applied alternately along the $\pm y$ -axes. Timings and gradients shapes of this CPMG sequence must be studied cautiously to avoid the superposition of stimulated echoes to the echoes of interest, based on the Extended Phase Graphs (EPG) theory (Weigel, 2015).

2.1.2.4. T_2 measurement

The goal of T_2 mapping is to provide a calculated image in which each pixel value quantitatively represents the average T_2 of the tissue within that voxel. In Eq. (2.2), SE sequences show a clear dependence on T_1 , T_2 , TE and TR. To assess T_2 properly, it is necessary to null the TE dependence on the longitudinal magnetization, which will introduce an unwanted T_1 dependence into the SE signal.

It is possible to reduce Eq. (2.2) to the simple form of Eq. (2.3) by setting TR to be much greater than T_1 and therefore TE (see Eq. (2.2)). It is much longer, but in this case, SAR should not exceed limits, even at UHF.

$$S \propto M_0 e^{-\frac{TE}{T_2}} (1 - e^{-\frac{TR}{T_1}}) \quad (2.3)$$

As TE is extended, the signal intensities in the images decrease in an exponential manner as described by Eq. (2.3). As any echo has the same TR/ T_1 dependence, assuming constant spin density, a series of images S_i is generated so that:

$$S_i(t) \propto S_0 e^{-\frac{TE_i}{T_2}} \quad (2.4)$$

Where the subscript i is used to denote the i -th image with echo time TE_i and S_0 is proportional to the PD. The acquisition of these multiples TE can be performed using a simple SE sequence repeated several times, but acquisition time can be prohibitive. In this case, spin-echo EPI is often preferred, using a short train of echoes to reduce T_2^* effects. T_2 CPMG, cautiously applied considering stimulated echoes as mentioned above, can also be used. A voxel-wise mono-exponential fitting procedure is performed on the dataset using least squares minimization, so that a value for T_2 is calculated for each voxel over the region of interest. In order to measure an accurate T_2 , a sufficient number of TE must be sampled to

define an exponential function. However, acquiring too many time points takes time, thus limiting the applicability in clinical routine.

2.1.2.5. T_1 measurement

To exacerbate T_1 weighting in Spin-echo images, contrast can be manipulated using a magnetization preparation module. It consists in flipping the longitudinal magnetization from the +Z to -Z axis using an “inversion pulse”. A time delay, TI , called the inversion time, is then provided to allow the inverted magnetization to recover towards its equilibrium value before applying the pulse of the subsequent spin-echo sequence, as shown in Figure 2.7. Tissues with different T_1 will recover at different rates, creating a T_1 contrast among them. The next RF excitation pulse will convert the differences in the longitudinal magnetization into differences in the transverse magnetization. Pulse sequences with an inversion pulse followed by a time delay prior to an RF excitation are known as “inversion recovery” (IR) sequences.

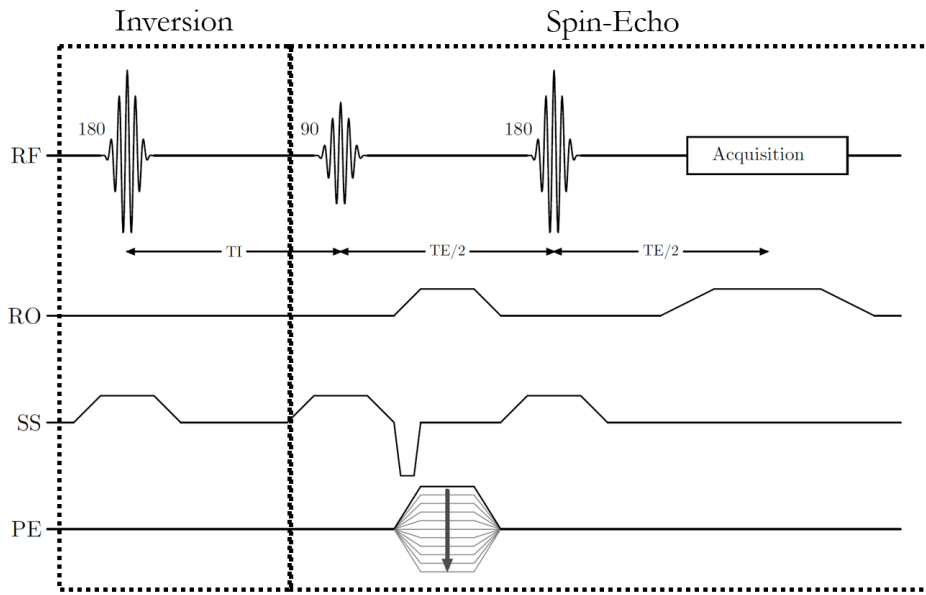


Figure 2.7 : Inversion Recovery Spin-Echo sequence diagram. A first inversion pulse of 180° is applied with a delay time of TI before the application of a Spin-Echo sequence.

Following an IR pulse of 180° , the available magnetization at the time of excitation is:

$$S(TI) = S_0 (1 - 2e^{-\frac{TI}{T_1}}) \quad (2.5)$$

Where $S(TI)$ is the signal measured at time TI , and is proportional to the T_1 -magnetization at that time, and S_0 is the signal that would be acquired from the equilibrium longitudinal magnetization.

IR pulse sequences have many applications and are widely used in clinical practice. In addition to producing images with a broad range of T_1 -weighted contrast, IR is also used to

generate selective signal attenuation, such as lipid suppression, fluid attenuation, and blood-signal nulling in black-blood angiography. IR sequences are also used to perform conventional T_1 mapping.

To map quantitatively T_1 , a series of IR images followed by a SE sequence are acquired from the same location, each with a different TI while keeping all other parameters identical. To avoid signal saturation, a long $TR > 5T_1$ must be used. The pixel intensity of the image is then plotted as a function of TI as shown in Figure 2.8. In this way, the recovery curve can be sampled and T_1 can be estimated by fitting Eq. (2.5) to the data.

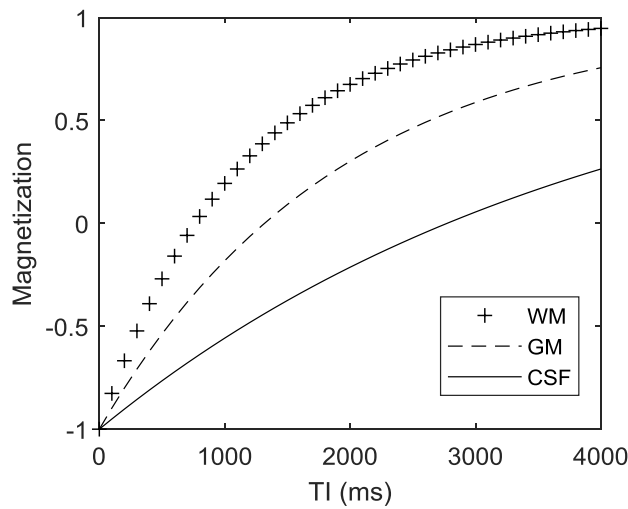


Figure 2.8: IR magnetization before excitation according to the inversion time. WM, GM and CSF exhibit different relaxation times. The fitting of this curve with Eq. (2.5) leads to an estimation of the corresponding T_1 of the tissue.

Provided that the inversion pulse is perfect across the whole sample, this will give an accurate measurement of T_1 . Of course, this inversion pulse combined with the very long acquisition time constitute limiting factors for an application in clinical routine at UHF.

2.1.2.6. Diffusion-weighted Spin-Echo

Diffusion imaging tracks the movement of water molecules in the presence of tissue micro-structure, which hinders and restricts the natural tendency of water to diffuse freely in all directions. To increase the sensitivity to diffusion, all diffusion imaging pulse sequences contain a diffusion-weighting scheme. In principle, diffusion weighting gradients can be incorporated into any pulse sequence, although sequences employing RF spin echoes are more popular than those based solely on gradient echoes.

To obtain diffusion-weighted imaging, the historical sequence of Stejskal-Tanner (Stejskal and Tanner, 1965), as described in Figure 2.9a, is usually used. It is a SE sequence, in which strong gradients are played in the readout direction, to encode and then decode spatial positions at a very fine scale.

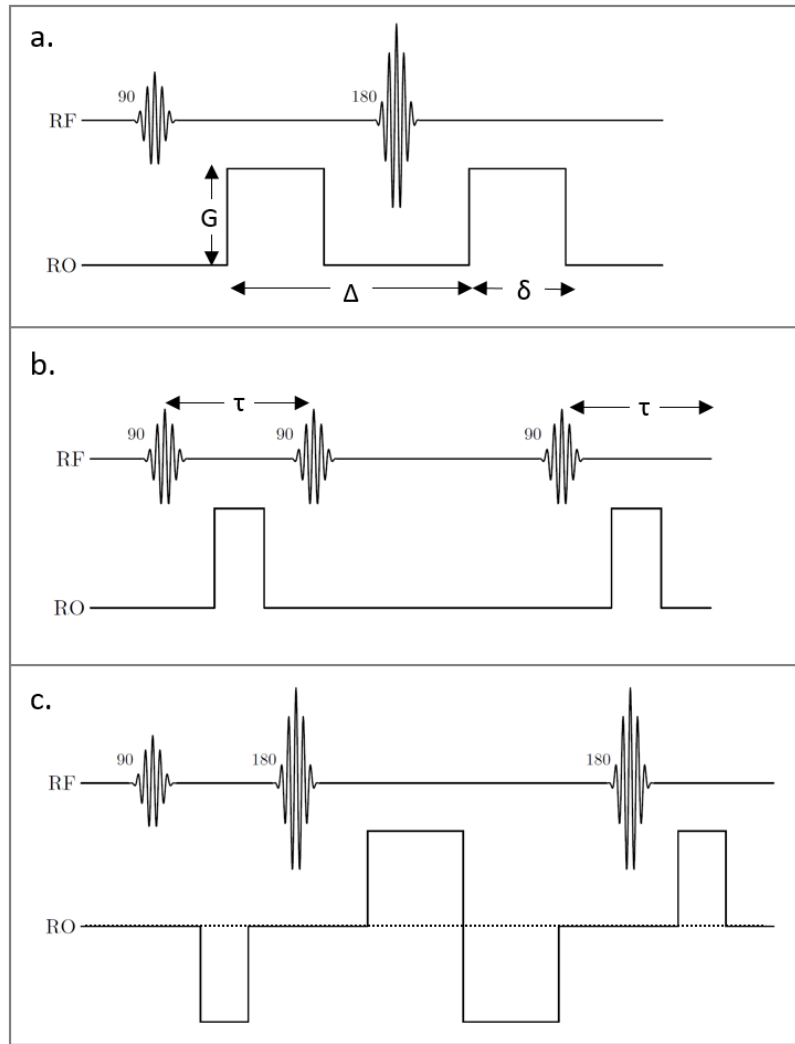


Figure 2.9 : (a) Diffusion-weighted spin echo scheme (Stejskal-Tanner sequence). A pulsed gradient, g , is introduced in the sequence, either side of the 180° refocusing pulse. The amplitude G , duration δ and timing of g determine the amplitude of the spin echo, while the inter-pulse delay Δ and the duration of the pulse define the diffusion time $t_d = \Delta - \frac{1}{3}\delta$. (b) Diffusion-Weighted Stimulated Echo Acquisition Mode (DW-STEAM) pulse sequence. The diffusion-weighting gradient can be applied to any axes. (c) Twice-refocused SE sequence showing added 180° refocusing pulse and gradients

In practice, other sequences can be used, such as STEAM (STimulated Echo Acquisition Mode) and Double Spin-Echo. STEAM consists in the application of three 90° -pulses with the same phase to produce a stimulated echo. The first two pulses are separated by a time delay τ , as shown in Figure 2.9b. After the same delay τ following the third pulse, a stimulated echo is produced. Two identical diffusion gradient lobes are applied during these τ intervals to obtain a diffusion weighting. This technique allows to retrieve high b -values with low TE compared to the method described above. However, as this method relies on the acquisition of a stimulated echo, the SNR is less than what would be expected for a primary echo.

While the usual SE diffusion sequence introduced by Stejskal and Tanner uses a single refocusing RF pulse, many SE diffusion sequence variants can be created. Adding RF refocusing pulses and splitting the gradients into shorter pulses of alternating polarity allows the reduction of residual fields during the on and off gradient transitions. It was originally proposed by (Reese et al., 1998) and is now very often used, usually built into an EPI k-space trajectory to reduce the acquisition time.

2.1.2.7. ADC measurement

In the presence of a gradient, molecular diffusion attenuates the MRI signal exponentially (Bernstein et al., 2004) :

$$S = S_0 e^{-bD} \quad (2.6)$$

Where S and S_0 are the voxel signal intensity with and without diffusion respectively, D is the diffusion coefficient along the direction of the applied diffusion gradient, and b is called the b -value, that controls the degree of diffusion weighting in the image. The b -value is related to an arbitrary single axis gradient waveform $G(t)$ by (Le Bihan et al., 1986):

$$b = \gamma^2 \int_0^{TE} \left[\int_0^t G(t') dt' \right]^2 dt \quad (2.7)$$

For rectangular lobes in a spin-echo pulse sequence used in the Stejskal-Tanner sequence, Figure 2.9, b is:

$$b = \gamma^2 \delta^2 G^2 \left(\Delta - \frac{\delta}{3} \right) \quad (2.8)$$

To measure the diffusion coefficient, different acquisitions with different diffusion weightings b will be used. A least-squares fit can then be implemented to solve Eq. (2.6). In the simplest case where two acquisitions $S(b_1)$ and $S(b_2)$ with different diffusion weightings b_1 and b_2 are used, diffusion can be retrieved using:

$$D = \frac{1}{b_1 - b_2} \ln \left(\frac{S(b_2)}{S(b_1)} \right) \quad (2.9)$$

2.1.2.8. PD measurement

All images acquired in MR are PD-weighted. Therefore, PD values can be measured from the image intensity in the absence of any T_1 or T_2 contrast. Practicalities from B_1 or B_0 heterogeneities may prevent this from being possible, and suitable corrections for T_1 and T_2 losses need to be made. Extracting such information using multiple Spin Echoes may be nonviable. Thus, Spin-Echo sequences are usually disregarded and replaced by Steady-State Free Precession (SSFP) sequences to perform several individual acquisitions for mapping all parameters influencing signal amplitudes, followed by correction of measured image intensities (Neeb et al., 2006, 2008).

2.1.3. Steady-State Free Precession (SSFP) sequences

When TR becomes significantly lower than T_1 and TE is lower than T_2 , a transverse magnetization remains at the end of TR after the application of a certain flip angle. Therefore, the next excitation pulse will act on the modified magnetization. To obtain images, this process of rotation and relaxation is repeated again and again. It can be shown that a steady state of the magnetization will be established after several TR periods ($\sim 5T_1$). That means that the values of the magnetization magnitude from corresponding time points in adjacent TR interval will be the same. This situation is called steady-state free precession (SSFP) and was formally first described by Carr (Carr, 1958).

Different steady states are established for different gradient switching patterns. SSFP techniques can be divided into two groups. First, “refocused” or “balanced” steady-state sequences, where both longitudinal and transverse magnetization are allowed to reach steady state; and second “spoiled” steady-state sequences, where the transverse magnetization is made zero, or spoiled, prior to every RF pulse, so that only the longitudinal magnetization attains steady state, at least theoretically.

2.1.3.1. Balanced SSFP

Balanced SSFP (b-SSFP) is a special type of SSFP sequence where each applied gradient pulse is compensated by a gradient pulse with opposite polarity within TR, to make sure that no uncontrolled transverse magnetization remains, as shown in Figure 2.10. In other words, the gradient-induced spins’ dephasing within TR is exactly zero. The only source of phase accrual is due to off-resonance precession, coming for example from field variations reflecting an imperfect shim. The well-shimmed voxels will be roughly characterized by a single resonance frequency, creating image contrast that reflects the local magnetic field in addition to T_1 and T_2 (Oppelt et al., 1986). This sequence goes by the name of “TrueFISP” on Siemens scanners, “Fiesta” for General Electrics and “Balanced FFE” for Philips equipment.

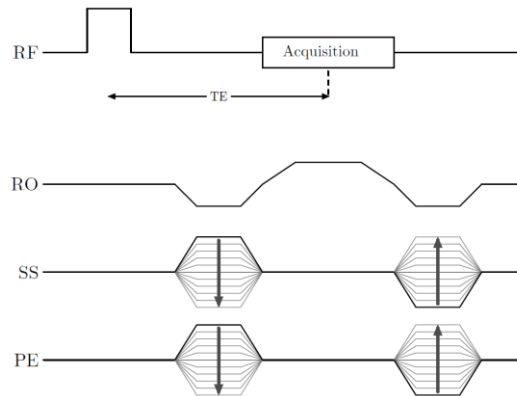


Figure 2.10 : 3D Balanced Steady-State Free Precession (b-SSFP) sequence diagram. Each axis displays compensated gradients areas at the end of a TR.

In typical applications, the achievable field homogeneity is approximately 50 Hz for the brain. A frequency offset ν (frequency difference between radiofrequency synthesizer of scanner and local precession frequency of the magnetization) results in a dephasing of $\theta = 2\pi\nu TR$ within TR. It is obvious that this additional dephasing leads to a modification of the resulting steady state, and hence to a certain deviation from the ideal oscillation around the Z-axis. This leads to the well-known “banding artifacts”, characterized by strong signal drops at regions where $\theta = \pm\pi$ (or when $\nu = \pm \frac{TR}{2}$) (Scheffler and Lehnhardt, 2003), shown in Figure 2.11.

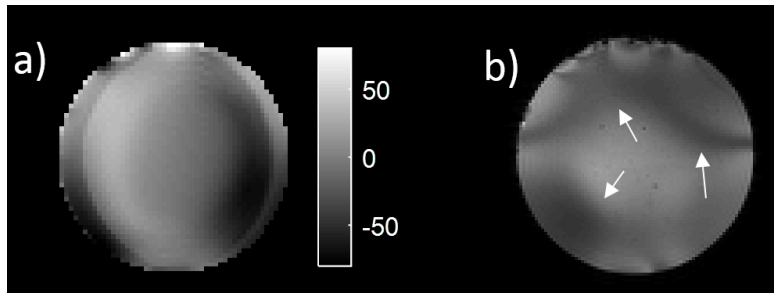


Figure 2.11 : (a) ΔB_0 map (in Hz) and (b) Balanced SSFP sequence applied at 7T on a phantom containing water and 1% of agar, with TR/TE=10/5ms and Flip Angle=20° with no phase offset. Banding artefact can be observed as highlighted by white arrows.

These banding-artefacts can be addressed by performing an alternation of the sign of the phase given to the RF pulse, as shown in Figure 2.12. As the accumulated phase is proportional to the repetition time TR, shortening the TR in the range of 7ms or less can also be done, especially because susceptibility variation is inevitable and can rarely be shimmed out completely. Work was done to combine multiple images with the bands shifted, which can be accomplished through alterations of the phase given to the RF pulse (Vasanawala et al., 2000).

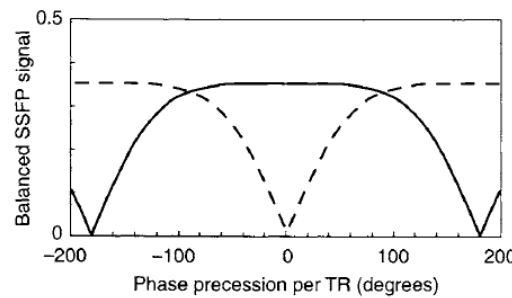


Figure 2.12 : Plot of a b-SSFP signal as a function of phase precession per TR of the transverse magnetization. When the RF pulses are sign alternated (solid line), strong signal results on resonance with phase precession of 0 and a minimum of the signal (a band) occurs at $\pm 180^\circ$. When the RF pulses are not sign alternated (dashed line), the curve is shifted so that the minimum occurs on resonance. Both curves repeat with a period of 360° . From (Bernstein et al., 2004)

If $TE = \frac{TR}{2}$, bSSFP signal can be derived (Bernstein et al., 2004):

$$S_{bSSFP} = \frac{M_0 \sin \alpha (1 - E_1)}{1 - (E_1 - E_2) \cos \alpha - E_1 E_2} \quad (2.10)$$

For $TR \ll T_2$,

$$S_{bSSFP} = \frac{M_0 \sin \alpha}{\left(\frac{T_1}{T_2}\right) (1 - \cos \alpha) + (1 + \cos \alpha)} \quad (2.11)$$

Because of this T_1/T_2 ratio, bSSFP sequences is said to have “ T_2/T_1 ” contrast weighting. There is a fairly complicated dependence of the signal on flip angle α , making it hard for clinicians to interpret such images. Moreover, high flip angles between 50–80° are required to generate the highest possible signal. This can easily exceed the SAR limits, especially in UHF applications.

2.1.3.2. Gradient spoiling

In a SSFP pulse sequence, a train of RF pulses is applied to the spin system, with time interval TR shorter than T_2 to accelerate acquisition time. Therefore, at the end of a TR , if not balanced, a residual transversal magnetization can remain. This residual will be subjected to the next RF pulse, and will produce a spurious signal that interferes with the desired signal, causing image artefacts, leading to potential errors on quantitative measurements (Haacke and Frahm, 1991; Haase et al., 1986), as shown in Figure 2.13a).

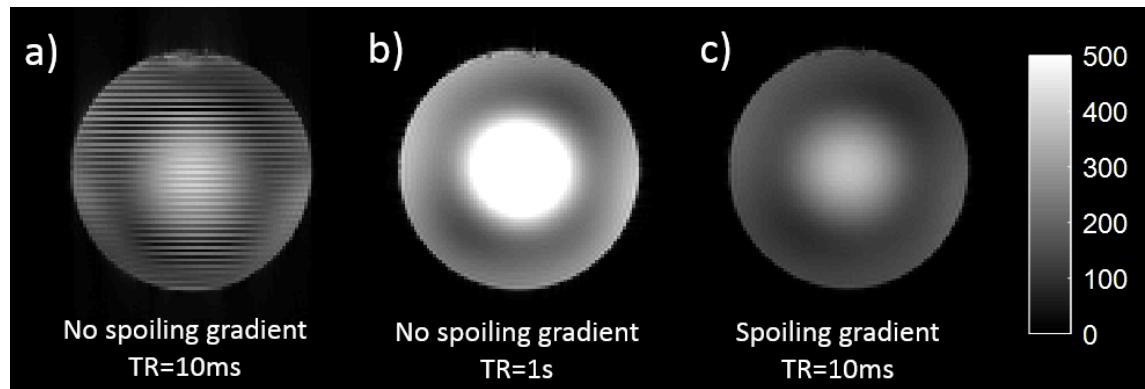


Figure 2.13 : SSFP sequence applied at 7T on a phantom containing water and 1% of agar, with $TR/TE=10/5$ ms and $FA=20^\circ$ with no phase offset and a) no gradient rewinder after readout, b) no gradient rewinder after readout and ‘natural spoiling’ with $TR=1$ s and c) $TR=10$ ms with a spoiling gradient in the readout direction. In a), signal interferences are clearly depicted in the phantom, from unspoiled transverse magnetization. In b), the transverse magnetization naturally attains its stationary state, at the cost of a long acquisition time. In c), the transverse magnetization is spoiled, thus accelerating acquisition time, at the cost of a loss of signal.

To eliminate the contribution of the various echoing pathways to the voxel signal, their phases need to be scrambled in such a manner that they add together in a destructive fashion and do not contribute to the signal following the RF pulse. This elimination of the transverse magnetization before each RF pulse is called “spoiling” the signal.

There are several ways to spoil a signal. The first way would be to use a TR long enough to naturally attain the steady state (see Figure 2.13 b)). But this technique is very long and not applicable in clinical routine. The second technique consists in adding a “spoiling gradient”, as shown in the sequence diagram Figure 2.14.

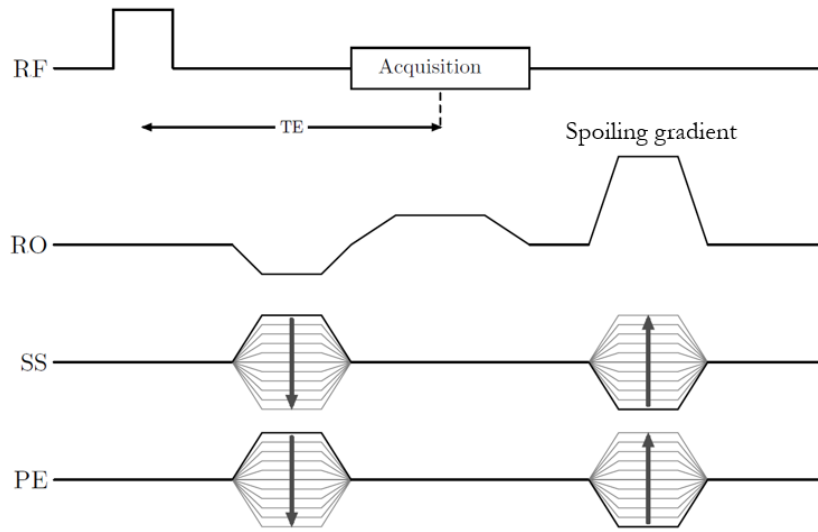


Figure 2.14 : SSFP sequence diagram with the use of a readout spoiling gradient.

If the same gradient pulses are applied during each TR, and magnetic field inhomogeneities are neglected, the phase φ of a spin at position z is given by Equation (2.12) (Bernstein et al., 2004).

$$\varphi(z) = \gamma z \int_0^{TR} G(t) dt = \gamma z M_{RO}, \quad 0 \leq t \leq TR \quad (2.12)$$

Where $G(t)$ is the applied gradient at time t and M_{RO} the total readout gradient moment within a TR. Under the influence of a spoiling gradient, the transverse magnetization will thus dephase along the direction of the gradient, according to their location, leading to signal cancellation. The overall phase dispersion $\Delta\varphi$ across the voxel is determined by the product of the gradient area M_{RO} and the voxel dimension across the gradient direction Δz , as shown in Eq.(2.13) .

$$\Delta\varphi = \gamma \Delta z M_{RO} \quad (2.13)$$

If the gradient area or the voxel dimension is sufficiently large, the phase dispersion will result in a greatly reduced net vector sum and consequently a decreased or nulled transverse

magnetization. Within an arbitrary voxel, the residual magnetization that remains in the transverse plane at the end of a pulse sequence can be expressed as (Bernstein et al., 2004):

$$M_{XY} = M_{XY_0} \left| \text{sinc} \frac{\Delta\phi}{2} \right| \quad (2.14)$$

It is interesting to note that when $\Delta\phi = \pm 2m\pi$ ($m = 1, 2, \dots$), the residual magnetization becomes zero. Equation (2.14) also indicates that either a positive or negative spoiler gradients can be used to dephase the magnetization because the sinc is an even function. The minimal phase dispersion required to spoil the unwanted transverse magnetization is typically determined by experiments. Here, the metric N_{RO} , defined in Eq. (2.15) will allow us to estimate the number of 2π dephasing along the RO direction.

$$N_{RO} = \frac{\Delta\phi}{2\pi} \quad (2.15)$$

Figure 2.13c) depicts the acquisition of a SSFP sequence with a spoiling gradient corresponding to $N_{RO}=1$. Therefore, using this metric, a balanced SSFP corresponds to a N_{RO} of 0, and the higher the N_{RO} , the more the sequence will be spoiled.

It is important to note here that the application of such spoiling gradient can increase the diffusion sensitivity of SSFP imaging, as demonstrated by (Buxton, 1993). Diffusion sensitivity increases with shorter TR, resulting in a signal attenuation of up to 50%, leading to a lower SNR, as well as an unwanted diffusion-weighting of the images.

These spoiling gradients do not destroy the transverse magnetization, but simply suppress its signal contribution. If the same spoiling gradient is used every TR, a fraction of the dephased magnetization will be rephased to form a signal echo in later TRs. Proper gradient spoiling requires a randomized gradient each TR to avoid this rephasing (Darrasse et al., 1986). But achieving a broad range of variable areas requires either very strong gradients or long TR, making this impractical under most circumstances, leading to severe image distortions due to eddy current problems (Frahm et al., 1987; Crawley et al., 1988).

Therefore, spoiling using a spoiling gradient with identical momentum from one TR to the other needs to be used in combination with a second spoiling method, called “radiofrequency spoiling”.

2.1.3.3. Radiofrequency spoiling

Radiofrequency spoiling uses the phase of the B_1 field to lead to an incoherent dephasing of the spins from one TR to the other. The transverse magnetization that is excited in one TR will therefore have a phase angle that is offset relative to the magnetization that persists from prior excitations. If the tip axes are chosen appropriately, fresh signal from the most recent

RF pulse will dominate, while residual transverse components will phase cancel. The RF excitation is then phase-cycled to a predetermined schedule. (Miller et al., 2011; Zur et al., 1991)

This solution was introduced in 1991 by Zur et al. (Zur et al., 1991). Let Φ_j be the phase of the B_1 field for the j -th RF pulse. One method is to use randomized phases Φ_j . But the effectiveness of the spoiling can fluctuate from TR to TR interval, leading to signal instability (Freeman and Hill, 1971). In practice, a quadratic schedule of phase angles has been shown to provide a stable signal. At each time interval TR, a phase is given to the RF pulse, Φ_j such that:

$$\Phi_j = \Phi_{j-1} + j\Phi_0, \quad j = 1, 2, 3, \dots \quad (2.16)$$

Where Φ_0 is a constant called the “phase increment”. Because $\Phi_j - \Phi_{j-1}$ in Eq. (2.16) is linearly proportional to j , the phase Φ_j varies quadratically with j . The phase for the j -th RF pulse is given in Eq.(2.17) by solving the difference equation (2.16). (Bernstein et al., 2004)

$$\Phi_j = \frac{1}{2}\Phi_0(j^2 + j + 2), \quad j = 0, 1, 2, \dots \quad (2.17)$$

The phase increment Φ_0 is an adjustable parameter. The SSFP contrast, and effectiveness of RF spoiling is critically dependent on its value. In order to find the optimum value of Φ_0 , the steady-state signal can be simulated as a function of its phase increment, and compared to the expression of the ideal steady-state signal, given in Eq. (2.18), considering a perfect spoiling is obtained.

$$S_{GRE} = M_0 \sin \alpha \frac{1 - \exp\left(-\frac{TR}{T_1}\right)}{1 - \cos \alpha \exp\left(-\frac{TR}{T_1}\right)} \exp\left(-\frac{TR}{T_2^*}\right) \quad (2.18)$$

where α is the RF flip angle. A simulation of the signal as a function of Φ_0 was performed, as shown in Figure 2.15.

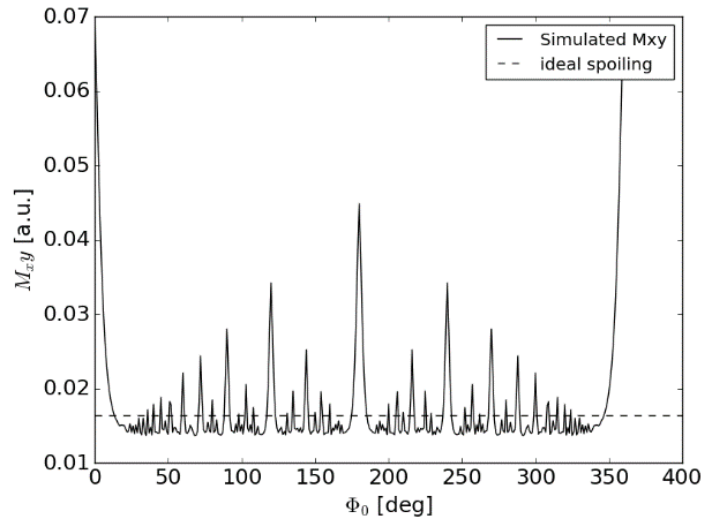


Figure 2.15 : Plot of the modulus of the transverse magnetization after 500TR as a function of phase increment Φ_0 , for $TR=5ms$, $\alpha=30^\circ$, $T_1=1100ms$, $T_2=55ms$ and a gradient spoiling such that $N_{RO}=1$. The simulated M_{xy} shows high dependence on phase increment. It is very close to the ideal spoiled signal (dashed line) for different phase increment values.

Peaks in the amplitude of this signal are observed for certain values of phase increment. Crawley et al. (Crawley et al., 1988) have shown that these peaks occur when Φ_0 is a rational fraction of 360° because of an incomplete destruction of the transverse residual magnetization. It varies according to the considered T_1 , T_2 and TR considered. The steady state signal is very close to the theoretical ideally spoiled signal for different Φ_0 . In practice, $\Phi_0 = 117^\circ$ was proposed by Zur et al., and different values are implemented on different scanner brands (e.g. $\Phi_0 = 117^\circ$, 150° or 50°), explaining some of the variability that may be encountered between scanners.

Figure 2.16 sums up the different cases of spoiling from a SSFP sequence with no rewind in the readout direction. It can be seen that both spoiling gradient and radiofrequency spoiling are needed to spoil the signal from transverse magnetization.

In the literature, SSFP sequences using both spoiling gradient and radiofrequency spoiling are called “FLASH” (Fast low-angle shot), or GRE (gradient echo) sequences under Siemens environment, “SPGR” (spoiled gradient echo) in General Electrics and “FFE” (fast field echo) in Philips scanners.

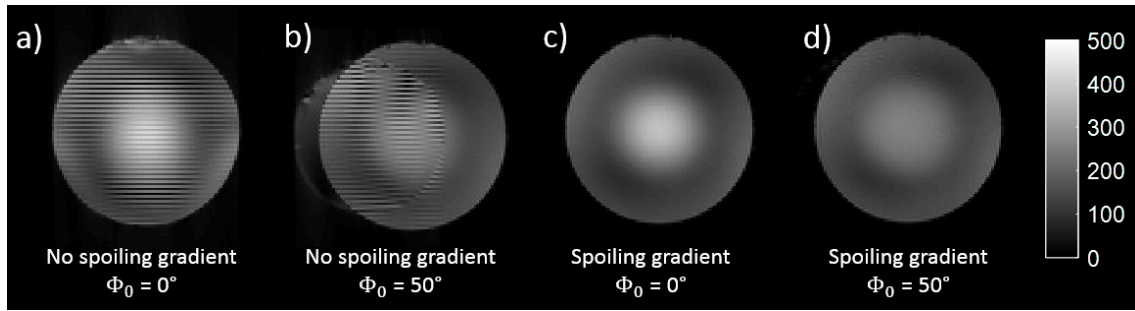


Figure 2.16 : SSFP sequence applied at 7T on a phantom containing water and 1% of agar ($T_1=3000\text{ms}$, $T_2=150\text{ms}$), with $TR/TE=10/5\text{ms}$ and $FA=20^\circ$ and a) with no phase offset and no gradient rewinder after readout, b) no gradient rewinder and a phase increment of 50° c) with a spoiling gradient in the readout direction of $N_{RO}=1$ and no phase offset and d) with a spoiling gradient in the readout direction of $N_{RO}=1$ and a phase increment of 50° . In a), signal interferences are clearly depicted in the phantom, from unspoiled transverse magnetization. In b), these interferences are still visible, although the phase increment reduce them. In c), the transverse magnetization is partly spoiled by the use of a spoiling gradient. In d), the transverse magnetization is completely spoiled, from both spoiling gradient and radiofrequency spoiling. This is the “FLASH” or “GRE” sequence case.

2.1.3.4. Quantification using SSFP

One can notice that conventional methods to measure T_1 , T_2 and ADC based on Spin-Echo adaptations, although accurate and unbiased, are quite long and not suitable for UHF applications. SSFP techniques show potential for rapid relaxometry with good spatial coverage and high resolution, as required for clinical acceptance and practice.

Relaxometry

Using a variable flip angle technique, the feasibility of high-resolution T_2 mapping was demonstrated in vivo based on two b-SSFP scans, however, requiring prior knowledge of the longitudinal relaxation (T_1) for accurate T_2 estimations (Deoni et al., 2003, 2005). Furthermore, bSSFP suffers from off-resonance related banding artifacts as discussed above, hampering its applicability at UHF.

Steady-state imaging methods are more generally used to achieve rapid T_1 mapping in the brain. The degree of T_1 -weighting of the images depends on the flip angle and TR of the pulse sequence, as shown in Eq. (2.18). So any of these can be altered to create a set of images with which T_1 measurement becomes possible. The most widespread method is called “VFA” for Variable Flip Angle, also known as DESPOT1. It involves the acquisition of multiple spoiled-GRE images at varying flip angle, enabling T_1 to be fitted in each voxel (Fram et al., 1987).

The extraction of T_1 using VFA is based on the expression of the steady state signal acquired in GRE (Eq. (2.18)) using a non-linear fitting. But the data are usually rearranged to fit a

linear form. Indeed, $\frac{S_{GRE}}{\tan \alpha}$ and $\frac{S_{GRE}}{\sin \alpha}$ are related by a linear relationship, allowing fitting with simple least squares linear regression (Deoni et al., 2003):

$$\frac{S_{GRE}(\alpha)}{\sin \alpha} = E_1 \frac{S_{GRE}(\alpha)}{\tan \alpha} + M_0(1 - E_1) \quad (2.19)$$

Where $E_1 = \exp(-\frac{TR}{T_1})$. Fram et al. (Fram et al., 1987) have shown that the acquisition of at least three signals corresponding to different flip angles provides enough data points to make a linear regression and deduce T_1 from the slope of the straight line. More recently, it has been shown that using VFA with two optimal flip angles gives good results too (Hurley et al., 2012), using a very simple expression of T_1 depending on their respective signals, S_{GRE1} and S_{GRE2} and corresponding flip angle, α_1 and α_2 :

$$T_1 = -TR \left(\ln \left(\frac{S_{GRE2} \sin \alpha_1 - S_{GRE1} \sin \alpha_2}{S_{GRE2} \sin \alpha_1 \cos \alpha_2 - S_{GRE1} \sin \alpha_2 \cos \alpha_1} \right) \right)^{-1} \quad (2.20)$$

The two optimal angles for VFA acquisitions can be determined analytically using the theory of propagation of errors. Minimization of the variance of T_1 gives two optimal angles:

$$\alpha_{opt1,2} = \arccos\left(\frac{E_1 \pm \sqrt{2}(E_1^2)}{2 - E_1^2}\right) \quad (2.21)$$

Flip angles of 5 and 20° are generally used. Such method is very sensitive to B_1 variations. As RF inhomogeneities cause the achieved flip angle to vary across the brain at UHF, the acquisition of additional scans to estimate flip angle maps has been proposed (Yarnykh, 2007). Parker et al. (Parker et al., 2001) showed that, by integrating over the slice profile and using a flip angle map, it was possible to obtain accurate multi-slice T_1 measurements using this approach, in times of the order of a few minutes.

Such method also requires complete spoiling of transverse magnetization. The effect of RF spoiling increment is therefore crucial in the accuracy of T_1 estimations and was studied by (Preibisch and Deichmann, 2009). Figure 2.17 highlights the necessity to correct for both B_1 inhomogeneities and incomplete spoiling to obtain an accurate T_1 estimation.

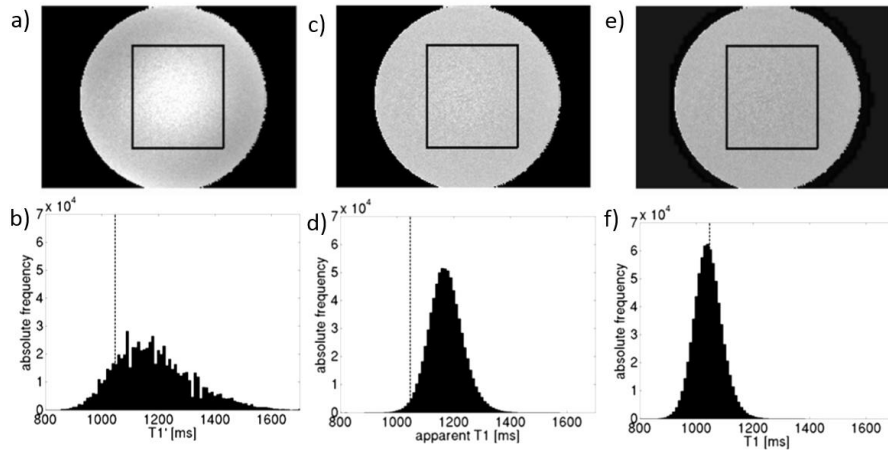


Figure 2.17: Central slice of a phantom T_1 map acquired with a phase increment of 50° and corresponding histogram of T_1 values inside the rectangular ROI : without any corrections (**a** and **b**), with correction for B_1 inhomogeneities (**c** and **d**), and with correction for incomplete spoiling (**e** and **f**). The dashed vertical line indicates the reference value. From (Preibisch and Deichmann, 2009)

Another possibility to assess T_1 using SSFP methods is to monitor the longitudinal relaxation after spin preparation by rapid acquisition of an image series. Several T_1 mapping techniques are based on this concept (Deichmann, 2005; Deichmann and Haase, 1992; Henderson et al., 1999; Shah et al., 2001; Steinhoff et al., 2001; Scheffler and Hennig, 2001), using a spoiled or balanced SSFP readout. Since these readouts continually excite the magnetization recovery, fresh magnetization is mixed and must be accounted for.

Proton Density

PD mapping is challenging, and great care has to be taken to correct for any image intensity bias that may impair the accuracy of measured results. PD can be expressed from M_0 as (Volz et al., 2012):

$$M_0 = PD \cdot C \cdot RP \quad (2.22)$$

Where RP is the profile of the receiver coil sensitivity and C is a constant scaling factor without spatial variation that depends on a variety of parameters such as the receiver gain setting and the scaling parameters used for image reconstruction.

From Eq. (2.18) and (2.22), it is clear that biases can be due to variations of T_1 , T_2 , T_2^* , inhomogeneities of the radiofrequency field B_1 , distortions of the static magnetic field B_0 , and intensity nonuniformities imposed by spatial variations of the receiver coil sensitivity profile. Thus, PD mapping methods usually comprise several individual acquisitions for mapping all the parameters influencing signal amplitude. The bias-free images are then converted into quantitative PD-maps by suitable normalization, where a value of 100 percent units (pu) corresponds to a PD of pure water at 37°C .

(Volz et al., 2012) proposed a PD-maps extraction of the whole-brain using three different sequences in 18 minutes. Variable Flip Angle, described above, was used for T_1 mapping. B_1 mapping described in (Volz et al., 2010) was used for flip angle correction of the T_1 maps. T_2^* mapping was acquired with two gradient echo data sets with different TE. Furthermore, the acquisition with the short TE was repeated once using the Body Coil (BC) for signal reception on the 3T scanner. This additional scan is required for obtaining the Head Coil (HC) receive profile (RP) according to:

$$RP(HC) = \frac{S(HC)}{S(BC)} B_1 \quad (2.23)$$

M_0 can also be determined from the image intensity (I) of a GRE image according to:

$$M_0 = \frac{I}{S_{GRE} \exp\left(-\frac{TE}{T_2^*}\right)} \quad (2.24)$$

Where S_{GRE} is defined in Eq. (2.18). Substituting Eq. (2.24) into Eq. (2.22) leads to the possible estimation of unbiased PD, given T_1 , T_2^* and RP determined pixel-wised using the above acquisitions.

In the absence of body coil, the RP can be derived from spoiled SSFP images with low flip angle chosen to minimize image contrast, and using the low-pass-filter method (Wang et al., 2005; Lecocq et al., 2015).

Diffusion

As explained by Buxton (Buxton, 1993), the SSFP signal is very sensitive to molecular diffusion because it is a sum of many echo paths, where most of these echoes are stimulated echoes that were generated by previous RF pulses in the SSFP pulse train. Hence the signal attenuation due to diffusion is larger than for Spin-Echo based diffusion sequences. The signal attenuation caused by diffusion in brain tissue was shown to be practically independent of T_1 and T_2 , enabling the determination of the diffusion constant D for any region in the image from a calculated lookup table (Zur et al., 1997). This method was used to measure diffusion constants in the brain. Results are shown in Figure 2.18.

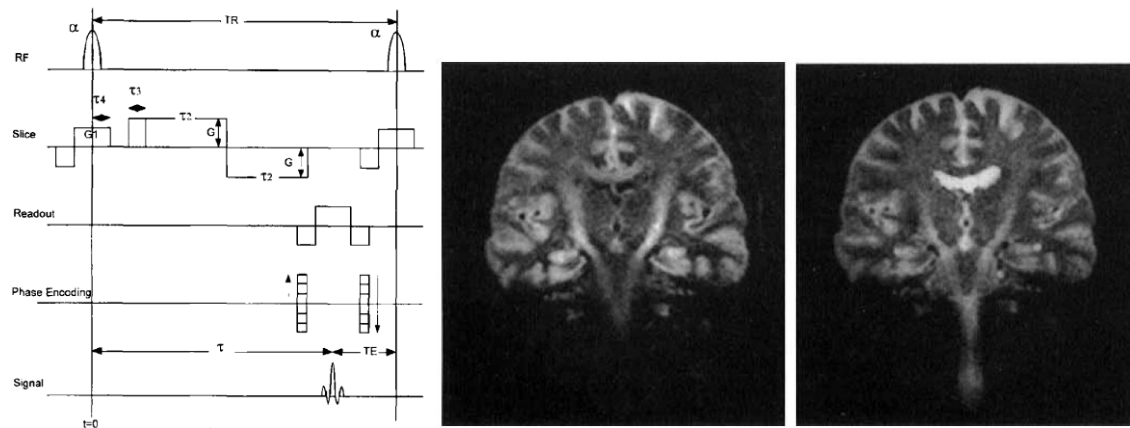


Figure 2.18 : Diffusion sensitive coronal head images: (b) and (c) were acquired by the pulse sequence in (a). In (b), the diffusion sensitizing gradient was normal to the image plane. In (c) the diffusion sensitizing gradient was oriented horizontally within the image plane. Imaging parameters for both images: $TR = 100\text{ms}$, $TE = 8\text{ms}$, $FA = 50^\circ$, $\tau_3 = 2\text{ms}$, $\tau_2 = 39\text{ms}$, $\tau_4 = 2\text{ms}$, $G = 0.8 \text{ Gauss.cm}^{-1}$, $G1 = 0.4 \text{ Gauss.cm}^{-1}$, $FOV = 22 \times 22 \text{ cm}$, matrix 120×130 , $NEX = 32$. From (Zur et al., 1997).

2.1.4. Conclusion

This section highlighted the possibilities to measure NMR parameters of interest such as PD, T_1 , T_2 and ADC in a robust manner. The measurement must not depend on any acquisition factor, but only reflect tissue properties and environment. The gold-standard measurements are performed using different variations of Spin-Echo sequence, but remains very long and hardly applicable in clinical routine at UHF. Steady-State Free Precession sequences have also been studied to provide fast imaging. The spoiling of the transverse magnetization remains an important factor to obtain unbiased measurements. These strategies seem more rapid, but maybe less rigorous with regards to biases that may occur.

These methods allowed to retrieve each quantitative parameter separately. Ideally, one would like to retrieve every available NMR parameter for a proper tissue characterization. It would help clinicians to provide better diagnostics, using cross-information and correlations between these parameters. However, obtaining such parameters with the conventional techniques presented above requires too much time to be applicable in clinical routine. For this reason, new approaches, measuring simultaneously several parameters are currently being developed, and attract considerable interest in the MR community.

2.2. Simultaneous multi-parametric mapping methods

One may expect that in many circumstances the combined measurement of several MR parameters during an exam would lead to a better diagnostic accuracy. The correlation of the multiple complementary NMR parameters could help in the interpretation of the physiological events. Such strategy has already been demonstrated successfully with other simultaneous multi-parametric method (Warntjes et al., 2008; Yu et al., 2017). A first possibility is to perform a sequential acquisition of the distinct parameters using different methods for each quantitative parameter extraction, but acquisition time can be very limiting. Moreover, motion and rescaling between acquisitions can render such approaches infeasible (Warntjes et al., 2007). In addition, interpolations between different scans with different voxel size or different bandwidth per pixel could lead to image deformations, further complicating such strategy. Another option is to perform a single acquisition and make the most of the different weightings information available in the complex signal. In this section, a brief and qualitative review of some simultaneous solutions proposed in the literature is presented chronologically. The feasibility of each method at 7T will also be discussed.

2.2.1. Inversion-Recovery TrueFISP

In 2004, (Schmitt et al., 2004), proposed an approach implementing an Inversion Pulse, followed by the acquisition of a train of bSSFP images. In this technique, the k-space encoding of the shots is arranged such that images are reconstructed at increasing time after the inversion pulse, to measure the evolution of signal intensity of tissue over a certain time.

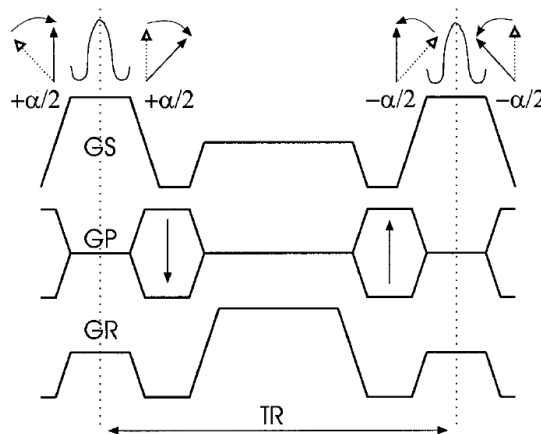


Figure 2.19 : Completely balanced TrueFISP sequence. The signed gradient areas of slice-select GS, phase-encoding GP, and readout-gradient GR are zero within one TR. Due to the complete refocusing of transverse magnetization, the longitudinal magnetization oscillates between $\pm\alpha/2$. From (Scheffler and Hennig, 2001)

Analytical expressions of the subsequent signal are proposed for the direct calculation of T_1 , T_2 , and relative PD from a IR-bSSFP signal time course. The signal of an IR-bSSFP for the n -th acquired TR is derived:

$$S(nTR) = S_{stst}(1 - INV \cdot \exp(-\frac{nTR}{T_1^*})) \quad (2.25)$$

Where S_{stst} is the bSSFP steady-state signal defined in Eq. (2.10). T_1^* is an apparent T_1 time, depending on the flip angle α , T_1 and T_2 , derived for $TR \ll T_{1,2}$ as : $T_1^* = \left(\frac{1}{T_1} \cos^2 \frac{\alpha}{2} + \frac{1}{T_2} \sin^2 \frac{\alpha}{2}\right)^{-1}$ and INV is an inversion factor indicating the ratio between the initial signal S_0 and the steady-state signal S_{stst} such as: $INV = 1 + \frac{S_0}{S_{stst}} = 1 + \frac{\sin \frac{\alpha}{2}}{\sin \alpha} \left(\left(\frac{T_1}{T_2} + 1 \right) - \cos \alpha \left(\frac{T_1}{T_2} - 1 \right) \right)$.

The acquired IR-bSSFP magnitude image series are fitted voxel-wised to the three-parameter function given in Eq. (2.25) using a least-squares fitting routine described in (Nekolla et al., 1992). From the resulting fit parameter maps, T_1 , T_2 and relative M_0 maps can be retrieved.

In this method, the measurements are sensitive to off-resonant spins as a bSSFP sequence is used. To reduce this effect, very short TR of 6ms was needed in the study. Such TR combined with the use of an inversion pulse makes this method incompatible with an application at UHF. Moreover, high dependence on flip angle distribution is encountered, and biases in T_1 , T_2 and M_0 are very likely to occur with B_1^+ heterogeneity.

2.2.2. QRAPTEST and QRAPMASTER

QRAPTEST

A quantification method called ‘‘Quantification of Relaxation times and Proton density by Twin-echo Saturation-recovery Turbo-field echo’’ (QRAPTEST) was introduced by (Warntjes et al., 2007) to determine simultaneously B_1^+ , T_1 , T_2^* and PD. This method is comparable to IR-TrueFISP, with two main modifications. First, a 90° saturation pulse is used instead of a 180° inversion pulse. Second, a spoiled SSFP sequence is implemented instead of a bSSFP and each excitation is followed by the acquisition of two separate echo acquisitions. T_1 is extracted from a mathematical derivation similar as in §2.2.1. and T_2^* can be obtained from the two intensity values (I_{E_1} and I_{E_2} at TE_1 and TE_2 respectively):

$$T_2^* = \frac{TE_2 - TE_1}{\ln\left(\frac{I_{E1}}{I_{E2}}\right)} \quad (2.26)$$

T_1 reliability is determined by the accuracy of flip angle. Therefore, the saturation pulse is seen as a variable to determine in the model, in order to correct for B_1 inhomogeneities. A factor of inhomogeneity is thus computed voxel-wised, and re-introduced in the problem to extract accurate parameters. Once T_1 and T_2^* are known, they can be combined with the absolute signal intensity of the image to calculate the PD, by correcting the signal with multiple weighting parameters.

In this approach, the estimation of T_1 , T_2^* and PD is performed, with less sensitivity to B_1 inhomogeneities than in the method presented in §2.2.1. Although small flip angles (4-8°) can be used, the need for a saturation pulse might still represent an issue for clinical implementation at $7T$, as this saturation will be spatially variable.

QRAPMASTER

A following work from the same research group presented an evolution of the method, called QRAPMASTER, standing for “Quantification of Relaxation Time and Proton Density by Multiecho acquisition of a saturation-recovery using Turbo spin-Echo Readout” (Warntjes et al., 2008). The acquisition is very similar to QRAPTEST described above. But in this case, a saturation pulse of 120° is used, followed by a SE acquisition of multiple echoes instead of a gradient-echo, leading to the estimation of T_2 instead of T_2^* .

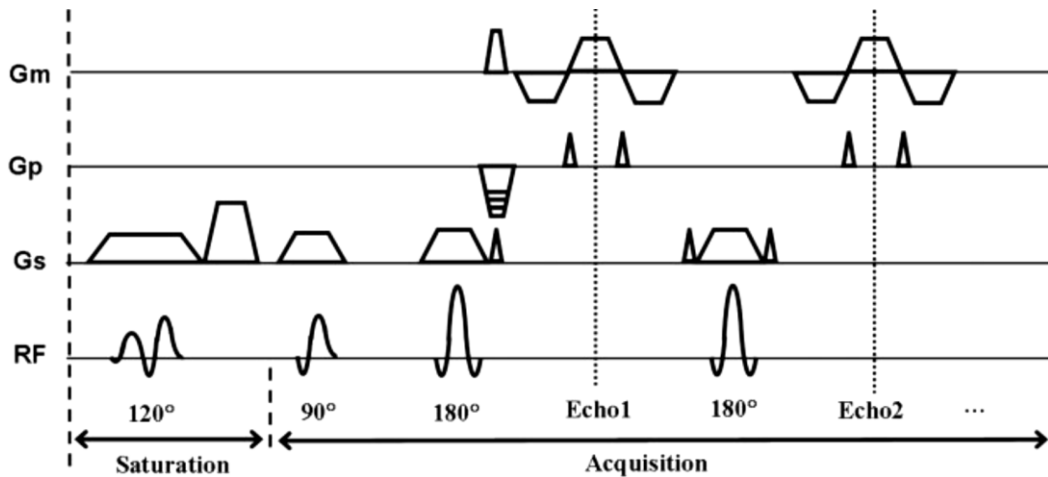


Figure 2.20 : Schematic representation of a single block of the QRAPMASTER quantification sequence. Shown are the measurement (G_m), phase-encoding (G_p), and slice-selection (G_s) gradients and the RF pulse amplitude over time. There are two phases in each block. In phase 1 (saturation), the 120° saturation pulse and subsequent spoiling acts on a slice m . In phase 2 (acquisition), the multiecho spin-echo acquisition is performed on slice n , using the 90° excitation pulse and multiple 180° refocusing pulses. The spin-echo acquisition is accelerated with an EPI readout scheme. From (Warntjes et al., 2008).

The complete quantification measurement consists of numerous scans with different delay times after the saturation. Hence, from the measured intensity at various delay times, a fit can be performed to retrieve T_1 , M_0 , and the effective local saturation flip angle. It is important to note that the local excitation flip angle estimation is not a straightforward estimation from this saturation angle map because it requires knowledge of the RF pulse profiles and the actual spin behavior in a particular B_1 field.

Applications

This quantitative MRI method is commercialized by a company called SyntheticMR. In 2014, a license agreement has been signed with GE Healthcare to make it available on SIGNA scanners under the name of “MAGiC” (Magnetic resonance Image Compilation). A cooperation and co-marketing agreement was signed with Philips Healthcare to provide this method in Philips 1.5 and 3T under the name of SyntAc.

Several studies have been done on the brain, studying peritumoral edema in malignant gliomas (Blystad et al., 2017), multiple sclerosis (Hagiwara et al., 2017) and brain development (Kim et al., 2017; McAllister et al., 2017). These studies were performed under 1.5 and 3T environments, but the method was never applied under UHF constraints.

2.2.3. Double Echo Steady-State (DESS), Diffusion-weighted DESS (DW-DESS) and Triple Echo Steady-State (TESS)

Double Echo Steady-State (DESS)

The Double-Echo Steady-State (DESS) method was originally published by (Welsch et al., 2009). Based on the theory of Bruder (Bruder et al., 1988), the simultaneous acquisition of two separate SSFP echoes allows the formation of two MR images with clearly different contrasts: S^+ , also called “FISP” (Fast Imaging Steady Precession), and S^- also called “PSIF” as it is a reversed FISP, shown in Figure 2.21a. The PSIF part of the sequence leads to a high T_2 contrast, whereas the FISP part provides images with a contrast dominated by T_1/T_2 ratio. The different T_2 -weighting of both echoes allows the calculation of quantitative T_2 maps based on their ratio. The ratio of these two signals becomes independent of T_1 if $\alpha \sim 90^\circ$. Therefore, T_2 values will have a certain dependence on T_1 , depending on the applied flip angle.

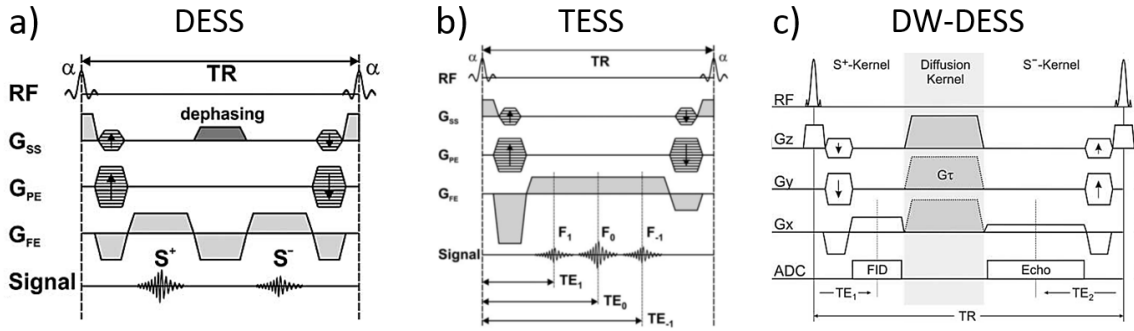


Figure 2.21 : **a)** DESS sequence acquisition, showing the acquisition of S^+ , corresponding to a “FISP” (Fast Imaging Steady Precession) acquisition, and S^- called “PSIF” as it is a reversed FISP. **b)** Illustration of a TESS sequence. The center free induction decay F_0 is flanked by a higher order FID to the left (F_1) and by the lowest order Echo (F_{-1}) to the right, with echo times TE_0 , TE_1 and TE_{-1} , respectively. From (Heule et al., 2014) **c)** A repetition of the DW-DESS sequence. In the frequency direction G_x , this consists of two fully rewound readout gradients separated by a spoiler gradient, which can then be combined with the preparatory gradients to save scan time. The duration (τ) and the amplitude (G) of the spoiler gradient (shaded area, Diffusion Kernel) can be set for each axis independently of the other imaging parameters. The signal from the first readout is referred to as the S^+ echo (or FID) and signal from the second readout as the S^- echo (or echo). The unbalanced spoiler gradient separates the two echoes in time and affects the diffusion weighting of the images. From (Bieri et al., 2012)

Triple Echo Steady-State (TESS)

As mentioned above, DESS sequence becomes independent of T_1 only in the limit of $\alpha \sim 90^\circ$. Unfortunately, SNR is especially poor in this limit, requiring considerably lower α in practice, leading to a systematic T_1 -related bias in the estimated T_2 values. To tackle this dependence, the “Triple Echo Steady State” method, proposed by (Heule et al., 2014), adapted a DESS sequence to acquire three echoes within every TR, as displayed in in Figure 2.21b. As proposed in DESS, the dependencies of the echoes on relaxation to quantify T_1 and T_2 is exploited. The following ratios are investigated:

$$S_{T_2}(T_1) = \frac{F_1}{F_0}, \quad S_{T_1}(T_2) = \frac{F_{-1}}{F_0 - F_1} \quad (2.27)$$

Where the use of subscript $T_2(T_1)$ means that the considered value is seen as a bound variable in the iterative procedure to extract T_2 and T_1 . Therefore, the signal ratio then only depends on one running variable, naming T_1 or T_2 . An iterative procedure is then implemented to extract T_2 and T_1 by performing golden section search (Press et al., 2007) until the calculated signal ratios converge to the actual measured ones, without the confounding influence of T_1 or T_2 respectively.

Results obtained on phantom at 1.5T and on cartilage at 3T exhibit unbiased T_2 estimations, whereas T_1 estimates show prominent sensitivity to transmit-field errors. Therefore, this

technique would not be suitable for UHF implementation. Also, acquisition time might become an issue as three echoes are needed to extract the information.

Diffusion-Weighted Double Echo Steady-State (DW-DESS)

The estimation of a supplementary parameter was introduced by the work of (Staroswiecki et al., 2012). The DESS sequence described above was modified by adding a diffusion-weighting gradient to improve control and flexibility of the diffusion sensitivity of the sequence. In the work of (Staroswiecki et al., 2012), a total of four magnitude images were retrieved from a pair of DW-DESS acquisitions shown in Figure 2.21c : one with low FA and large spoiler gradient area (high diffusion sensitivity) and a second with high FA and small spoiler gradient area (low diffusion sensitivity).

The simultaneous assessment of T_1 , T_2 and ADC for each voxel was performed by a fit that minimizes the sum of the squared errors between measured and modeled values for the three ratios S_1^-/S_1^+ , S_2^-/S_2^+ and S_1^+/S_2^+ . Although the fit should also be able to estimate T_1 , the values were not reported in the paper because the imaging parameters were not optimized for T_1 estimations. Also, diffusion effects show a prominent sensitivity on relaxation times. To tackle this issue, (Bieri et al., 2012) have demonstrated that in the rapid pulsing regime ($TR \ll T_2$), the diffusion-weighted signal reduction for the S^+/S^- signal ratio is to a high degree relaxation-insensitive. Thus, using a second-order Taylor series expansion of the equation for S^+/S^- , the authors were also able to estimate relaxation-insensitive diffusivity.

(Gras et al., 2017b) proposed a general framework for the optimization of the DW-DESS sequence protocol. The solution ensures that the signal dependence with diffusion coefficient and the relaxation times can be disentangled in an optimal way, provided that an additional transmit field B_1 is acquired. An extension of the protocol exploring three orthogonal gradient directions, thereby giving access to the mean diffusivity in a medium with anisotropic diffusion was also proposed. Through the reported acquisitions at 3T, in the brain, a certain bias was observed in the estimation of T_2 values, and T_1 to a lesser extent, compared to gold-standard acquisitions. It was attributed to physiological motion during the diffusion-weighted scans, as well as B_1^+ effects.

2.2.4. Magnetic Resonance Fingerprinting (MRF)

Magnetic Resonance Fingerprinting (MRF) was originally published by (Ma et al., 2013). This technique aims at providing simultaneous measurements of T_1 , T_2 , relative PD, and off-resonance frequency. MRF relies on deliberately varying acquisition parameters such as flip angle, TR and the trajectory in k-space, in a pseudorandom way such that each tissue generates

a unique signal evolution (see Figure 2.22). An inversion recovery pulse is played at the beginning of the acquisition sequence to enhance T_1 differences between tissues. Ideally, this acquisition strategy is supposed to generate uncorrelated signals for each tissue. For each TR, an undersampled image is reconstructed. Signal evolutions corresponding to acquisition parameters are simulated for a wide variety of tissue parameter combinations and collected in a database, called a dictionary. After the acquisition, a pattern recognition algorithm is used to find the dictionary entry that best represents the acquired signal evolution of each voxel. The parameters that were used to simulate the resulting best match are then assigned to the voxel. The base image series are not useful by themselves, but each voxel contains a signature fingerprint isolated from the undersampling artifacts that will be used later on for the dictionary matching. The total number of time points can vary from acquisition to acquisition, ranging from 1000 (Ma et al., 2013) to 2500 (Chen et al., 2016) as function of the image resolution, the undersampling ratio or the matching approach used for example.

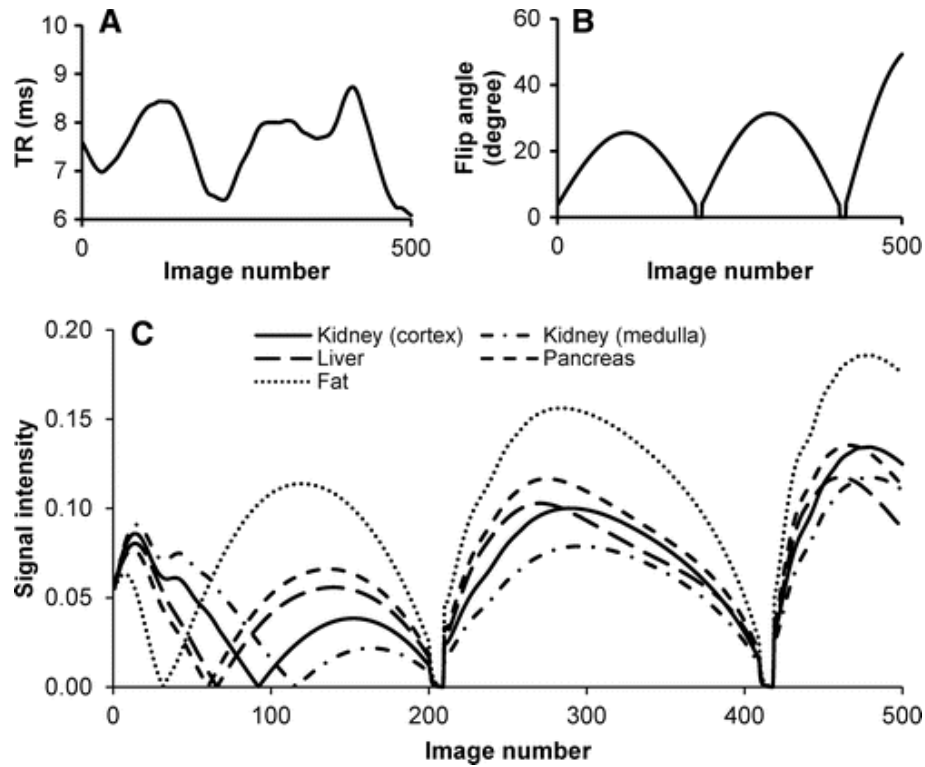


Figure 2.22 : Simulation of signal evolution curves for FISP MR fingerprinting. A, B : Example of first 500 points of repetition time (TR) and flip angle patterns. C : Signal evolution curves for multiple tissues in the abdomen created by using the patterns in A and B. T_1 and T_2 values, respectively, used to generate the curves included 1140 and 75 ms for the renal cortex, 1540 and 80 ms for the renal medulla, 820 and 35 ms for the liver, 720 and 45 ms for the pancreas, and 400 and 70 ms for fat. Illustration from (Chen et al., 2016).

The initial implementation of MRF (Ma et al., 2013) was based on a bSSFP because of its sensitivity to T_1 , T_2 and B_0 heterogeneity. The MRF framework has also been applied to other

sequence such as FISP or “Quick Echo Splitting NMR Technique” (QUEST) to avoid the banding artifacts, while still sensitive to T_1 and T_2 components (Jiang et al., 2015, 2017).

The brain and abdominal MRF framework has been tested a clinical environment. Data were acquired with FISP acquisitions on patients with a brain tumor and breast cancer metastatic to the liver. Longer T_1 was observed in the metastatic lesions compared to the surrounding tissues. It has been shown in six patients with metastatic adenocarcinoma that the mean T_1 and T_2 values in the metastatic adenocarcinoma are significantly higher than the ones of the surrounding tissues (Chen et al., 2016).

MRF needs to be associated with a B_1 map, unless added to the dictionary. In the latter case, the reconstruction strategy becomes undermined by the large database needed for high dimensional multi-parametric data (Cloos et al., 2016). Furthermore, the accuracy of the dictionary simulations is crucial for a correct estimation of the parameters. Even a slight modification of a sequence requires a new computation of the corresponding dictionary.

The uniqueness of the different signal components is also essential. Otherwise, MRF can be subjected to biases in the ‘Fingerprints’, coming from magnetization transfer (Hilbert et al., 2017) or the used gradients area (Anderson et al., 2017). Early motion during the acquisition was also found to lead to severe errors in parameters quantification (Xu et al., 2017). Therefore, this technique seems very powerful and attracted a lot of attention from the community, but many parameters remain to be untangled for accurate estimations. The time efficiency of the method also remains unclear compared to other existing methods.

2.2.5. MR-Spin TomogrAphy in Time domain (MR-STAT)

The work of (Sbrizzi et al., 2015, 2018), published a quantification method called MR-Spin TomogrAphy in Time domain (MR-STAT). Here, a 2D balanced gradient-echo sequence is used, using Cartesian encoding. A total of 32 full k-spaces are acquired, with no waiting times. The flip-angles are chosen randomly between 5° and 75° , as shown in Figure 2.23. The excitation phases alternate between 0 and 180° , and the sequence is preceded by an inversion pulse. First applications have shown results obtained at 3T assessing T_1 and T_2 (van der Heide et al., 2017; Sbrizzi et al., 2018).

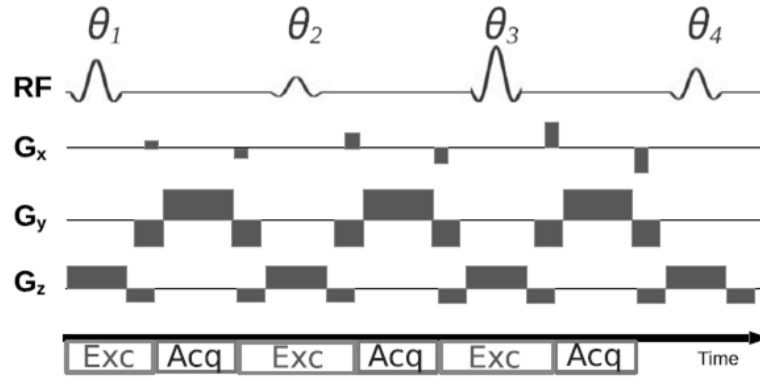


Figure 2.23 : Fragment of a MR-STAT data acquisition sequence. The spatially selective RF pulse is called by the flip angle θ_i . G_x and G_y are encoding gradients. G_z is the slice-selective gradient. Note that the excitation (Exc) and acquisition (Acq) intervals follow one another without interruption, that is, the fixed echo and repetition times are the shortest possible. From (Sbrizzi et al., 2018)

In this method, the quantitative MR problem is treated as a dynamic system identification process, used in seismology. The system equations are inverted to match the response of the MR scanner to the data in time domain, thus the intermediate FFT step is not necessary. This approach has become possible thanks to advances in numerical optimization and computing power. In MRF, incoherent aliasing artifacts in the images add a large stochastic component to the measured signal. MR-STAT method wants to eliminate this stochastic component by treating the entire problem (signal localization and parameter estimation) as one large-scale inversion problem. Relationship between sequence parameters and accuracy of reconstruction is explicit and can be exploited for optimal sequence design.

This emerging method would thus theoretically be able to consider the systems imperfections together with relaxation times to estimate. MR-STAT is dictionary-free, and the model does not require knowledge of RF transmit fields, off-resonance or PD. However, the accuracy and reproducibility of the extracted results still need to be studied, as well as time efficiency.

2.2.6. Quantitative Imaging using Configuration States (QuICS)

2.2.6.1. Acquisition strategy

As described in the preceding section, SSFP signal depends on many parameters, such as T_1 , T_2 , flip angle, and diffusion. Quantitative Imaging using Configuration States (QuICS), published and patented by Ludovic de Rochefort in 2015 (de Rochefort, 2015, 2016), is based on the sequential and/or periodically interleaved acquisitions of several k-space with different contrasts obtained by varying radiofrequency spoiling, flip angle, and/or spoiling gradient area. With the proper tools to understand the very complex underlying signal behavior,

QuICS makes the most of this complicated dependence to unambiguously interpret the signal in steady-state images. It provides an efficient algorithm allowing to compute the magnetization after repeated pulses of any amplitude, phase and gradient spoiling.

2.2.6.2. Signal modelling in the configuration state formalism

Introducing a spoiling gradient G generally produces a dephasing such that all phases between 0 and 2π are present within each voxel. Let's denote z as the spoiling gradient axis. The gradient waveform $G(t)$ is chosen such that a constant area remains between two TRs. This area is proportional to a spatial frequency shift Δk_z , and equivalently inversely proportional to a distance a corresponding to a 2π dephasing between two TRs (Eq. (2.28)). a will be referred to as the “spoiling distance” in this context, and TR appears as the diffusion time.

$$\Delta k_z = \frac{1}{a} = \frac{\gamma}{2\pi} \int_0^{TR} G(t) dt \quad (2.28)$$

To study this constant area while accounting for the pixel size along the readout direction, Δz , “ N_{RO} ” was used, reflecting the number of 2π dephasing as defined in Eq.(2.15), page 47.

In that framework, magnetization can be described in space or in spatial frequencies. The latter description was proposed long ago and originally referred to as the configuration states description (Pauly et al., 1991; Roux and Hinks, 1993), similar to the extended phase graph description (Hennig, 1991a, 1991b; Scheffler, 1999; Weigel, 2015), and in which only discrete spatial frequencies are needed due to the constant dephasing between TRs. The longitudinal and transverse magnetization, M_Z and M_{XY} , can respectively be decomposed into discrete Fourier series, as described in Eq. (2.29) and (2.30).

$$M_Z = \sum_{k=-\infty}^{\infty} m_{zk} Z^{-k} \quad (2.29)$$

$$M_{XY} = \sum_{k=-\infty}^{\infty} m_{xyk} Z^{-k} \quad (2.30)$$

where k corresponds to the configuration state or “order”, also called “coherent” states in literature linked by “pathways” determined by the gradient dephasing. The complex exponential $Z = \exp(-i2\pi \cdot \Delta k_z \cdot z)$ is introduced as a base function to describe the spatial modulations between two excitations. m_{zk} and m_{xyk} represent the coefficients of the discrete Fourier series.

In this framework, magnetization components for each configuration state k can be computed and the action of RF pulses, modulated in amplitude and phase, with relaxation and diffusion effects can be modeled using three numerical operations: linear filtering, linear

combinations and index shifting. Indeed, the application of a spoiling gradient after the n -th excitation will leads to a coefficient shift of the transverse magnetization M_{xy_n} before the next excitation as described in Eq. (2.31):

$$M_{XY_{n+1}} = Z^{-1} \times M_{XY_n} \quad (2.31)$$

Similarly, the relaxation can be modeled as an attenuation of the signal (Eq. (2.32) and (2.33)) (Scheffler, 1999).

$$M_{z_{n+1}} = (1 - E_1) + E_1 \times M_{z_n} \quad (2.32)$$

$$M_{XY_{n+1}} = E_2 \times M_{XY_n} \quad (2.33)$$

where $E_1 = \exp\left(-\frac{TR}{T_1}\right)$ and $E_2 = \exp\left(-\frac{TR}{T_2}\right)$.

Free diffusion can be seen as Gaussian filtering of the components, as shown by Eq.(2.34) and (2.35) (Freed et al., 2001; Kaiser et al., 1974).

$$M_{Z_{n+1}} = D_z * M_{Z_n} \quad (2.34)$$

$$M_{XY_{n+1}} = D_{xy} * M_{XY_n} \quad (2.35)$$

Where $D_z = \sum_{k=-\infty}^{k=\infty} \exp\left(-D \cdot TR \cdot \left(\frac{2\pi}{a}\right)^2\right)^{k^2} Z^{-k}$ and D is the free diffusion coefficient, and $D_{xy} = \sum_{k=-\infty}^{k=\infty} \exp\left(-D \cdot TR \cdot \left(\frac{2\pi}{a}\right)^2\right)^{k^2+k+\frac{1}{3}} Z^{-k}$ for a constant gradient.

Finally, RF spoiling with a quadratic phase increment Φ_0 can be modeled as a convolution of the longitudinal and transversal polynomials, as explained in Eq. (2.36) and (2.37).

$$M_{Z_{n+1}} = S * M_{Z_n} \quad (2.36)$$

$$M_{XY_{n+1}} = S * M_{XY_n} \quad (2.37)$$

Where $S = \sum_{k=-\infty}^{k=\infty} Y^{-k} Z^{-k}$, with $Y = \exp(-i\Phi_0)$ where the description is done in a demodulated rotating frame with the apparent RF frequency (as a quadratic phase cycling is equivalent to a linear frequency sweep). Considering the expression of S , the convolutions from Eq. (2.36) and (2.37) are equivalent to a multiplication of each term of index k by a different phase term Y^{-k} . The effect of the flip angle in this demodulated frame is to mix (rotate) terms depending on the current flip angle with then same index between longitudinal and transverse components.

The magnetization expressed in this constantly evolving frame reaches a steady state for each order of coherence k . Then, a second order recurrence relation on m_{xy_k} can be derived where three consecutive orders are linked, in Eq. (2.38), from which m_{z_k} will be deduced in Eq. (2.39) using a fast tridiagonal matrix inversion algorithm, leading to an efficient SSFP complex signal calculation for a given set of acquisition parameters (de Rochefort, 2016):

$$-a_k m_{xy_{k-1}} + b_k m_{xy_k} - c_k m_{xy_{k+1}} = r_{-1} \delta_{k+1} + r_0 \delta_k \quad (2.38)$$

$$d_k m_{z_k} = e_n m_{xy_k} - d_n m_{xy_{k-1}} \quad (2.39)$$

where $a_k, b_k, c_k, d_k, e_k, r_{-1}, r_0$ can be expressed as a function of $Y, E_1, E_2, D_z, D, TR, FA$ and δ is a Dirac delta function. This tridiagonal linear system can be solved efficiently to calculate the steady-state with relaxation and diffusion effects.

To illustrate the sensitivity of the model to the parameters in realistic experimental conditions, let's consider the simplest case of constant RF amplitude and spoiling gradient for several contrasts. Only quadratic phase cycling will be used to vary the signal, and only the first echo will be considered, corresponding to the configuration state $k = 0$, leading to a measured steady-state magnetization of m_{xy_0} . The sensitivity of the SSFP signal to phase cycling is illustrated in Figure 2.24, which provides a representation of real and imaginary parts of m_{xy_0} depending on the spoiling phase increment value.

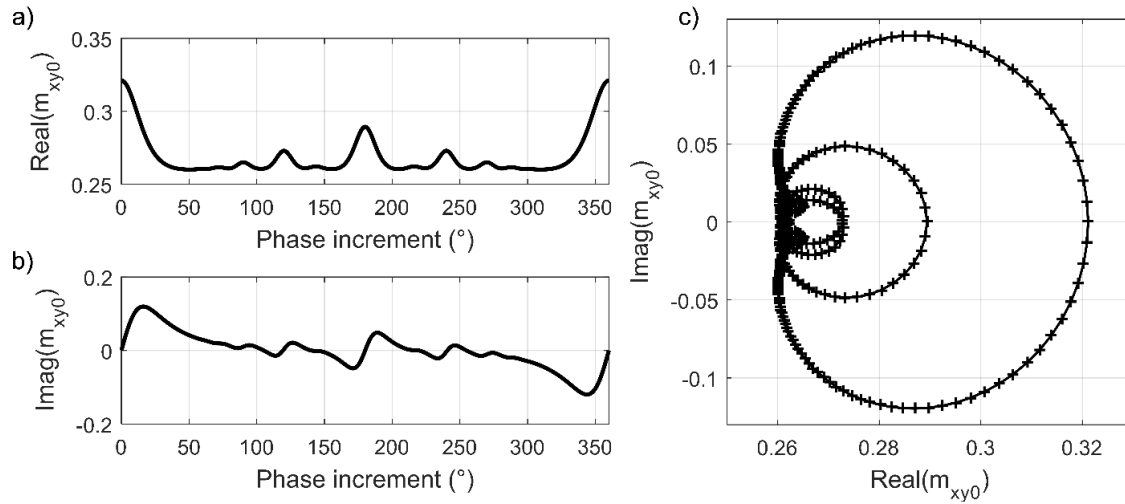


Figure 2.24. Real (a) and imaginary (b) part of the theoretical transverse magnetization signal for a voxel resulting for $T_1/T_2=60/50\text{ms}$, $\text{ADC}=1.3 \times 10^3 \text{mm}^2/\text{s}$, and acquisition parameters $TR=10\text{ms}$, $FA=45^\circ$, resolution of 6mm^3 and a constant spoiling gradient $N_{RO}=47$ corresponding to a spoiling distance of $a=0.128\text{mm}$. The associated complex plane is also displayed (c), where each cross corresponds to a different RF spoiling increment, sampled for each degree of from 0 to 360° . The maximum real value with null imaginary part corresponds to RF spoiling increment of $0^\circ/360^\circ$.

As explained above, T_1 and T_2 relaxations induce an attenuation of the magnetization components (Scheffler, 1999), while diffusion acts as Gaussian filtering (Freed et al., 2001; Kaiser et al., 1974). Figure 2.25 provides complex representations of signals obtained with different T_1 , T_2 , and ADC values for the same acquisition parameters, indicating that the SSFP model is sensitive to any variation of one of these NMR physical parameters. Therefore, choosing wisely the applied N_{RO} , phase increments and flip angle(s) will allow a proper sensitivity to the NMR parameters of interest PD, T_1 , T_2 and ADC using this complex signal behavior.

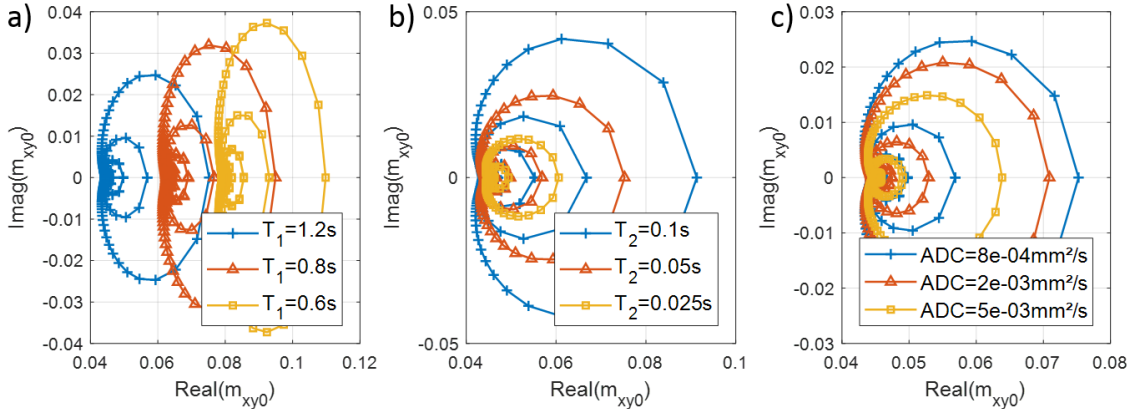


Figure 2.25. Complex representation of simulated signals sampled for each degree of RF spoiling increment from 0 to 360°, $TR=10ms$, $FA=20^\circ$, resolution of $1mm^3$ and $N_{RO}=4$ varying T_1 (a), T_2 (b) and ADC(c), otherwise fixed to respectively 1.2s, 50ms and $0.8 \times 10^{-3} mm^2/s$. This figure highlights the contrast variations that can be obtained depending on the relaxation times and diffusion.

2.2.6.3. Quantitative extraction

To perform the quantitative extraction from the multiple SSFP contrasts, post-processing is performed using Matlab (The Mathworks, Natick, USA) and DICOM complex images. Here, we will also consider the simplest case where only the $k = 0$ configuration state is acquired.

- Off-resonance removal

First, the acquired contrasts are grouped into a single measurement vector, denoted $m_{xy_{0,mes}}$. Global phase drifts are removed, assuming a linear temporal evolution between the first and last volumes that need to be acquired in the same conditions. A phase map is estimated using the complex sum of volumes with 0° , 360° and 180° RF phase increments, in which off-resonance effects as well as motion during scanning induce phase dispersion:

$$\varphi_{TE} = \varphi_1 + \gamma \Delta B_0 TE + \varphi_v \quad (2.40)$$

Which includes a potential dephasing φ_1 between emission and reception, field inhomogeneities ΔB_0 and possible velocity encoding φ_v . It is then subtracted from all volumes providing the SSFP phase-induced maps corrected for the phase at echo time, and thus for B_0 inhomogeneities.

- Inverse problem formulation

To perform the quantitative extraction of the different NMR parameters, the Gaussian noise statistics allows us to express our inverse problem in terms of a least-square minimization of the complex measured signal to the complex signal model:

$$\min_{M_0, T_1, T_2, ADC, \alpha} \left\| m_{xy0,mes} - M_0 \times m_{xy0}(T_1, T_2, ADC, \alpha) \right\|^2 \quad (2.41)$$

Where m_{xy0} represents the complex signal at TE, including relaxation and diffusion attenuations. Multiple solutions can be used to solve this least-square problem. Here, an implementation based on the combination of a dictionary-comparison, followed by the application of Gauss-Newton algorithm is proposed.

- Initialization step: dictionary comparison

To have optimal initial values $M_{0init}, T_{1init}, T_{2init}, ADC_{init}, \alpha_{init}$, one could imagine to start the iterative algorithm with fixed values, close to what is expected in vivo. But this strategy might be sub-optimal and not universal for different tissues or phantoms to image. Another solution would be to perform a comprehensive research into a 4 dimensional dictionary, corresponding to T_1, T_2, ADC and α . M_{0init} could then be deduced from the retrieved initial values as it is a scaling factor (See Eq. (2.41)). But considering for example 32 possibilities for each dimension would lead to a comparison with a discrete grid of $32^4 = 1,048,576$ possibilities. Comparing our signal with over a million values for each voxel would be very long and restrictive for a routine implementation.

Therefore, for an initialization purpose, a non-exhaustive research into a 4-dimensional dictionary can be considered sufficient. Different algorithms exist in literature and could be applied to achieve this task. Here, the employed strategy consisted in finding the best path in this dictionary until the best match with our signal is encountered. For a given location in the dictionary, M_0 is estimated with a least-square fit to the current dictionary model and the minimal norm from Eq.(2.41) is computed for the closest neighbors (two in each dimension). If the residual is smaller for a neighbor, the current point is updated and the process repeated. The algorithm ends when the central point is the smallest residual, as compared to its neighbors. The corresponding coarse T_1, T_2, ADC, α and M_0 estimates are noted $T_{1init}, T_{2init}, ADC_{init}, FA_{init}, M_{0init}$ and are used for the following non-linear fit.

- Gauss-Newton least-square fitting algorithm

This initialization step is followed by a Gauss-Newton least-square fitting algorithm. It is based on the Jacobian matrix, expressed as real and imaginary parts:

$$J = \begin{pmatrix} \text{real}(m_{xy_0}) & \text{real}\left(\frac{\partial m_{xy_0}}{\partial T_1}\right) & \text{real}\left(\frac{\partial m_{xy_0}}{\partial T_2}\right) & \text{real}\left(\frac{\partial m_{xy_0}}{\partial ADC}\right) & \text{real}\left(\frac{\partial m_{xy_0}}{\partial \alpha}\right) \\ \text{imag}(m_{xy_0}) & \text{imag}\left(\frac{\partial m_{xy_0}}{\partial T_1}\right) & \text{imag}\left(\frac{\partial m_{xy_0}}{\partial T_2}\right) & \text{imag}\left(\frac{\partial m_{xy_0}}{\partial ADC}\right) & \text{imag}\left(\frac{\partial m_{xy_0}}{\partial \alpha}\right) \end{pmatrix} \quad (2.42)$$

From the previously extracted initial conditions vector $[M_0_{init}, T_1_{init}, T_2_{init}, ADC_{init}, \alpha_{init}]^T$, the Jacobian matrix can be numerically computed. An update vector can then be obtained from:

$$[dM_0, dT_1, dT_2, dADC, d\alpha]^T = (J^H J)^{-1} J^H \begin{bmatrix} \text{real}(m_{xy_0}) - \text{real}\left(\frac{m_{xy_0,mes}}{S}\right) \\ \text{imag}(m_{xy_0}) - \text{imag}\left(\frac{m_{xy_0,mes}}{S}\right) \end{bmatrix} \quad (2.43)$$

Where J^H represents the Hermitian of the Jacobian matrix. The addition of this update vector to the preceding initial estimate refines the solution. M_0 can then be re-estimated as $M_0 \times (1 + dM_0)$ and used to normalize the signal for the next iteration. The procedure is repeated until the relative variation of the residual norm given by Eq. (2.41) is sufficiently small. Repeated voxel-wised, this iterative and non-linear method allows the retrieval of multiple quantitative maps of the proton density, T_1 , T_2 , ADC and flip angle.

Considering the Gaussian nature of the noise in MRI, characterized by its identical variance σ^2 on the real and imaginary parts, the Fisher Information Matrix (FIM) can be defined as in Eq. (2.44).

$$FIM = \left(\frac{\sigma}{|M|}\right)^2 (J^H J)^{-1} \quad (2.44)$$

Its inverse represents the covariance matrix of the noise, on the basis of which the Cramer-Rao lower boundaries can be extracted in order to estimate the precision on the fitted parameters. This FIM will be crucial in QuICS method, both for fitting and for optimal acquisition design, as will be discussed in Chapter 3.

This generic fitting procedure can be adapted equally well to transient signal fitting or to include acquisitions obtained in an interleaved or sequential manner by varying the series of RF pulses, as described in (de Rochefort, 2016). So far, QuICS has been applied in the steady-state regime, on a phantom at 1.5T on a Philips equipment. Data show promising results in the simultaneous estimation of M_0 , T_1 , T_2 , ADC and flip angle (de Rochefort, 2015).

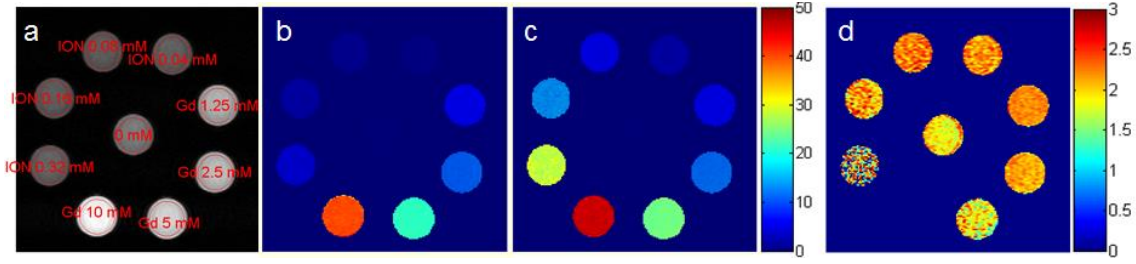


Figure 2.26 : QuICS preliminary results at 1.5T on Philips equipment. (a) Sample locations and compositions, (b) R_1 in s^{-1} (c) R_2 in s^{-1} (d) ADC in $10^9 m.s^{-1}$. Imaging was performed at 1.5 T (Philips Achieva) using a quadrature head coil for reception. Gd-chelate (10, 5, 2.5, 1.25, 0 mM, Dotarem, Guerbet) and iron oxide nanoparticle (0.32, 0.16, 0.08, 0.04, 0 mM, CL-30Q02-2, Molday ION, Biopal) solutions were prepared. Scan parameters were $TR/TE=9.2/4ms$, acquisition matrix $168 \times 84 \times 9$ and voxel size $0.5 \times 1 \times 8mm$, reconstructed voxel size $0.47 \times 0.47 \times 8mm$, bandwidth $217Hz/pix$, $Tacq=21min$, $\alpha=45^\circ$, 180 RF spoiling steps with 2° phase increments, acquisition of the $k=0$ state. Flip angle was set to 45° to accelerate reconstruction.

Although a flip angle 45° was used in this publication, small flip angles should be sufficient to extract information. As FA can be considered as a variable to estimate, the method has the possibility to be robust to B_1^+ inhomogeneities. B_0 heterogeneities are also taken into account in the signal model, as shown in Eq. (2.40). Therefore, this method seems to be suitable for clinical UHF MRI.

2.3. Objectives and challenges

Quantitative MRI offers the opportunity to get access to unique information. Its clinical potential has been demonstrated, mainly for tissue characterization, detection of pathological changes and medical follow-up. However, the clinical acceptance will only come with a rapid and accurate way to produce images. Many methods have been proposed to perform simultaneous multi-parametric mapping. Despite the growing interest in UHF to obtain better images, these in vivo quantitative mappings are virtually non-existent beyond 3T, as their implementation lies in the capacity to overcome a number of specific UHF MRI limits. Hence, finding the optimal strategy to provide fast and accurate quantitative results, compatible at any field strength, remains an important and challenging question. A work of (van Valenberg et al., 2017) studied the time efficiency of different methods based on Bloch equations, and no direct conclusions were drawn. As it would be impossible to implement properly all of the methods mentioned above in the time course of a thesis to answer this question, a choice needed to be made on which method to apply at 7T, based on the existing tools, clues and intuitions we had in the laboratory. Given the advantages provided by QuICS for an UHF application, the objective of this PhD thesis was to implement QuICS to perform multi-parametric maps in vivo at 7T in a clinically-relevant time.

First, as clinical acceptance lies in the reproducibility of the data, Chapter 3 will be dedicated to the development of an appropriate acquisition strategy to avoid any instrumental or physiological factor during the acquisition at 7T. The acquisition will also be optimized to fasten the acquisition time. Such sequence setup will be validated in vitro on phantoms. In Chapter 4, we look for the best solution to limit B_1^+ heterogeneities and demonstrate the possibility to apply QuICS in vivo on human brain in a clinically-viable time. Then, in Chapter 5, a first application of the method to a complex nucleus such as sodium nucleus will be performed in vitro. Different sodium molecular environments will be investigated to explore the ability of the method to probe varying properties with very different values from what can be encountered in proton.

This work benefited from close collaborations with different research institutes. Dr. Ludovic de Rochefort (CRMBM, Aix-Marseille University) provided the developed tools to reconstruct quantitative images and shared his work and knowledge about the method he patented during all the project. Dr. Mathieu Santin and Dr. Romain Valabrègue from Institut du Cerveau et de la Moelle Epinière (ICM, Paris) greatly helped in the research of an efficient and unbiased acquisition protocol, in the Chapter 3. Dr. Julien Lamy (ICube, Strasbourg University) provided a secured platform to share and exchange codes and data between partners, and Dr. Paulo Loureiro de Sousa (ICube) provided insights about quantitative MRI. Dr. Redha Abdeddaïm and Dr. Marc Dubois (Institut Fresnel, Marseille) provided guidance to manipulate new materials for B_1^+ mitigation.

This project was also the occasion to form an internal collaboration at Neurospin, with the X-nuclei team, represented by Dr. Arthur Coste, Dr. Fawzi Boumezbeur and Dr. Cécile Lerman, as well as the coil team, with the objective to study the sodium properties.

All these collaborations were greatly helped by the ‘Agence Nationale pour la Recherche’ (ANR) thanks to the grant ‘Infrastructure d’avenir en Biologie Santé - ANR-11-INBS-0006’. This thesis work was made possible thanks to the precious funding from Paris-Sud/Paris-Saclay University and the additional support from H2020 project called “MCUBE”. This manuscript also contains some findings made during my master’s internship about dielectric shimming using new materials, financed by the French ANR through the “CODENUM” project.

Chapter 3.

Implementation and validation of a multiple contrasts spoiled SSFP sequence for simultaneous multiparametric extractions at 7T

This chapter contains methods & principles, in §3.1.1 and §3.1.3, that were accepted for publication as abstract in the proceedings of the European Society for Magnetic Resonance in Medicine and Biology 2016, and presented as a talk.

L. Leroi, L. de Rochefort, M. Santin, F. Mauconduit, R. Valabregue, D. Le Bihan, C. Poupon, A. Vignaud, « Simultaneous multiparametric quantitative extraction at 7 Tesla using QuICS », proceedings of the European Society for Magnetic Resonance in Medicine and Biology 2016, Vienna, abstract # 272.

Performing quantitative MRI can be achieved using different strategies, as described in Chapter 2. Our choice was made to perform simultaneous multi-parametric assessment using the QuICS method described in §2.2.6. Indeed, it can simultaneously retrieve M_0 , FA, T_1 , T_2 and ADC. It presents assets to be used at UHF as it includes B_0 and B_1^+ assessment to correct for their heterogeneities. It has been applied at 1.5T (de Rochefort, 2015), but never translated to ultra-high field MRI.

In this chapter, we will first validate the proper functioning of the QuICS quantification process in the simplest conditions, using a 1Tx/Rx coil and agar phantom at 7T. Then, we will make the use of phased array coils possible, as they are commonly used in clinical routine at UHF. Such coils will allow us to accelerate acquisition time using clever imaging techniques such as GRAPPA (Griswold et al., 2002) or SENSitivity Encoding (SENSE) (Pruessmann et al., 1999). As quantitative MRI relies on reproducibility and accuracy, we will then check the performance of a simple protocol over time. Finally, to meet clinical needs, we will further reduce acquisition time by developing an appropriate acquisition strategy using Fisher Information Matrix and Cramer-Rao lower bound, testing its efficiency on ex-vivo baboon brain. The objective of this chapter is therefore to be confident on the applicability of the method in order to translate it in vivo, in optimum conditions at 7 Tesla.

3.1. Materials and methods

3.1.1. Phantom validation using 1Tx/1Rx

To ascertain the proper functioning of the QuICS at 7T, a first implementation of the method was performed on a 7T Magnetom MRI (Siemens Healthcare, Erlangen, Germany) using the simplest coil available, a birdcage head coil 1Tx/1Rx (Invivo Corp., Gainesville, USA), to assess the NMR properties of a spherical phantom filled with water, 1% agar and 0.4%NaCl.

A spoiled SSFP sequence was implemented to acquire 45 different contrasts sequentially, by varying only radiofrequency spoiling increments Φ_0 , sampled every 2° from 0° to 10° and 350° to 360° , and every 10° from 20° to 340° , to probe the entire complex plane, as described in Figure 2.24, page 66. The spoiling gradient was restricted to the readout direction, with fixed $N_{RO}=1$. The nominal flip angle was fixed as well, chosen arbitrarily at 45° . Scanning parameters were TR/TE 12ms/5.1ms, voxel size $1.3 \times 1.3 \times 5.0 \text{ mm}^3$, and a bandwidth=220Hz/pixel, leading to a total acquisition time of 32min15s.

The data were fitted voxel-wised to the Bloch-Torrey equation to estimate M_0 , R_1 , R_2 , B_1^+ and ADC using the calculation approach based on the configuration states formalism presented in Chapter 2.

Actual T_1 , T_2 and ADC of the phantom were assessed separately using respectively gold-standard methods. For T_1 assessment, an Inversion-Recovery Turbo Spin-Echo was repeated for different inversion times with $TR/TE=10000/8.1\text{ms}$, a resolution of $1\text{x}1\text{x}5\text{mm}^3$ and a turbo factor of 3, leading to an acquisition time of 14min32 per inversion time. Investigated inversion times ranged from 50 to 5000ms: [50 100 300 500 700 1000 3000 5000]ms.

For the assessment of T_2 , a multi Spin-Echo sequence was used with a resolution of $1\text{x}1\text{x}8\text{mm}^3$, a TR of 10s and varying $TE=[14\ 20\ 28\ 40\ 56\ 79\ 112\ 158\ 224\ 316\ 500]\text{ms}$. The total acquisition time for a volume with an EPI factor of 3 was 14min40.

To measure the diffusion in the readout direction, double Spin-Echo diffusion EPI was applied with b -values of 0, 500 and 1000s/mm^2 . TR/TE were set to $5000/76\text{ms}$. The use of an EPI factor of 80 lead to an acquisition time of 1min37 for a $2.4\text{x}2.4\text{mm}^2$ resolution and a slice thickness of 5mm.

3.1.2. Phantom validation using $1T_x/32R_x$ and phase combination

3.1.2.1. Phase incoherences: the need for an efficient phase combination

In conventional MRIs with a 1.5T static field, the B_1 field is created by whole-body coils embedded in the device. However, at UHF, birdcages of smaller sizes, organ-specific, are used to obtain an emission as homogeneous as possible, with acceptable SAR and SNR. But to recover an optimal SNR coverage of the entire region of interest, it is necessary to use several coils. We then speak of a phased array of reception coils inside the transmitting antenna.

When using such technology, each coil has its own RF signal reception channel and produces an image of the anatomical region close to it. The different images obtained are then combined to form a composite image. Phase images combination usually relies on the sum of the spatial complex data (p_j) for each coil j as shown in Eq. (3.1).

$$\varphi_I(x, y, z) = \arg \left(\sum_{j=1}^{N_c} p_j(x, y, z) \right) \quad (3.1)$$

Where $\varphi_I(x, y, z)$ is the phase at (x, y, z) coordinates, and N_c is the number of receiving coils.

But this classic method is based on the assumption that all sensitivities are spatially uniform such that there are no spatially varying sensitivity weighting and identical phase. However, if the number of receiving coils increases, the decrease in their size induces a concentrated reception of the signal at the periphery of the area to be observed. This offers a very good SNR on the periphery, but the signal will be dramatically attenuated in the center of the image (see Figure 3.1). The heterogeneity of the signal intensity greatly complicates further analysis based on complex data, as this sensitivity profile variations will impair magnitude as well as phase images.

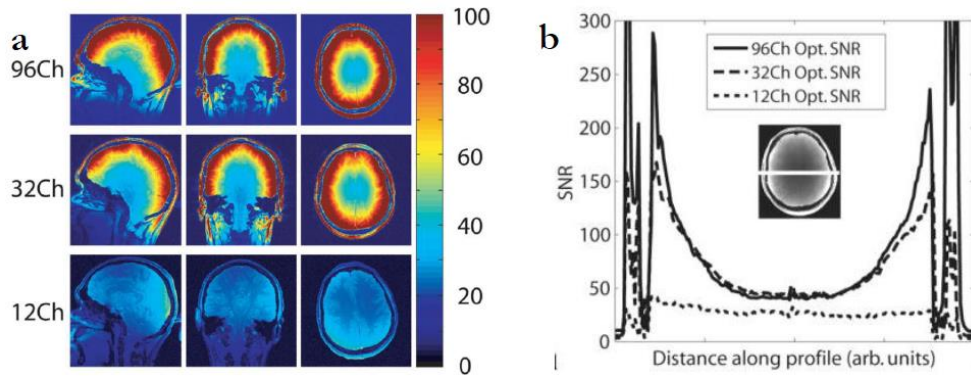


Figure 3.1: (a) SNR maps for optimum SNR combination derived from gradient echo scans at 3T for 96, 32 and commercial 12 channel coils. (b) SNR profiles through axial slices passing approximately through the corpus callosum for the 96-channel coil (solid line), 32-channel coil (dashed line), and commercial 12-channel coil (dotted line). From (Wiggins et al., 2009).

Combining phase information using the classic summed complex data will therefore lead to interferences and regions of signal cancellation. Phase images calculated in this way frequently show wraps that terminate within the object, corresponding to a complete signal cancellation, known as “open-ended fringe lines”, or phase incoherencies, as shown in Figure 3.2.

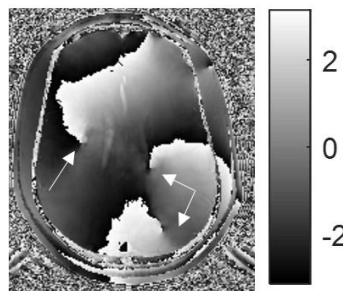


Figure 3.2: Axial Dicom phase image (in radians) of in vivo human brain acquired at 7T using a spoiled SSFP sequence and a 32-channel receiving coil. Several open-ended fringe lines can be observed, as highlighted by the white arrows.

In QuICS, the phase variations are of great interest. Therefore, the relative receiver coils phases need to be corrected while images are combined, in order to obtain consistent data, avoiding any signal loss.

3.1.2.2. Performing phase combination

As the complex coil sensitivities (i.e. the relative phase and amplitude of each receiver coil throughout the imaging volume) are usually not known, some methods in the literature are trying to assess them directly from the complex images (Walsh et al., 2000). These self-calibration methods typically result in optimal magnitude images, but still tend to experience inconsistencies and failures in phase determination (Robinson et al., 2011). Other methods implement phase filtering, with a high pass filter to eliminate the slowly varying receiver phase as in (Koopmans et al., 2008). Another strategy is to combine the multiple coils after adding a constant phase offset to each channel to equalize the phase at a point and yield approximate phase equalization throughout the image volume (Hammond et al., 2008).

Here, an extension of the phase equalization technique, currently being patented by Dr. Mathieu Santin (Institut du Cerveau et de la Moëlle Epinière) was applied (Santin, 2018). In this method, a reference receiver coil, denoted *Ref* is created, to which the measurements of each receiver coil are referenced and then combined to obtain an optimal phase distribution estimate. The different raw data of images obtained are thus rephased to be uncorrelated of the sensitivity of their own respective coil.

To compute this reference coil, a first step of correction of phases from complex data is necessary. This step is intended to standardize each channel in terms of phase. The correction factor for the j -th coil, φ_j , is the phase of the sum of the complex acquired data p_j :

$$\varphi_j = \arg \left(\sum_{x,y,z} p_j(x, y, z) \right) \quad (3.2)$$

Where x , y and z vary to describe the volume of interest. The subtraction of this correction factor to the acquired data leads to the corrected signal \tilde{p}_j :

$$\tilde{p}_j(x, y, z) = p_j(x, y, z) e^{-i\varphi_j} \quad (3.3)$$

The reference coil *Ref*, for the current time t , can then be computed by linear combination of the coils. Here, the linear combination comprises a weighting by the inverse of the sum of the modules of the set of data obtained:

$$Ref = \sum_{j=1}^{N_c} \frac{\tilde{p}_j(x, y, z)}{\sum_{k=1}^{N_c} |p_k(x, y, z)|} \quad (3.4)$$

Ref is computed once and kept in memory for the series of different contrasts. The raw data acquired can then be rephased with respect to the reference coil determined, so that their phases no longer depend on their respective sensitivities. To do so, a phase difference

$\delta_j(x, y, z)$ between the complex image and the corresponding complex data from the reference coil is computed:

$$\delta_j(x, y, z) = \arg(p_j(x, y, z)) - \arg(Ref(x, y, z)) \quad (3.5)$$

A 3D Hanning low-pass filter is applied to this difference to remove noise-related phase components, leading to the low-pass filtered difference $\langle \delta_j(x, y, z) \rangle$. Complex data for each coil, $\hat{p}_j(x, y, z)$, are obtained by subtracting this filtered difference from the original data:

$$\hat{p}_j(x, y, z) = p_j(x, y, z)e^{-i\langle \delta_j(x, y, z) \rangle} \quad (3.6)$$

It is this operation that substitutes the sensitivity phase components of the different coils by the same phase component specific to the reference coil. Then follows the generation of a complex image p by summing the data complex data \hat{p}_j , weighted by the diagonal elements of its covariance matrix R .

$$p(x, y, z) = \sum_{j=1}^{N_c} \frac{1}{R_{j,j}(x, y, z)} \hat{p}_j(x, y, z) \quad (3.7)$$

The implementation of this reconstruction makes the correction of this instrumental bias possible, leading to proper phase images to analyze.

3.1.2.3. Experimental application

The above algorithm was implemented under Siemens ICE (Image Calculation Environment) programming environment to provide the reconstruction of the images on the MR console, in DICOM format. To validate the phase reconstruction algorithm, the acquisition of a spoiled SSFP was performed on a spherical oil phantom, using a 1Tx/32Rx head coil (Nova Medical, Wilmington, MA, USA).

QuICS was then performed using same acquisition parameters as in §3.1.1. The only modification was the addition of a GRAPPA acceleration factor of 3, leading to a total acquisition time of 16min30sec instead of 32min15s, for the same field-of-view of 256x256x160mm³ and resolution of 1.3x1.3x5.0mm³.

3.1.3. Reproducibility of the method

As quantitative MRI relies on the reliability and reproducibility of the results, the same protocol as presented in §3.1.1. was repeated over 6 months using both a transceiver birdcage coil and a 1Tx/32Rx head coil, over the same spherical phantom containing 1% agar and 0.4%NaCl. Some gold-standard measurements, described in §3.1.1, were performed to check for possible variations of the phantom properties over time.

3.1.4. Accelerating acquisition time

3.1.4.1. Fisher information matrix and Cramér-Rao lower bound

To optimize the acquisition time for clinical applications, the number of contrasts to acquire needs to be limited. The selection of the most informative flip angle, RF spoiling Φ_0 and N_{RO} steps can be performed using the Fisher Information Matrix (FIM) in the optimal experimental design framework. Let's denote the parameters to estimate θ_k , $k=[1,2,3,4,5]$, corresponding to PD, FA, T_1 , T_2 , ADC. One needs to consider the signal S_i , modeled by the Bloch equations corresponding to a set of acquisition parameters (prescribed FA, RF spoiling increment, N_{RO} , TR, resolution, etc.) with variance σ . The FIM, for a number of observed data N_{meas} , is defined in Eq.(3.8):

$$FIM_{jk} = \sum_{i=1}^{N_{meas}} \frac{1}{\sigma^2} \frac{\partial S_i}{\partial \theta_j} \frac{\partial S_i}{\partial \theta_k} \quad (3.8)$$

It was also presented in §2.2.6.3. (see page 69), in Eq.(2.44). The FIM measures the information one sample gives to estimate the parameter θ_k and therefore evaluates the quality of discrimination of the selected sample. A Fisher information close to zero indicates that a sample provides no clue for the estimation of the parameter θ_k . This FIM is closely linked to the Cramér-Rao lower bound (CRLB), defined in Eq. (3.9), which gives a lower bound of the error σ_{θ_k} made in the estimation of the considered parameter θ_k (Alexander, 2008; Anastasiou and Hall, 2004).

$$\sigma_{\theta_k} \geq CRLB_k = \sqrt{FIM_{kk}^{-1}} \quad (3.9)$$

To restrict the acquisition protocol to the most informative contrasts, the cost function to minimize, CF , is defined as the sum of the normalized CRLB over the number of parameters to estimate, $N_{par} = 5$ (Eq. (3.10)).

$$CF = \sum_{k=1}^{N_{par}} \frac{\sigma_{\theta_k}^2}{\theta_k^2} \quad (3.10)$$

Optimizing this FIM will therefore be a crucial element in QuICS method. It will both improve the results from the Gauss-Newton fitting algorithm, partly relying on its assessment, thus obtaining accurate quantitative extractions, as well as help shortening the acquisition strategy.

To perform the acquisition strategy optimization, a Self-Organizing Migration Algorithm was implemented (Zelinka, 2004) by Dr. Romain Valabrégue from Institut du Cerveau et de la Moëlle Epinière.

3.1.4.2. SOMA algorithm

The Self-Organizing Migration Algorithm (SOMA) is a general-purpose, stochastic optimization algorithm. The approach is based on the idea of a series of “migrations” by a fixed set of individuals. It can be applied to any cost-minimization problem with a bounded parameter space, and is robust to local minima.

At first, a table containing all possibilities of RF increments, flip angles and N_{RO} given the targeted ranges of PD, T_1 , T_2 , FA, and ADC is created and stored in computer’s memory. SOMA works on a population of candidate solutions, initialized randomly distributed over the search space at the beginning of the optimization process. First, the randomly generated population is evaluated and the solution with the highest fitness becomes “the leader”. Then all individuals will “migrate” towards this leader for a certain distance, called path length, in n steps of defined length, with a randomly perturbed path. The cost function defined in Eq. (3.10) will calculate the fitness of each individual during its migration and assign the best fit to the parameters. A new population is generated and this process is repeated until the number of given migration is over. The best solutions of all the migrations are then assigned to the parameters N_{RO} , flip angle and RF increment to acquire the corresponding contrasts.

3.1.4.3. Experimental validation

In order to assess this optimization process on a phantom closer to in vivo conditions where different T_1/T_2 pairs can be encountered, an ex-vivo baboon brain in FluorinertTM, a liquid with high dielectric strength and a magnetic susceptibility closer to that of water, was used.

The SOMA algorithm was applied using 200 migrations. The targeted tissues parameters corresponded to the ranges expected in vivo at 7T : $T_1 = [0.3; 3.5]$ s, $T_2 = [0.01; 0.2]$ s and ADC was fixed to $0.8 \cdot 10^{-9} \text{m}^2 \cdot \text{s}^{-1}$ (Marques and Norris, 2018). The allowed FA varied from 1 to 25 degrees to restrict SAR as much as possible, and N_{RO} ranged from 1 to 11, where 11 was the maximum reachable gradient given the TR/TE of respectively 10/1.3ms. The resolution was set to $1.3 \times 1.3 \times 5.0 \text{mm}^3$ in a field-of-view of $256 \times 256 \times 165 \text{mm}^3$. A 1Tx/32Rx head coil was used, allowing to the application of a GRAPPA acceleration factor of 3, leading to an acquisition time of 36sec per volume. The total acquisition time for 12 volume was therefore of 7min12.

Gold-standard acquisitions were also acquired as described in §3.1.1 to compare the consistency of the quantitative results.

3.2. Results

3.2.1. 1Tx/1Rx application

The measured signal of the central pixel for the 45 different RF spoiling increment Φ_0 , and the corresponding theoretical fit are shown in the complex plane in Figure 3.3. The fitting curve is very close to the measured values. Over the central slice, mean R_1 was $0.297 \pm 0.018 s^{-1}$, R_2 $6.71 \pm 0.046 s^{-1}$ and ADC $1.92 \pm 0.12 \times 10^{-9} m^2/s$ (Figure 3.4). Compared to gold-standard measurements, it represents an under-estimation of respectively 10.8%(R_1), 2.1%(R_2) and 4.0%(ADC). Standard deviation values over the slice indicate a limited spatial dependence regardless of the severe B_1^+ inhomogeneity encountered at 7T using a 1Tx/1Rx coil. The R_2 map also shows the ability of the method to detect structures in the phantom, as heterogeneities are observed in the top of the agar phantom.

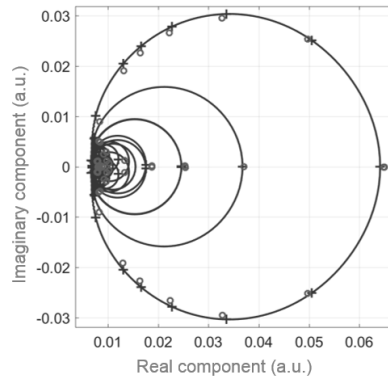


Figure 3.3 : Measured signal for each RF increment (dots) and fit (curve) displayed in the complex plane for the central pixel of central slice of the phantom. Maximum real value corresponds to a RF increment of 0° .

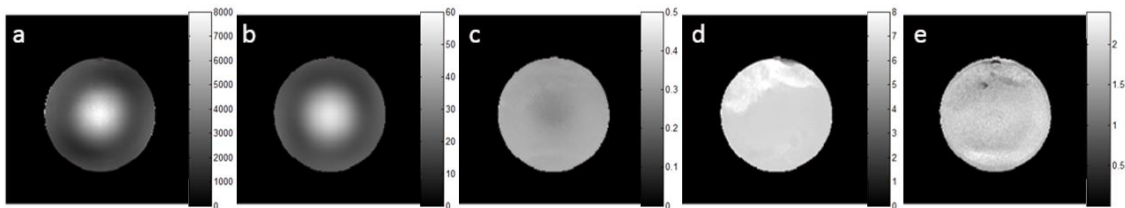


Figure 3.4 : QuICS quantitative multiparametric extraction on a 1Tx/1Rx birdcage coil. Fitted parameters maps for the central slice of the phantom are shown: M_0 (a), flip angle in degrees (b), R_1 and R_2 in s^{-1} (c, d), diffusion map in $10^{-9} m^2.s^{-1}$ (e). A higher density has been detected in the upper area in (d) and (e), showing the potential of the method to distinguish some heterogeneities of signal.

3.2.2. 1Tx/32Rx application

The DICOM image displayed in Figure 3.5a shows a typical phase incoherence encountered at 7T using the classic reconstruction method of sum-of-square, available on scanner, with a 1Tx/32Rx coil. The implementation of the phase combination algorithm described in §3.1.2.2 corrects this phase incoherence, as shown in Figure 3.5b. A remaining “wrap” jump of 2π remains, but can be easily removed using a phase unwrapping algorithm, as it does not constitute a signal cancellation.

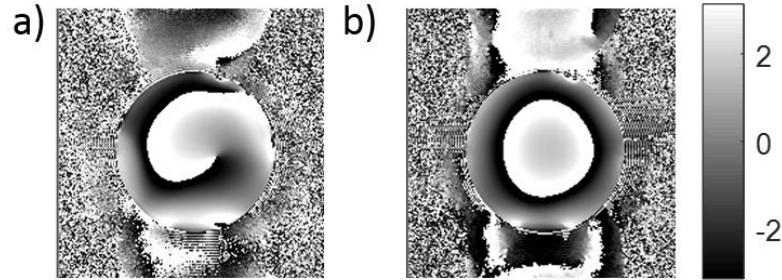


Figure 3.5 : 7T acquisitions of an oil phantom using a spoiled SSFP sequence on a 1Tx/32Rx coil. DICOM images of phase (in rad) with Siemens standard reconstruction (a) and using the algorithm described above (b) are shown. The phase in (b) is more homogeneous than (a), and discontinuities encountered in (a) have disappeared in (b).

The application of QuICS on a 1Tx/32Rx coil using this reconstruction algorithm resulted in mean R_1 was $0.345 \pm 0.032 \text{ s}^{-1}$, R_2 $6.73 \pm 0.575 \text{ s}^{-1}$ and diffusion $1.94 \pm 0.21 \times 10^{-9} \text{ m}^2/\text{s}$ over the central slice of an agar phantom (Figure 3.6). Compared to gold-standard measurements, it represents an over-estimation of respectively 3.6%(R_1), 2.4%(R_2) and 3.0%(ADC).

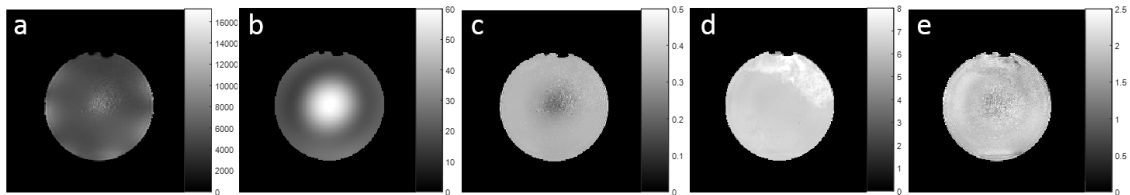


Figure 3.6 : QuICS quantitative multiparametric extraction on a 1Tx/32Rx coil. Fitted parameters maps for the central slice of the phantom are displayed M_0 (a), flip angle in degrees (b), R_1 and R_2 in s^{-1} (c, d), diffusion map in $10^{-9} \text{ m}^2 \cdot \text{s}^{-1}$ (e). The reception profile can be seen on the M_0 map. The same higher density has been detected in the upper area in R_2 and ADC, showing the potential of the method to distinguish some heterogeneities of signal.

These preliminary results validated the implementation of a QuICS protocol using 45 contrasts in 16min30 using a clinical 1Tx/32Rx coil.

3.2.3. Reproducibility of the results

Figure 3.7 shows the measurements of mean T_1 , T_2 and ADC over the central slice made over approximately 6 months. These results present a very good accuracy over time, as the values are well-estimated and present no bias. These measures are also repeatable over the same day, as the experiment was reproduced five times on the 18/07/2016, leading to the same values. Finally, the low variability of estimations over time demonstrate the reproducibility of the method for this acquisition protocol.

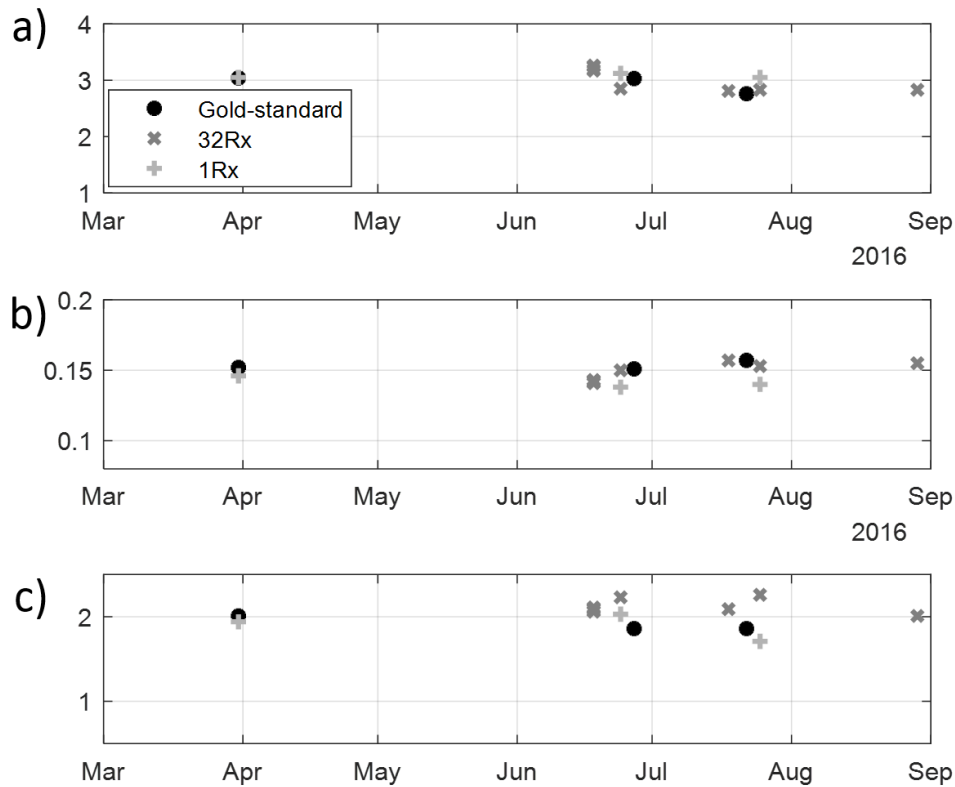


Figure 3.7 : Reproducibility of the same repeated protocol in the estimation of T_1 in seconds (a), T_2 in seconds (b) and ADC in mm^2/ms (c), with gold-standard measurements, using either a 1Tx or a 32Rx coil. Results show low variability over the large period of time.

Altogether, this protocol respects the Quantitative Imaging Biomarkers specifications, described by the Quantitative Imaging Biomarkers Alliance Metrology Working Group (Sullivan et al., 2015), to be applied in clinical routine. Unfortunately, its resolution of $1.3 \times 1.3 \times 5.0 \text{ mm}^3$ in approximately 16 minutes remains too coarse and too long to be relevant on a human brain. In addition, for in vivo application on the whole brain at high isotropic resolution, the acquisition time is expected to be dramatically lengthened. Therefore, the acquisition strategy was optimized by selecting the most informative contrasts to determine the desired parameters.

3.2.4. Optimized protocol

The most informative N_{RO} , flip angle and RF spoiling increment contrasts retrieved from the SOMA algorithm and are displayed in Table 3.1.

Contrast #	1	2	3	4	5	6	7	8	9	10	11	12
FA (°)	24	19	9	6	13	25	20	18	25	24	25	24
RF incr. (°)	0	358	2	358	2	5	349	343	358	5	358	360
N_{RO}	2	11	11	11	11	2	2	3	11	11	2	2

Table 3.1 : Acquisition setup resulting from the optimization process for an acquisition of $1.3 \times 1.3 \times 5.0 \text{ mm}^3$ with 12 contrasts, leading to a total acquisition time of 7min12.

The corresponding acquisitions, shown in Figure 3.8, exhibit substantial fluctuation in the signal intensity, both in magnitude and phase

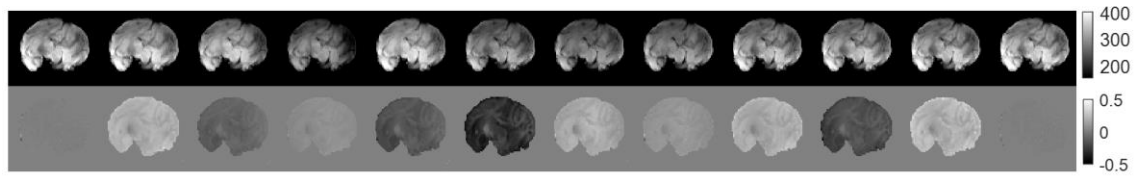


Figure 3.8: Normalized magnitudes (upper row) and phases (lower row) contrasts obtained on an ex-vivo baboon brain in fluorinert at 7T when acquiring the acquisition setup from Table 3.1, at a $1.3 \times 1.3 \times 5.0 \text{ mm}^3$ resolution.

Results of the underlying quantitative extraction are shown in Figure 3.9, together with gold-standard acquisitions for comparison purpose. Globally, a great consistency can be observed between gold-standard acquisitions and QuICS extractions. Unlike agar phantoms, a shorter T_2 compared to the gold-standard Spin Echo method is reported using QuICS. The same trend is observed in the literature of multi-parametric quantitative mapping based on SSFP contrasts, and might be explained by magnetization transfer effects not encountered in the model (Hilbert et al., 2017), diffusive mechanisms (Anderson et al., 2017) or motion corruption (O'Halloran et al., 2015; Gras et al., 2017b), corrupting the steady-state by introducing additional phase to the transverse magnetization and leading to loss of signal and varying contrasts.

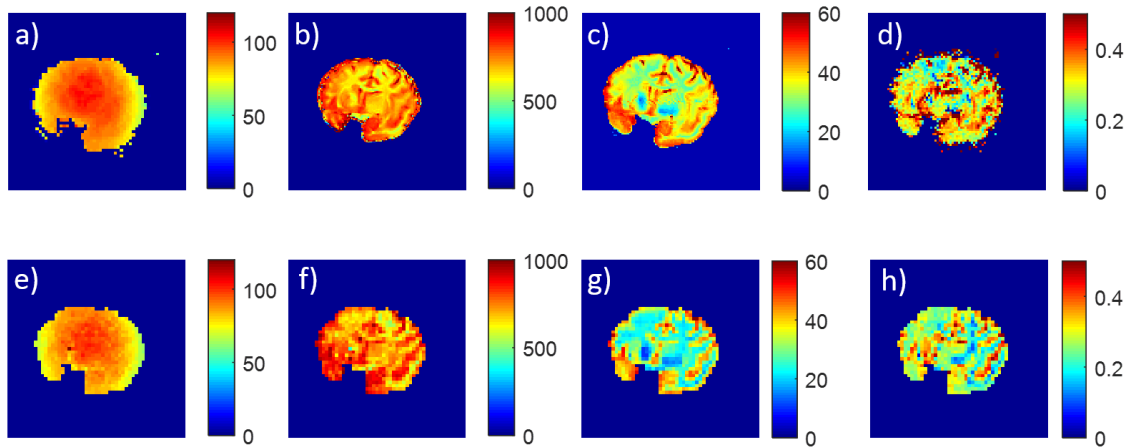


Figure 3.9: Quantitative maps obtained on an ex-vivo baboon brain in fluorinert at 7T. The first row shows results produced using gold-standard methods: Actual Flip Angle (AFI) for the flip angle assessment in degrees (a), Inversion-Recovery for T_1 in ms (b), Multi Spin-Echo (MSE) for T_2 in ms (c) and Double Spin Echo Diffusion EPI for diffusion, in mm^2/ms (d). The second row shows the QuICS extraction with same units. e) FA map, f) T_1 map, g) T_2 maps, h) mono-directional ADC maps in the readout encoding direction.

The experiments carried out so far validated the QuICS extraction process at 7T on various phantoms, from pre-acquisition contrast optimization to MR acquisitions, images reconstruction, and post-processing quantitative extraction.

3.3. Conclusion

The method is now optimized to provide accelerated multi-parametric extractions at 7T in optimum conditions. First, we ensured that the images reconstruction were consistent and that a simple protocol was reproducible over time. Then, we accelerated the acquisition time by using the potential of multiple receiving coils, allowing the use of acceleration factors relying on parallel imaging such as GRAPPA. In addition, we significantly reduced the acquisition time by optimizing the number of contrasts to acquire using Fisher Information Matrix and Cramer-Rao lower bound. We evaluated the protocol on an ex-vivo baboon brain, and were able to retrieve multiple parameters in a single acquisition, in agreement with gold-standard results. The quantitative extraction pipeline seems now ready for in vivo applications, under UHF constraints for accurate multiparametric mapping of tissue properties.

Chapter 4.

In vivo simultaneous multi-parametric quantitative MRI under UHF constraints

This chapter contains methods and results in §4.3.1. patented and under license (Multiwave Innovation, Marseille):

L. Leroi, R. Abdeddaim, S. Enoch, P. Sabouroux, G. Tayeb, N. Bonod, B. Larrat, E. Georget, A. Vignaud ; Procédé de contrôle de la répartition du champ magnétique radiofréquence dans un système d'imagerie par résonance magnétique. Reference: WO/2017/198914 A1.

These results were also accepted for publication as abstract in the proceedings of the International Society for Magnetic Resonance in Medicine and presented as an e-poster:

L. Leroi, A. Vignaud, P. Sabouroux, E. Georget, B. Larrat, S. Enoch, G. Tayeb, N. Bonod, A. Amadon, D. Le Bihan, R. Abdeddaïm, « B_1^+ homogenization at 7T using an innovative meta-atom », proceedings of the ISMRM 2016, Singapore, p. 3531

This chapter contains methods & results in §4.3.1 that are published in Physical Review X:

L. Leroi, M. Dubois, Z. Raolison, R. Abdeddaim, T. Antonakakis, J. de Rosny, A. Vignaud, P. Sabouroux, E. Georget, B. Larrat, G. Tayeb, N. Bonod, A. Amadon, F. Mauconduit, C. Poupon, D. Le Bihan, S. Enoch, “Kerker Effect in Ultra High Field Magnetic Resonance Imaging”, Physical Review X, 2018, in press

4.1. Introduction

In the vast majority of clinical investigations, MRI has been used as contrast weighted-imaging technique since such acquisitions are fast and compatible with clinical routine. Quantifying directly physical properties such as T_1 , T_2 , or PD is a main objective for the early detection of pathologies and their characterization, along with a proper patient's follow-up, becoming possible in multiple centers. The combined measurement of several MR parameters during an exam is expected to lead to a better diagnostic accuracy. Indeed, the correlation of multiple complementary NMR parameters could help in the interpretation of physiopathological events. Such strategy has already been demonstrated successfully with other simultaneous multi-parametric methods (Warntjes et al., 2008; Yu et al., 2017).

Originally, quantitative MRI required sequential implementation of PD, T_1 , T_2 , and B_1^+ mapping methods, leading to long examination times. More recently, multi-parametric approaches have emerged to simultaneously map relaxation times and PD, as detailed in §2.1.3.4 and §2.2. However, so far, multi-parametric qMRI has shown limitations, particularly at UHF, where there are larger susceptibility effects and FA inhomogeneity. Some approaches use saturation pulses that increase the SAR and some require long and complex post-processing (Cloos et al., 2016).

The objective of this study is to apply a qMRI technique based on a Steady-State Free Precession (SSFP) sequence at UHF, compatible with daily acquisitions conditions. This has two main consequences. Firstly, the sequence will need to be fast and to use low flip angles to be compatible with clinical routine. Secondly, results need to be unbiased and reliable in any situation.

In this chapter, we will first study the sensitivity of QuICS to flip angle heterogeneity for in vivo acquisitions and show how the B_1^+ heterogeneity is limiting the performances at 7T in the human brain. Then, we will present how to mitigate the B_1^+ field using meta-materials. This work was initiated during my master's internship and continued during the timeframe of this thesis. Finally, we will perform in vivo acquisitions using parallel transmission with an optimized and constrained protocol in order to provide fast and reliable multi-parametric extractions at 7T in a clinically relevant time.

4.2. Setup formulation for in vivo acquisitions in optimal conditions

QuICS relies on multi-contrast images acquired with various spoiling conditions. Once in vivo, under low spoiling conditions, images can present blurring and ghosting coming from

the motion of the CSF, induced by pulsatile flow, as can be seen in Figure 4.1a, pointed by the white arrow. The application of flow-compensation using gradient moment nulling in 3 directions attenuates this artefact observed near the CSF (see Figure 4.1b). Unfortunately, new shadings appear in other parts of the brain, coming from higher orders of velocity that cannot be nulled within an adequate TE.

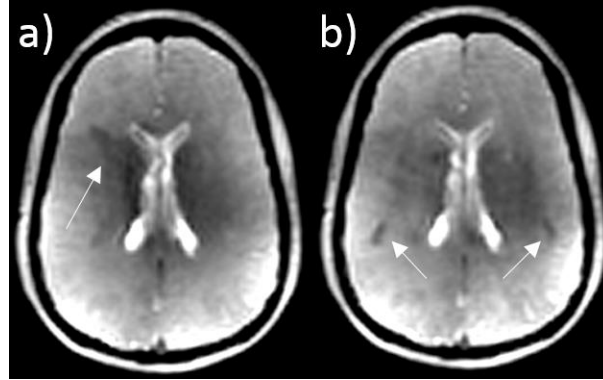


Figure 4.1: (a) Low spoiled image, with flip angle = 19° , RF Increment = 1° , $N_{RO} = 2$. Flow artefact can be seen near the CSF, as pointed by the white arrow. (b) Same contrast as a), with flow compensation applied in three directions. The initial artefacts have disappeared, but residual artefacts coming from higher orders of velocity are still encountered as shown by the arrows.

Experimentally, we could observe that the intensity of this flowing artefact varies depending on the subject, but that a value of $N_{RO} \geq 4$ could prevent such artefact, for any chosen RF spoiling increment. In addition, in this first series of experiments, we noticed that different spoiling gradients led to different steady-state eddy currents and consequently slightly different spatially inhomogeneous phase that needs to be accounted for. To avoid such effects, the choice was made to add a constraint to the optimization process, fixing the N_{RO} values to 4. This new constraint restricts our capability to retrieve ADC easily, as diffusion weighting will be identical for all contrasts.

To fit in our specifications to apply QuICS at UHF in a clinical environment, the technique needs to use low flip angle to keep SAR as low as possible while maintaining an acceptable SNR. Consequently, another constraint was added to the contrasts optimization, limiting FA to a maximum value of 30° .

In addition, in these in vivo experiment, the one-dimensional diffusion that could be retrieved on phantoms in the previous chapter was discarded. Indeed, such estimation was relevant for isotropic phantoms, but would bring only little information to clinicians in anisotropic media such as human brain (Basser et al., 1994). A proper trace ADC estimation would require multiple spoiling directions (N_{PE} , N_{SS}). More contrasts would therefore be needed, leading to a prohibitive acquisition time for clinical routine. Eddy currents would also need to be cautiously corrected in that situation to provide reliable results.

Considering these new constraints related to in vivo conditions, the optimized protocol derived in the previous chapter for baboon brain scanning is not compatible with in vivo acquisitions. The SOMA optimization algorithm based on Cramér-Rao lower bound presented in §3.1.4, page 80, was therefore used to select the 11 most informative contrasts, taking these constraints into account. Resulting acquisition parameters are shown in Table 4.1.

Considered scanning parameters were $TR/TE=11ms/3.3ms$, $bandwidth=650Hz/px$. The image resolution was set to $1x1x3mm^3$ in a $256x160x160mm^3$ field-of-view, leading to a total acquisition time of 16 minutes 36.

Contrast #	1	2	3	4	5	6	7	8	9	10	11
FA (°)	30	8	29	3	29	13	28	8	29	17	30
RF incr. (°)	0	358	9	1	77	359	1	2	1	358	360

Table 4.1: Acquisition setup resulting from the optimization process for an acquisition $1x1x3mm^3$ in 16minutes, leading to 11 contrasts.

To determine the sensitivity of such acquisition protocol to FA variations, in-silico simulations using brute-force Monté-Carlo were performed. The acquisition setup presented above was simulated, varying the FA from 0 to 60° with a precision of 1° , using 10,000 samples per FA. Results of these simulations are displayed in Figure 4.2.

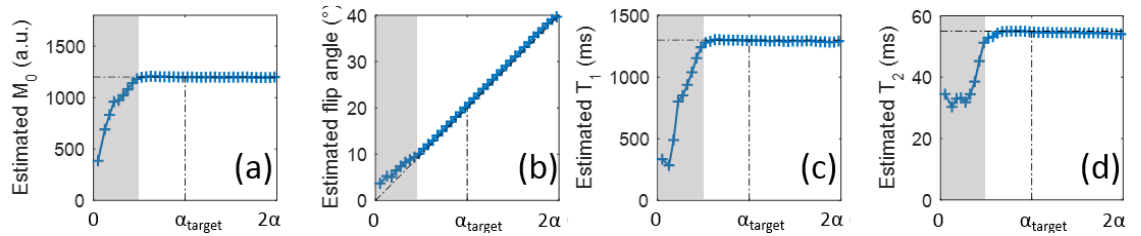


Figure 4.2: Brute-force Monte-Carlo simulations of M_0 (a), FA(b), T_1 (c) and T_2 (d) estimations as a function of effective FA, in order to account for its variations at UHF, considering ADC fixed to $0.8 \cdot 10^{-3} mm^2.s^{-1}$. Targeted T_1 and T_2 are 1400ms and 55ms respectively, corresponding to human white matter. This figure illustrates that for a FA lower than $\alpha_{target}/2$ (shaded area), the quantitative extraction process will fail to obtain reliable values of T_1 , T_2 , FA and M_0 .

These simulations show that the technique is robust to B_1^+ heterogeneity only to a certain extent for most of the parameters. If the flip angle is lower than half of the targeted flip angle, NMR parameters will not be evaluated properly. In the human brain at 7T, such loss of B_1^+ is expected to be encountered, especially in cerebellum and parietal lobes, as shown in §1.2.2. Applying such a protocol in vivo will probably lead to severe signal drops in areas where the B_1^+ is too low. Therefore, to apply QuICS in optimal conditions, we need to find a solutions to tackle these B_1^+ heterogeneities encountered in the human brain.

4.3. Limiting B_1^+ heterogeneities at 7T

Large B_1^+ inhomogeneities lead to substantial variations of the flip angle across the field-of-view, resulting in variable SNR and image contrast. To globally restore B_1^+ homogeneity in the volume would help obtaining unbiased contrasts in QuICS. But beyond this applicability for QuICS, finding an optimal solution to homogenize the flip angle distribution would more generally represent a game-changer in the development of 7T technology. Different strategies, introduced in §1.2.3, can be used for that purpose. A first option is proposed in literature, called “dielectric shimming”, based on the addition of high dielectric constant materials in the coil. We will discuss our involvement in the development of an innovative solution in this context. A second proposition, more complex, is based on parallel transmission and relies on the interferences of multiple transmission coils to retrieve a homogeneous B_1^+ . We will then discuss the integration of such technique into the QuICS method.

4.3.1. B_1^+ homogenization using meta-materials

4.3.1.1. Introduction

The introduction of relative High Dielectric Constant (HDC) materials in radiofrequency (RF) coils has been shown to address efficiently the local B_1^+ inhomogeneity in UHF MRI with limited SAR constraints (Teeuwisse et al., 2012a). HDC materials act as a secondary RF field source modifying the global RF distribution in the transmit coil (Brink et al., 2016; Yang et al., 2006). Literature reports that they can be made out of CaTiO_3 (Teeuwisse et al., 2012a) or BaTiO_3 (Teeuwisse et al., 2012b) powders mixed with de-ionized or deuterated water, or monolithic blocks of lead zirconium titanate (PZT) (Rupprecht et al., 2013).

Unfortunately, none of the proposed compositions are really fulfilling the requirements to be used in high field clinical routine. HDC pads represent an important bulk in the coil, they reduce patient’s comfort, and they degrade rapidly. Some materials can be expensive and, like BaTiO_3 , referenced as toxic according to international regulation EC 1272/2008. To foster the RF transmission and avoid these inconveniences, Dr. Redha Abdeddaïm from Institut Fresnel proposed a solution based on the use of a metamaterial structure, acting like a magnetic resonator in the coil.

Metamaterials are composite materials, whose effective properties mimic a material that is not available in nature. They are generally periodic structures, which can be dielectric or metallic, most often made of resonant cells. These materials can be considered as homogeneous, and investigated using usual electromagnetic characteristics. Their development

started from 1999, when Pendry demonstrated the possibility to obtain simultaneously a negative permittivity and permeability, never observed in natural materials (Pendry et al., 1999). Metamaterials are therefore currently the subject of many studies, whether in the field of imaging or telecommunications.

Several existing implementations of metamaterials have already been proposed for moderate field MRI to homogenize the B_1^+ field or enhance the SNR and the penetration depth (Freire et al., 2010; Holloway et al., 2012; Radu et al., 2009; Shchelokova et al., 2018; Wiltshire et al., 2001) and to a lesser extent for ultra-high field MRI to enhance performance and decoupling of surface coils (Connell et al., 2015; Georget et al., 2017; Hurshkainen et al., 2016; Jouvaud et al., 2016; Slobozhanyuk et al., 2016). Here, the proposed solution is based on the introduction of a passive metamaterial structure to locally enhance the B_1^+ field of a conventional volume coil.

However, the cautious study of scattering of the metamaterial needs to be undertaken. A crucial aspect for the control of radiation lies in the ability to tailor simultaneously the electric and magnetic response of a scatterer. This was first theoretically envisioned by Kerker et al. (Kerker et al., 1983), for a particle with specific values of permittivity and permeability, that the induced electric dipole and magnetic dipole radiation can strongly interfere, thus leading to strong scattering anisotropy. These effects were recently measured in the microwave regime (Geffrin et al., 2012) and are referred to as “first” and “second” Kerker condition corresponding to a zero-backward scattering and a near-zero forward scattering depending on the excitation frequency. Taking advantage of this physical effect in the RF range would allow control of the RF field distribution in a MRI volume coil.

In this work, we propose a new method based on metamaterial to improve the RF field homogeneity in UHF volume coils. We demonstrate that the RF field distribution of a birdcage coil can be controlled by inserting a “meta-atom” between the sample and the coil. A meta-atom can be designed using a single resonator element to build up more complex unit cell using coupling mechanism (Meinzer et al., 2014). The meta-atom considered here is based on a set of four hybridized resonant metallic wires. It will be referred as hybridized meta-atom (HMA) in the following. First, we will model the birdcage coil and HMA structure in order to study their effects in simulation. We will then experimentally validate both these simulations and an analytic approach developed to describe the interaction between the HMA and a birdcage coil depending on its length. Finally, we will demonstrate that the HMA can controllably redistribute and reshape the RF electromagnetic field within in a 7T MRI scanner with a better efficiency than conventional dielectric shimming.

4.3.1.2. Materials and methods

- Coil and metamaterials modeling

The metamaterial used here was a set of telescopic resonators made of four 2mm diameter copper rods, placed at the four corners of a rectangle of sides 1.5cm and 2cm, forming a rectangular parallelepiped in order to create a magnetic mode (Abdeddaim et al., 2011; Kanté et al., 2009), as displayed in Figure 4.3a. The length of the HMA can be tuned between 20cm and 100cm, and was set to 41cm for this first experiment.

To study the best location of the HMA in the coil, as well as the SAR induced to the patients, it is important to study the behavior of such a scatterer in simulations. Therefore, a birdcage coil 1Tx/1Rx, as well as the metamaterial were modeled using CST software (Computer Simulation Technology AG, Framingham, MA, USA). The coil was modeled according to the patent filed by Invivo Corporation in 2008 (Saylor, 2008).

Simulations were compared to experimental validation experiments using a birdcage head coil 1Tx/1Rx (Invivo Corp., Gainesville, USA) and a Specific Anthropomorphic Mannequin phantom (SPEAG, Zürich, Switzerland) on a 7T Magnetom MRI (Siemens Healthcare, Erlangen, Germany).

B_1^+ distribution at 7T were retrieved using an AFI sequence (Yarnykh, 2007) with a field-of-view of $256 \times 256 \times 144 \text{ mm}^3$ and a resolution of 4mm isotropic. The target flip angle was fixed to 60° . TRs were chosen such as $TR_1 + TR_2 = 130 \text{ ms}$ and $TR_1/TR_2 = 5$. Echo time was 3.06ms and the BW fixed to 1560Hz/px. Such acquisition parameters allowed to retrieve an AFI images in 5 minutes.

- Theoretical and experimental HMA length optimization

MRI acquisitions can be affected by a combination of many parameters such as: the size, the shape and the relative permittivity of the subject. Dr. Marc Dubois from Institut Fresnel developed an analytic approach in order to derive the Kerker conditions depending on the HMA length (Dubois et al., 2018). The derived model was then used to describe the interaction between the HMA and birdcage coil field excitation.

An experimental validation of this theoretical model was performed. In order to quantify the effect of the HMA depending on its length, B_1^+ maps were acquired for thirty different lengths of the HMA, from 40 to 60cm. An oil spherical phantom was used for that purpose, and the averaged flip angle values in a region of interest (ROI) depicted by a red circle in Figure 4.6d was investigated for each length. The experimental setup is displayed in Figure 4.6c.

These thirty experimental B_1^+ maps were acquired using an accelerated strategy, namely the XFL sequence (Amadon et al., 2010). Acquisitions were performed in the coronal direction, using a $5010\mu\text{s}$ 90° versed Shinnar-Leroux saturation pulse (Amadon et al., 2010; Pauly et al., 1991) with a time-to-bandwidth product of 9. Sequence parameters for a 4mm in-plane resolution with a FOV of $256 \times 256 \times 176 \text{ mm}^3$ were $\text{TR}/\text{TE} = 20\text{s}/3.06\text{ms}$, $\text{FA} = 3^\circ$, $\text{BW} = 1560\text{Hz}/\text{px}$. The acquisition time was of 40 seconds with no acceleration factor.

- Comparison with HDC pad in a realistic phantom

The HMA placed at 2cm from the phantom has been compared to a BaTiO_3 pad, currently one of the most efficient solution found in the literature (O'Brien et al., 2014; Teeuwisse et al., 2012b). The permittivity of the BaTiO_3 mixture designed is close to $\epsilon_r = 220$ which is optimal for a 1-cm thick pad (Neves et al., 2018). The mixture is sealed in a plastic box of dimensions $12 \times 10 \times 1 \text{ cm}^3$ and placed on the right side of the SAM phantom, as shown in Figure 4.3b and c.

B_1^+ maps were acquired using the same AFI sequence (Yarnykh, 2007) as described above.

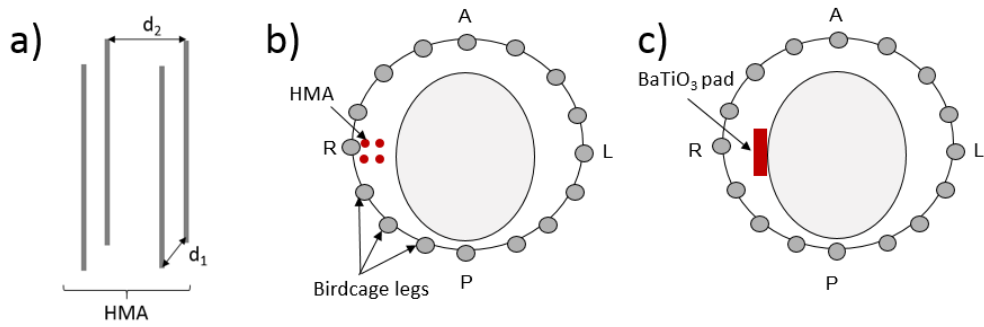


Figure 4.3 : (a) Sketch of the HMA configuration. Four copper rods are placed at the four corners of a rectangle of sides $d_1 = 1.5\text{cm}$ and $d_2 = 2\text{cm}$. (b) Axial slice of the experimental scheme, showing the position of a metamaterial (red circles) and (c) a BaTiO_3 pad next to the specific anthropomorphic phantom in the birdcage 1Tx/1Rx coil.

- Signal to noise ratio evaluation

In order to fully assess the performances of our RF shimming approach, we explore the effect of the HMA structure in terms of signal to noise ratio. The SNR obtained with the birdcage alone will be considered as a reference and we will observe the impact of the HMA when inserted within the coil. Every acquisition will be performed with the same input power.

To do so, we obtained a PD-weighted image of the phantom using a gradient echo sequence with $\text{TR} = 5\text{s}$, $\text{TE} = 1.9\text{ms}$, $\text{FA} = 90^\circ$, $\text{BW} = 1563\text{Hz}/\text{px}$, field of view of 256mm^2 on 64×64 pixels with 4mm isotropic voxel size. For this PD weighting with $\text{TR} > 5T_1$, the signal S_{GRE} obtained in function of the position r is:

$$S_{GRE}(r) = M_0(r)E_2R(r)\sin(\theta(r)) \quad (4.1)$$

With $M_0(r)$ the longitudinal magnetization available, $R(r)$ the reception profile, $\theta(r)$ the flip angle map and $E_2 = e^{-TE/T_2^*}$. This last factor has a reduced impact since TE is lower than T_2^* . The excitation profile $\theta(r)$ is removed from the signal expression using an XFL acquisition as described above, in order to compute the corrected SNR maps as follows:

$$SNR(r) = \frac{\langle M_0(r)R(r) \rangle}{std(S_{GRE_{0V}})} \quad (4.2)$$

Where $S_{GRE_{0V}}$ is a measure of real noise with no RF power during the sequence.

4.3.1.3. Results

- Coil and metamaterials modeling

The developed 1Tx/1Rx simplified coil model is shown in Figure 4.4.

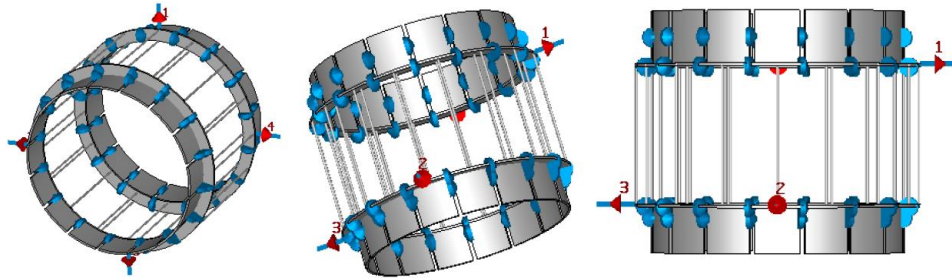


Figure 4.4: Coil model on CST software, showing power supply (in red) and capacities (in blue).

The simulation study of a HMA placed at 2cm at the right of the phantom is displayed in Figure 4.5, first row. The empirical verification of B_1^+ distribution, in Figure 4.5 second row, demonstrates both the consistency of the coil model, and the efficiency of the HMA structure to mitigate the B_1^+ distribution on a phantom with a human geometrical shape.

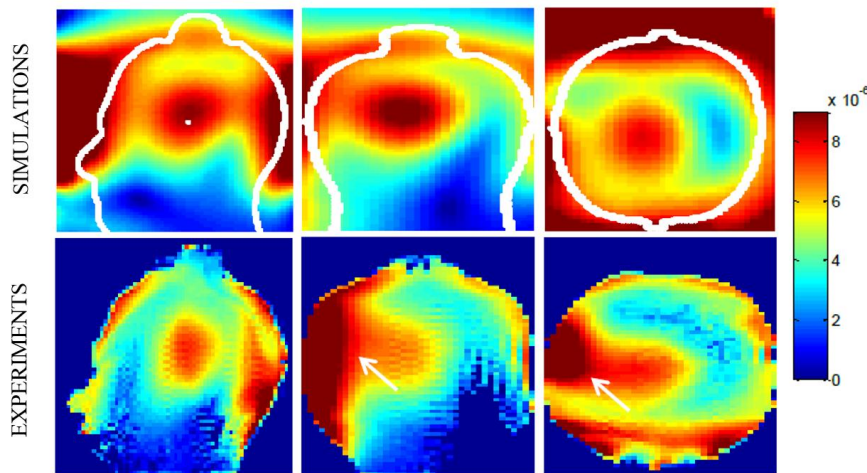


Figure 4.5. First row: Simulation of the B_1^+ field (in Tesla) for a metamaterial placed as in Figure 4.3. Second row: B_1 field from AFI MRI acquisition corresponding to the above simulation (in Tesla). White arrows show enhanced regions.

- Length optimization

Results of the obtained flip angle depending on the HMA length are displayed in Figure 4.6a. When the HMA is present we observe an increase of B_1^+ field in the phantom near the HMA. This effect is related to the increase of the local magnetic field when a resonant mode is excited. When the length is further tuned, we are able to decrease drastically the B_1^+ field when the backward scattering condition is reached at a length equal to 49 cm. Then, we observe an even stronger increase in the near B_1^+ field at the forward scattering condition length (49.5 cm). The experimental and theoretical analytical results show a very good agreement, which confirms our interpretation of the HMA behavior.

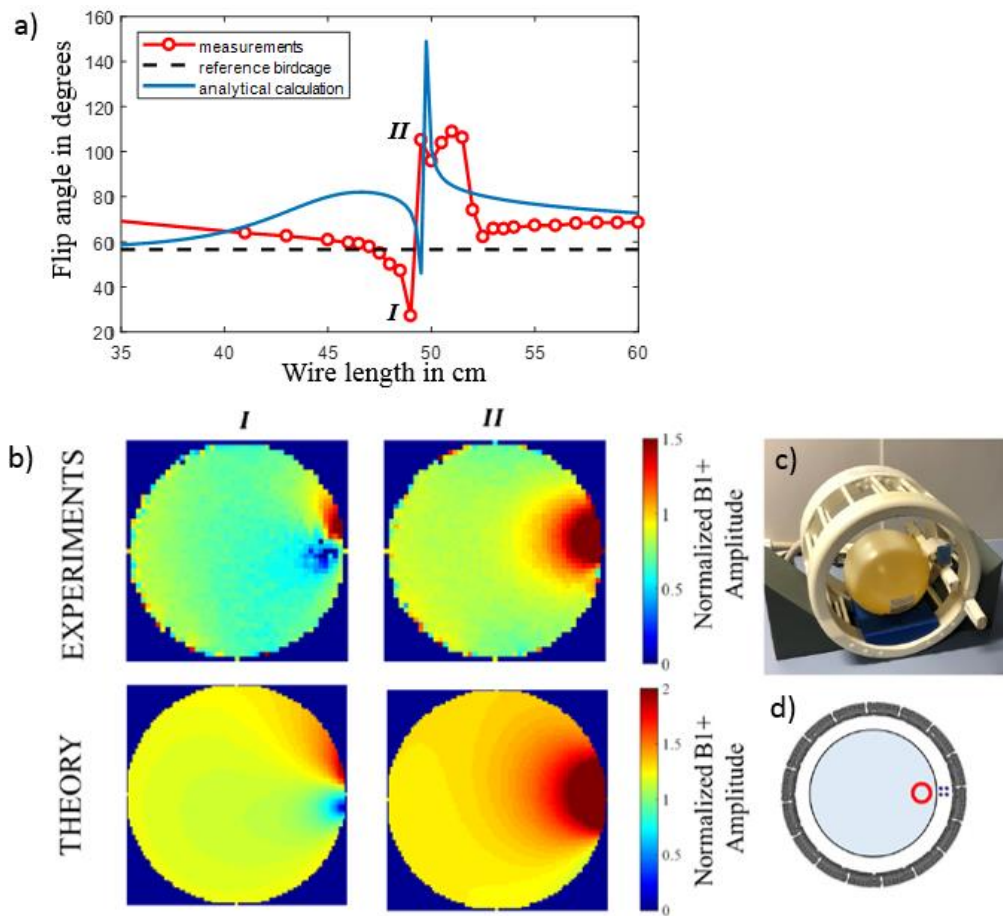


Figure 4.6 : a) Average flip angle in a ROI in the peripheral region of the phantom close to the HMA (denoted in the schematic view of theory in (d)), as a function of the HMA length from MRI experiments. The dotted line indicates the reference value (without HMA), the blue line shows analytical results, and the red line the experimental measurements. (b) Top: Normalized B_1^+ maps measured for two lengths of interest namely 49cm and 49.5cm. Each corresponds to the Kerker conditions with an enhancement or cancellation of the B_1^+ field close to the HMA. Bottom: Normalized field maps obtained from the theoretical calculations for the two Kerker conditions. HMA length from left to right are 49.6cm and 49.8cm. (c) Pictures of the experimental setup showing the positioning of the HMA in the birdcage coil. (d) Schematic view of experimental configuration inside the MRI scanner: birdcage coil (dark gray), HMA (4 rods) and oil phantom, $\epsilon_r = 3.4$ (light gray). The ROI investigated for mean FA is depicted in red.

- Comparison with HDC pad in realistic phantoms

The results for the reference birdcage with no shimming material are presented in Figure 4.7a. The characteristic inhomogeneous RF field pattern is observed. Adding a BaTiO_3 pad in the coil, as presented in Figure 4.7b, leads to a strong amplitude increase in the area close to the pad. However, the pad configuration is not able to fill the gap between the side of the phantom and the central spot meaning that the dispersion of B_1^+ amplitude values remains broad. A measurement performed with a 42cm long HMA placed at 2cm from the right side of the phantom, Figure 4.7c, provides a similar enhancement of the B_1^+ amplitude on the right side of the SAM phantom. Nonetheless, the HMA configuration is such that we are able to merge the two high amplitude spots into one large area with low dispersion in terms of B_1^+ amplitude values. These results clearly show the benefits of the metamaterial approach developed here compared to the actual benchmark in terms of RF passive shimming.

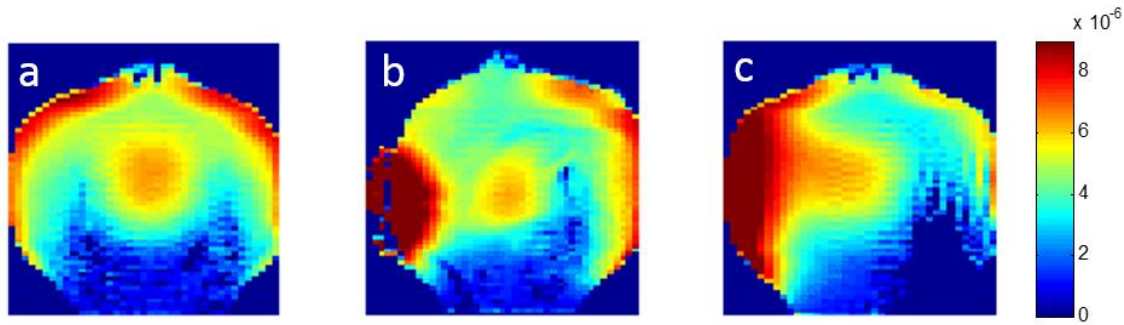


Figure 4.7: Measured B_1^+ coronal maps (in μT) of the SAM phantom: (a) with SAM only (b) in the presence of a BaTiO_3 pad on the right side and (c) replacing the pad with a 42cm long HMA. HMA is located 2cm away from the phantom.

- Signal to noise ratio evaluation

PD-weighted images are presented in Figure 4.8a-b for the reference case and in the presence of HMA. SNR maps, independent from the flip angle heterogeneity, are shown in Figure 4.8c-d. SNR enhancement map is shown in Figure 4.8e.

Figure 4.8a-b demonstrate a local enhancement of the signal in the vicinity of the HMA. This is a consequence of the RF shimming observed in the previous results. Nevertheless Figure 4.8c-d show that even at the same input power, and after correction for flip angle heterogeneity bias, receiving SNR is locally improved by the HMA insertion. This result can be interpreted through reciprocity principle (Hoult, 2000b) where a gain in transmission can also be observed in reception. We observe a maximum of 150% enhancement in the original dark spot produced by the birdcage alone. These results show that besides the clear advantage of local B_1^+ enhancement provided by the HMA, the reception path benefit also from the presence of the HMA within the birdcage coil.

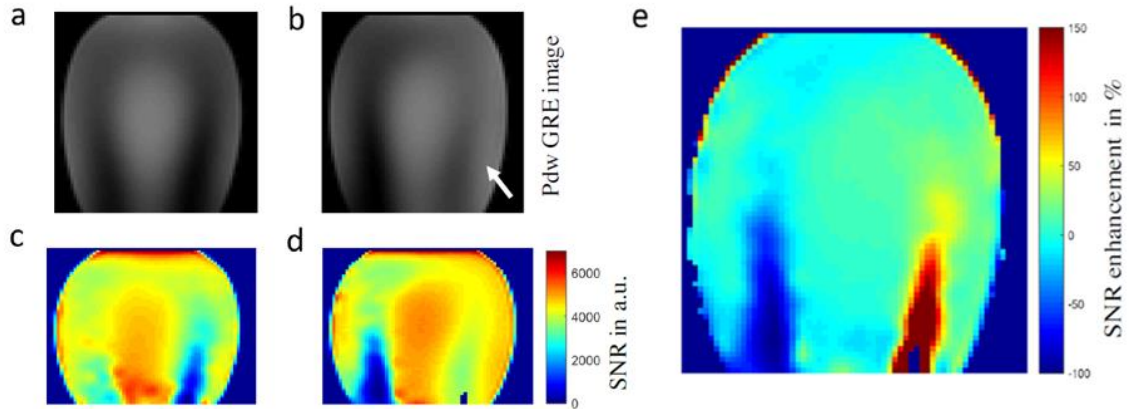


Figure 4.8: Measurements of SNR with and without HMA on SAM phantom. (a) Proton density weighted coronal image with birdcage and (b) with 42cm long HMA inserted (metamaterial along the right side of the phantom). Local enhancement can be visually identified by the white arrow along the HMA. (c) Corrected SNR maps (arbitrary units) obtained with the birdcage alone and (d) in presence of HMA. (e) Calculated SNR enhancement map in percentage. It confirms a strong SNR enhancement close to the HMA but also a slight improvement on a relatively large part of the phantom volume.

4.3.1.4. Discussion

The results presented above demonstrate a strong impact of the HMA on the B_1^+ field locally for UHF MRIs. Besides its clear effect on the RF field distribution, HMA structure has the potential to overcome limitations of dielectric pads: it has a smaller size, and can be set further away from the patient. Contrarily to dielectric pads, metallic metamaterials are not subject to aging and thus will keep their performance along time. In addition, they are cost effective and very easy to manufacture. HMA equivalent dielectric constant is also tunable by simply modifying the length and the distance between the rods. Thus, in a first approach, HMAs could be used similarly to dielectric pads but accessing a higher degree of control in the RF field distribution. In addition, we have shown that we could strongly increase or reduce the B_1^+ field when the Kerker scattering conditions are set.

The realistic coil model developed in this study will be used in future work to optimize the location of several HMA to improve not only the local B_1^+ , but also the global B_1^+ distribution in the whole brain at 7T. But before implementing such a solution in vivo, some questions need to be addressed and will be the topic of later work. First, we need to ensure the safety of the patient and compliance with the SAR standards. Simulations of an exact and mastered coil architecture will be needed to assess accurately the impact of HMA on the induced SAR. A human model for which the tissue properties exactly correspond to those of the human brain will be used for that purpose. Furthermore, the interferences of this HMA structure with a specific receiving phased array need to be examined before implementing in a state-of-the-art routine clinical coil.

Obviously, this HMA structure cannot be adopted yet for QuICS in vivo acquisitions to homogenize the global B_1^+ distribution. A cautious study on the induced SAR and B_1^+ distribution optimization needs to be undertaken first. The current length of HMA represents a major impediment to use HMA in clinical routine as well. In the meantime, advances were made in the lab in the development of parallel RF transmission, especially improving its ability to address B_1^+ heterogeneities using a plug-and-play solution. We decided to investigate its potential for QuICS' FA mitigation.

4.3.2. Parallel transmission: universal pulses for brain applications

Parallel transmission (pTx), as introduced in §1.2.3.2, consists in placing several independent RF transmitters around the subject, instead of a single one on standard MR coils. A much more homogeneous excitation is obtained by taking advantage of RF interference and dynamic modulation during the excitation (Grissom et al., 2006). These additional degrees of freedom provide a better control of the magnetization but also raise challenging problems in terms of workflow and safety.

PTx can be implemented using either static or dynamic shimming. In both cases, the B_1^+ field and the static field (ΔB_0) distributions of the subject must be known, as they show a strong dependence to the inserted load. To date, the measurement of those maps combined with data extraction, processing, and sophisticated pulse design can easily require 15 min or more (Cloos et al., 2012; Deniz et al., 2016), which decreases by the same amount the time available for acquiring clinically relevant data. However, in practice, for a given type of examination, for example on the brain, these variations in B_1^+ and B_0 can change only moderately.

Recently, the work of (Gras et al., 2017a) took advantage of this observation and described a strategy using the reproducibility of the brain shape to provide a plug-and-play solution, called “Universal Pulses”. Based on B_1^+ and ΔB_0 maps from 6 subjects at 7T, forming a representative database, a 3D nonselective Universal Pulse (UP) was derived to robustly mitigate the RF field inhomogeneity problem over a population of 6 other subjects. To generalize the FA homogenization simultaneously over multiple subjects, an optimal pair of RF coefficients (x) and trajectories (k) minimizing the maximum root mean square error over N_s subjects was derived, as described in Eq. (4.3).

$$\min_{x,k} \left(\max_{1 \leq i \leq N_s} \|A_i(x, k) - \alpha_t\|_2 \right) \quad (4.3)$$

with A_i a Bloch operator that returns the FA generated by the corresponding RF and trajectory pair (x, k) , and α_t the target FA.

The results, displayed in Figure 4.9 for one subject, show the potential of the universal pulses to globally homogenize the B_1^+ distribution.

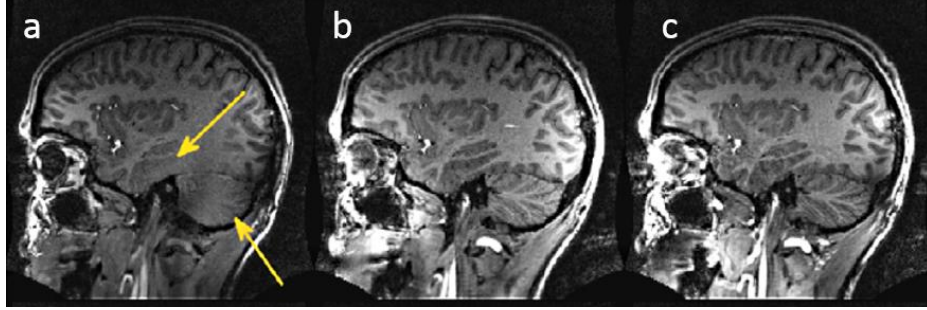


Figure 4.9 Native (no reception profile correction) 7T MPRAGE images for one subject, using (a) standard circularly-polarized rectangular pulse, (b) universal pulse and (c) subject-based tailored pulse on an 8Tx/32Rx coil. The universal pulses are able to greatly mitigate the RF field inhomogeneity problem without B_1 and ΔB_0 measurements (yellow arrows), while satisfying various hardware and safety constraints. From (Gras et al., 2017a).

These results suggest that the use of parallel transmission could become completely transparent to the user, thus simplifying considerably the workflow and offering a solution to make the great potential of UHF scanners more accessible to anyone. Indeed, for a given a coil and sequence, this solution provides a pulse applicable to any patient in the scanner, avoiding a great loss of time and efficiency in clinical routines for the brain. Thus, the application of such technique would allow to easily apply QuICS at UHF with adjusted B_1^+ maps to obtain accurate quantification of tissues in a clinical setting.

4.4. QuICS application in vivo using parallel transmission

Universal pulses seem promising to obtain a homogeneous B_1^+ while conserving clinically viable protocols. In this section, we will apply such 3D non-selective excitation and compare it with a rectangular pulse impulsion in circularly-polarized mode, corresponding to a classic pulse in single transmit systems. We will obtain in vivo results in a clinically-relevant time and compare our extractions with literature values and gold-standard measurements.

4.4.1. Materials and methods

Acquisitions were performed at 7T using a 8Tx/32Rx head coil (Nova Medical, Wilmington, MA, USA) firstly with a non-selective 500 μ s rectangular pulse in circularly-polarized mode, corresponding to a classic single transmit experiment, and secondly with a non-selective Universal Pulse (UP) (Gras et al., 2017a) to obtain a very homogeneous flip angle distribution. The duration of the UP was adapted to 3.25ms in order to obtain the same mean input power

of 1.8W in both acquisitions. A schematic sequence diagram of the SSFP sequence with universal pulse implementation for one transmitting channel is shown in Figure 4.10.

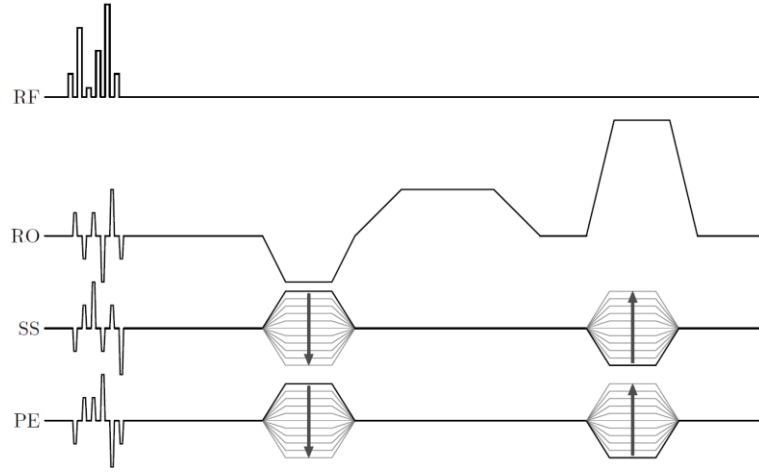


Figure 4.10: QuICS sequence diagram for 3D non-selective acquisition showing a schematic view of Universal Pulse with RF for one transmit channel. A spoiler in the readout direction corresponding to a N_{RO} of 4 is implemented here.

The applied QuICS protocol is the one derived in section 4.2. and displayed in Table 4.1, page 91, respecting the constraints of $N_{RO}=4$ and $FA \leq 30^\circ$, with $TR/TE=11ms/3.3ms$, bandwidth=650Hz/px. The image resolution was set to $1x1x3mm^3$ in a $256x160x160mm^3$ field-of-view. Acquisitions were made in transverse orientation. To avoid aliasing artefacts, an oversampling of 100% was added in the phase direction, leading to a total acquisition time of 16 minutes 36.

Gold-standard measurements were performed to compare T_1 and T_2 values. To retrieve T_2 , a multi Spin-Echo sequence was used with a resolution of $2x2x3mm^3$, a TR of 8s and three TE of 10, 30 and 50ms. The three corresponding images were acquired in 18 minutes with an EPI factor of 3. To retrieve T_1 , VFA was applied rather than an Inversion-Recovery Spin-Echo, in order to reduce both acquisition time and SAR at 7T. Two GRE images with flip angles of 5 and 20° with $TR/TE=14/3ms$, a resolution of $1x1x3mm^3$, were acquired in 3min17. To correct for B_1^+ heterogeneity, the needed flip angle map was retrieved using an AFI sequence described in §4.3.1.2. at a $4x4x3mm^3$ resolution in 5min20. T_1 mapping was therefore corrected for both B_1 inhomogeneities and incomplete spoiling, as recommended in (Preibisch and Deichmann, 2009).

4.4.2. Results

Quantitative extractions with rectangular pulse, mimicking the single transmit coil, shown in Figure 4.11a, display a very heterogeneous flip angle dispersion, as expected. A signal drop

is encountered in cerebellum as well as in temporal lobes for all the extracted parameters, confirming the above Monté-Carlo in-silico simulations from §4.2. On the contrary, when applying UP, results displayed in Figure 4.11b show a more homogeneous flip angle map, and acceptable quantitative results over the whole brain.

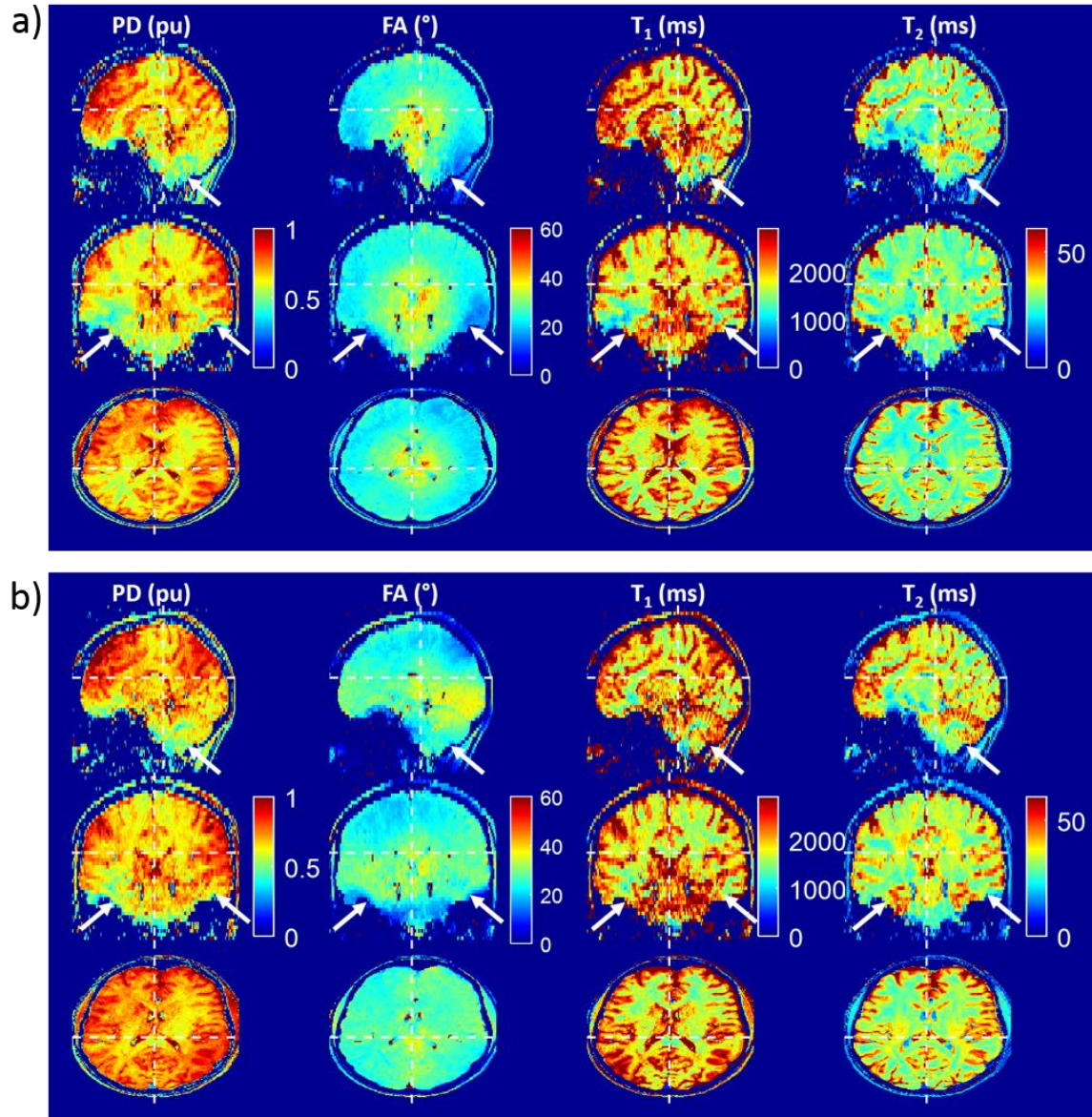


Figure 4.11: 7T 3D QuICS ($1 \times 1 \times 3 \text{ mm}^3$) quantitative extraction for PD, flip angle, T_1 and T_2 maps using (a) rectangular pulse (b) Universal Pulse excitation. Displayed slices are depicted in the 3 different orientations by white dotted lines. In (a), QuICS fails to estimate properly the quantitative parameters in the cerebellum and parietal lobes, due to a to high FA heterogeneity, as highlighted by arrows. In (b), the flip angle distribution is much more homogeneous, and the QuICS extraction was successful in the whole brain, even in areas where there was a lack of signal in (a).

To assess to which extent QuICS estimations are accurate, a comparison of the extracted quantitative maps was performed with gold-standard measurements and is displayed in Figure 4.12. Distributions of quantitative values over a slice show an overestimation of T_1 values

of 20%. For T_2 , over the measured slice, QuICS estimations were in agreement with gold-standard measurements. All these measured values are in the range of what is usually encountered in literature at 7T (Marques and Norris, 2018).

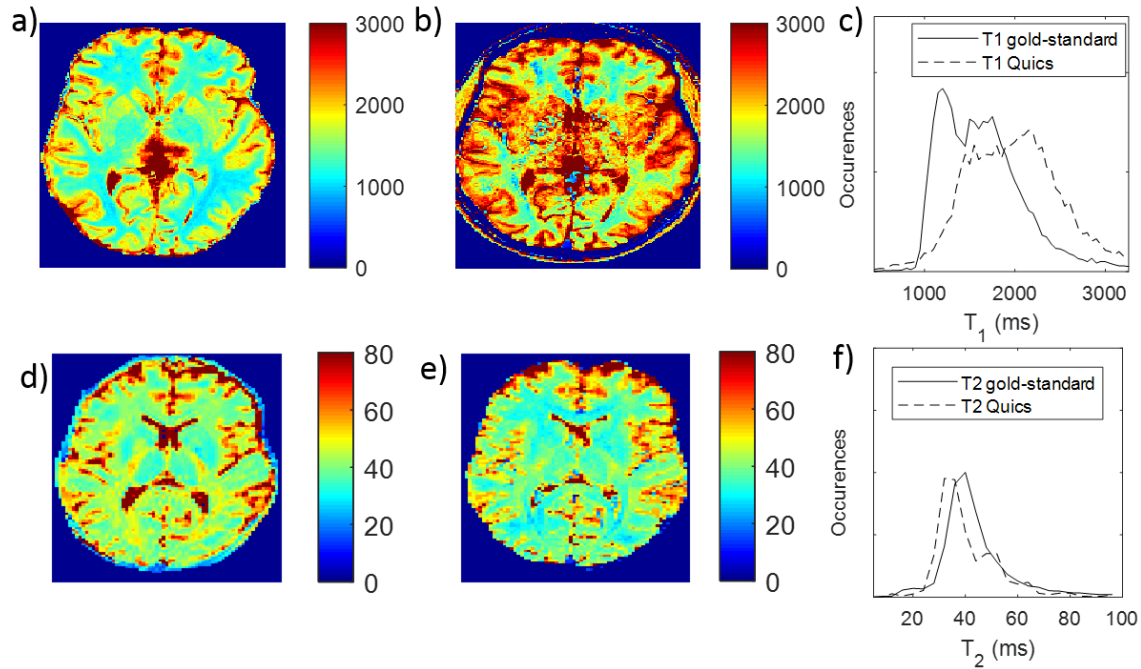


Figure 4.12: T_1 maps of an axial slice at 7T from VFA acquisition (a) and QuICS extraction (b) in ms. The corresponding distributions are displayed in (c). T_2 map measured with multi Spin-Echo method (d) and QuICS (e) with an interpolated resolution of 2mm in-plane, to correspond to gold-standard resolution. Distributions of T_2 for the slices presented in (d) and (e) are presented in (f). For T_1 , QuICS curve seems shifted, showing the overestimation of T_1 . VFA T_1 exhibits a peak at 1200ms, whereas QuICS present the corresponding peak at 1500ms, demonstrating an overestimation of 20% over the slice. For T_2 , values are very consistent.

4.4.3. Discussion

This work is the first application of QuICS at UHF. 3D quantitative extraction of PD, FA, T_1 , and T_2 was performed at 7T at a $1 \times 1 \times 3 \text{ mm}^3$ resolution in 16 minutes 36s over the whole brain. Such acquisition time is compatible with clinical routine and could be shortened easily by diminishing the acquisition oversampling and changing the acquisition orientation.

The 3D preliminary results shown in Figure 4.11 confirmed the ability of the UP to efficiently mitigate the B_1^+ field using an 8Tx/32Rx coil on a SSFP sequence. These results also confirmed the Monté-Carlo simulations, presented in §4.2, showing a relevant extraction when the effective FA was greater than half of the targeted FA.

Comparisons were made between QuICS and established methods. On the one hand, T_2 estimations were performed over a single slice in 18 minutes using multi Spin-Echo technique, with an in-plane resolution of 2mm^2 . Comparisons with QuICS demonstrate the ability of the quantification process to accurately measure different T_2 relaxation times and differentiate neighboring tissues.

On the other hand, T_1 maps were retrieved in 9 minutes using VFA. Usually, T_1 estimations from this technique are overestimating the real T_1 values. Therefore, here, T_1 maps were corrected for B_1^+ heterogeneities and incomplete spoiling, to avoid this bias (Preibisch and Deichmann, 2009). When compared with QuICS, an overestimation of 20% was observed in our T_1 quantification. This might be explained by some motion observed between the different QuICS contrasts during the exam. A motion correction technique, applied to both magnitude and phase images, could improve the results accuracy and maybe explain this discordance. Moreover, residual CSF flow motion could also be corrupting the steady-state by introducing additional phase to the transverse magnetization and leading to loss of signal (Gras et al., 2017b; O'Halloran et al., 2015). Finally, magnetization transfer effects, not considered in our QuICS model, might play a role in this issue (van Gelderen et al., 2016), as the perturbation of the magnetization from protons of lipids and macromolecules might affect relaxation rates. Further study would be required to understand the underlying phenomenon, and more data would be needed to draw a meaningful conclusion about this QuICS T_1 bias.

Nevertheless, it does not invalidate the approach, because dictionary-based multiparametric methods come with a long post-processing step (Cloos et al., 2016). Here, the extraction of quantitative maps directly from DICOM images was achieved in approximately 1.5 minutes per slice, leading to a total of 82 minutes for the 56 slices of the 3D volume. This process could easily be improved using parallel computing, opening perspectives for a clinical workflow compatibility.

QuICS has already proven to be able to retrieve a one-dimensional apparent diffusion coefficient map, at the expense of a longer scan time on phantoms (Leroi et al., 2017; de Rochefort et al., 2016). The acquisition of more contrasts would allow such an extraction, but was not implemented in this experiment. Indeed, in anisotropic media such as human brain, such information would be of limited interest for clinicians. The addition of spoiling gradients in other directions using “ N_{ss} ” and “ N_{pe} ” additional degrees of freedom may lead to the extraction of a trace ADC value. In such scenario, Eddy current will need to be carefully examined and compensated.

In future work, non-Cartesian trajectories will also be implemented to reduce TA while obtaining high-resolution quantitative maps in a clinically-relevant time, with new patterns of

optimized k-space filling (Lazarus et al., 2017). The method could also be applied using slice-selective Universal Pulses (Gras et al., 2017c) to reduce head-foot oversampled coverage.

The next step of this work will be to evaluate the robustness and reliability of the approach over several healthy volunteers. Such quantitative method paves the way for clinical research studies at UHF. First, we can imagine studies scanning a specific cohort of patients with an identified disease and compare them with a healthy population of matched age and sex. For example, a pathology such as Parkinson reported shorter T_2 in the brain. In advanced stage of the disease, this T_2 shortening is exacerbated in certain regions (Vymazal et al., 1999). Differences in NMR parameters may therefore lead to potential new diagnosis triggers for physicians.

Chapter 5.

^{23}Na quantitative MRI: an in vitro demonstration

This chapter contains methods and results that were accepted for publication in the journal Magnetic Resonance Imaging, and as abstract in the proceedings of the International Society for Magnetic Resonance in Medicine 2017.

L. Leroi, A. Coste, L. de Rochefort, M. Santin, R. Valabrègue, F. Mauconduit, E. Giacomini, M. Luong, E. Chazel, J. Valette, D. Le Bihan, C. Poupon, F. Boumezbeur, C. Rabrait-Lerman, A. Vignaud, “Simultaneous multi-parametric mapping of Total sodium concentration, T_1 , T_2 and ADC at 7 Tesla using a Multi-contrast unbalanced SSFP”, Magnetic Resonance Imaging, 2018, vol. 53, p. 156-163.

L. Leroi, A. Coste, L. de Rochefort, M. Santin, R. Valabrègue, F. Mauconduit, M.-F. Hang, E. Chazel, J. Bernard, M. Luong, E. Giacomini, D. Le Bihan, C. Poupon, F. Boumezbeur, C. Rabrait-Lerman, A. Vignaud, « Simultaneous multi-parametric and quantitative estimation of ^{23}Na physical properties at 7 Tesla using QuICS », ISMRM 2017, Honolulu, USA, #5627.

In this chapter, we leave apart proton (^1H) imaging to focus on sodium (^{23}Na). Our interest in ^{23}Na MRI originates from its involvement in cellular homeostasis and viability. Quantifying physical properties of ^{23}Na could be of benefit to assess more specifically pathological changes in cellular stability accompanying neuroinflammatory or neurodegenerative diseases. Due to its lower NMR sensitivity, ^{23}Na MRI remains challenging, resulting in images with low SNR and poor resolutions. In addition, ^{23}Na relaxation times are much shorter than the ones encountered in ^1H . In this context, applying QuICS to sodium imaging represents a good demonstration of the potential of the method to retrieve different quantitative NMR parameters values.

5.1. Introduction

Sodium (^{23}Na) yields the second most NMR sensitive nucleus in biological tissues after Hydrogen (^1H). ^{23}Na MRI offers insights into pathologies through novel metabolic information that classic proton MR imaging cannot access, potentially improving patient care in this way. A wide literature deals with the investigation of sodium compartmentalization with the aim to separate intracellular ^{23}Na from the total sodium content as a marker of cell viability *in vivo*. However, the complexity to untangle such information makes these results debatable (Thulborn, 2018). Indeed, most of the studies are currently focusing on Total Sodium Concentration (TSC) which, non-exhaustively, has been shown to be beneficial to study tissue viability after stroke, to detect malignant tumors and to assess drug resistance before chemotherapy, Huntington's disease and multiple sclerosis in the brain, as well as acute myocardial infarction in the heart (Madelin and Regatte, 2013). In some studies, proton DWI or contrast-enhanced MRI is also proposed and recommended to increase the sensitivity and specificity of the diagnosis (Jacobs et al., 2009). Thus, the opportunity to quantitatively retrieve ^{23}Na TSC in addition to several other NMR properties such as T_1 , T_2 or Apparent Diffusion Coefficient (ADC) specific to ^{23}Na in a single experiment is of interest to improve the detection, the investigation of the physiopathology of various diseases and the evaluation of potential treatments, for an enhanced follow-up.

To date, the precise determination of the above-cited quantitative parameters requires the sequential implementation of several methods, as was demonstrated in the past (Morrell et al., 2016; Staroswiecki et al., 2009; Zbyn et al., 2009). None of them addressed ^{23}Na DWI so far. Sodium diffusion has only been assessed in rat brain (Goodman et al., 2005) and rat skeletal muscle using shift-reagent aided MR Spectroscopy (Babsky et al., 2008). Therefore, the simultaneous, fast and robust mapping of ^{23}Na NMR properties constitutes a challenging, relevant and exciting prospect for biomedical research.

The aim of this work was to demonstrate the experimental feasibility of the QuICS approach on ^{23}Na to assess simultaneously in a single sequence total ^{23}Na NMR properties in vitro. Although ^{23}Na is usually modeled using a density operator evolution under the Liouville equation, the magnetization behavior will be approximated to follow a single- T_2 simplified model weighted by its various contributions. It is performed at 7T to take advantage of the larger SNR (Pohmann et al., 2015). The robustness of the approach was evaluated in different physicochemical environments presenting variations of relaxation times, ADC and concentrations, corresponding to different in vivo tissues. To the knowledge of the authors, this phantom study is the first simultaneous multi-parametric quantitative extraction reported in the context of ^{23}Na MRI, and in particular the first 3D mapping of its ADC. Applicability to clinical acquisitions will be also discussed.

5.2. Materials and methods

5.2.1. In-silico experimental setup formulation

In this study, only phase cycling was used to modulate the SSFP contrast. Thus, to determine the most adequate N_{RO} and FA to use to accurately assess the targeted sodium relaxations ($T_1=60\text{ms}$, $T_2=50\text{ms}$) and ADC properties ($\text{ADC}=1.3\times 10^{-3} \text{ mm}^2/\text{s}$) under the scanning conditions described in the following section, simulations using brute-force Monte-Carlo SSFP were performed. The range of tested FA varied from 0 to 100° with a precision of 1° , using 10,000 samples per FA. To account for the coil receiving profile and associated FA and SNR variations, the voxel magnetization at thermal equilibrium, M_0 , was proportionally adapted to the considered FA from empirical measurements. The range of tested N_{RO} varied from 1 to 47, corresponding to a diffusion sensitivity of $b=\text{TR}*(2\pi/a)^2$ ranging from 0.02 to $48.4 \text{ s}\cdot\text{mm}^{-2}$ between two RF pulses. The latter was the limit of our system given the chosen TR of 20ms and pixel size of 6mm^3 isotropic.

5.2.2. MRI acquisitions

MRI acquisitions were performed on an investigational 7 Tesla MRI scanner (Siemens Healthineers, Erlangen, Germany) using a homemade hemi-cylindrical 1Tx/1Rx ^{23}Na coil (Figure 5.2a). FA was calibrated assuming that the reference voltage would allow to get a global mean FA equal to the targeted FA in the whole phantom. Acquisitions consisted in a repeated 3D non-selective Cartesian unbalanced SSFP with different contrasts. Scanning parameters were $\text{TR}/\text{TE}=20\text{ms}/3.2\text{ms}$, $\text{bandwidth}=220\text{Hz}/\text{px}$. The image resolution was 6mm^3 isotropic in a $192\times 192\times 160\text{mm}^3$ field-of-view. FA and N_{RO} were set respectively to 45°

and 47, according to the results from the optimization process described above (Figure 5.1). 11 contrasts were selected with RF spoiling increments = [0, 20, 100, 110, 130, 170, 190, 230, 250, 340, 360]° to sample the complex plane. Using 25 averages, the acquisition time (TA) of a volume was 7 minutes, leading to a total TA of 1h18min.

MR spectroscopic measurements of ground-truth T_1 , T_2 and ADC were performed on a 7 Tesla preclinical scanner (Pharmascan, Bruker, Ettlingen, Germany) using a small home-made dual-resonance ²³Na/¹H birdcage coil and gold-standard methods. Single Voxel Spectroscopy (SVS) data were acquired from a large 30 mm³ voxel. For T_1 assessment, an Inversion Recovery (IR) LASER sequence (Garwood and DelaBarre, 2001; Slotboom et al., 1991) was used, varying the inversion time from 5 to 100ms by 10ms steps, with TR/TE=500/13ms, BW=4kHz and an inversion pulse of 2ms. Then, T_2 and ADC were measured using a STEAM sequence (Moonen et al., 1992; van Zijl et al., 1989), acquiring respectively seventeen different TE from 2 to 120ms and five b-values from 0 to 1200 s/mm² with two diffusion gradient polarities to get rid of cross-terms with selection gradients. Acquisition parameters were set to TR/TM = 500/10ms, TE=10ms, BW=4kHz and excitation pulse of 500μs. The consecutive SVS acquisitions for these three parameters took about 1h35min.

To test our method's ability to probe sodium NMR properties, experiments were conducted on a series on phantoms using the setup shown Figure 5.2a. First, three phantoms (150mL glass containers, diameter=3cm) containing the same CSF physiological NaCl concentration of 150mM were investigated, with 0, 2 and 5% agar gel to reduce the relaxation times of ²³Na, to mimic brain or cartilage properties. Second, to test the quantification of sodium concentrations, phantoms of 30, 50 and 100 mM NaCl were imaged with a reference tube of 150mM in the same configuration. Finally, to increase the viscosity of our saline solutions (Hara et al., 2014; Winfield et al., 2016) and probe varying apparent ADCs of ²³Na, 5 to 15% w/w sucrose (Sigma-Aldrich, Saint Louis, USA) was added in the 150mL tubes.

MRS measurements were performed using tubes filled with similar compositions, using a concentration of 150mM NaCl. One reference tube was assessed, in addition with one tube containing 5% of agar gel and one containing 15% of sucrose.

5.2.3. Data analysis

Total sodium concentration maps were retrieved from the ratio between M_0 and B_1^- , where the sensitivity profile B_1^- was estimated from the FA distributions, by applying the reciprocity principle (Hoult, 2000b). The concentrations were estimated for each adjacent tube using the tube of 150mM as an external reference for concentration.

Due to the hemi-volumic coverage of our coil (Figure 5.2.a), a substantial sensitivity bias was observed across our images. In order to limit the impact of this inhomogeneous SNR on the estimation of the NMR properties of ^{23}Na , a region-of-interest (ROI) was defined in each phantom to keep the upper part, where the FA was systematically higher than 40° (Figure 5.2.b-f), as observed in the experimental setup formulation results (Figure 5.1). Estimations were performed by assessing the mean over the pixels respecting this criteria over the whole phantom, leading to robust estimations.

5.3. Results

Results of the protocol optimization process are presented in Figure 5.1. It shows that FA and N_{RO} need to be respectively set to 45° and to 47, to get reliable estimations. As shown in Figure 5.2, regions of interests were also defined in each phantom to assess results where the FA was systematically higher than 40° .

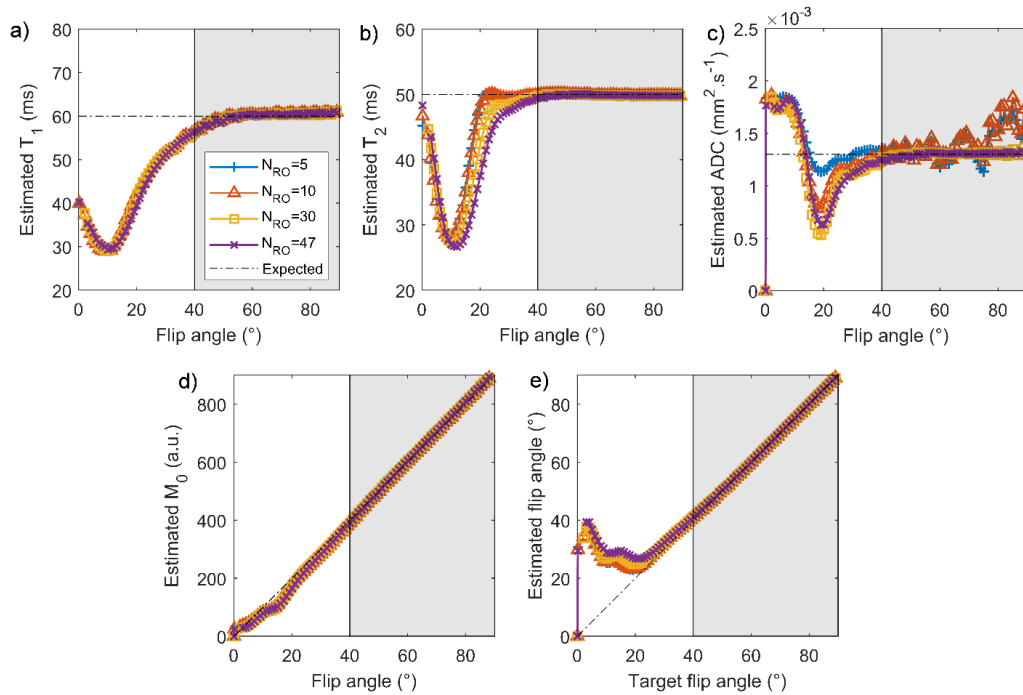


Figure 5.1: Brute-force Monte-Carlo simulations of ^{23}Na T_1 (a), T_2 (b), ADC(c), M_0 (d) and FA(e) estimations as a function of spoiling gradient moment (N_{RO}) applied in the readout direction and FA, in order to account for its variations due to the coil profile. TR was set to 20ms, RF spoiling increments = [0, 20, 100, 110, 130, 170, 190, 230, 250, 340, 360]°, pixel size $\Delta z = 6\text{mm}$ and expected $T_1 = 60\text{ms}$, $T_2 = 20\text{ms}$ and $\text{ADC} = 1.3 \times 10^3 \text{mm}^2 \cdot \text{s}^{-1}$. To account for the coil receiving profile and associated FA and SNR variations, M_0 varied with FA. On the one hand, this figure illustrates that choosing a FA higher than 40° (shaded area) and the highest spoiling gradient momentum avoids bias and leads to the most accurate estimations for T_1 , T_2 and ADC. In another hand, results obtained with FA below 40° and lower N_{RO} cannot be considered because a large bias and uncertainty in the estimations are observed. M_0 and FA estimations are more robust to FA variations, as a FA of 20° seems sufficient to estimate these parameters.

As illustrated in Figure 5.3a, ^{23}Na concentrations were accurately estimated, relative quantification errors being below 15%. Likewise, the ADCs were estimated for the sucrose-enriched (5-15%w/w) saline phantoms (Figure 5.3b). SVS measurements lead to very similar results for both the reference and the 15% sucrose tubes.

To study the robustness of the method, different measurements were conducted varying the relaxation properties of the phantom using agar from 0 to 5%, to mimic different human tissue properties. Results displayed in Figure 5.3c show the consistency of the mean T_1 and total T_2 over the defined ROIs compared to SVS measurements. Similar values were also reported at 7T (Nagel et al., 2016).

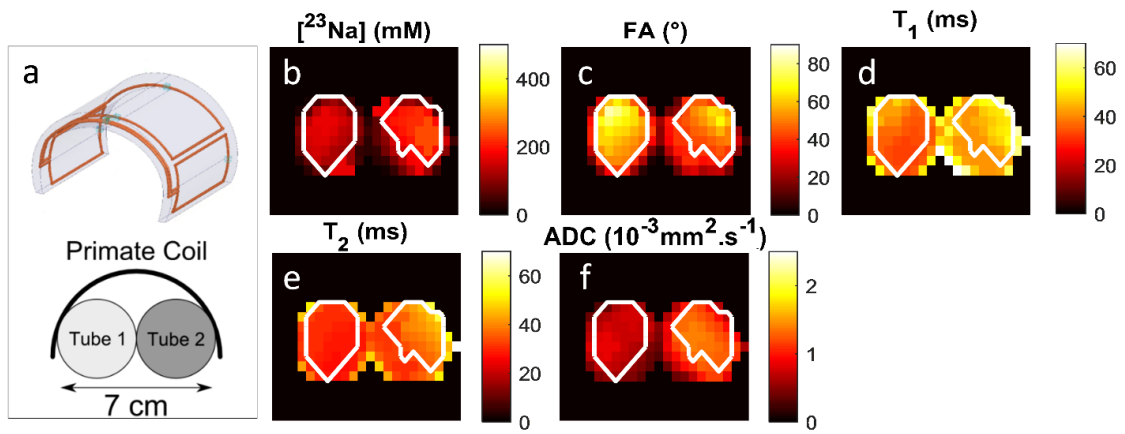


Figure 5.2 : Schematic of our hemi-volumic ^{23}Na RF coil with positioning of phantoms (a) and multi-parametric transverse maps obtained using the QuICS method: ^{23}Na concentration (b), FA in degrees (c), T_1 and T_2 in ms (d, e) and ADC in $10^3\text{mm}^2.\text{s}^{-1}$ (f). The white ROI delimits the region where $\text{FA} > 40^\circ$, in agreement with results on experimental setup formulation, Figure 5.1. In this experiment, tube 1 (left) contained saline water with a physiological CSF concentration of 150mM with 2% agar and tube 2 (right) contained the same saline water without agar. Total sodium concentration map was retrieved from the ratio between M_0 and B_1 , where the sensitivity profile B_1 was estimated from the FA distributions, by applying the reciprocity principle (60). The concentration for tube 2 was estimated using tube 1 as a reference. Over the ROI, results exhibit homogeneous and significantly different relaxation times between the two phantoms.

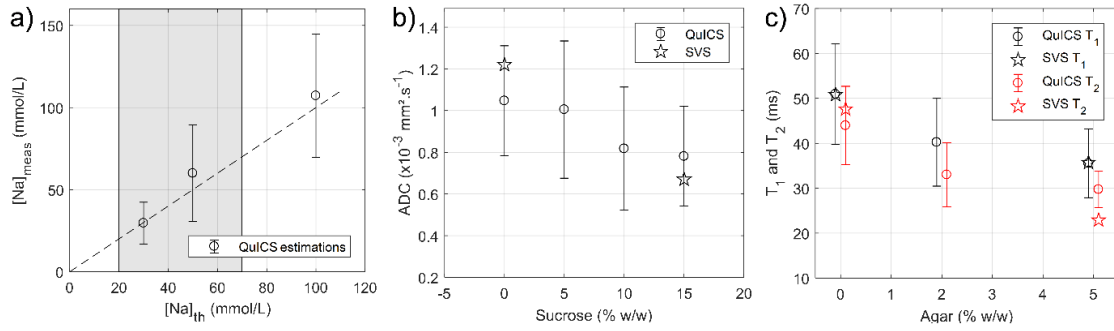


Figure 5.3 : a) Expected dilution and experimental estimations obtained with QuICS for realistic physiological total ^{23}Na concentrations of gray matter and white matter (shaded area). Measured concentrations tend to align with the first bisector (dashed line). b) Estimated ADC values at 21°C for four phantoms of 150mM NaCl and various sucrose mass fractions, with associated standard deviations. Results show a decreasing evolution of diffusion depending on sucrose concentration, confirming observations from (Hara et al., 2014; Laubach et al., 1998a; Winfield et al., 2016) and DW-STEAM measurements. c) Estimated T_1 and T_2 for three phantoms of 150mM NaCl and various agar concentrations.

5.4. Discussion

In this work, 3D simultaneous multi-parametric extraction of total T_2 , T_1 , sodium concentration, ADC and flip angle at 7T was performed at 6mm^3 isotropic resolution in 1h18. To some extent, these maps are insensitive for B_0 heterogeneity, as these variations are accounted for in the model. Sodium concentrations corresponded to the preparations; relaxation rates were in agreement with MRS gold-standard measurements; ADC measurements were consistent with data and a measurable reduction in ADC was obtained while adding sucrose. The ^{23}Na ADC maps were estimated along a single spoiling gradient direction, assuming the diffusion weighting of a single quantum coherence NMR signal, which is relevant for most sodium ions in an isotropic media (Goodman et al., 2005).

An acquisition protocol that allows reliable assessment of 3D quantitative maps was determined on the basis of our Monte-Carlo simulations (Figure 5.1). Our *in vitro* data validates this proof-of-concept acquisition set-up and demonstrates the feasibility of simultaneous multi-parametric quantitative extraction (Figure 5.3). Indeed, estimated relaxation times at 21°C were consistent with the presented gold-standard measurements using respectively IR-LASER for T_1 and STEAM for T_2 assessments and with values from literature obtained using non-localized Inversion-Recovery and spin-echo sequences at 22°C at 7T (Nagel et al., 2016).

Large physiological concentrations variations were also studied, with an extraction of TSC leading to precision better than 15%. Diffusion estimations for reference saline solution tube is consistent with the gold-standard measurements. Despite an extensive interest for ^{23}Na diffusion in food processing (Bertram et al., 2005; Guiheneuf et al., 1997; Hansen et al.,

2008), sodium diffusion assessment could be found in the chemistry literature at $1.300 \pm 0.005 \times 10^{-3} \text{ mm}^2 \cdot \text{s}^{-1}$ using a conductimetric cell at 25°C for a 50mM saline solution (Ribeiro et al., 2010). This value is consistent with our estimations, as temperatures are in a similar range and concentration should have limited effect on diffusion. Here, modifying viscosity with sucrose reduced ADC, as verified in spectroscopy and observed in ¹H literature (Laubach et al., 1998a).

We succeeded in assessing large physiological range of total sodium concentrations, relaxations and ADCs, corresponding to various *in vivo* tissues, from cartilage to brain. The relatively high standard deviations obtained in Figure 5.2b-d could be due to a low SNR from B_1^+ heterogeneity induced by the hemi-volumic Tx/Rx primate coil. The latter could be tackled using a birdcage coil to access the targeted angle more homogeneously.

²³Na has a peculiar sensitivity to its molecular environment through quadrupolar interactions. Therefore, its relaxation times exhibit bi-exponential curves in complex media such as tissues or agar gels. For T_1 relaxation, where short and long components accounts for respectively 20 and 80% of the ²³Na signal (Jaccard et al., 1986; Zhang et al., 2010), the bi-exponential recovery is rarely observed, leading to the estimation of a mono-exponential T_1 ranging from 10 to 60ms. For T_2 relaxation, the respective contributions of its long ($T_{2 \text{ long}} \approx 15\text{-}60\text{ms}$) and short ($T_{2 \text{ short}} < 5\text{ms}$) components are considered to be about 40 and 60% of the signal respectively (at zero TE). These bi-exponential or mono-exponential relaxation times varies *in vivo* depending on the investigated tissue (Foy and Burstein, 1990; Ridley et al., 2018), its intracellular and extracellular volume fractions, and the sodium levels in those two compartments (Foy and Burstein, 1990; Hutchison Robert B. and Shapiro Joseph I., 1991). The intracellular volume fraction is approximately 80% of the tissues with a sodium concentration of 10-15mM, and the extracellular volume fraction is around 20%, with a sodium concentration of 125-150mM. Like most ²³Na MRI approach aiming at the extraction of quantitative parameters, QuICS estimates apparent TSC, T_1 , T_2 , ADC reflecting the weighted sum of all those short, long, intra and extracellular components depending on the chosen acquisition parameters. Nevertheless, if any of the intra/extra or long/short T_2 compartments encounters fluctuations related to the metabolic state of the tissue or varying molecular environment of the sodium ions, one may expect QuICS to exhibit sensitivity to such variations, as other single parameter ²³Na qMRI techniques have already shown. . In our case, given the long TE of 3.2ms, the total T_2 mainly reflects the long component of the T_2 .

While one could regret this rather poor specificity, QuICS should compensate this weakness by finding specificity in the correlation of the multiple complementary NMR parameters, helping in the interpretation of the physio-pathological events. Such strategy has already been demonstrated successfully with other simultaneous multi-parametric method in ¹H MRI

(Warntjes et al., 2008; Yu et al., 2017), where the same kind of objections could be done regarding compartmentalization of water in biological tissues.

The experiments reported in this study present a proof-of-concept of the potential of QuICS approach to assess simultaneously a broad spectrum of ^{23}Na properties. To date, a combination of separate state-of-the-art TSC, T_1 and T_2 measurements at the spatial resolution we used is more competitive than what we propose (Morrell et al., 2016; Staroswiecki et al., 2009; Zbyn et al., 2009). Nevertheless, we add a very important parameter, namely the ADC, which has a strong clinical potential to characterize ^{23}Na micro-environment. Additionally, acquisition time TA could be reduced in the future, performing an in-depth optimization of the acquisition protocol over FA, TR, N_{RO} , T_1 , T_2 and ADC ranges to study the sensitivity and robustness of the method. For example, ADC required high spoiling gradients (Figure 5.1c). Using different N_{RO} , or equivalently different diffusion weighting b-values from one contrast to another, is expected to enhance the precision in the determination of the ADC coefficient (de Rochefort et al., 2016). In the present study, only single direction ADC measurements has been performed along the readout axis. This was enough in the context of homogeneous phantoms, to be extended to an average global ADC. In vivo, this will not be the case in the vast majority of the organs and several spoiling directions will be mandatory to properly extract this parameter. Limiting the TA will require to only focus on selecting the most valuable steps playing with FA, RF and gradient spoiling including for the latest several orthogonal directions. Such an optimization has been demonstrated to be achievable using optimal design approaches based on reducing the Cramér-Rao lower bound (Valabrégue and de Rochefort, 2016; Zhao et al., 2016). To reduce TA even more, non-Cartesian sampling sequence could be used to improve SNR. Combining such sampling strategy with a nonlinear iterative reconstruction algorithm would also provide an increase of SNR and enable sub-sampling to reduce TA (Coste et al., 2016; Gnahn and Nagel, 2015; Madelin et al., 2012). These improvements would be at the cost of a broadening of the effective Point Spread Function (PSF) in the reconstructed image, which can be optimized depending on the targeted application. The use of a birdcage coil to access the targeted FA more homogeneously over the region of interest, combined with a received-phase array coil to retrieve more signal would also help increasing available signal and further reduce TA or increase resolution (Shajan et al., 2016). In the latter case, the sensitivity profile of the coil will be corrected using a post-processing algorithm to still be able to extract TSC (Santin, 2018).

5.5. Conclusion and perspectives

In conclusion, this work is the first application of a simultaneous multi-parametric estimation method to ^{23}Na nucleus. The method showed its ability to accurately retrieve varying ^{23}Na concentrations, total relaxation times evolution and ADC. Measured parameters were in range of previously reported values in the literature and effective gold-standard measurements. Current acquisitions will be improved to reduce TA and resolution, while increasing SNR with the goal of obtaining a clinically-relevant scan time. The simultaneous quantitative assessment of several NMR physical parameters could pave the way to a new diagnostic process, where correlations between different tissues properties might lead to improve the patient outcome (Warntjes et al., 2008; Yu et al., 2017).

General conclusion and perspectives

At present, most of the radiological diagnoses are based on the physicians' reading skills. Interpretations of images lie in their ability to detect a lesion or a structural anomaly in an organ based on weighted images. But the expertise of the radiologist can be fooled, in particular in the case of diffuse disorders that change the entire signal of an organ without causing anatomical changes (de Sousa et al., 2012). Pathological or therapeutic follow-ups suffer from the lack of available quantitative NMR parameters and leave the physician with only qualitative and limited information to assess the course of a disease or treatment.

To provide such NMR quantitative parameters, conventional methods exist but remain too long to be applied in clinical routine. Recently, new strategies, providing simultaneously multiples parameters have emerged in literature (Gras et al., 2017b; Ma et al., 2013; de Rochefort, 2016; Sbrizzi et al., 2018; Schmitt et al., 2004; Warntjes et al., 2008). Finding the optimal method to provide fast and accurate quantitative results, compatible with any field strength, remains an important and challenging field of investigation. Within the scope of this thesis, a technique was implemented to simultaneously retrieve 3D maps of proton density, T_1 , T_2

and flip angle under UHF constraints with possible application in clinical settings. We succeeded, both in vitro and in vivo, to perform Quantitative imaging using Configuration States (QuICS) at 7T.

First, we ensured that the retrieved images presented no bias, in order to extract reliable information from the acquired data. We also managed to reduce acquisition time by collecting only the needed contrasts to produce fast quantitative results on ex-vivo baboon brain.

To apply this technique on human brain in vivo, a solution to mitigate the B_1^+ field was investigated, based on metamaterials. It has demonstrated its ability to locally enhance the B_1^+ distribution. However, further improvements need to be studied before a possible application in a clinical setting. In this work, the size of the structure was found to influence the B_1^+ distribution. The combination of several meta-atoms in the coil may lead to a global B_1^+ enhancement. Therefore, a study to optimize the number, location and precise architecture of the metamaterial introduced in the coil will be the topic of future work.

Meanwhile, progresses were made in the use of parallel transmission during the timeframe of this thesis, by Dr. Gras and Dr. Boulant in the laboratory. P_{TX}, usually very complex and fearsome for MRI physicists, has now become user-friendly thanks to the introduction of the Universal Pulses strategy, providing a plug-and-play excitation and abolishing the computing waste of time. Therefore, QuICS was applied in vivo with universal pulses excitations. Quantitative maps of the whole-brain at a resolution of $1 \times 1 \times 3 \text{ mm}^3$ were successfully obtained in an acquisition time of 18 minutes.

The method was then applied to an exotic nucleus such as Sodium. QuICS showed its ability to retrieve very short relaxation times. Different environments corresponding to in vivo properties were investigated and the technique was able to retrieve the Total Sodium Concentration, T_1 , T_2 , flip angle and one-direction ADC simultaneously, for the first time in ^{23}Na MR imaging.

So far, a one-dimensional ADC was retrieved on phantoms. This value is relevant in isotropic media, but becomes of limited information for in vivo exams. To extract a three-dimensional ADC in vivo, the acquisition of more contrasts would be necessary. Implementing spoiling gradients in different directions using N_{SS} and N_{PE} might help in the estimation of a “trace ADC” value.

In future work, acquisition time will be further improved by implementing non-Cartesian k-space trajectories. QuICS was also patented with various possibilities. The acquisition of multiple configuration states might be of interest to speed up the acquisition time. Varying the TR might be a possibility to add a new degree of freedom to the model.

Perspectives

Much progress has been made during this thesis to provide an efficient quantitative MRI strategy, clinically applicable at UHF. But the objective of our field of research is not only to discuss new methods and to estimate their potential for medical use. We must also show how to integrate them into algorithms to improve diagnoses specificity, otherwise they will remain of academic interest only.

Being able to label organs with robust values of relevant, reliable and reproducible intra-individual parameters regardless of the machine used would represent a game-changer in the diagnoses process. If such labeling was performed for healthy, but also pathological subjects, as a function of age and sex, then we could consider to not only detect and characterize lesions, as do the radiologists currently based on weighted anatomical images, but also automatically characterize tissues and thus produce semi-automated diagnoses proposed by a possible “Clinical Decision Support System”.

We may therefore consider the implementation of a supervised learning algorithm, acquiring knowledge from quantitative examples annotated by a medical expert and performing population data classification. An artificial intelligence inference engine would compare the currently scanned subject with reference values, and make different proposals about possible diagnoses to the clinician. The ability of such tool to discriminate between two pathologies or even different stages of the disease may be enhanced by the multiplicity of parameters extracted from the sequence (Yu et al., 2017). Its suggestions, based on cross-correlations of multiple NMR parameters, would therefore be more secured and specific. Automated diagnoses based on quantitative MRI would represent a completely new paradigm for clinicians that could revolutionize the use of MR and the role of physicians.

Publications

1. Patent

L. Leroi, R. Abdeddaim, S. Enoch, P. Sabouroux, G. Tayeb, N. Bonod, B. Larrat, E. Georget, A. Vignaud *Procédé de contrôle de la répartition du champ magnétique radiofréquence dans un système d'imagerie par résonance magnétique*. Reference: WO/2017/198914 A1. 2017.

2. Peer-reviewed journals

L. Leroi, A. Coste, L. de Rochefort, M. Santin, R. Valabrégue, F. Mauconduit, E. Giacomini, M. Luong, E. Chazel, J. Valette, D. Le Bihan, C. Poupon, F. Boumezeur, C. Rabrait-Lerman, A. Vignaud, “Simultaneous multi-parametric mapping of Total sodium concentration, T_1 , T_2 and ADC at 7 Tesla using a Multi-contrast unbalanced SSFP”, *Magnetic Resonance Imaging*, pp. 156-163, 2018. (see Appendix 1)

L. Leroi, M. Dubois, Z. Raolison, R. Abdeddaim, T. Antonakakis, J. de Rosny, A. Vignaud, P. Sabouroux, E. Georget, B. Larrat, G. Tayeb, N. Bonod, A. Amadon, F. Mauconduit, C. Poupon, D. Le Bihan, S. Enoch, “Kerker Effect in Ultra High Field Magnetic Resonance Imaging”, *Physical Review X*, 2018, in press. (see Appendix 2)

A. L. Neves, **L. Leroi**, Z. Raolison, N. Cochinaire, T. Letertre, R. Abdeddaim, S. Enoch, J. Wenger, J. Berthelot, A.-L. Adenot-Engelvin, N. Mallejac, F. Mauconduit, A. Vignaud, P. Sabouroux, “Compressed perovskite aqueous mixtures near their phase transitions show very high permittivities : New prospects for high-field MRI dielectric shimming” *Magnetic Resonance in Medicine*, pp. 1753–1765, 2018.

A. L. Neves, **L. Leroi**, N. Cochinaire, R. Abdeddaim, P. Sabouroux, and A. Vignaud, “Mimicking the Electromagnetic Distribution in the Human Brain: A Multi-frequency MRI Head Phantom”, *Applied Magnetic Resonance*, pp. 213–226, 2017.

Under review:

Z. Raolison, R. Abdeddaim, **L. Leroi**, M. Ducbois, M. Luong, A.L. Nueves, F. Mauconduit, S. Enoch, N. Mallejac, P. Sabouroux, A.-L. Adenot-Engelvin, A. Vignaud, “Evaluation of a new long-lasting silicon carbide based dielectric pad for ultra-high field MRI”, *Magnetic Resonance in Medicine*, 2018, under Review.

3. Oral presentations in International Conference

L. Leroi, L. de Rochefort, M. Santin, F. Mauconduit, R. Valabregue, D. Le Bihan, C. Poupon, A. Vignaud, « Simultaneous multiparametric quantitative extraction at 7 Tesla using QuICS », proceedings of the European Society for Magnetic Resonance in Medicine and Biology 2016, Vienna, Austria, #272. (See appendix 3)

A. L. Neves, **L. Leroi**, N. Cochinaire, R. Abdeddaim, P. Sabouroux, A. Vignaud, « A Simple Approach Towards a Multi-Frequency MRI Head Phantom », proceedings of the 11th European Conference on Antennas and Propagation, 2017, Paris, France, #1570315571.

A. Vignaud, Z. Raolison, M. Dubois, **L. Leroi**, A. L. Neves, F. Mauconduit, S. Enoch, N. Malléjac, P. Sabouroux, A.-L. Adenot-Engelvin, R. Abdeddaïm, « Ultra-high Field MRI radiofrequency excitation inhomogeneities mitigation in the head: optimization of dielectric pad mixture and locations », proceeding of International Symposium on Nanophotonics and Metamaterials, St-Petersburg, Russia, June 2018.

4. Posters presentations in International Conference

H. Carrié, L. El Gueddari, H. Cherkaoui, E. Dohmatob, **L. Leroi**, P. Ciuciu, « Multi-Contrast Dictionary Learning for 2D Compressed Sensing MRI Reconstruction », proceedings of the IEEE International Symposium on Biomedical Imaging 2018, Washington, USA, #695.

Z. Raolison, R. Abdeddaïm, **L. Leroi**, A. L. Neves, F. Mauconduit, S. Enoch, N. Malléjac, P. Sabouroux, A.-L. Adenot-Engelvin, A. Vignaud, « Evaluation of a new long-lasting silicon carbide based dielectric pad for ultra-high field MRI », proceedings of the International Society for Magnetic Resonance in Medicine 2018, Paris, France, #2664.

L. De Rochefort, **L. Leroi**, R. Valabrègue, O. Girard, G. Duhamel, M.D. Santin, P. Loureiro de Sousa, J. Lamy, F. Mauconduit, R.-M. Dubuisson, G. Guillot, A. Vignaud, « Multi-parametric maps from multi-contrast Steady-State Sequences on Multiple Manufacturers and Fields », proceedings of the 34th European Society for Magnetic Resonance in Medicine and Biology 2017, Barcelona, Spain, #456.

A. L. Neves, R. Abdeddaïm, S. Enoch, J. Wenger, J. Berthelot, A.-L. Adenot-Engelvin, N. Malléjac, F. Mauconduit, **L. Leroi**, A. Vignaud, P. Sabouroux, « Optimization via Ultra-high Permittivity Materials of Pad Effects in Dielectric Shimming at 7 Tesla MRI », proceedings of the International Society for Magnetic Resonance in Medicine 2017, Honolulu, USA, #2674.

L. Leroi, L. de Rochefort, F. Mauconduit, M. Santin, R. Valabrègue, D. Le Bihan, C. Poupon, A. Vignaud, « Quantitative MRI: towards fast and reliable T_1 , T_2 and proton density

mapping at ultra-high fields », 1er Forum Franco-Québécois d'Innovation en santé, Montréal, Canada, 2016.

5. E-posters presentations in International Conference

L. Leroi, A. Coste, L. de Rochefort, M. Santin, R. Valabrègue, F. Mauconduit, M.-F. Hang, E. Chazel, J. Bernard, M. Luong, E. Giacomini, D. Le Bihan, C. Poupon, F. Boumezbeur, C. Rabrait-Lerman, A. Vignaud, « Simultaneous multi-parametric and quantitative estimation of ^{23}Na physical properties at 7 Tesla using QuICS », proceedings of the International Society for Magnetic Resonance in Medicine 2017, Honolulu, USA, #5627. (See appendix 3)

L. Leroi, A. Vignaud, P. Sabouroux, E. Georget, B. Larrat, S. Enoch, G. Tayeb, N. Bonod, A. Amadon, D. Le Bihan, R. Abdeddaïm, « B_1^+ homogenization at 7T using an innovative meta-atom », proceedings of the International Society for Magnetic Resonance in Medicine 2016, Singapore, #3531. (See appendix 3)

Abbreviations and acronyms

α	Flip Angle
ϵ	Permittivity
γ	Gyromagnetic ratio
σ	Standard deviation
ω_0	Larmor frequency
ADC	Apparent Diffusion Coefficient
b	diffusion weighting constant
B_0	Static Magnetic Field
B_1^+	Coil transmission field
B_1^-	Coil reception profile
bSSFP	Balanced Steady-State Free Precession
CNR	Contrast to Noise Ratio
CPMG	Carr-Purcell-Meiboom-Gill sequence
CSF	Cerebro-Spinal Fluid
DESS	Double-Echo Steady-State
EPG	Extended Phase Graph
EPI	Echo-Planar Imaging
FA	Flip Angle
FOV	Field-of-View
GM	Grey Matter
GRAPPA	GeneRalized Autocalibrating Partial Parallel Acquisition
GRE	Gradient Recalled Echo
IR	Inversion Recovery
M_0	Equilibrium Magnetization
MRF	Magnetic Resonance Fingerprinting
MRI	Magnetic Resonance Imaging
MR-STAT	Magnetic Resonance Spin TomogrAphy in Time domain
NMR	Nuclear Magnetic Resonance
PD	Proton Density
PE	Phase-Encoding
pTx	Parallel Transmission

qMRI	Quantitative Magnetic Resonance Imaging
QRAPMASTER	Quantification of Relaxation time And Proton density by Multi-echo Acquisition of a SaTuration-recovery using turbo spin Echo Readout
QRAPTEST	Quantification of Relaxation times And Proton density by Twin-Echo Saturation recovery
QuICS	Quantitative Imaging using Configurations States
RF	RadioFrequency
RO	Readout
ROI	Region of Interest
SAR	Specific Absorption Rate
SD	Spin Density
SE	Spin Echo
SNR	Signal to Noise Ratio
SPGR	SPoiled Gradient Echo
SS	Slice-Selection
SSFP	Steady-State Free Precession
STEAM	STimulated Echo Acquisition Mode
SVS	Single Voxel Spectroscopy
T ₁	Spin Lattice Relaxation Time
T ₂	Spin-spin Relaxation Time
TA	Acquisition Time
TE	Echo Time
TESS	Tripe Echo Steady-State
TI	Inversion Time
TR	Repetition Time
TSC	Total Sodium Concentration
TSE	Turbo Spin Echo
UHF	Ultra-High Field
VFA	Variable Flip Angle
WM	White Matter

Résumé court en Français (French abstract)

Contexte

La tomodensitométrie (TDM), la tomographie par émission de positons (TEP) et l'imagerie par résonance magnétique (IRM) sont les techniques d'imagerie tridimensionnelle les plus connues utilisées en routine clinique. Bien que chacune d'entre elles ait ses mérites, la TDM et la TEP impliquent toutes deux des radiations ionisantes et offrent soit un contraste limité des tissus mous, soit une résolution relativement grossière. En revanche, l'IRM permet d'obtenir des images de résolution submillimétrique, tout en facilitant de multiples mécanismes de contrastes qui peuvent être exploités pour différencier les tissus et/ou indiquer diverses conditions pathologiques. Actuellement, les diagnostics cliniques d'IRM sont principalement basés sur des images qualitatives pondérées, où le signal est lié aux propriétés tissulaires de manière non linéaire, et dépend de facteurs externes, tels que le scanner utilisé pour l'acquisition par exemple. L'IRM quantitative est une technique d'imagerie qui regroupe les techniques susceptibles d'extraire un ou plusieurs paramètres physiques pertinents pour le diagnostic, accessibles en RMN. De nombreux paramètres peuvent être extraits. Le temps de relaxation longitudinale T_1 , relaxation transversale T_2 , densité de proton (PD), coefficient apparent de diffusion (ADC) sont les principaux paramètres qui seront d'intérêt dans notre étude. L'IRM quantitative offre un bénéfice par rapport à l'imagerie de

pondération classiquement utilisée, notamment pour la détection, la caractérisation physiopathologique mais aussi pour le suivi thérapeutique des pathologies cérébrales. Il existe un grand nombre de séquences en mesure de récupérer ce type d'informations. Tofts y a consacré un livre (Tofts, 2005) qui fait référence dans le domaine. Longtemps pourtant, malgré leurs potentiels, ces techniques sont restées pour la plupart peu utilisées car souvent trop longues pour une routine clinique. Elles ont aussi pâti de la variabilité des mesures pouvant être synthétisées dans la littérature du fait de la dépendance des résultats aux méthodes d'acquisition utilisées, à leurs paramétrages, à la configuration du matériel, ou encore à la marque de l'IRM utilisé.

Plus récemment se sont développées des méthodes d'acquisitions capables de mesurer plusieurs paramètres simultanément. Là aussi, une littérature pléthorique a vu le jour avec quelques méthodes réputées qui ont émergé, susceptibles de mesurer PD, T_1 et T_2 , comme Look-Locker (Schmitt et al., 2004), QRAPMASTER (Warntjes et al., 2008), ou TESS (Heule et al., 2014). Plus récemment, un article dans *Nature* a fait sensation en mettant sous les projecteurs une nouvelle technique appelée MR Fingerprinting (MRF) (Ma et al., 2013).

Malgré l'arrivée d'IRMs toujours plus puissants et un intérêt grandissant démontré par la constante augmentation du nombre de scanners à ultra-haut champ (UHF) supérieurs à 3T, ces cartographies *in vivo* sont quasiment inexistantes de la littérature au-delà de 3T. En effet, l'utilisation de tels appareils nécessite l'affranchissement de limites physiques, empêchant de pouvoir les utiliser à leur plein potentiel en l'état. En particulier, l'inhomogénéité de la transmission radiofréquence (RF), du champ magnétique statique B_0 , les mouvements physiologiques et/ou involontaires du patient à haute résolution spatiale, et la longueur des examens lorsqu'on cherche de très hautes résolutions représentent chacun des défis à résoudre avant de pouvoir pleinement mettre à profit les IRM UHF. La communauté réalise de nombreux travaux pour avancer dans ce sens et des solutions existent pour contrecarrer ces difficultés.

Par conséquent, trouver la stratégie optimale pour fournir des résultats quantitatifs rapides et précis, compatibles de 1.5 à 7T, demeure un champ d'investigation important. Un travail de (van Valenberg et al., 2017) a étudié l'efficacité temporelle de certaines de ces méthodes basées sur des simulations d'évolution du signal en IRM. Aucune conclusion directe n'a pu être tirée quant à une solution optimale. Le développement d'une méthode d'acquisition multiparamétrique simultanée compatible avec les UHF nécessite que celle-ci soit à la fois robuste aux hétérogénéités de champ magnétique B_0 et radiofréquence B_1^+ . L'objectif était ici également de pouvoir extraire le maximum de paramètres. Nous avons donc pris le parti d'implémenter une méthode inventée par le Dr Ludovic de Rochefort et appelée « QUantitative Imaging using Configuration States » (QuICS) (de Rochefort, 2015, 2016).

Méthode d'imagerie quantitative multi-paramétrique simultanée

QuICS repose sur l'acquisition séquentielle de plusieurs images ayant des contrastes différents, obtenues par variation du spoiling radiofréquence, de l'angle de bascule et/ou du gradient de spoiling appliqué lors de l'acquisition. Avec les outils appropriés pour modéliser le comportement du signal résultant très complexe, QuICS tire le meilleur parti de cette évolution compliquée pour interpréter sans ambiguïté le signal des images. La méthode se base sur un algorithme récursif efficace permettant de calculer l'aimantation après des impulsions radiofréquences répétées de différentes amplitudes et phases, et de différents gradients.

Après les acquisitions, une minimisation au sens des moindres carrés entre le signal modélisé et le signal acquis est réalisée pour chaque voxel. Cet ajustement entre les données expérimentales et le modèle théorique permet d'extraire PD, FA, T_1 , T_2 mais aussi l'ADC en s'affranchissant dans une certaine mesure des hétérogénéités de B_0 et B_1^+ .

Mise en place d'un protocole viable pour des acquisitions cliniques sous contraintes des IRM UHF

Dans un premier temps, nous nous sommes attachés à limiter autant que possible différents facteurs qui pourraient biaiser ou fausser le processus d'extraction quantitative. Nous avons donc porté notre attention sur les biais provenant de source instrumentale. Dans une utilisation en routine clinique à UHF, des antennes munies de réseau phasé de canaux de réception sont classiquement utilisées. En effet, elles permettent d'améliorer le rapport signal sur bruit, mais aussi de réduire le temps d'acquisition des images, en utilisant des techniques telles que GRAPPA (Griswold et al., 2002) ou SENSE (Pruessmann et al., 1999). Cependant, de telles antennes peuvent également être la source d'un biais expérimental si un algorithme de reconstruction adéquat n'est pas utilisé pour combiner le signal capté par chacun des canaux de réception. Nous avons donc mis en place une méthode de reconstruction des images de phase, inventée par le Dr. Mathieu Santin (Institut du Cerveau et de la Moelle Epinière, Paris) (Santin, 2018). Une telle reconstruction permet de s'affranchir d'éventuelles erreurs dans la reconstruction des images détectées par les différents canaux à notre disposition.

Par la suite, afin d'obtenir un temps d'acquisition compatible avec une application en routine clinique, nous nous sommes penchés sur la question du nombre de contrastes nécessaires pour aboutir à un résultat convaincant. Avec l'aide du Dr Romain Valabrègue, nous avons cherché à optimiser le protocole d'acquisition en étudiant la borne inférieure de Cramer-Rao (Valabrègue and de Rochefort, 2016). Pour une résolution de $1.3 \times 1.3 \times 5 \text{ mm}^3$ dans un champ de vue de $256 \times 256 \times 160 \text{ mm}^3$, nous avons réduit le nombre de contrastes nécessaires de 45 à

12, en jouant astucieusement sur l'angle de bascule, le spoiling de gradient et le spoiling radiofréquence. Nous avons testé ce protocole optimisé pour réaliser des mesures sur fantôme homogène remplis d'eau avec 1% d'agar, puis sur un cerveau de babouin ex-vivo. Nous avons comparé nos résultats aux méthodes dites « gold-standards » existantes, trop longues pour être appliquées en pratique clinique. Nous avons pu faire la démonstration du bon fonctionnement de cette stratégie, comme le démontre la Figure 1.

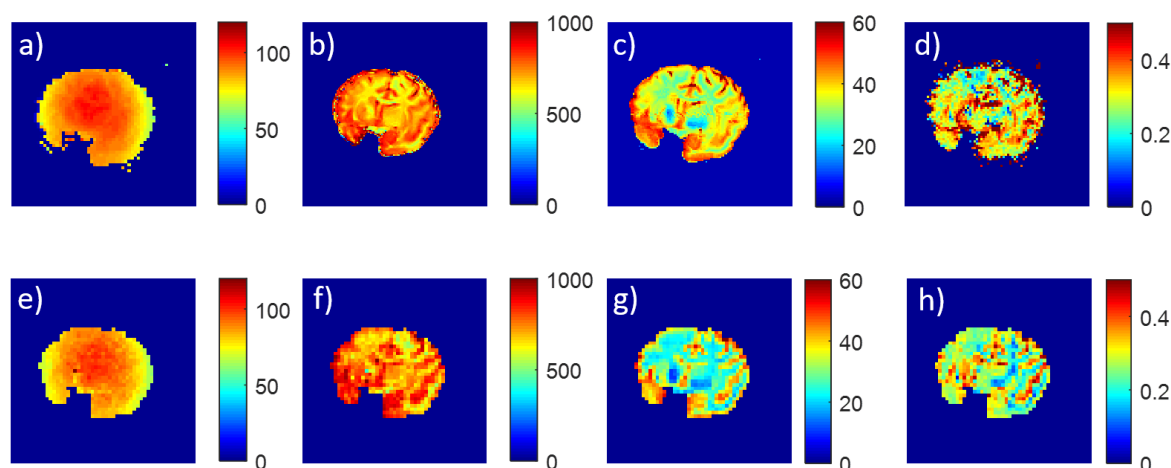


Figure 1: Cartographie quantitatives obtenues sur un cerveau de babouin ex-vivo dans du fluorinert à 7T en 7min12. La première ligne montre les résultats produits avec des méthodes conventionnelles, après plusieurs heures : Actual Flip Angle (AFI) pour l'estimation de l'angle de bascule en degrés (a), Inversion-Récupération pour le T_1 en ms (b), Multi Spin-Echo pour T_2 en ms (c) et Double Spin Echo Diffusion EPI pour la diffusion, en mm^2/ms (d). La deuxième ligne montre l'extraction obtenue avec QuICS avec les mêmes unités e) angle de bascule, f) T_1 , g) T_2 , h) ADC monodirectionnelle dans la direction d'encodage de lecture.

Nous avons ainsi développé une stratégie d'acquisition adaptée pour une applicabilité in vivo, dans des conditions optimales à 7 Tesla, sous contraintes cliniques.

Acquisitions in vivo à UHF

Quelques simulations in-silico nous nous ont montré l'importance d'obtenir un angle de bascule homogène afin d'obtenir des résultats quantitatifs acceptables. La solution la plus élégante pour homogénéiser ce champ reste à ce jour la « transmission parallèle », qui repose sur l'utilisation d'antennes munies de multiples canaux de transmission, dont l'interaction permet l'obtention d'un champ parfaitement homogène. Cependant, cette technique demande un temps de calcul pour chaque individu pouvant aller jusqu'à 15 minutes pendant l'examen, rendant une telle technologie difficilement applicable en routine clinique. Partis du constat que ces hétérogénéités sont similaires d'un volontaire à un autre pour un type d'examen donné, par exemple sur le cerveau, (Gras et al., 2017a) ont pu fournir une solution

« clés en main », appelée «Universal Pulses». Les résultats de leur étude suggèrent que l'utilisation de la transmission parallèle peut devenir totalement transparente pour l'utilisateur, ce qui pourrait rendre le grand potentiel des scanners UHF plus accessible à tous en simplifiant le flux d'exams.

Une acquisition QuICS a donc été réalisée à 7T en appliquant une excitation RF standard, et cette excitation universelle sur un volontaire sain, à une résolution de $1 \times 1 \times 3 \text{ mm}^3$, en 16 minutes. Les résultats, Figure 2, montrent les extractions quantitatives tridimensionnelles résultantes à 7T. L'utilisation de pulses universels permet l'homogénéisation de l'angle de bascule et les paramètres quantitatifs ont été extraits avec succès dans le cerveau entier.

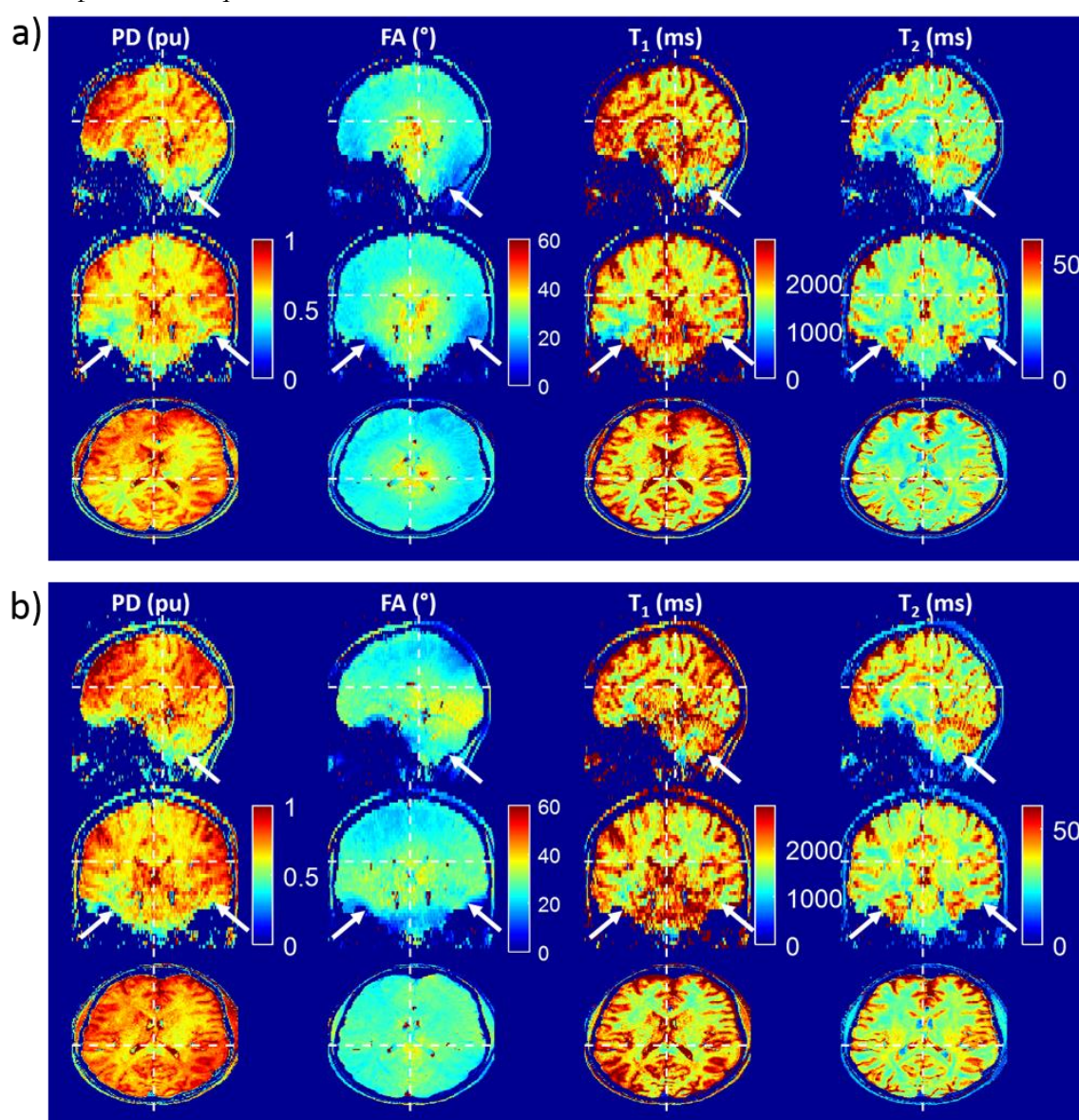


Figure 2: Extraction quantitative 3D QuICS à 7T ($1 \times 1 \times 3 \text{ mm}^3$) pour PD, FA, T₁ et T₂ en utilisant (a) une impulsion standard et (b) une impulsion universelle. Les coupes affichées sont représentées dans les 3 orientations différentes par des pointillés blancs. La distribution de l'angle de bascule est bien plus homogène en (b) et l'extraction de QuICS est performante dans tout le cerveau.

Acquisitions quantitatives sur sodium

Le sodium (^{23}Na) est le deuxième noyau le plus sensible à la RMN dans les tissus biologiques après l'hydrogène (^1H). L'IRM du sodium offre un aperçu des pathologies grâce à des informations métaboliques inédites, auxquelles l'imagerie par résonance magnétique des protons classique ne permet pas d'accéder. Une vaste littérature étudie la teneur totale en sodium comme marqueur de la viabilité cellulaire *in vivo*. La concentration totale de sodium (TSC) s'est par exemple révélée bénéfique pour étudier la viabilité tissulaire après un accident vasculaire cérébral, pour détecter les tumeurs malignes ou encore pour évaluer la résistance aux médicaments avant la chimiothérapie, la maladie de Huntington et la sclérose en plaques dans le cerveau, ainsi que l'atteinte myocardique aiguë dans le cœur (Madelin and Regatte, 2013). Dans certaines études, la diffusion protonique ou l'IRM avec injection de produit de contraste est également proposée et recommandée pour augmenter la sensibilité et la spécificité du diagnostic (Jacobs et al., 2009). Ainsi, la possibilité de récupérer la concentration de ^{23}Na en plus de plusieurs autres propriétés RMN quantitatives telles que T_1 , T_2 ou le Coefficient de Diffusion Apparent (ADC) en une seule expérience est intéressante pour améliorer la détection, l'étude de la physiopathologie de diverses maladies et l'évaluation de traitements potentiels.

À ce jour, la détermination précise des paramètres quantitatifs susmentionnés en imagerie du sodium nécessite la mise en œuvre séquentielle de plusieurs méthodes, comme cela a été démontré par le passé (Morrell et al., 2016; Staroswiecki et al., 2009; Zbyn et al., 2009). Aucune de ces études n'a pu acquérir une imagerie de diffusion du sodium jusqu'à présent. La diffusion du sodium n'a été évaluée que dans le cerveau du rat (Goodman et al., 2005) et le muscle squelettique du rat en utilisant la spectroscopie et l'injection de réactif de déplacement, hautement toxique pour l'homme (Babsky et al., 2008).

Le travail réalisé ici avait pour objectif de démontrer la faisabilité expérimentale de QuICS sur le sodium pour évaluer simultanément en une seule séquence les propriétés de RMN de ^{23}Na *in vitro*.

Le schéma expérimental utilisé lors des expériences est présenté en Figure 3a. Différents environnements physico-chimiques présentant des variations des temps de relaxation, d'ADC et de concentration, correspondant à différents tissus humains, ont été investigués pour démontrer la robustesse de l'approche. Les cartographies quantitatives obtenues après ajustement du signal de 11 contrastes différents obtenus en 1h18 sont représentées en Figure 3. Les résultats présentés en Figure 4 démontrent que nous avons réussi à évaluer une large gamme physiologique de concentrations de sodium, de relaxations et d'ADC, correspondant à divers tissus *in vivo*, allant du cartilage au cerveau.

Cette étude sur fantôme est la première extraction quantitative multiparamétrique simultanée rapportée dans le cadre de l'IRM ^{23}Na , et en particulier la première cartographie 3D de son ADC.

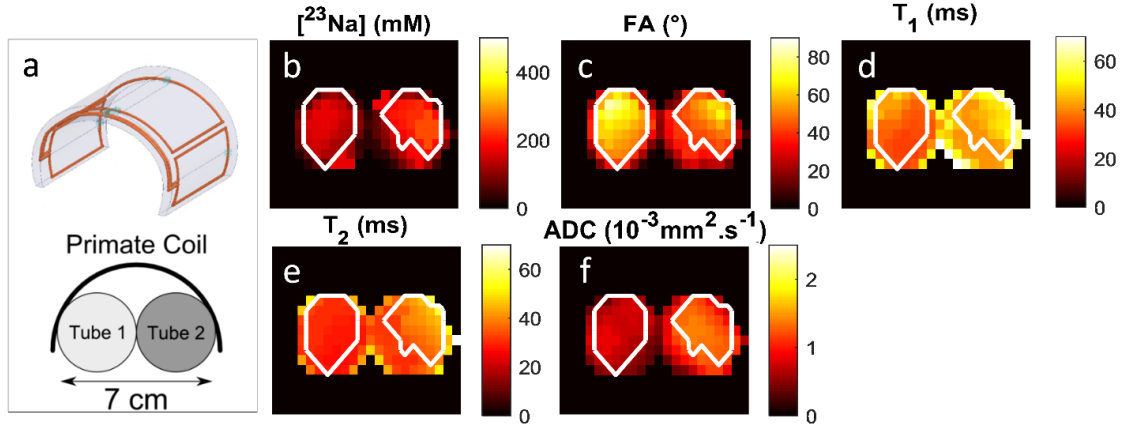


Figure 3 : Schéma expérimental de l'antenne héli-volumique ^{23}Na utilisée ^{23}Na avec positionnement des fantômes (a) et cartes axiales multiparamétriques obtenues avec la méthode QuICS: concentration de ^{23}Na (b), angle de bascule (FA) en degrés (c), T_1 et T_2 en ms (d, e) et ADC en $10^{-3}\text{mm}^2\cdot\text{s}^{-1}$ (f). La région d'intérêt en blanc délimite la région où $\text{FA} > 40^\circ$. Dans cette expérience, le tube 1 (à gauche) contenait de l'eau saline avec une concentration physiologique de liquide céphalo-rachidien de 150 mM avec 2% d'agar et le tube 2 (à droite) contenait la même eau saline sans agar.

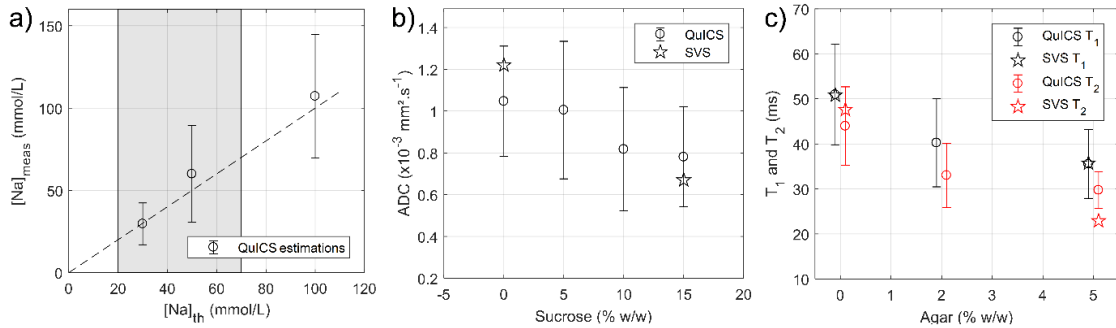


Figure 4 : a) Dilution théorique et estimations expérimentales obtenues avec QuICS pour des concentrations physiologiques réalistes de ^{23}Na dans la matière grise et la substance blanche (zone ombrée). Les concentrations mesurées ont tendance à s'aligner sur la première bissectrice (ligne pointillée). b) Valeurs estimées de l'ADC à 21°C pour quatre échantillons de NaCl de 150 mM avec diverses fractions massiques de sucrose, avec les écarts-types associés. Les résultats montrent une évolution décroissante de la diffusion en fonction de la concentration de saccharose, confirmant les observations de (Hara et al., 2014; Laubach et al., 1998b; Winfield et al., 2016) et les mesures spectroscopiques réalisées à 7T (SVS). c) T_1 et T_2 estimés pour trois fantômes de 150 mM de NaCl et diverses concentrations d'agar.

Conclusion et perspectives

Une méthode permettant la récupération simultanée et rapide de paramètres NMR tels que PD, T_1 , T_2 et potentiellement l'ADC a été mise en place et validée sur des fantômes ainsi que sur l'homme. Des cartes quantitatives du cerveau entier à une résolution de $1 \times 1 \times 3 \text{ mm}^3$ ont été obtenues un temps d'acquisition de 18 minutes, permettant ainsi une possible applicabilité en routine clinique.

La méthode a également montré sa capacité à récupérer des temps de relaxation très courts sur un noyau exotique tel que le sodium. Différents environnements correspondant à des propriétés *in vivo* ont été étudiés et la technique a réussi à récupérer simultanément la concentration totale en Sodium, T_1 , T_2 , l'angle de bascule et l'ADC unidirectionnel.

Dans les travaux futurs, le temps d'acquisition sera réduit en mettant en œuvre des trajectoires d'acquisition de l'espace de Fourier non cartésiennes. Jusqu'à présent, un ADC unidimensionnel a été récupéré sur les fantômes. Cette valeur est pertinente dans les milieux isotropes, mais devient une information limitée pour les examens *in vivo*. Pour extraire ce paramètre sur l'homme, l'acquisition de plus de contrastes serait nécessaire. L'implémentation de gradients de spoiling dans différentes directions pourra aider à estimer une valeur de tri-dimensionnelle d'ADC. QuICS a également été breveté avec diverses possibilités. L'acquisition de plusieurs états de configuration pourrait être envisagée pour accélérer le temps d'acquisition. Varier le TR pourrait aussi être une possibilité, permettant ainsi d'ajouter un nouveau degré de liberté au modèle.

Pouvoir étudier les organes avec des valeurs robustes de paramètres intra-individuels pertinents, fiables et reproductibles, quelle que soit la machine utilisée, révolutionnerait le processus de diagnostic. De nombreux progrès ont été réalisés au cours de cette thèse pour fournir une stratégie d'IRM quantitative efficace, applicable cliniquement à UHF. Dans les prochaines étapes, il sera nécessaire d'accumuler et de traiter des données saines et pathologiques sur de grandes populations, en fonction de l'âge et du sexe. On pourrait alors envisager non seulement de détecter et de caractériser les lésions, comme le font actuellement les radiologues basés sur des images anatomiques pondérées, mais aussi caractériser les tissus et ainsi proposer aux médecins un système d'aide à la décision clinique.

Appendices: Articles and abstracts submitted as first author

Appendix 1: Simultaneous multi-parametric mapping of total sodium concentration, T_1 , T_2 and ADC at 7 T using a multi-contrast unbalanced SSFP



Contents lists available at ScienceDirect

Magnetic Resonance Imaging

journal homepage: www.elsevier.com/locate/mri

Technical note

Simultaneous multi-parametric mapping of total sodium concentration, T_1 , T_2 and ADC at 7 T using a multi-contrast unbalanced SSFP

Lisa Leroi^{a,1}, Arthur Coste^{a,1}, Ludovic de Rochefort^b, Mathieu D. Santin^{c,d}, Romain Valabregue^{c,d}, Franck Mauconduit^e, Eric Giacomini^a, Michel Luong^a, Edouard Chazel^a, Julien Valette^f, Denis Le Bihan^a, Cyril Poupon^a, Fawzi Boumezeur^a, Cécile Rabrait-Lerman^a, Alexandre Vignaud^{a,*}

^a NeuroSpin, CEA, DRF/JOLIOT, Université Paris-Saclay, Gif-sur-Yvette, France

^b CRMBM, UMR 7339, Aix-Marseille University, Marseille, France

^c CENIR, Centre de NeuroImagerie de Recherche, Paris, France

^d ICM, Inserm U 1127, CNRS UMR 7225, Sorbonne Universités, UPMC Université Paris 06 UMR S1127, Institut du Cerveau et de la Moelle épinière, Paris, France

^e Siemens Healthineers, Saint-Denis, France

^f Commissariat à l'Energie Atomique et aux Energies Alternatives (CEA), Direction de la Recherche Fondamentale (DRF), Institut de Biologie François Jacob, MIRCen, Fontenay-aux-Roses, France

ARTICLE INFO

Keywords:

Non proton MRI
Sodium
 T_1 mapping
 T_2 mapping
Diffusion

ABSTRACT

Purpose: Quantifying multiple NMR properties of sodium could be of benefit to assess changes in cellular viability in biological tissues. A proof of concept of Quantitative Imaging using Configuration States (QuICS) based on a SSFP sequence with multiple contrasts was implemented to extract simultaneously 3D maps of applied flip angle (FA), total sodium concentration, T_1 , T_2 , and Apparent Diffusion Coefficient (ADC).

Methods: A 3D Cartesian Gradient Recalled Echo (GRE) sequence was used to acquire 11 non-balanced SSFP contrasts at a $6 \times 6 \times 6$ mm³ isotropic resolution with carefully-chosen gradient spoiling area, RF amplitude and phase cycling, with TR/TE = 20/3.2 ms and 25 averages, leading to a total acquisition time of 1 h 18 min. A least-squares fit between the measured and the analytical complex signals was performed to extract quantitative maps from a mono-exponential model. Multiple sodium phantoms with different compositions were studied to validate the ability of the method to measure sodium NMR properties in various conditions.

Results: Flip angle maps were retrieved. Relaxation times, ADC and sodium concentrations were estimated with controlled precision below 15%, and were in accordance with measurements from established methods and literature.

Conclusion: The results illustrate the ability to retrieve sodium NMR properties maps, which is a first step toward the estimation of FA, T_1 , T_2 , concentration and ADC of ^{23}Na for clinical research. With further optimization of the acquired QuICS contrasts, scan time could be reduced to be suitable with in vivo applications.

1. Introduction

Sodium (^{23}Na) yields the second strongest NMR signal among biologically relevant NMR-active nuclei. ^{23}Na MRI offers insights into pathologies through novel metabolic information that classic proton MR imaging cannot access, potentially improving patient care in this way. Multiple publications deal with the investigation of sodium compartmentalization with the aim to separate intracellular ^{23}Na from the total sodium content as a marker of cell viability in vivo. However,

the complexity to untangle such information makes these results debatable [1]. Indeed, most of the studies are currently focusing on Total Sodium Concentration (TSC) which, non-exhaustively, has been shown to be beneficial to study tissue viability after stroke, to detect malignant tumors and to assess drug resistance before chemotherapy in rats glioma [2], Huntington's disease and multiple sclerosis in the brain, as well as acute myocardial infarction in the heart [3]. In some studies, proton Diffusion-Weighted Imaging or contrast-enhanced MRI is also proposed and recommended to increase the sensitivity and specificity of

* Corresponding author at: CEA Saclay, Neurospin, Bat 145, 91191 Gif-sur-Yvette, France.

E-mail address: alexandre.vignaud@cea.fr (A. Vignaud).

¹ These authors contributed equally to this work

<https://doi.org/10.1016/j.mri.2018.07.012>

Received 20 April 2018; Received in revised form 23 July 2018; Accepted 23 July 2018
0730-725X/ © 2018 Elsevier Inc. All rights reserved.

the diagnosis [4]. Thus, the opportunity to quantitatively retrieve ^{23}Na TSC in addition to several other NMR properties such as T_1 , T_2 or Apparent Diffusion Coefficient (ADC) specific to ^{23}Na in a single experiment is of interest to improve the detection, the investigation of the physiopathology of various diseases and the evaluation of potential treatments, for an enhanced follow-up.

To date, the precise determination of the above-cited quantitative parameters requires the sequential implementation of several methods, as was demonstrated in the past [5–7]. None of them addressed ^{23}Na DWI so far, as several challenges need to be tackled. First, ^{23}Na very short relaxation times together with poor signal to noise ratio leads to a difficult detection. In addition, its 4-fold lower gyromagnetic ratio leads to approximately a 15-fold reduction in the effective b-values. Sodium diffusion has only been assessed in rat brain [8] and rat skeletal muscle using shift-reagent aided MR Spectroscopy [9]. Therefore, the simultaneous, fast and robust mapping of ^{23}Na NMR properties constitutes a challenging, relevant and exciting prospect for biomedical research. For the mapping of ^1H , several methods have been developed recently to provide combined measurements of T_1 and T_2 [10–14] or T_2^* [15] and ADC [16,17] within a single acquisition. Some approaches use saturation pulses that are increasing the specific absorption rate and some require long and complex post-processing [18]. Recently, a method to perform combined multi-parametric mapping of magnetization (M_0), flip angle (FA), global T_1 , T_2 and mono-dimensional ADC altogether has been proposed [19,20]. This technique, called Quantitative Imaging using Configuration States (QulCS), uses different contrasts generated from a Steady-State Free Precession (SSFP) sequence, by varying acquisition parameters such as phase cycling, spoiling gradient and FA. The multiple steady-states acquired then depend on the underlying physical parameters such as M_0 , T_1 , T_2 , ADC and the actual FA. The simplified description using the configuration states enables to precisely describe the signal under the Bloch-Torrey equation, and quantify the physical parameters through straightforward fitting [21,22]. Although ^{23}Na is usually modeled using a density operator evolution under the Liouville equation, the magnetization behavior will be approximated to follow a single- T_2 simplified model weighted by its various contributions.

The aim of this work was to demonstrate the experimental feasibility of this approach on ^{23}Na to assess simultaneously in a single sequence total ^{23}Na NMR properties in phantoms experiments. It is performed at 7 T to take advantage of the larger SNR [23]. The robustness of the approach was evaluated in different physicochemical environments presenting variations of relaxation times, ADC and concentrations, corresponding to different *in vivo* tissues. To the knowledge of the authors, this phantom study is the first simultaneous multi-parametric quantitative extraction reported in the context of ^{23}Na MRI, and in particular the first 3D mapping of its ADC. Applicability to clinical acquisitions will be also discussed.

2. Material and methods

2.1. Signal modeling and quantitative extraction principles

Balanced SSFP sequences are sensitive to B_0 inhomogeneity as the phase accumulated between two TRs is leading to the widely known banding-artifacts [24]. Introducing a spoiling gradient G generally produces a much larger phase inhomogeneity such that the banding artifact becomes unapparent, as all phases between 0 and 2π are present within each voxel. Let us denote z the spoiling gradient axis. The gradient waveform $G(t)$ is chosen such that a constant area remains between two TRs. As shown in Eq. (1), this area is proportional to a spatial frequency shift Δk_z , and inversely proportional to a “spoiling distance”, a , corresponding to a 2π dephasing between two TRs (Eq. 1).

$$\Delta k_z = 1/a = \frac{\gamma}{2\pi} \int_0^{TR} G(t) dt \quad (1)$$

In the sequence, we choose to parametrize this spoiling distance a as a ratio of the readout-pixel size Δz , using an integer N defined such that:

$$a = \frac{\Delta z}{N} \quad (2)$$

To further indicate the amount of spoiling area applied respectively along the read-out, the phase encoding and slice selection directions, we introduce the numbers N_{RO} , N_{PE} and N_{SS} . Therefore, setting the parameters $N_{RO} \geq 1$, $N_{PE} = N_{SS} = 0$ in the sequence imposes the spoiling area along the read-out axis, and ensures that the sequence is spoiled with a dephasing superior to 2π over the pixel size.

In that framework, magnetization can be described in space or in terms of spatial frequencies. The latter description was proposed long ago and originally referred to as the configuration states description [25,26], similar to the extended phase graph description [27–30], and in which only discrete spatial frequencies are needed due to the constant dephasing between TRs. The longitudinal and transverse magnetization, M_z and M_{xy} , can respectively be decomposed into discrete Fourier series, as described in Eq. (3) and Eq. (4).

$$M_z = \sum_{k=-\infty}^{\infty} m_{zk} Z^{-k} \quad (3)$$

$$M_{xy} = \sum_{k=-\infty}^{\infty} m_{xyk} Z^{-k} \quad (4)$$

where k corresponds to the configuration state, also called “coherent” states in literature linked by “pathways” determined by the gradient dephasing. The complex exponential $Z = \exp(-i2\pi \cdot \Delta k_z \cdot z)$ is introduced as a base function to describe the spatial modulations between two excitations. m_{zk} and m_{xyk} represent the coefficients of the discrete Fourier series.

After several excitations at constant RF amplitude, a steady-state is reached. As the spoiling distance a is chosen smaller than the voxel size, the measured signal corresponds to m_{xy0} , the only non-vanishing term after averaging Eq. (4) over the pixel size.

The steady state's contrast can then be manipulated using quadratic RF cycling. It was originally proposed by Zur and colleagues [31] to reduce stimulated echo formation and provide a steady-state closer to T_1 -weighted fully spoiled sequences. It has been shown that very different steady-states can be obtained depending on the chosen spoiling increment, in particular with few degrees producing a strongly T_2 -contrast [32–34]. Therefore, the SSFP model is influenced by phase cycling. Its sensitivity is illustrated in Fig. 1, which provides a representation of real and imaginary parts of m_{xy} , the steady-state transverse magnetization, depending on the spoiling phase increment value.

SSFP contrast can also be influenced by tissues properties such as T_1 , T_2 and diffusion. In the configuration state description, T_1 and T_2 relaxations induce an attenuation of the magnetization components [29], while diffusion acts as Gaussian filtering [35,36]. The full derivation of the steady-state signal, accounting for acquisition parameters as well as relaxation and free diffusion can be found in [19].

Fig. 2 provides complex representations of signals obtained with different T_1 , T_2 , and ADC values for the same acquisition parameters, indicating that the SSFP model is sensitive to any variation of one of these physical parameters. Therefore, choosing appropriate N_{RO} and phase increments will allow a proper extraction of M_0 , T_1 , T_2 and ADC fitting the signal behavior.

To perform the quantitative extraction from the multiple SSFP contrasts, post-processing was performed using Matlab (The Mathworks, Natick, USA) and DICOM complex images. First, the acquired contrasts were grouped into a single measurement vector, S_{meas} . Global phase drifts were then removed, assuming a linear temporal evolution between the first and last volumes acquired in the same conditions. A gradient-echo phase map was estimated using the complex sum of volumes with 0° and 180° RF phase increments. It was then

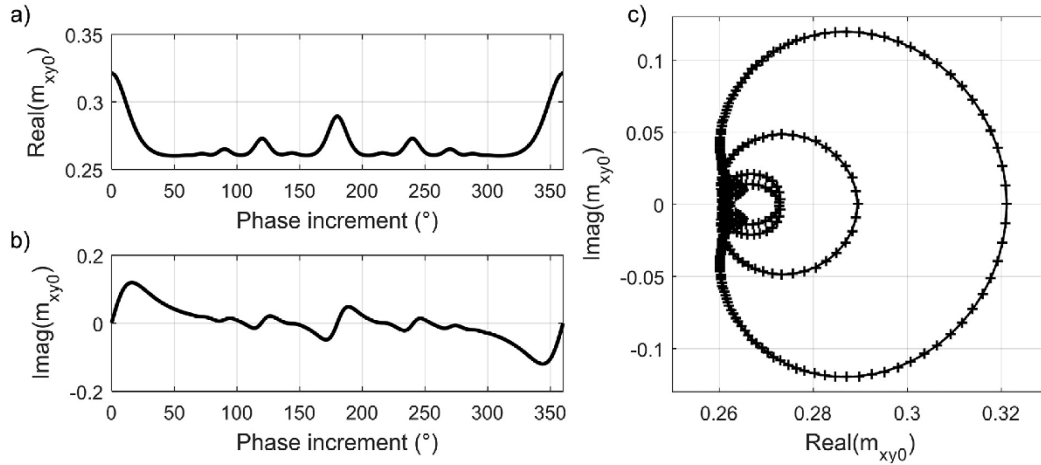


Fig. 1. Real (a) and imaginary (b) part of the theoretical transverse magnetization signal for a voxel resulting for sodium physical constants $T_1/T_2 = 60/50$ ms, $\text{ADC} = 1.3 \times 10^{-3} \text{ mm}^2/\text{s}$, and acquisition parameters $\text{TR} = 10$ ms, $\text{FA} = 45^\circ$, resolution of 6 mm^3 and a constant spoiling gradient corresponding to $N_{\text{RO}} = 47$ ($a = 0.128 \text{ mm}$). The associated complex plane is also displayed (c), where each cross corresponds to a different RF spoiling increment, sampled for each degree of from 0 to 360° . The maximum real value with null imaginary part corresponds to RF spoiling increment of $0^\circ/360^\circ$.

subtracted from all volumes providing the SSFP phase-induced maps corrected for the phase at echo time, and thus for B_0 inhomogeneities.

The quantification was then performed by a least-squares fit between S_{meas} and the model derived from Bloch-Torrey Eq. (19). A Gauss-Newton algorithm was implemented for that purpose, with a numerical evaluation of the Jacobian matrix, and an initialization step consisting in the comparison of S_{meas} with a dictionary of $50 \times 50 \times 30 \times 20$ values corresponding to $R_1 = [0.01; 50] \text{ s}^{-1}$, $R_2 = [0.01; 50] \text{ s}^{-1}$, $\text{ADC} = [0.01; 3] \times 10^{-3} \text{ mm}^2/\text{s}^{-1}$ and $\text{FA} = [0.045; 90]^\circ$ covering expected range of values for ^{23}Na in the studied compositions. FA was considered as a variable to be determined here, as its degree of inhomogeneity can become large especially when using local transmit coils.

2.2. In-silico experimental setup formulation

In this study, only phase cycling was used to modulate the SSFP contrast. Thus, to determine the most adequate N_{RO} and FA to use to accurately assess the targeted sodium relaxations ($T_1 = 60$ ms, $T_2 = 50$ ms) and ADC properties ($\text{ADC} = 1.3 \times 10^{-3} \text{ mm}^2/\text{s}$) under the scanning conditions described in the following section, simulations

using brute-force Monte-Carlo SSFP were performed. The range of tested FA varied from 0 to 100° with a precision of 1° , using 10,000 samples per FA. To account for the coil receiving profile and associated FA and SNR variations, the voxel magnetization at thermal equilibrium, M_0 , was proportionally adapted to the considered FA from empirical measurements. The range of tested N_{RO} varied from 1 to 47, corresponding to a diffusion sensitivity of $b = \text{TR} \cdot (2\pi/a)^2$ ranging from 0.02 to $48.4 \text{ s} \cdot \text{mm}^{-2}$ between two RF pulses. The latter was the limit of our system given the chosen TR of 20 ms and pixel size $\Delta z = 6 \text{ mm}$.

2.3. MRI acquisitions

MRI acquisitions were performed on an investigational 7 T MRI scanner (Siemens Healthineers, Erlangen, Germany) using a homemade hemi-cylindrical single channel Tx/Rx ^{23}Na coil (Fig. 4a). FA was calibrated assuming that the reference voltage would allow to get a global mean FA equal to the targeted FA in the whole phantom. Acquisitions consisted in a repeated 3D non-selective Cartesian unbalanced SSFP with different contrasts. Scanning parameters were $\text{TR}/\text{TE} = 20 \text{ ms}/3.2 \text{ ms}$, bandwidth = $220 \text{ Hz}/\text{px}$. The image resolution was 6 mm^3 isotropic in a $192 \times 192 \times 160 \text{ mm}^3$ field-of-view, and a pulse duration of

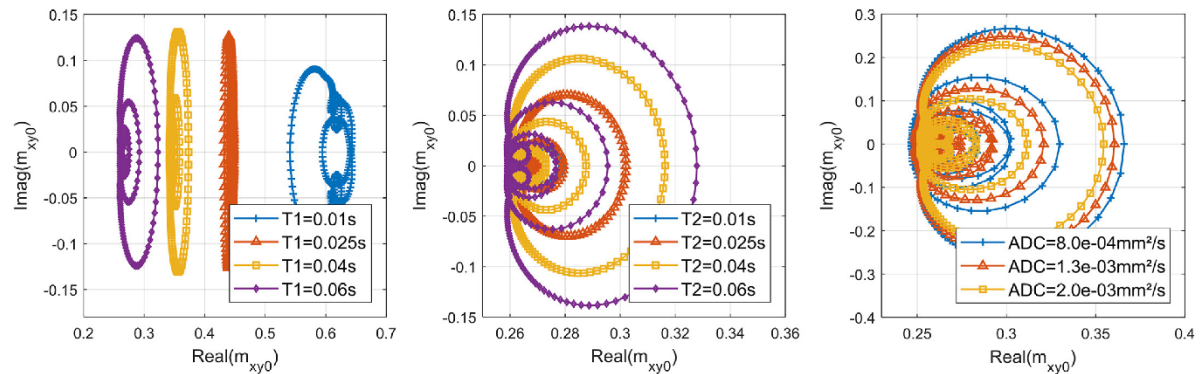


Fig. 2. Complex representation of simulated signals sampled for each degree of RF spoiling increment from 0 to 360° , $\text{TR} = 10$ ms, $\text{FA} = 45^\circ$, resolution of 6 mm^3 and $N_{\text{RO}} = 47$ ($a = 0.18 \text{ mm}$) varying T_1 (a), T_2 (b) and ADC(c), otherwise fixed to respectively 60 ms, 50 ms and $1.3 \times 10^{-3} \text{ mm}^2/\text{s}$. This figure highlights the contrast variations that can be obtained depending on the relaxation times and diffusion.

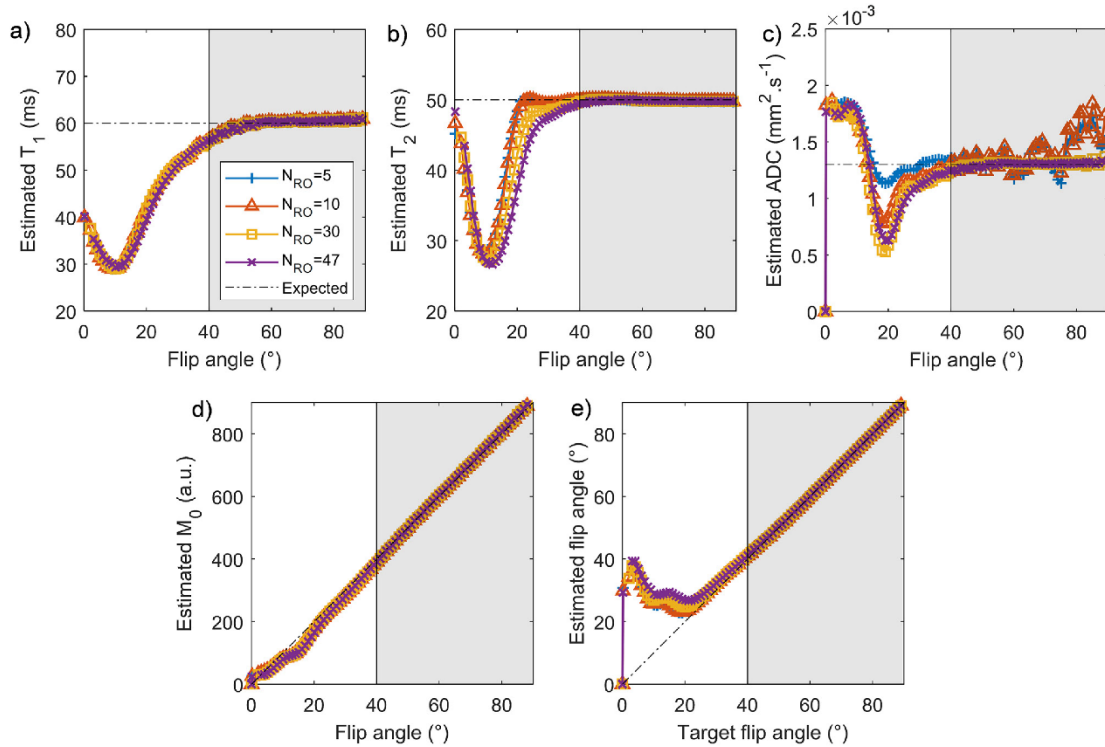


Fig. 3. Brute-force Monte-Carlo simulations of ^{23}Na T_1 (a), T_2 (b), ADC(c), M_0 (d) and FA(e) estimations as a function of spoiling gradient moment (N_{RO}) applied in the readout direction and FA, in order to account for its variations due to the coil profile. TR was set to 20 ms, RF spoiling increments = [0, 20, 100, 110, 130, 170, 190, 230, 250, 340, 360]°, pixel size $\Delta z = 6$ mm and expected $T_1 = 60$ ms, $T_2 = 20$ ms and $\text{ADC} = 1.3 \times 10^{-3} \text{ mm}^2 \cdot \text{s}^{-1}$. To account for the coil receiving profile and associated FA and SNR variations, M_0 varied with FA. On the one hand, this figure illustrates that choosing a FA higher than 40° (shaded area) and the highest spoiling gradient momentum avoids bias and leads to the most accurate estimations for T_1 , T_2 and ADC. In another hand, results obtained with FA below 40° and lower N_{RO} cannot be considered because a large bias and uncertainty in the estimations are observed. M_0 and FA estimations are more robust to FA variations, as a FA of 20° seems sufficient to estimate these parameters.

500 μs . FA and N_{RO} were set respectively to 45° and 47, according to the results from the optimization process described above (see Fig. 3). 11 contrasts were selected with RF spoiling increments = [0, 20, 100, 110, 130, 170, 190, 230, 250, 340, 360]° to sample the complex plane (Fig. 1c). Using 25 averages, the acquisition time (TA) of a volume was 7 min, leading to a total TA of 1 h 18 min.

MR spectroscopic measurements of ground-truth T_1 , T_2 and ADC were performed on a 7 T preclinical scanner (Pharmascan, Bruker, Ettlingen, Germany) using a small home-made dual-resonance $^{23}\text{Na}/^1\text{H}$ birdcage coil and gold-standard methods. Single Voxel Spectroscopy (SVS) data were acquired from a large 30 mm³ voxel. For T_1 assessment, an Inversion Recovery (IR) LASER sequence [37,38] was used, varying the inversion time from 5 to 100 ms by 10 ms steps, with TR/TE = 500/13 ms, BW = 4 kHz and an inversion pulse of 2 ms. Then, T_2 and ADC were measured using a STEAM sequence [39,40], acquiring respectively seventeen different TE from 2 to 120 ms and five b-values from 0 to 1200 s/mm² with two diffusion gradient polarities to get rid of cross-terms with selection gradients. Acquisition parameters were set to TR/TM = 500/10 ms, TE = 10 ms, BW = 4 kHz and excitation pulse of 500 μs . The consecutive SVS acquisitions for these three parameters took about 1 h 35 min.

To test our method's ability to probe sodium NMR properties, experiments were conducted on a series on phantoms using the setup shown Fig. 4a. First, three phantoms (150 mL glass containers, diameter = 3 cm, Fig. 4) containing the same CSF physiological NaCl concentration of 150 mM were investigated, with 0, 2 and 5% agar gel

to reduce the relaxation times of ^{23}Na , to mimic brain or cartilage properties. Second, to test the quantification of sodium concentrations, phantoms of 30, 50 and 100 mM NaCl were imaged with a reference tube of 150 mM in the same configuration. Finally, to increase the viscosity of our saline solutions [41,42] and probe varying apparent ADCs of ^{23}Na , 5 to 15% w/w sucrose (Sigma-Aldrich, Saint Louis, USA) was added in the 150 mL tubes.

MRS measurements were performed using tubes filled with similar compositions, using a concentration of 150 mM NaCl. One reference tube was assessed, in addition with one tube containing 5% of agar gel and one containing 15% of sucrose.

2.4. Data analysis

Total sodium concentration maps were retrieved from the ratio between M_0 and B_1^- , where the sensitivity profile B_1^- was estimated from the FA distributions, by applying the reciprocity principle [43]. The concentrations were estimated for each adjacent tube using the tube of 150 mM as an external reference for concentration.

Due to the hemi-volumic coverage of our coil (Fig. 4a), a substantial sensitivity bias was observed across our images. In order to limit the impact of this inhomogeneous SNR on the estimation of the NMR properties of ^{23}Na , a region-of-interest (ROI) was defined in each phantom to keep the upper part, where the FA was systematically higher than 40° (Fig. 4b–f), as observed in the experimental setup formulation results (Fig. 3). Estimations were performed by assessing the

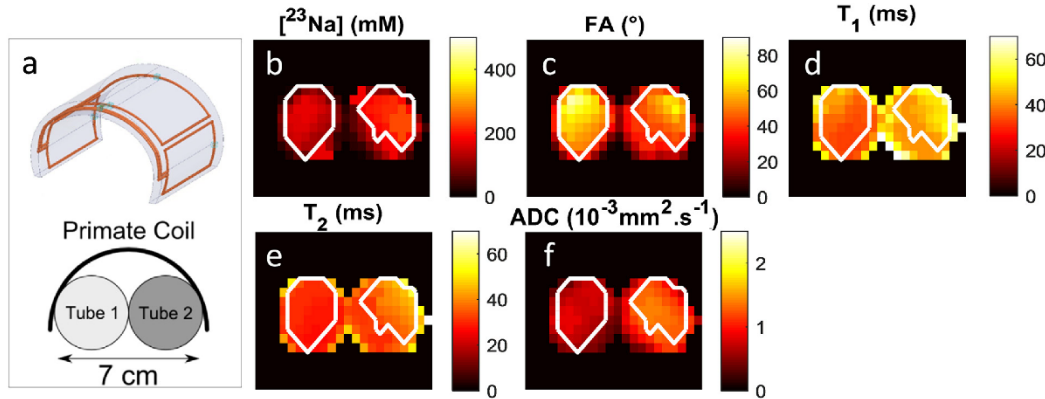


Fig. 4. Schematic of our hemi-volumic ^{23}Na RF coil with positioning of phantoms (a) and multi-parametric transverse maps obtained using the QuICS method: ^{23}Na concentration (b), FA in degrees (c), T_1 and T_2 in ms (d, e) and ADC in $10^{-3} \text{ mm}^2 \cdot \text{s}^{-1}$ (f). The white ROI delimits the region where $\text{FA} > 40^\circ$, in agreement with results on experimental setup formulation, Fig. 3. In this experiment, tube 1 (left) contained saline water with a physiological CSF concentration of 150 mM with 2% agar and tube 2 (right) contained the same saline water without agar. Total sodium concentration map was retrieved from the ratio between M_0 and B_1^- , where the sensitivity profile B_1^- was estimated from the FA distributions, by applying the reciprocity principle [60]. The concentration for tube 2 was estimated using tube 1 as a reference. Over the ROI, results exhibit homogeneous and significantly different relaxation times between the two phantoms.

mean over the pixels respecting this criteria over the whole phantom, leading to robust estimations.

3. Results

Results of the protocol optimization process are presented in Fig. 3. It shows that FA and N_{RO} need to be respectively set to 45° and to 47, to get reliable estimations. As shown in Fig. 4, regions of interests were also defined in each phantom to assess results where the FA was systematically higher than 40° .

As illustrated in Fig. 5a, ^{23}Na concentrations were accurately estimated, relative quantification errors being below 15%. Likewise, the ADCs were estimated for the sucrose-enriched (5–15%w/w) saline phantoms (Fig. 5b). SVS measurements lead to very similar results for both the reference and the 15% sucrose tubes.

To study the robustness of the method, different measurements were conducted varying the relaxation properties of the phantom using agar from 0 to 5%, to mimic different human tissue properties. Results displayed in Fig. 5c show the consistency of the mean T_1 and total T_2 over the defined ROIs compared to SVS measurements. Similar values were also reported at 7 T [44].

4. Discussion

In this work, 3D simultaneous multi-parametric extraction of total sodium concentration and total T_2 , T_1 , ADC and flip angle at 7 T was performed at 6 mm^3 isotropic resolution in 1 h18. To some extent, these maps are insensitive for B_0 heterogeneity, as these variations are accounted for in the model. Sodium concentrations corresponded to the preparations; relaxation rates were in agreement with MRS gold-standard measurements; ADC measurements were consistent with data and a measurable reduction in ADC was obtained while adding sucrose. The ^{23}Na ADC maps were estimated along a single spoiling gradient direction, assuming the diffusion weighting of a single quantum coherence NMR signal, which is relevant for most sodium ions in an isotropic media [8].

An acquisition protocol that allows reliable assessment of 3D quantitative maps was determined on the basis of our Monte-Carlo simulations (Fig. 3). Data obtained during phantoms experiments validates this proof-of-concept acquisition set-up and demonstrates the feasibility of simultaneous multi-parametric quantitative extraction (Fig. 4). Indeed, estimated relaxation times at 21°C were consistent with the presented gold-standard measurements using respectively IR-

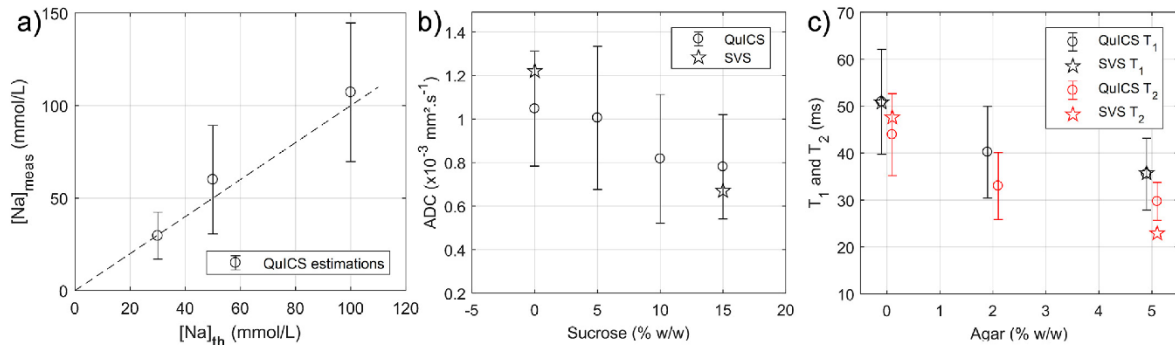


Fig. 5. a) Expected dilution and experimental estimations obtained with QuICS for realistic total ^{23}Na concentrations. Measured concentrations tend to align with the first bisector (dashed line). b) Estimated ADC values at 21°C for four phantoms of 150 mM NaCl and various sucrose mass fractions, with associated standard deviations. Results show a decreasing evolution of diffusion depending on sucrose concentration, confirming observations from [41,42,49] and DW-STEAM measurements. c) Estimated T_1 and T_2 for three phantoms of 150 mM NaCl and various agar concentrations. As expected, relaxation times are decreased when adding agar. SVS-measurements are consistent with the QuICS estimations.

LASER for T_1 and STEAM for T_2 assessments and with values from literature obtained using non-localized Inversion-Recovery and spin-echo sequences at 22 °C at 7 T [44].

Large physiological concentrations variations were also studied, with an extraction of TSC leading to precision better than 15%. Diffusion estimations for reference saline solution tube is consistent with the gold-standard measurements. Despite an extensive interest for ^{23}Na diffusion in food processing [45–47], sodium diffusion assessment could be found in the chemistry literature at $1.300 \pm 0.005 \times 10^{-3} \text{ mm}^2 \cdot \text{s}^{-1}$ using a conductimetric cell at 25 °C for a 50 mM saline solution [48]. This value is consistent with our estimations, as temperatures are in a similar range and concentration should have limited effect on diffusion. Here, modifying viscosity with sucrose reduced ADC, as verified in spectroscopy and observed in ^1H literature [49].

We succeeded in assessing a large range of total sodium concentrations, relaxations and ADCs. The environments investigated here are usually studied in literature to mimic various *in vivo* tissues, from cartilage to brain. The relatively high standard deviations obtained in Fig. 5b–d could be due to a low SNR from B_1^+ heterogeneity induced by the hemi-volumic Tx/Rx primate coil. The latter could be tackled using a birdcage coil to access the targeted angle more homogeneously. Simulations with lower SNR were also performed and demonstrate that a higher flip angle should be targeted in low SNR regions (See Supplementary Material).

^{23}Na has a peculiar sensitivity to its molecular environment through quadrupolar interactions. Therefore, its relaxation times exhibit bi-exponential curves in complex media such as tissues or agar gels. For T_1 relaxation, where short and long components accounts for respectively 20 and 80% of the ^{23}Na signal [50,51], the bi-exponential recovery is rarely observed, leading to the estimation of a mono-exponential T_1 ranging from 10 to 60 ms. For T_2 relaxation, the respective contributions of its long ($T_{2\text{ long}} \approx 15\text{--}60$ ms) and short ($T_{2\text{ short}} < 5$ ms) components are considered to be about 40 and 60% of the signal respectively (at zero TE). These bi-exponential or mono-exponential relaxation times varies *in vivo* depending on the investigated tissue [52,53], its intracellular and extracellular volume fractions, and the sodium levels in those two compartments [53,54]. The intracellular volume fraction is approximately 80% of the tissues with a sodium concentration of 10–15 mM, and the extracellular volume fraction is around 20%, with a sodium concentration of 125–150 mM. Like most ^{23}Na MRI approach aiming at the extraction of quantitative parameters, QuICS estimates apparent TSC, T_1 , total T_2 and ADC reflecting the weighted sum of all those short, long, intra and extracellular components depending on the chosen acquisition parameters. In our case, given the long TE of 3.2 ms, the total T_2 mainly reflects the long component of the T_2 . Nevertheless, if any of the intra/extra or long/short T_2 compartments encounters fluctuations related to the metabolic state of the tissue or varying molecular environment of the sodium ions, one may expect QuICS to exhibit sensitivity to such variations, as other single parameter ^{23}Na qMRI techniques have already shown.

While one could regret this rather poor specificity, QuICS should compensate this weakness by finding specificity in the correlation of the multiple complementary NMR parameters, helping in the interpretation of the physio-pathological events. It can be considered as an alternative paradigm of investigation for ^{23}Na data, comparable to strategies successfully applied with other simultaneous multi-parametric method in ^1H MRI [11,55], where the same kind of objections could be done regarding compartmentalization of water in biological tissues.

The experiments reported in this note present a proof-of-concept of the potential of QuICS approach to assess simultaneously a broad spectrum of ^{23}Na properties. To date, a combination of separate state-of-the-art TSC, T_1 and T_2 measurements at the spatial resolution we used is more competitive than what we propose [5–7]. Nevertheless, we add a very important parameter, namely the ADC, which has a strong clinical potential to characterize ^{23}Na micro-environment. Additionally,

acquisition time TA could be largely reduced in the future, performing an in-depth optimization of the acquisition protocol over FA, TR, N_{RO} , T_1 , T_2 and ADC ranges to study the sensitivity and robustness of the method. For example, ADC required high spoiling gradients (Fig. 3c). Using different N_{RO} , or equivalently different diffusion weighting b-values from one contrast to another, is expected to enhance the precision in the determination of the ADC coefficient [21]. In the present study, only single direction ADC measurements has been performed along the readout axis. This was enough in the context of homogeneous phantoms, to be extended to an average global ADC. *In vivo*, this will not be the case in the vast majority of the organs and several spoiling directions will be mandatory to properly extract this parameter. Limiting the TA will require to only focus on selecting the most valuable steps playing with FA, RF and gradient spoiling including for the latest several orthogonal directions. Such an optimization has been demonstrated to be achievable using optimal design approaches based on reducing the Cramér-Rao lower bound [56,57]. To reduce TA even more, non-Cartesian sampling sequence could be used to improve SNR. Combining such sampling strategy with a nonlinear iterative reconstruction algorithm would also provide an increase of SNR and enable sub-sampling to reduce TA [58–60]. These improvements would be at the cost of a broadening of the effective Point Spread Function (PSF) in the reconstructed image, which can be optimized depending on the targeted application. The use of a birdcage coil to access the targeted FA more homogeneously over the region of interest, combined with a received-phase array coil to retrieve more signal would also help increasing available signal and further reduce TA or increase resolution [61]. In the latter case, the sensitivity profile of the coil will be corrected using a post-processing algorithm to still be able to extract TSC [62]. SAR simulations were carried out considering a reference voltage consistent with *in vivo* acquisitions on a dual resonant 1Tx/1Rx birdcage coil. For *in vivo* applications, the pulse duration would need to be lengthened to 700 μs instead of 500 μs to respect SAR international standards.

5. Conclusion

In conclusion, this work is the first application of a simultaneous multi-parametric estimation method to ^{23}Na nucleus. The method showed its ability to retrieve varying ^{23}Na concentrations, total relaxation times evolution and ADC. Measured parameters were in range of previously reported values in the literature and effective gold-standard measurements. Current acquisitions will be improved to reduce TA and resolution, while increasing SNR with the goal of obtaining a clinically-relevant scan time. The simultaneous quantitative assessment of several NMR physical parameters could pave the way to a new diagnostic process, where correlations between different tissues properties might lead to improve the patient outcome [11,55].

Declarations of interest

None.

Acknowledgments

This work was partly funded by the French program “Investissement d’Avenir” run by the ‘Agence Nationale pour la Recherche’; the grant reference is ‘Infrastructure d’avenir en Biologie Santé - ANR-11-INBS-0006’.

Appendix A. Supplementary data

Supplementary data to this article can be found online at <https://doi.org/10.1016/j.mri.2018.07.012>.

References

- [1] Thulborn KR. Quantitative sodium MR imaging: a review of its evolving role in medicine. *NeuroImage* 2018;168:250–68. <https://doi.org/10.1016/j.neuroimage.2016.11.056>.
- [2] Schepkin VD, Bejarano FC, Morgan T, Gower-Winter S, Ozambela M, Levenson CW. In vivo magnetic resonance imaging of sodium and diffusion in rat glioma at 21.1 T. *Magn Reson Med* 2012;67:1159–66. <https://doi.org/10.1002/mrm.23077>.
- [3] Madelin G, Regatte RR. Biomedical applications of sodium MRI in vivo. *J Magn Reson Imaging* 2013;38:511–29. <https://doi.org/10.1002/jmri.24168>.
- [4] Jacobs MA, Ouwerkerk R, Kamel I, Bottomley PA, Kim HS. Proton, diffusion-weighted imaging, and sodium (^{23}Na) MRI of uterine leiomyomata after MR-guided high intensity focused ultrasound: a preliminary study. *J Magn Reson Imaging* 2009;29:649–56. <https://doi.org/10.1002/jmri.21677>.
- [5] Staroswiecki E, Nnewiwe A, Bangerter NK, Daniel BL, Hargreaves BA. In vivo sodium imaging and relaxometry of the breast at 3 T. *Proc. Intl. soc. mag. reson. med.* 17. 2009. p. 2129.
- [6] Morrell G, Kaggie J, Stein M, Parker S, Bangerter NK. Rapid high-resolution sodium relaxometry in human breast. *Proc. Intl. soc. mag. reson. med.* 24. 2016. p. 404.
- [7] Zbyn S, Juras V, Bogner W, Szomolanyi P, Welsch GH, Bitsansky M, et al. Sodium in vivo measurement of T1 and T2 ρ relaxation times of articular cartilage at 7 T. *Proc. Intl. soc. mag. reson. med.* 17. 2009. p. 3997.
- [8] Goodman JA, Kroenke CD, Bretthorst GL, Ackerman JHH, Neil JJ. Sodium ion apparent diffusion coefficient in living rat brain. *Magn Reson Med* 2005;53:1040–5. <https://doi.org/10.1002/mrm.20444>.
- [9] Babsky AM, Topper S, Zhang H, Gao Y, James JR, Hekmatyar SK, et al. Evaluation of extra- and intracellular apparent diffusion coefficient of sodium in rat skeletal muscle: effects of prolonged ischemia. *Magn Reson Med* 2008;59:485–91. <https://doi.org/10.1002/mrm.21568>.
- [10] Schmitt P, Griswold MA, Jakob PM, Kotas M, Gulani V, Flentje M, et al. Inversion recovery TrueFISP: quantification of T1, T2, and spin density. *Magn Reson Med* 2004;51:661–7. <https://doi.org/10.1002/mrm.20058>.
- [11] Warntjes JBM, Leinhard OD, West J, Lundberg P. Rapid magnetic resonance quantification on the brain: optimization for clinical usage. *Magn Reson Med* 2008;60:320–9. <https://doi.org/10.1002/mrm.21635>.
- [12] Ma D, Gulani V, Seiberlich N, Liu K, Sunshine JL, Duerk JL, et al. Magnetic resonance fingerprinting. *Nature* 2013;495:187–92. <https://doi.org/10.1038/nature11971>.
- [13] Heule R, Ganter C, Bieri O. Triple echo steady-state (TESS) relaxometry. *Magn Reson Med* 2014;71:230–7. <https://doi.org/10.1002/mrm.24659>.
- [14] Stöcker T, Keil F, Vahedipour K, Brenner D, Pracht E, Shah NJ. MR parameter quantification with magnetization-prepared double echo steady-state (MP-DESS). *Magn Reson Med* 2014;72:103–11. <https://doi.org/10.1002/mrm.24901>.
- [15] Warntjes JBM, Dahlqvist O, Lundberg P. Novel method for rapid, simultaneous T1, T2, and proton density quantification. *Magn Reson Med* 2007;57:528–37. <https://doi.org/10.1002/mrm.21165>.
- [16] Staroswiecki E, Granlund KL, Alley MT, Gold GE, Hargreaves BA. Simultaneous estimation of T2 and apparent diffusion coefficient in human articular cartilage in vivo with a modified three-dimensional double echo steady state (DESS) sequence at 3 T. *Magn Reson Med* 2012;67:1086–96. <https://doi.org/10.1002/mrm.23090>.
- [17] Gras V, Farrier E, Grinberg F, Shah NJ. Diffusion-weighted DESS protocol optimization for simultaneous mapping of the mean diffusivity, proton density and relaxation times at 3 T. *Magn Reson Med* 2017;78:130–41. <https://doi.org/10.1002/mrm.26353>.
- [18] Cloos MA, Knoll F, Zhao T, Block KT, Bruno M, Wiggins GC, et al. Multiparametric imaging with heterogeneous radiofrequency fields. *Nat Commun* 2016;7:12445. <https://doi.org/10.1038/ncomms12445>.
- [19] de Rochefort L. Method and device for imaging by magnetic resonance. 2016. (WO 2016/180947 A1).
- [20] de Rochefort L. Encoding with radiofrequency spoiling, equilibrium states and inverse problem for parametric mapping. *Proc. Intl. soc. mag. reson. med.* 23. 2015. p. 445.
- [21] de Rochefort L, Guillot G, Dubuisson R-M, Valabrégué R. In vivo feasibility of multiparametric mapping based on fast steady-state sequences. *Proc. Intl. soc. mag. reson. med.* 24. 2016. p. 1823.
- [22] Leroi L, de Rochefort L, Santin MD, Mauconduit F, Valabrégué R, de Sousa PL, et al. Simultaneous multiparametric quantitative extraction at 7 Tesla using QulCS. *European Society for Magnetic Resonance in Medicine*; 2016. p. 272.
- [23] Pohmann, Speck, Scheffler. Signal-to-noise ratio and MR tissue parameters in human brain imaging at 3, 7, and 9.4 Tesla using current receive coil arrays. *Magn Reson Med* 2015;75:801–9. <https://doi.org/10.1002/mrm.25677>.
- [24] Epstein FH, Mugler JP, Brookeman JR. Spoiling of transverse magnetization in gradient-echo (GRE) imaging during the approach to steady state. *Magn Reson Med* 1996;35:237–45. <https://doi.org/10.1002/mrm.1910350216>.
- [25] Pauly J, Roux PL, Nishimura D, Macovski A. Parameter relations for the Shinnar-Le Roux selective excitation pulse design algorithm. *IEEE Trans Med Imaging* 1991;10:53–65. <https://doi.org/10.1109/42.75611>.
- [26] Roux PL, Hinks RS. Stabilization of echo amplitudes in FSE sequences. *Magn Reson Med* 1993;30:183–90. <https://doi.org/10.1002/mrm.1910300206>.
- [27] Hennig J. Echoes—how to generate, recognize, use or avoid them in MR-imaging sequences. Part I: fundamental and not so fundamental properties of spin echoes. *Concepts Magn Reson* 1991;3:125–43. <https://doi.org/10.1002/cmr.1820030302>.
- [28] Hennig J. Echoes—how to generate, recognize, use or avoid them in MR-imaging sequences. Part II: echoes in imaging sequences. *Concepts Magn Reson* 1991;3:179–92. <https://doi.org/10.1002/cmr.1820030402>.
- [29] Scheffler K. A pictorial description of steady-states in rapid magnetic resonance imaging. *Concepts Magn Reson* 1999;11:291–304. [https://doi.org/10.1002/\(SICI\)1099-0534\(1999\)11:5<291::AID-CMR2>3.0.CO;2-J](https://doi.org/10.1002/(SICI)1099-0534(1999)11:5<291::AID-CMR2>3.0.CO;2-J).
- [30] Weigel M. Extended phase graphs: dephasing, RF pulses, and echoes - pure and simple. *J Magn Reson Imaging* 2015;41:266–95. <https://doi.org/10.1002/jmri.24619>.
- [31] Zur Y, Wood ML, Neuringer LJ. Spoiling of transverse magnetization in steady-state sequences. *Magn Reson Med* 1991;21:251–63. <https://doi.org/10.1002/mrm.1910210210>.
- [32] Ganter C. Steady state of gradient echo sequences with radiofrequency phase cycling: analytical solution, contrast enhancement with partial spoiling. *Magn Reson Med* 2006;55:98–107. <https://doi.org/10.1002/mrm.20736>.
- [33] Bieri O, Scheffler K, Welsch GH, Trattinnig S, Mamisch TC, Ganter C. Quantitative mapping of T2 using partial spoiling. *Magn Reson Med* 2011;66:410–8. <https://doi.org/10.1002/mrm.22807>.
- [34] de Sousa PL, Vignaud A, Caldas de Almeida Araújo E, Carlier PG. Factors controlling T2 mapping from partially spoiled SSFP sequence: optimization for skeletal muscle characterization. *Magn Reson Med* 2012;67:1379–90. <https://doi.org/10.1002/mrm.23131>.
- [35] Kaiser R, Bartholdi E, Ernst RR. Diffusion and field-gradient effects in NMR Fourier spectroscopy. *J Chem Phys* 1974;60:2966–79. <https://doi.org/10.1063/1.1681477>.
- [36] Freed DE, Scheven UM, Zielinski LJ, Sen PN, Hürlimann MD. Steady-state free precession experiments and exact treatment of diffusion in a uniform gradient. *J Chem Phys* 2001;115:4249–58. <https://doi.org/10.1063/1.1389859>.
- [37] Garwood M, Delabarre L. The return of the frequency sweep: designing adiabatic pulses for contemporary NMR. *J Magn Reson* 2001;153:155–77. <https://doi.org/10.1006/jmr.2001.2340>.
- [38] Slotboom J, Mehlkopf AF, Bovée WMMJ. A single-shot localization pulse sequence suited for coils with inhomogeneous RF fields using adiabatic slice-selective RF pulses. *J Magn Reson* 1991;95:396–404. [https://doi.org/10.1016/0022-2364\(91\)90229-M](https://doi.org/10.1016/0022-2364(91)90229-M).
- [39] van Zijl PC, Moonen CT, Alger JR, Cohen JS, Chesnick SA. High field localized proton spectroscopy in small volumes: greatly improved localization and shimming using shielded strong gradients. *Magn Reson Med* 1989;10:256–65.
- [40] Moonen CTW, Sobering G, van Zijl PCM, Gillen J, von Kienlin M, Bizzi A. Proton spectroscopic imaging of human brain. *J Magn Reson* 1992;98:556–75. [https://doi.org/10.1016/0022-2364\(92\)90007-T](https://doi.org/10.1016/0022-2364(92)90007-T).
- [41] Hara M, Kuroda M, Ohmura Y, Matsuzaki H, Kobayashi T, Murakami J, et al. A new phantom and empirical formula for apparent diffusion coefficient measurement by a 3 Tesla magnetic resonance imaging scanner. *Oncol Lett* 2014;8:819–24.
- [42] Winfield JM, Collins DJ, Priest AN, Quest RA, Glover A, Hunter S, et al. A framework for optimization of diffusion-weighted MRI protocols for large field-of-view abdominal-pelvic imaging in multicenter studies. *Med Phys* 2016;43:95–110. <https://doi.org/10.1118/1.4937789>.
- [43] Hoult DI. The principle of reciprocity in signal strength calculations—a mathematical guide. *Concepts Magn Reson* 2000;12:173–87. [https://doi.org/10.1002/1099-0534\(2000\)12:4<173::AID-CMR1>3.0.CO;2-Q](https://doi.org/10.1002/1099-0534(2000)12:4<173::AID-CMR1>3.0.CO;2-Q).
- [44] Nagel AM, Umthum R, Rösler MB, Ladd ME, Litvak I, Gorkov PL, et al. ^{39}K and ^{23}Na relaxation times and MRI of rat head at 21.1 T. *NMR Biomed* 2016;29:759–66. <https://doi.org/10.1002/nbm.3528>.
- [45] Hansen CL, van der Berg F, Ringgaard S, Støckilde-Jørgensen H, Karlsson AH. Diffusion of NaCl in meat studied by ^1H and ^{23}Na magnetic resonance imaging. *Meat Sci* 2008;80:851–6. <https://doi.org/10.1016/j.meatsci.2008.04.003>.
- [46] Bertram HC, Holdsworth SJ, Whittaker AK, Andersen HJ. Salt diffusion and distribution in meat studied by ^{23}Na nuclear magnetic resonance imaging and relaxometry. *J Agric Food Chem* 2005;53:7814–8. <https://doi.org/10.1021/jf051017+>.
- [47] Guhenneuf TM, Gibbs SJ, Hall LD. Measurement of the inter-diffusion of sodium ions during pork brining by one-dimensional ^{23}Na magnetic resonance imaging (MRI). *J Food Eng* 1997;31:457–71. [https://doi.org/10.1016/S0260-8774\(96\)00085-4](https://doi.org/10.1016/S0260-8774(96)00085-4).
- [48] Ribeiro ACF, Lobo VMM, Sobral AJFN, Soares HTFC, Esteso ARJ, Esteso MA. Diffusion coefficients of sodium fluoride in aqueous solutions at 298.15 K and 310.15 K. *Acta Chim Slov* 2010;57:410–4.
- [49] Laubach HJ, Jakob PM, Loeblad KO, Baird AE, Bovo MP, Edelman RR, et al. A Phantom for diffusion-weighted imaging of acute stroke. *J Magn Reson Imaging* 1998;8:1349–54. <https://doi.org/10.1002/jmri.1880080627>.
- [50] Jaccard G, Wimperis S, Bodenhausen G. Multiple-quantum NMR spectroscopy of S = 3/2 spins in isotropic phase: a new probe for multiexponential relaxation. *J Chem Phys* 1986;85:6282–93. <https://doi.org/10.1063/1.451458>.
- [51] Zhang Y, Poirer-Quinot M, Springer CS, Balschi JA. Discrimination of intra- and extracellular $^{23}\text{Na}^+$ signals in yeast cell suspensions using longitudinal magnetic resonance relaxography. *J Magn Reson* 2010;205:28–37. <https://doi.org/10.1016/j.jmr.2010.03.018>. (San Diego Calif).
- [52] Ridley B, Nagel AM, Bydder M, et al. Distribution of brain sodium long and short relaxation times and concentrations: a multi-echo ultra-high field ^{23}Na MRI study. *Sci Rep* 2018;8:4357. <https://doi.org/10.1038/s41598-018-22711-0>.
- [53] Foy BD, Burstein D. Interstitial sodium nuclear magnetic resonance relaxation times in perfused hearts. *Biophys J* 1990;58:127–34. [https://doi.org/10.1016/S0006-3495\(90\)82358-4](https://doi.org/10.1016/S0006-3495(90)82358-4).
- [54] Hutchison Robert B, Shapiro Joseph I. Measurement of intracellular sodium with NMR methods. *Concepts Magn Reson* 1991;3:215–36. <https://doi.org/10.1002/cmr.1820030404>.
- [55] Yu AC, Badve C, Ponsky LE, et al. Development of a combined MR fingerprinting and diffusion examination for prostate cancer. *Radiology* 2017;283:729–38. <https://doi.org/10.1148/radiol.2017161599>.
- [56] Valabrégué R, de Rochefort L. Fisher information matrix for optimizing the

- acquisition parameters in multi-parametric mapping based on fast steady-state sequences. *Proc. intl. soc. mag. reson. med.* 24. 2016. p. 1569.
- [57] Zhao B, Haldar JP, Setsompop K, Wald LL. Optimal experiment design for magnetic resonance fingerprinting. 38th annual international conference of the IEEE engineering in medicine and biology society (EMBC) 2016. p. 453–6. <https://doi.org/10.1109/EMBC.2016.7590737>.
- [58] Coste A, Chauffert N, Vignaud A, Ciuciu P, Boumezeur F, Weiss P, et al. Assessment of benefit to use a non-Cartesian trajectory and nonlinear reconstruction method compared to a Cartesian strategy for fast 31P MRI. *Proc. intl. soc. mag. reson. med.* 24. 2016. p. 3940.
- [59] Madelin G, Chang G, Otazo R, Jerschow A, Regatte RR. Compressed sensing sodium MRI of cartilage at 7T: preliminary study. *J Magn Reson* 2012;214:360–5. <https://doi.org/10.1016/j.jmr.2011.12.005>.
- [60] Gnahn C, Nagel AM. Anatomically weighted second-order total variation reconstruction of ^{23}Na MRI using prior information from ^1H MRI. *NeuroImage* 2015;105:452–61. <https://doi.org/10.1016/j.neuroimage.2014.11.006>.
- [61] Shajan G, Mirkes C, Buckenmaier K, Hoffmann J, Pohmann R, Scheffler K. Three-layered radio frequency coil arrangement for sodium MRI of the human brain at 9.4 Tesla. *Magn Reson Med* 2016;75:906–16. <https://doi.org/10.1002/mrm.25666>.
- [62] Santin MD. Pending Patent, #1759804/1000427656.

Appendix 2: Kerker Effect in Ultrahigh-Field Magnetic Resonance Imaging

Kerker Effect in Ultrahigh-Field Magnetic Resonance Imaging

Marc Dubois,¹ Lisa Leroi,² Zo Raolison,² Redha Abdeddaim,^{1,*} Tryfon Antonakakis,³ Julien de Rosny,⁴ Alexandre Vignaud,² Pierre Sabouroux,¹ Elodie Georget,^{2,†} Benoit Larrat,² Gérard Tayeb,¹ Nicolas Bonod,¹ Alexis Amadon,² Franck Mauconduit,⁵ Cyril Poupon,² Denis Le Bihan,² and Stefan Enoch^{1,‡}

¹Aix Marseille Univ, CNRS, Centrale Marseille, Institut Fresnel, 13013 Marseille, France

²CEA, DRF, JOLIOT, NeuroSpin, UNIRS, Université Paris-Saclay, 91191 Gif-sur-Yvette Cedex, France

³Multiwave Innovation AG, 1228 Geneva, Switzerland

⁴ESPCI Paris, PSL Research University, CNRS, Institut Langevin, 75005 Paris, France

⁵Siemens Healthineers, 93210 Saint Denis, France

 (Received 27 April 2018; revised manuscript received 26 July 2018; published 27 September 2018)

Ultrahigh-field (UHF) magnetic resonance imaging (MRI) systems are getting a lot of attention as they ensure high intrinsic signal-to-noise ratio resulting in higher spatial and temporal resolutions as well as better contrast. This promises improved clinical results with regard to morphological as well as functional and metabolic capabilities. Traditionally, MRI relies on volume coils (birdcage) able to deliver a homogeneous radio frequency field exciting the nuclei magnetic spin. However, this strategy is hindered at UHF because of the rf field inhomogeneities yielded by the increased Larmor frequency. A standard approach consists of inserting passive dielectric elements within the volume coil in order to locally enhance the rf field and mitigate these inhomogeneities. However, the lack of control over their electromagnetic properties prevents the development of optimal solutions. Here, a single meta-atom is used to achieve efficient and tunable rf field control in UHF MRI. We demonstrate theoretically and experimentally a full overlap between the electric dipolar and magnetic dipolar resonances of the meta-atom. This interaction is precisely tuned to reach the so-called Kerker scattering conditions when illuminated in the near field by a birdcage coil. At these conditions, a strong enhancement or suppression of the rf field is achieved in the vicinity of the meta-atom within the MRI volume coil.

DOI: [10.1103/PhysRevX.8.031083](https://doi.org/10.1103/PhysRevX.8.031083)

Subject Areas: Metamaterials

I. INTRODUCTION

Since its discovery in the early 1970s, magnetic resonance imaging (MRI) scanners have become one of the most efficient diagnostic tools available for medical imaging. Also, over time, their magnetic field strength (B_0) has been steadily increased to enhance signal-to-noise ratio (SNR) [1]. Such a gain could be used to improve image sensitivity and spatial and/or temporal resolutions. Ultrahigh-field (UHF) MRI ($B_0 \geq 7$ T) is identified as a potential candidate to detect early symptoms of serious neurodegenerative pathologies such as Alzheimer's disease [2]. This increasing B_0 induces a proportional increase of the Larmor or precessional frequency of the nucleus spin

and a decrease of the corresponding wavelength (λ_0) for the radio-frequency excitation field. Consequently, the typical human body size (diameter of the head is around 16 cm) becomes non-negligible compared to the wavelength (λ at 7 T is equal to 11 cm in the body) and interferences can occur leading to bright and dark zones. At 7 T, rf field distribution in the human head presents a bright center and a weak periphery when transmit volume coils are used [Fig. 1(a)] [3]. This induces locally major losses in contrast or shadowing on the images depending on the MR acquisition strategy [white arrows in Figs. 1(b) and 1(c)]. Note that these losses appear in regions where the rf field drops below a threshold value around 40% of the maximum value. Such artifacts make UHF MRIs inadequate for several diagnostic purposes and represent a major bottleneck for a global application to the clinical environment.

Different approaches have been proposed to tackle this problem. The first one consists of using high dielectric constant pads surrounding the region of interest to locally enhance the rf field [4,5]. Unfortunately, major drawbacks prevent their use in high-field clinical routine: performance decay over time and ecotoxicity of the active substances used conventionally [6].

*redha.abdeddaim@fresnel.fr

†Now at: Multiwave Innovation, Marseille, France.

‡stefan.enoch@fresnel.fr

Published by the American Physical Society under the terms of the *Creative Commons Attribution 4.0 International license*. Further distribution of this work must maintain attribution to the author(s) and the published article's title, journal citation, and DOI.

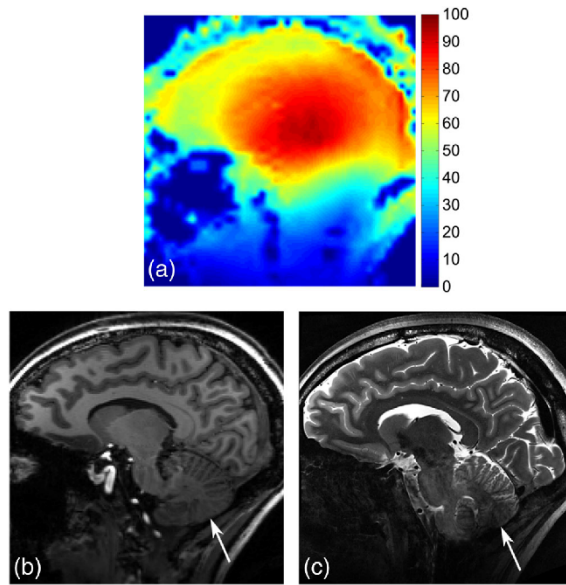


FIG. 1. 7 T sagittal MR images of a human brain slice obtained with various acquisition sequences: (a) Flip-angle ($FA \propto B_1^+$) map acquired using the actual flip-angle imaging sequence (color bar in degree). (b) T1-weighted magnetization-prepared rapid gradient echo sequence. (c) T2-weighted turbo spin echo sequence. Those images have been acquired with a birdcage coil for excitation and a 32-loops phased array for reception. Notice (a) the large B_1^+ field heterogeneity over the head (dispersion of $\sim 30\%$). When FA is too far from the target, as is the case here in the cerebellum (white arrows), it leads to loss in contrast (b) or even worse to shadowing (c) depending on the acquisition strategy.

Another solution, called parallel rf transmission, has been introduced. It consists in placing several independent rf transmitters around the subject, instead of a single one on standard MR systems. Taking advantage of rf interference and dynamic modulation during the excitation, it is possible to obtain a much more homogeneous excitation [7]. These additional degrees of freedom provide a better control of the magnetization but also raise challenging problems in terms of workflow and safety. None of the solutions described above has been fully satisfactory for UHF MRI. To date, only the single transmit channel volume coil has received approval for 7 T MRI clinical applications [8].

Recently, metamaterials have been introduced to control rf fields in the MRI context. Metamaterials are composite materials, most often made of resonant cells, whose effective properties mimic a homogeneous material that is not available in nature. Several implementations of metamaterials have been used to homogenize the field, enhance the SNR and the penetration depth for moderate field MRI [9–16] and to a lesser extent for UHF MRI to enhance performances and the decoupling of surface coils [13,17–20]. However, none of these works has tackled the problem of the field

inhomogeneity in UHF MRI volume coils. The latest developments propose to merge a metamaterials approach and high permittivity dielectric materials in order to access multiple degrees of freedom for the local enhancement of the rf field in MRI volume coils [21].

A crucial aspect for the control of radiation lies in the ability to tailor simultaneously the electric and magnetic responses of a single scatterer. This was first theoretically envisioned by Kerker *et al.* [22]: for a particle with specific values of permittivity and permeability, the fields scattered by the induced electric and magnetic dipoles can interfere, thus leading to strong scattering anisotropy. This scattering anisotropy was recently measured in the microwave regime [23] and is referred to as first and second Kerker conditions corresponding to a zero backward scattering and a near-zero forward scattering depending on the excitation frequency. The Kerker conditions can also be extended to the case of a near-field excitation when considering an electric dipole emitter coupled with a scatterer with strong electric and magnetic responses [24]. We want to take advantage of this physical effect in the rf range in order to control the rf field distribution in a MRI volume coil. However, the large dielectric constant required and the lack of space between the coil and the subject led us to dismiss the use of dielectric materials.

In this paper, we propose a new passive method based on metamaterials to improve the rf field control in UHF volume coils. We demonstrate that the rf field distribution of a birdcage coil can be controlled by inserting a meta-atom between the sample and the coil. A meta-atom can be designed using a single resonator element to build up a more complex unit cell using a coupling mechanism [25]. The meta-atom considered is based on a set of four hybridized resonant metallic wires. It is referred to as a hybridized meta-atom (HMA) in the following. First, we use an analytic approach based on impedance matrices in order to characterize the hybridization mechanism and derive the Kerker conditions. This model is used to describe the interaction between the HMA and a plane wave excitation as well as a near-field excitation (i.e., birdcage coil). Finally, we demonstrate experimentally that the HMA can controllably redistribute and reshape the rf electromagnetic field within a commercial birdcage coil in a 7 T MRI scanner.

II. RESULTS

A. Kerker conditions from HMA with far-field illumination

A structure composed of several coupled resonators will present a new set of hybrid resonances. This effect is particularly striking when strong near-field coupling occurs as the distance between resonators decreases with respect to the wavelength considered. We apply this strategy in order to design our HMA structure with strong electric and

magnetic effective induced dipoles. It is composed of four z -oriented thin metallic wires located at the corners of a rectangle of sides $d_1 = 1.5$ cm and $d_2 = 2$ cm. A single wire mainly interacts with the electric field along its axis and presents an electric resonance when its length approaches a multiple of half a wavelength. However, when several wires are used with subwavelength separation, the coupling or hybridization between the wires cannot be neglected when describing the response of the whole structure. Scattering and interactions of electromagnetic fields with objects are often characterized by the electric and magnetic polarizabilities. Although it is useful while studying scattering from Mie particles [26], the impedance matrix approach borrowed from the antenna community is well suited for our problem. This approach is based on the derivation of the impedance matrix Z_{ij} of the system, where i and j stand for the resonators' indexes. This matrix connects the different currents and voltages present in every element of the array and can be used to predict the behavior of complex arrangements of resonators [27]. The diagonal elements of this matrix give the self-impedance of each isolated wire whereas the off-diagonal elements are the mutual impedances between the wires. This mutual impedance represents the open circuit voltage induced on a wire if one of its neighbors is excited. Thus, the contribution of the near field to the mutual impedance directly depends on the separation distance between the wires considered. As we consider only wires of length shorter than a full wavelength (almost 1 m at 297.2 MHz), we can assume that the current along z is a sinusoidal function as in Eq. (1):

$$I(z) = I_0 \frac{\sin[k(\frac{L}{2} - |z|)]}{\sin(k\frac{L}{2})}. \quad (1)$$

Within this assumption, one can calculate the self- and mutual impedances of the system from a standard analytical derivation described in Eq. (2), where E_{ij} corresponds to the z component of the electric field produced by the wire j along the wire i :

$$Z_{ij} = -\frac{1}{I_{0i}I_{0j}} \int_{-L/2}^{L/2} E_{ij}(z) I_i(z) dz. \quad (2)$$

The analytical derivation of Eq. (2) is described in full detail in the Supplemental Material [28]. Once all the Z -matrix elements are evaluated, it is possible to access the electrical currents on every wire for a given driving voltage (currents and voltages are vectors) with the relation $I = Z^{-1}V$. As we would like to characterize the response of passive wires (i.e., short-cut antenna), it is necessary to introduce a fifth wire represented in green in the sketch in Fig. 2(a) as a driven element while the HMA wires remain passive. In this specific case, the Z matrix is a 5×5 matrix that can be computed at a frequency of 297.2 MHz (Larmor

frequency of the hydrogen nucleus at 7 T). When placed in the far field of the HMA, the driven element acts as a plane wave source. We can access the current amplitude and phase in each wire of the HMA by inverting the Z matrix and use $V = [1; 0; 0; 0; 0]$ as a voltage input (indices from 2 to 5 represent the short-cut HMA wires). A final step consists of calculating the radiated power P_{rad} from the HMA. This requires the complex current and the positions of the HMA wires yet again assuming sinusoidal current distribution along z . We first calculate the radiation intensity $U(\theta, \phi)$ from the four HMA wires and then perform the integration over all solid angles to obtain the total radiated power P_{rad} :

$$U(\theta, \phi) = \frac{1}{8\pi^2 c \epsilon_0} \left| \sum_{p=2}^5 I_p \frac{\cos(k\frac{L}{2} \cos \theta) - \cos(k\frac{L}{2})}{\sin(k\frac{L}{2}) \sin \theta} \times e^{jk \sin \theta (x_p \cos \phi + y_p \sin \phi)} \right|^2, \quad (3)$$

$$P_{\text{rad}} = \int_0^\pi \int_0^{2\pi} U(\theta, \phi) \sin \theta d\theta d\phi. \quad (4)$$

As shown in Fig. 2(b), we calculate the power radiated by the HMA (solid red line) as a function of the wire length for a given plane wave excitation. A control case is done with a single wire located at the origin. One can observe that the HMA response shows two maxima, each one associated with a different hybrid resonance. The first broad peak at 0.47 m corresponds to the excitation of a dipolar electric mode where the four wires are excited in phase with the same amplitude (i.e., symmetric mode). The second sharp peak at 0.5 m corresponds to a dipolar magneticlike mode where the currents between the wires in $y = 0$ and $y = d_2$ are out of phase (i.e., antisymmetric mode). Because of the strong coupling within the HMA, the magnetic dipolar resonance presents a very high quality factor. On the other hand, the electric dipolar resonance of the HMA is significantly wider than the one obtained from a single wire. The structure of these hybrid resonances has been described previously for single magnetic mode volume coil applied to small animal MRI [17].

Interactions of electric and magnetic modes help to gain control over the electromagnetic fields. Recent studies have put stress on backward and forward scattering control [23,26], near-field to far-field control, and possibilities opened for antennas [24]. Such a control over the scattered field requires the existence of two overlapping modes, which excludes single electric dipole coils or magnetic dipole coils [Fig. 2(b)]. These works follow a path opened by the seminal paper published by Kerker *et al.* [22]. Although most of these studies have considered dielectric resonators, we show here that we can obtain the same effect using HMA. In the case of dielectric resonators, specific

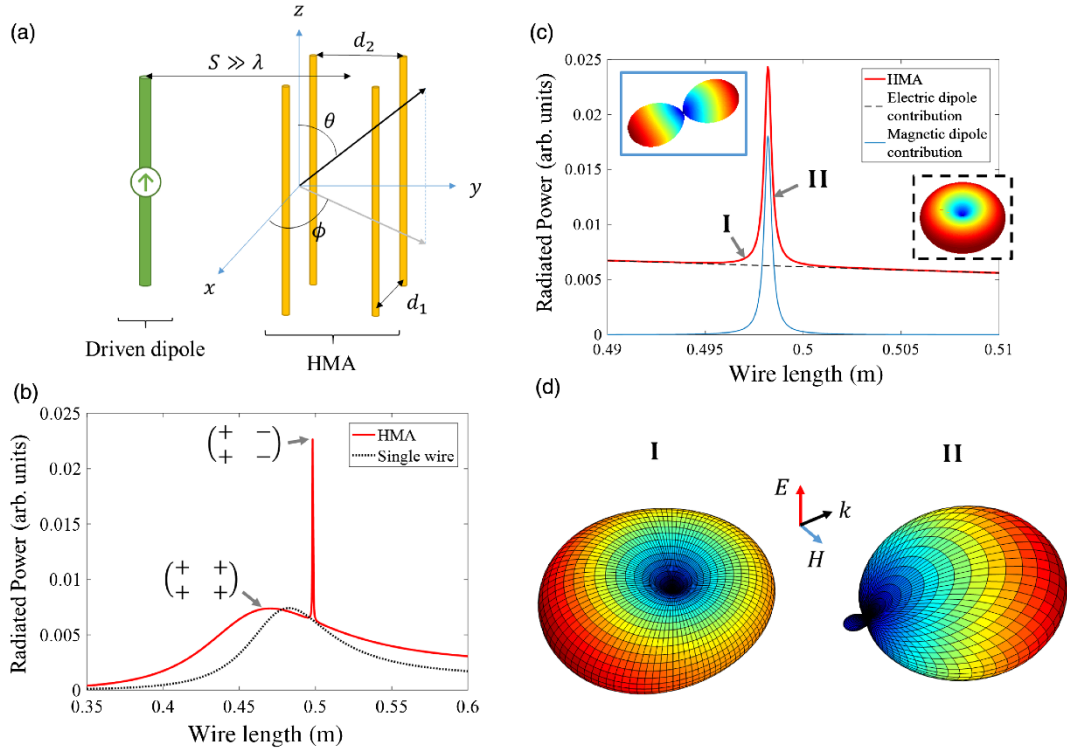


FIG. 2. (a) Sketch of the HMA configuration. Four metallic wires oriented along z are placed at the four corners of a rectangle of sides $d_1 = 1.5$ cm and $d_2 = 2$ cm. A fifth wire is used as a source located at a distance S large compared to the wavelength at 297.2 MHz. Such a configuration allows us to study the response of the HMA with a plane wave excitation. All wires have a diameter of 2 mm. (b) Radiated power from the HMA (solid red line) as a function of the wire length (excitation frequency 297.2 MHz is kept constant) is compared with the power radiated by a single wire (dashed black line) of the same varying length. The inset shows the phase of the current within the four wires of the HMA. This is evidence of the hybridization mechanism leading to a broad dipolar electric resonance and a sharp magnetic dipolar resonance. (c) Radiated power from the HMA on a narrow window (solid red line). Dashed black line and solid thin blue line show the isolated contributions of the two resonances excited in the HMA. The two insets show the radiation pattern of the magnetic dipolar resonance and the electric dipolar resonance. (d) Far-field radiation pattern at the two Kerker conditions (HMA lengths denoted above). The first one presents a reduction of the forward scattered field while a cancellation of the backward scattered field is observed at the second position.

index of refraction and diameter are required to control the number of excited modes and their overlap [24]. The dimensions and the spacing of the wires in our HMA structure are carefully chosen to obtain analog behavior. In our theoretical framework, the intensity radiated in the forward and backward directions is obtained with $\phi = \pi/2$ and $\theta = \pm\pi/2$, respectively; they are derived from Eq (3):

$$U_{\text{fwd,bwd}} = \frac{|\sum_{p=2}^N Z_{1p}^{-1} e^{\pm j\gamma_p}|^2}{8\pi^2 c \epsilon_0 \tan^2(k \frac{L}{2})}. \quad (5)$$

As shown in Fig. 2(c), we can separate the response of the HMA onto the two different resonant contributions within the length range where these two modes coexist. The insets in Fig. 2(c) show the two radiation patterns obtained when the contributions are isolated. The electric dipolar resonance resembles a donut as the current distribution is

invariant by rotation around the z axis. This is not the case for the magnetic dipolar resonance, which shows a variation on both angles. Strong scattering anisotropy is obtained when these two behaviors are combined for wire lengths of 49.6 and 49.8 cm [Fig. 2(d)], due to interference between the two overlapping resonances. These specific lengths correspond to the Kerker conditions: a reduction of the forward scattering (49.6 cm) and a cancellation of the backward scattering (49.8 cm). They are obtained for precise interaction of electric and magnetic responses within the HMA. A detailed derivation of the conditions based on the existence of electric and magnetic dipolar modes in dielectric particles can be found in Ref. [26]. This is the first demonstration of scattering anisotropy or Kerker conditions from a single HMA. The following demonstrates that these Kerker conditions can be used to control the rf field distribution in a birdcage MRI volume coil.

B. Control of rf field within the MRI volume coil

A sketch of the considered geometry is presented in Fig. 3(a). Our birdcage model is composed of 16 z -oriented wires (called legs) of length 28 cm equally spaced on a cylinder of radius 13 cm. The HMA is located at a distance $S = 2.5$ cm of the rightmost birdcage leg. As explained in the Introduction, the magnetic spin of hydrogen is sensitive to the B_1^+ component of the magnetic field. This polarization is obtained while working in the rotating frame at the Larmor frequency considered. In the following, we use the convention $B_1^+ = 1/2[B_x + iB_y]$. Birdcage coils have been mostly used for their ability to provide a highly homogeneous B_1^+ distribution when driven in quadrature. The current on each leg I_i is described as $I_i = I_0[\cos(\theta_i) - i\sin(\theta_i)]$, with $\theta_i = \{[2\pi(i-1)]/N\}$, and N the total number of legs. Knowing the current within each leg, we are able to calculate the B_1^+ distribution using the Biot-Savart formulation [29]. Details of the derivation are presented in the Supplemental Material [28].

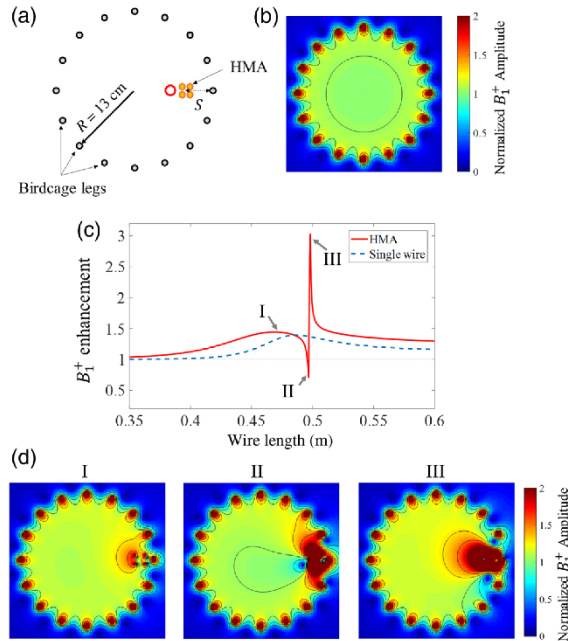


FIG. 3. (a) Sketch of the considered geometry for the insertion of the HMA inside a birdcage model. The birdcage is composed of 16 legs on a 26-cm-diameter cylinder. The legs are 28 cm long and the HMA is located at $S = 2.5$ cm from the first leg. Red circle denotes the ROI for the B_1^+ enhancement plot. (b) B_1^+ amplitude calculated in a quadrature driven empty birdcage. (c) B_1^+ enhancement in the ROI with respect to the empty birdcage in function of the HMA length. The solid red line corresponds to the HMA and the blue dashed line corresponds to the single wire case. (d) Calculated B_1^+ amplitude maps with the HMA for three lengths of interest shown in (c), respectively, 47.5, 49.6, and 49.8 cm.

$$B(x, y) = \begin{pmatrix} B_x \\ B_y \end{pmatrix} = \frac{I\mu_0}{4\pi(x^2 + y^2)\sqrt{x^2 + y^2 + \frac{L^2}{4}}} \begin{pmatrix} yL \\ -xL \end{pmatrix}. \quad (6)$$

These equations give the in-plane components of the magnetic field obtained in the median plane of a z -oriented thin wire of length L located in $(0,0)$. The Biot-Savart quasistatic approximation is valid with an empty birdcage coil as the diameter represents a quarter of the wavelength. The amplitude of B_1^+ is shown in Fig. 3(b); it is used as a reference value. In order to obtain the currents on the HMA wires, we derive the impedance matrix when considering that the driven element is in the near field of the HMA ($S = 2.5$ cm). Once we have the current distribution of the HMA, we can use Eq. (6) to calculate the magnetic field produced by the 16 birdcage legs and the four HMA wires with varying lengths. Then, a coherent sum of all the magnetic fields is realized before extracting the amplitude of B_1^+ . The results for varying HMA lengths are presented in Figs. 3(c) and 3(d). The graph shows the B_1^+ enhancement in the region of interest (ROI) delimited in the sketch (the red circle is 1 cm away from the HMA). The B_1^+ amplitude maps are given for three specific HMA lengths labeled on the solid red line. Once again we can observe a broad enhancement (+50%) of the B_1^+ field close to the HMA between 40 and 49 cm. A sharp resonant effect is observed around 50 cm which shows a cancellation of the B_1^+ amplitude at 49.6 cm followed by a threefold increase of the B_1^+ amplitude close to the HMA at 49.8 cm. These calculations demonstrate that the HMA scattering properties have a significant impact on the circularly polarized B_1^+ near-field amplitude in the birdcage coil. It is also very clear that the mode hybridization occurring in the HMA structure outperforms the single wire case in terms of bandwidth and enhancement factor. Moreover, the enhancement and the reduction of the B_1^+ amplitude both have a valuable impact on the MRI acquisition: it offers the ability to measure areas of the head which did not receive enough power initially and can also reduce the amplitude in the overexposed area that could potentially present safety issues [30].

C. Experimental demonstration of Kerker conditions in MRI

MRI acquisition can be affected by a combination of many parameters, such as the size, the shape, and the relative permittivity of the subject. First, we decide to use a spherical phantom with low permittivity in order to strictly validate the theoretical behavior of the HMA. We realized a set of telescopic resonators made of four coupled metallic rods (radius equal to 0.5 mm) located at the corners of a rectangle of sides $d_1 = 1.5$ cm and $d_2 = 2$ cm. The length of the HMA can be tuned between 20 and 100 cm. The telescopic configuration and the size of the HMA were

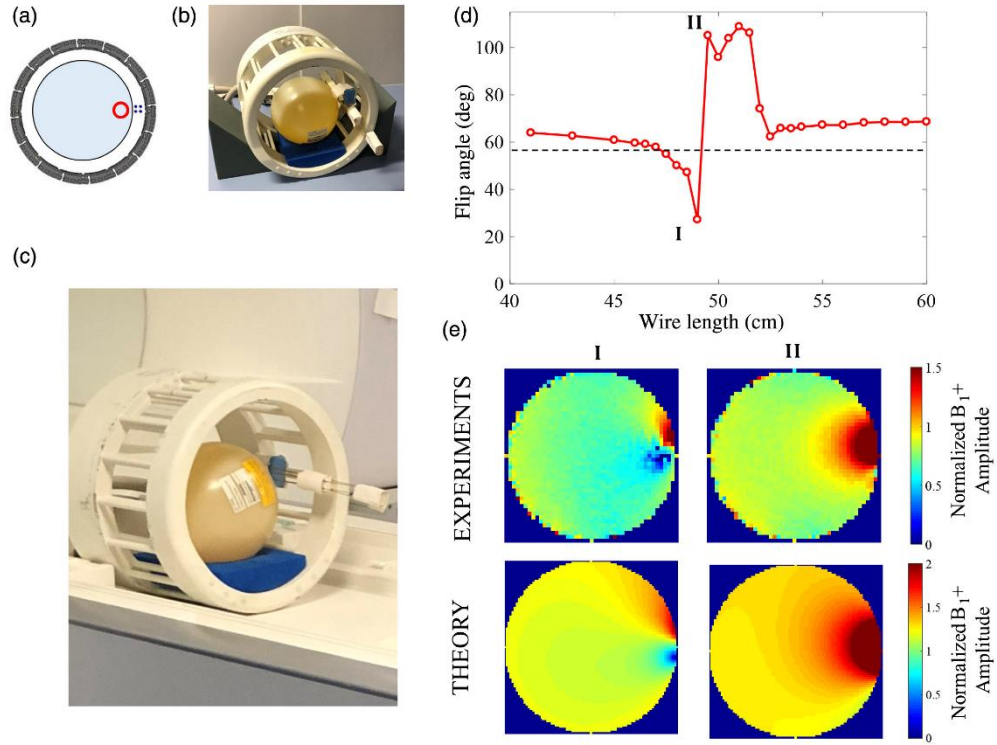


FIG. 4. (a) Schematic view of experimental configuration inside the 7 T MRI: birdcage coil (dark gray), HMA (4 blue rods), and oil phantom $\epsilon_r = 3.4$ (light gray). (b),(c) Pictures of the experimental setup, positioning of the HMA in the birdcage coil and into the MRI scanner. (d) Average flip-angle magnitude in the ROI [red circle in (a)] as a function of the HMA length. The dashed line indicates the reference value (without HMA). (e) Top: Normalized axial B_1^+ maps measured for two lengths of interest, namely, 49 and 49.5 cm. Each corresponds to the Kerker conditions with an enhancement or cancellation of the B_1^+ field close to the HMA. Bottom: Normalized field maps obtained from the theoretical calculations for the two Kerker conditions. HMA length from left to right at the calculated Kerker conditions (49.6 and 49.8 cm, respectively). A circular mask is applied to reproduce the phantom dimensions.

selected to keep the same configuration in all the experiments (i.e., to have continuously varying configurations). Experiments were performed using a birdcage head coil 1Tx/1Rx (Invivo Corp., Gainesville, FL) and a 16-cm-diameter spherical phantom filled with oil [Fig. 4(b)] on a 7 T Magnetom MRI (Siemens Healthineers, Erlangen, Germany) [Fig. 4(c)]. A sketch of the experimental configuration is given in Fig. 4(a). B_1^+ maps were acquired with a magnetization-prepared turbo-Fast Low Angle Shot sequence (XFL) [31] with varying HMA lengths. In order to quantify the effect of the HMA, we have defined a ROI depicted by a red circle in Fig. 4(a). The images were acquired for 30 different lengths of the HMA (all images are shown in Supplemental Material [28]) and we have computed the averaged flip-angle values (proportional to B_1^+) in the ROI for each length. Figure 4(d) shows the obtained values of averaged flip angle with respect to the length, while the dashed line shows the averaged value in the same region without HMA. When the HMA is present we observe an increase of B_1^+ field in the phantom on the right, i.e., near the HMA. This effect is related to the

increase of the local magnetic field when a resonant mode is excited. When the length is further tuned, we are able to decrease drastically the B_1^+ field when the backward scattering condition is reached at a length equal to 49 cm. Then we observe an even stronger increase in the near B_1^+ field at the forward scattering condition length (49.5 cm). The experimental results are compared to theoretical prediction and show a very good agreement which confirms our interpretation of the HMA behavior.

D. rf inhomogeneities reduction in realistic phantoms

In this experimental section, we demonstrate that the HMA can reduce the rf field inhomogeneities when inserted close to a phantom reproducing the electromagnetic behavior of the human body. We use a 16-cm-diameter sphere filled with an agar-agar gel with high permittivity $\epsilon_r = 74.2$ and high conductivity $\sigma = 0.87$ S/m. The B_1^+ distribution observed is highly inhomogeneous with a maximum at the center surrounded by a ringlike minimum region when measured with the birdcage alone [Fig. 5(b)]. This illustrates

the impact of the wavelength reduction in the human body, as previously described in the Introduction (Fig. 1). A sketch of the experimental configurations is given in Fig. 5(a). The HMA is located on the right-hand side of the phantom, and three ROIs are highlighted. The black circle corresponds to the whole phantom while the green and red circles are located in the center and in the vicinity of the HMA, respectively. B_1^+ maps are measured with varying HMA lengths between 30 and 60 cm with the same telescopic metallic wires. Figure 5(c) presents the B_1^+ maps obtained for two lengths of interest corresponding to the maximum (at 46.5 cm) and minimum (at 49.5 cm) B_1^+ amplitude in the vicinity of the HMA. The resonances within the HMA structure are responsible for the enhancement and the cancellation of the local B_1^+ amplitude. More importantly than the local

enhancement, the presence of the HMA also affects the amplitude of the central spot which is highly beneficial to the homogeneity of the rf field. This effect is clearly perceived in Fig. 5(d), representing the field average in the three ROIs depicted in Fig. 5(a). Indeed, one can see that the values averaged in the central spot (green line) and in the vicinity of the HMA (red line) are equal for a HMA length of 46.5 cm. Moreover, Fig. 5(c) shows that the B_1^+ amplitude is homogeneous in the area between the HMA and the center of the sphere, contrary to the strong dispersion of values obtained with the birdcage alone denoted by the dashed line in Fig. 5(d). Note that this control over the rf field distribution does not perturb the matching of the birdcage coil. The measured total transmitted power at a constant input voltage (133 V) decreases by 2% at 46.5 cm length, whereas it reaches a minimum of 6% at 49.5 cm length. This result clearly demonstrates our ability to reduce the dispersion of the rf field amplitude in the phantom without inducing perturbations over the original coil properties.

Finally, we perform a comparison of the performances obtained on a specific anthropomorphic mannequin (SAM) phantom (SPEAG, Zurich, Switzerland) with our HMA and the reference high dielectric constant pads used in literature [32] based on a mixture of BaTiO_3 and water. B_1^+ maps are acquired with an actual flip-angle imaging sequence [33]. The results for the birdcage with SAM alone are presented in Fig. 6(a). Once again, the characteristic inhomogeneous rf field pattern is obtained. The permittivity of the BaTiO_3 mixture designed is close to $\epsilon_r = 220$, which is optimal for a 1-cm-thick pad [5]. The mixture is sealed in a plastic box of dimensions $12 \times 10 \times 1 \text{ cm}^3$ and placed on the right-hand side of the SAM phantom. The effect of the BaTiO_3 pad is presented in Fig. 6(b). A strong amplitude increase is observed in the area close to the pad. However, the pad configuration is not able to fill the gap between the side of the phantom and the central spot, meaning that the dispersion of B_1^+ amplitude values remains broad. A final measurement is realized with a 42-cm-long HMA placed at 2 cm from the right-hand side of the phantom. The HMA provides a similar enhancement of the B_1^+ amplitude on the right-hand side of the SAM phantom. Nonetheless, the HMA configuration is such that we are able to merge the two high-amplitude spots into one large area with low dispersion in terms of B_1^+ amplitude values. This is highly beneficial to the SNR and biological contrast recovery for *in vivo* MRI applications. Furthermore, it clearly shows the benefits of the metamaterial approach developed here compared to the actual benchmark in terms of rf passive shimming.

E. Signal-to-noise ratio evaluation

In order to fully assess the performances of our rf shimming approach, we explore the effect of the HMA structure in terms of signal-to-noise ratio. In this section, we compare the signal-to-noise ratio obtained with the

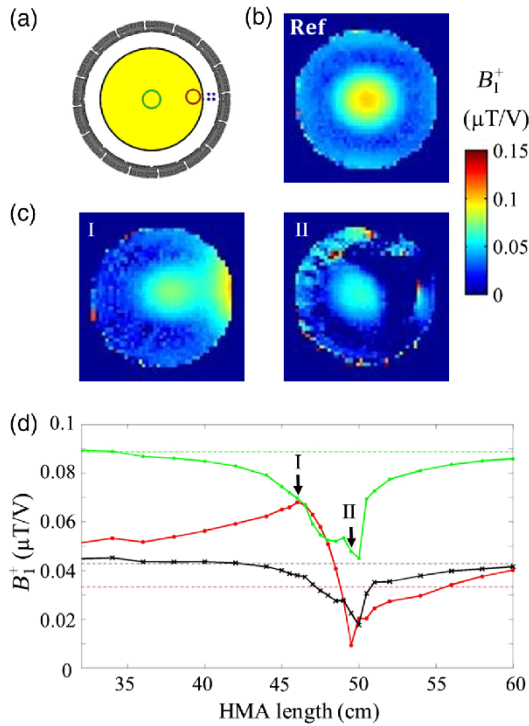


FIG. 5. (a) Schematic view of experimental configuration inside the 7 T MRI: birdcage coil (dark gray), HMA (4 blue rods), and phantom (yellow). (b),(c) Measured B_1^+ maps (in $\mu\text{T/V}$) of the gel spherical phantom ($\epsilon_r = 74.2$, $\sigma = 0.87 \text{ S/m}$) (b) without HMA and (c) for various HMA lengths: (I) 46.5 cm and (II) 49.5 cm. (d) Average B_1^+ magnitude in the three color-marked ROIs (a) as a function of the HMA length. The black solid line corresponds to the whole phantom. The green solid line corresponds to the central region of the phantom (1.85 cm radius). The red solid line corresponds to the right-hand region of the phantom (1.5 cm radius). The horizontal dotted lines indicate the reference value (without HMA) for each ROI. The three vertical arrows denote the three lengths of interest depicted above.

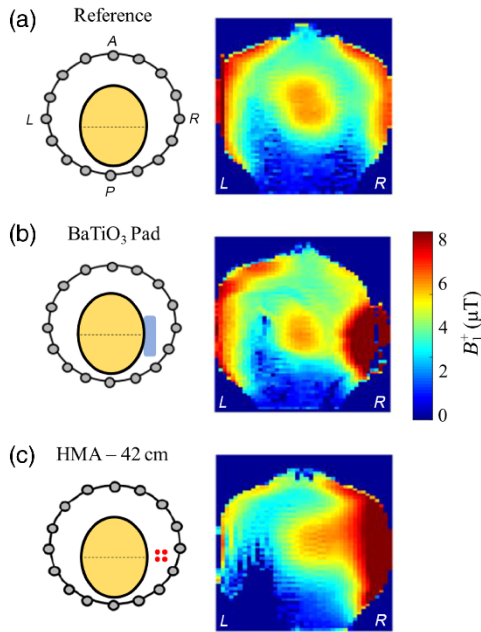


FIG. 6. (a)–(c) Left: Schematic view of the experimental configurations inside the 7 T MRI: birdcage legs in gray circles, specific anthropomorphic mannequin (SAM) in yellow, positioning of the BaTiO₃ pad in blue (b) and HMA in red dots (c). The horizontal dotted line shows the imaging plane. Right: Measured B_1^+ coronal maps (in μT) of the SAM phantom: (a) with SAM only, (b) in the presence of a BaTiO₃ pad on the right-hand side, and (c) replacing the pad with a 42-cm-long HMA. HMA is located 2 cm away from the phantom.

birdcage alone as a reference and observe the impact of the HMA when inserted within the coil. To do so, we use a gradient echo sequence to obtain a proton weighted image of the phantom. These results are presented in Figs. 7(a) and 7(b) for the reference case and in the presence of HMA. In a second measurement, we use XFL sequence to acquire the excitation profile. These two maps are then used to calculate the SNR maps independently from the flip-angle heterogeneities [Figs. 7(c) and 7(d)]. Finally, we compute the SNR enhancement map [Fig. 7(e)] as the ratio of the two corrected SNRs measured with and without the HMA. More details are presented in Sec. IV. All the measurements are done with the same input power and sequence parameters. First of all, there is almost no decay in the coil efficiency once the HMA is inserted. The autocalibration of the system leads only to a 1% increase once the HMA is set in position. Figures 7(a) and 7(b) demonstrate a local enhancement of the signal in the vicinity of the HMA. This is a consequence of the rf shimming observed in the previous results. Nevertheless, Figs. 7(c) and 7(d) show that even at the same input power, and after correction for flip-angle heterogeneity bias, receiving SNR is locally improved by the HMA insertion. This result can be

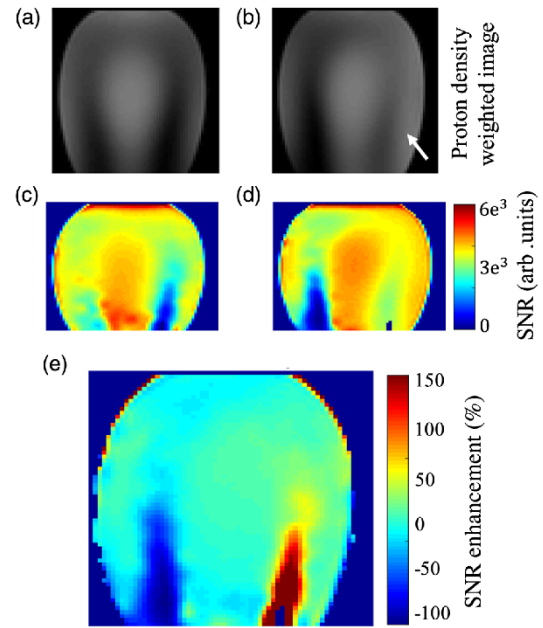


FIG. 7. SNR measurement with and without HMA on SAM phantom. (a) Proton density weighted (PDW) coronal image with birdcage and (b) with 42-cm-long HMA inserted (metamaterial along the right-hand side of the phantom). Local enhancement can be visually identified by the white arrow along the HMA. (c) Corrected SNR maps (arbitrary units) obtained with the birdcage alone and (d) in presence of HMA. (e) Calculated SNR enhancement map in percentage. It confirms a strong SNR enhancement close to the HMA but also a slight improvement on a relatively large part of the phantom volume.

interpreted through the reciprocity principle [34], where gain in transmission can also be observed in reception from the linearly polarized magnetic field emitted by the HMA. Moreover, it also goes with a better noise figure in reception as the noise level measured at the analog-to-digital converter is reduced by 9%. Consequently, we obtain an enhancement of the SNR over the right hemisphere of the phantom. We observe a maximum of 150% enhancement in the original dark spot produced by the birdcage alone. One can notice a reduction of the SNR within the dark spot located on the opposite side, as previously observed with a single dielectric pad. This results show that besides the clear advantage of local B_1^+ enhancement provided by the HMA, the reception path benefits also from the presence of the HMA within the birdcage coil.

III. CONCLUSION

In conclusion, the results we present here demonstrate a strong impact of HMA on the B_1^+ field and local SNR for UHF MRIs. Besides their clear effect on the rf field distribution, HMA structures have the potential to overcome

limitations of the dielectric pads. As metallic metamaterials are not subject to aging, they will keep their performance along time; moreover, they are cost effective and very easy to manufacture. The HMA equivalent dielectric constant is also tunable by simply modifying the length and the distance between the rods. Thus, in a first approach, HMAs could be used similarly to dielectric pads but allowing a higher degree of control in the rf field distribution. In addition, we show that we could strongly increase or reduce the B_1^+ field when the Kerker scattering conditions are set. Decreasing the B_1^+ field in specific regions may also have applications for shielding metallic implants [30], for example. The developed solution could be directly used to improve functional MRI imaging. Indeed, it has not been fully optimized for imaging but should be seen as a proof of concept of the control of the rf emission for UHF MRI. Future work will consider a combination of several HMA structures inside the coil to not only restore locally the B_1^+ excitation but also improve the B_1^+ dispersion in the whole brain at 7 T [35]. In addition to the padding route, a different approach could be developed considering the HMAs and the birdcage coil as a whole, which should be designed in order to be insensitive to individual variability [36].

IV. METHOD

Validation experiments were performed on a homemade 16-cm-diameter spherical phantom containing 1% agar and 0.4% NaCl ($\epsilon_r = 74.5$, $\sigma = 0.78$ S/m) and on a specific anthropomorphic mannequin phantom (SPEAG, Zurich, Switzerland) filled with HT0300 liquid ($\epsilon_r = 45.3$, $\sigma = 0.87$ S/m) using a birdcage 1Tx/1Rx head coil (Invivo Corp., Gainesville, FL) in a 7 T Magnetom MRI scanner (Siemens Healthineers, Erlangen, Germany).

Experimental B_1^+ maps were acquired with the XFL MRI sequence [31,37,38] in the coronal direction. It is based on a 2D Turbo-FLASH readout sequence, acquired once with a 5 ms 90° Shinnar-Leroux minimum-phase saturation pulse (SAT) [37,39] with a time-to-bandwidth product of 9, and once without (REF). Sequence parameters for a 4 mm in-plane resolution with a field of view of $256 \times 256 \times 176$ mm³ were TR = 20 s, TE = 3.06 ms, FA = 7°, BW = 1560 Hz/px. The XFL acquisition time lasted 40 s without any acceleration factor. Considering that longitudinal relaxation can be neglected between the SAT pulse and the first REF pulse, a flip-angle map can be calculated with the following expression:

$$\alpha = \cos^{-1} \left(\frac{S_{\text{SAT}}}{S_{\text{REF}}} \right), \quad (7)$$

where S_{SAT} and S_{REF} are saturation and reference magnitude signal images. The B_1^+ field map can then be extracted using the following formula:

$$B_1^+ = \frac{\alpha}{360\gamma \int_0^\tau \text{SAT}(t)dt}, \quad (8)$$

where α is the measured flip angle in degrees, γ is the gyromagnetic ratio in Hz/μT, τ is the saturation pulse duration, and $\text{SAT}(t)$ is the waveform of the saturation pulse in volts.

Proton density weighted images used in Sec. II E are obtained with a gradient echo sequence with TR = 5 s, TE = 1.9 ms, FA = 90°, BW = 1563 Hz/px, field of view of 256 mm² on 64×64 pixels with 4 mm isotropic voxel size. For this proton density weighting with TR > 5T₁, the signal s_{GRE} obtained in the function of the position r is

$$s_{\text{GRE}}(r) = M_0(r)E_2R(r)\sin\theta(r), \quad (9)$$

with $M_0(r)$ the longitudinal magnetization available, $R(r)$ the reception profile, the flip-angle map $\theta(r)$, and the factor $E_2 = e^{-\text{TE}/T_2}$. This last factor has a reduced impact since TE is lower than T₂. The excitation profile $\theta(r)$ is removed from the signal expression in order to compute the corrected SNR map as follows:

$$\text{SNR}(r) = \frac{\langle M_0(r)R(r) \rangle}{\text{std}(s_{\text{GRE}-0\text{V}})}, \quad (10)$$

where $s_{\text{GRE}-0\text{V}}$ is a measure of real noise with no rf power during the sequence.

ACKNOWLEDGMENTS

The project leading to this publication has received funding from Excellence Initiative of Aix-Marseille University–A*MIDEX, a French “Investissements d’Avenir” programme. It has been partly funded by France Life Imaging Grant No. ANR-11-INBS-0006. It has received funding from the European Union’s Horizon 2020 Research and Innovation programme under Grant Agreement No. 736937. We also thank Institut Carnot STAR for support.

R. A., M. D., and S. E. worked on the physics and the basic principles of the HMA for UHF-MRI. M. D., R. A., L. L., A. V., and S. E. worked on the modeling and the design of the HMA. MRI experiments were conducted by L. L., Z. R., and A. V. A. A. and F. M. developed the B_1^+ mapping MRI sequence. All authors contributed to the analysis and redaction of the manuscript.

M. D. and L. L. contributed equally to this work.

-
- [1] R. Pohmann, O. Speck, and K. Scheffler, *Signal-to-Noise Ratio and MR Tissue Parameters in Human Brain Imaging at 3, 7, and 9.4 Tesla Using Current Receive Coil Arrays*, *Magn. Reson. Med.* **75**, 801 (2016).
 - [2] C. Boutet, M. Chupin, S. Lehericy, L. Marrakchi-Kacem, S. Epelbaum, C. Poupon, C. Wiggins, A. Vignaud, D. Hasboun, B. Defontaine *et al.*, *Detection of Volume Loss in*

- Hippocampal Layers in Alzheimer's Disease Using 7 T MRI: A Feasibility Study*, *Neuroimage Clin.* **5**, 341 (2014).
- [3] P.-F. Van de Moortele, C. Akgun, G. Adriany, S. Moeller, J. Ritter, C. M. Collins, M. B. Smith, J. T. Vaughan, K. Ugurbil, *B1 Destructive Interferences and Spatial Phase Patterns at 7 T with a Head Transceiver Array Coil*, *Magn. Reson. Med.* **54**, 1503 (2005).
- [4] A. G. Webb, *Dielectric Materials in Magnetic Resonance, Concepts Magn. Reson., Part A* **38A**, 148 (2011).
- [5] A. L. Neves, L. Leroi, Z. Raolison, N. Cochinaire, T. Leterre, R. Abdeddaim, S. Enoch, J. Wenger, J. Berthelot, A.-L. Adenot-Engelvin *et al.*, *Compressed Perovskite Aqueous Mixtures Near Their Phase Transitions Show Very High Permittivities: New Prospects for High-Field MRI Dielectric Shimming*, *Magn. Reson. Med.* **79**, 1753 (2018).
- [6] T. P. A. O'Reilly, A. G. Webb, and W. M. Brink, *Practical Improvements in the Design of High Permittivity Pads for Dielectric Shimming in Neuroimaging at 7 T*, *J. Magn. Reson.* **270**, 108 (2016).
- [7] W. Grissom, C.-y. Yip, Z. Zhang, V. A. Stenger, J. A. Fessler, and D. C. Noll, *Spatial Domain Method for the Design of RF Pulses in Multicoil Parallel Excitation*, *Magn. Reson. Med.* **56**, 620 (2006).
- [8] FDA 510(k) premarket approval under No. K170840 for Magnetom Terra 7 T, Oct. 2017.
- [9] M. C. K. Wiltshire, J. B. Pendry, I. R. Young, D. J. Larkman, D. J. Gilderdale, and J. V. Hajnal, *Microstructured Magnetic Materials for RF Flux Guides in Magnetic Resonance Imaging*, *Science* **291**, 849 (2001).
- [10] M. J. Freire, L. Jelinek, R. Marques, and M. Lapine, *On the Applications of $\mu = -1$ Metamaterial Lenses for Magnetic Resonance Imaging*, *J. Magn. Reson.* **203**, 81 (2010).
- [11] X. Radu, D. Garraay, and C. Craeye, *Toward a Wire Medium Endoscope for MRI Imaging*, *Metamaterials* **3**, 90 (2009).
- [12] C. L. Holloway, E. F. Kuester, J. A. Gordon, J. O'Hara, J. Booth, and D. R. Smith, *An Overview of the Theory and Applications of Metasurfaces: The Two-Dimensional Equivalents of Metamaterials*, *IEEE Trans. Antennas Propag.* **54**, 10 (2012).
- [13] A. P. Slobzhanyuk, A. N. Poddubny, A. J. E. Raaijmakers, C. A. T. van den Berg, A. V. Kozachenko, I. A. Dubrovina, I. V. Melchakova, Y. S. Kivshar, and P. A. Belov, *Enhancement of Magnetic Resonance Imaging with Metasurfaces*, *Adv. Mater.* **28**, 1832 (2016).
- [14] A. V. Shchelokova, C. A. T. van den Berg, D. A. Dobrykh, S. B. Glybovski, M. A. Zubkov, E. A. Brui, D. S. Dmitriev, A. V. Kozachenko, A. Y. Efimtcev, A. V. Sokolov *et al.*, *Volumetric Wireless Coil Based on Periodically Coupled Split-Loop Resonators for Clinical Wrist Imaging*, *Magn. Reson. Med.* **80**, 1726 (2018).
- [15] A. V. Shchelokova, A. P. Slobzhanyuk, I. V. Melchakova, S. B. Glybovski, A. G. Webb, Y. S. Kivshar, and P. A. Belov, *Locally Enhanced Image Quality with Tunable Hybrid Metasurfaces*, *Phys. Rev. Applied* **9**, 014020 (2018).
- [16] A. V. Shchelokova, A. P. Slobzhanyuk, P. de Bruin, I. Zivkovic, E. Kallos, P. A. Belov, and A. Webb, *Experimental Investigation of a Metasurface Resonator for In Vivo Imaging at 1.5 T*, *J. Magn. Reson.* **286**, 78 (2018).
- [17] C. Jouvaud, R. Abdeddaim, B. Larrat, and J. De Rosny, *Volume Coil Based on Hybridized Resonators for Magnetic Resonance Imaging*, *Appl. Phys. Lett.* **108**, 023503 (2016).
- [18] I. R. O. Connell, K. M. Gilbert, M. A. Abou-Khousa, and R. S. Menon, *Design of a Parallel Transmit Head Coil at 7 T with Magnetic Wall Distributed Filters*, *IEEE Trans. Med. Imaging* **34**, 836 (2015).
- [19] A. A. Hurshkainen, T. A. Derzhavskaya, S. B. Glybovski, I. J. Voogt, I. V. Melchakova, C. A. T. van den Berg, and A. J. E. Raaijmakers, *Element Decoupling of 7T Dipole Body Arrays by EBG Metasurface Structures: Experimental Verification*, *J. Magn. Reson.* **269**, 87 (2016).
- [20] E. Georget, M. Luong, A. Vignaud, E. Giacomini, E. Chazel, G. Ferrand, A. Amadon, F. Mauconduit, S. Enoch, G. Tayeb *et al.*, *Stacked Magnetic Resonators for MRI RF Coils Decoupling*, *J. Magn. Reson.* **275**, 11 (2017).
- [21] R. Schmidt, A. Slobzhanyuk, P. Belov, and A. Webb, *Flexible and Compact Hybrid Metasurfaces for Enhanced Ultra High Field In Vivo Magnetic Resonance Imaging*, *Sci. Rep.* **7**, 1678 (2017).
- [22] M. Kerker, D.-S. Wang, and C. L. Giles, *Electromagnetic Scattering by Magnetic Spheres*, *J. Opt. Soc. Am.* **73**, 765 (1983).
- [23] J.-M. Geffrin, B. García-Cámara, R. Gómez-Medina, P. Albella, L. S. Froufe-Pérez, C. Eyraud, A. Litman, R. Vaillon, F. González, M. Nieto-Vesperinas *et al.*, *Magnetic and Electric Coherence in Forward- and Back-Scattered Electromagnetic Waves by a Single Dielectric Subwavelength Sphere*, *Nat. Commun.* **3**, 1171 (2012).
- [24] B. Rolly, J.-M. Geffrin, R. Abdeddaim, B. Stout, and N. Bonod, *Controllable Emission of a Dipolar Source Coupled with a Magneto-Dielectric Resonant Subwavelength Scatterer*, *Sci. Rep.* **3**, 3063 (2013).
- [25] N. Meinzer, W. L. Barnes, and I. R. Hooper, *Plasmonic Meta-Atoms and Metasurfaces*, *Nat. Photonics* **8**, 889 (2014).
- [26] M. Nieto-Vesperinas, R. Gomez-Medina, and J. J. Saenz, *Angle-Suppressed Scattering and Optical Forces on Submicrometer Dielectric Particles*, *J. Opt. Soc. Am. A* **28**, 54 (2011).
- [27] S. J. Orfanidis, *Electromagnetic Waves and Antennas* (Rutgers University, New Brunswick, NJ, 2002).
- [28] See Supplemental Material at <http://link.aps.org/supplemental/10.1103/PhysRevX.8.031083> for details (1) experimental flip angle maps in function of HMA length, (2) details on impedance matrix derivation, and (3) details on Biot-Savart derivation and B_1^+ field.
- [29] P. Boisssoles, *Mathematical and Numerical Problems from Nuclear Magnetic Resonance Imaging*, Ph.D. thesis, Université Rennes 1, 2005.
- [30] M. J. P. van Osch and A. G. Webb, *Safety of Ultra-High Field MRI: What Are the Specific Risks?*, *Curr. Radiol. Rep.* **2**, 61 (2014).
- [31] A. Amadon, F. Mauconduit, A. Vignaud, and N. Boulant, *Slice Profile Corrections in the XFLI (Magnetization-Prepared Turbo-Flash) B1-Mapping Sequence*, in *Proceedings of the 20th Annual Meeting of ISMRM, Toronto, 2015*, Vol. 23, p. 2377.

- [32] W. M. Teeuwisse, W. M. Brink, K. N. Haines, and A. G. Webb, *Simulations of High Permittivity Materials for 7 T Neuroimaging and Evaluation of a New Barium Titanate-Based Dielectric*, *Magn. Reson. Med.* **67**, 912 (2012).
- [33] V. L. Yarnykh, *Actual Flip-Angle Imaging in the Pulsed Steady State: A Method for Rapid Three-Dimensional Mapping of the Transmitted Radiofrequency Field*, *Magn. Reson. Med.* **57**, 192 (2007).
- [34] D. Hoult, *The Principle of Reciprocity in Signal Strength Calculations—A Mathematical Guide*, *Concepts Magn. Reson., Part A* **12**, 173 (2000).
- [35] R. Abdeddaim, S. Enoch, P. Sabouroux, G. Tayeb, N. Bonod, A. Vignaud, B. Larrat, E. Georget, and L. Leroi, *Method for Controlling the Distribution of the RF Magnetic Field in a Magnetic Resonance Imaging System*, France Patent No. WO/2017/198914 A1 (2017).
- [36] V. Gras, A. Vignaud, A. Amadon, D. Bihan, and N. Boulant, *Universal Pulses: A New Concept for Calibration-Free Parallel Transmission*, *Magn. Reson. Med.* **77**, 635 (2017).
- [37] A. Amadon, N. Boulant, M. A. Cloos, E. Giacomini, C. J. Wiggins, M. Luong, G. Ferrand, and H. P. Fautz, *B1-Mapping of an 8-Channel TX-Array over a Human-Head-Like Volume in Less than 2 Minutes: The XEP Sequence*, in *Proceedings of the 20th Annual Meeting of ISMRM, Stockholm, 2010*, Vol. 18, p. 2828.
- [38] S. Chung, D. Kim, E. Breton, and L. Axel, *Rapid B_1^+ Mapping Using a Preconditioning RF Pulse with Turbo-flash Readout*, *Magn. Reson. Med.* **64**, 439 (2010).
- [39] J. Pauly, P. Le Roux, D. Nishimura, and A. Macovski, *Parameter Relations for the Shinnar-Le Roux Selective Excitation Pulse Design Algorithm (NMR Imaging)*, *IEEE Trans. Med. Imaging* **10**, 53 (1991).

Appendix 3: Abstracts accepted in international conferences

272

Simultaneous multiparametric quantitative extraction at 7 Tesla using QuICS

L. Leroi¹, L. De Rochefort², M. Santin³, F. Mauconduit⁴,
R. Valabregue³, D. Le Bihan¹, C. Poupon¹, A. Vignaud¹
¹DRF/I2BM/NeuroSpin/UNIRS, CEA, Gif-sur-Yvette/France,
²IR4M UMR8081, Univ. Paris-Sud CNRS Univ. Paris-Saclay, Orsay/
France, ³CENIR, ICM, Hôpital Pitié-Salpêtrière, Paris/France,
⁴Healthcare department, Siemens, Saint-Denis/France

Purpose/Introduction: Recently, quantitative simultaneous multiparametric approaches have attracted considerable interest [1]–[5], aiming for a viable implementation in clinical routines for any field strength. Indeed, it may allow earlier detection of pathological changes or unbiased assessment of treatments across different sites. Here, we apply for the first time at 7Tesla an innovative method to achieve Quantitative Imaging using Configuration States (QuICS) described in [6]. This method allows to assess M_0 , R_1 , R_2 and diffusion while correcting for B_0 and B_1 inhomogeneity.

Subjects and Methods: MRI acquisitions were performed on a 7T Magnetom MRI (Siemens Healthcare, Erlangen, Germany) using a birdcage head coil 1Tx/1Rx (Invivo Corp., Gainesville, USA). A 3D gradient echo sequence was used to acquire 45 different radiofrequency spoiling increments sequentially. Spoiling gradient was restricted to the readout direction, having half momentum of the readout gradient momentum. Scan parameters were TR/TE 12 ms/5.1 ms, voxel size $1.3 \times 1.3 \times 5.0 \text{ mm}^3$, Bw 220 Hz/px, total TA 32min15 s. We used a spherical phantom filled with water, 1 % agar and 0.4 % NaCl. The data were fitted voxel-wised to Bloch–Torrey equation to estimate M_0 , R_1 , R_2 , B_1^+ and ADC as well as errors using an efficient calculation approach based on configuration states formalism [6], [7] and Fisher information matrix [8]. Actual R_1 , R_2 and ADC of the phantom were assessed separately using respectively gold-standard Inversion-Recovery Turbo Spin-Echo, multi Spin-Echo and double Spin-Echo diffusion EPI sequences.

Results: The fit between the measured signal of the central pixel and the theoretical signal depending on the RF spoiling increment is shown in the complex plane in Fig. 1. Over the central slice, mean R_1 was $0.297 \pm 0.018 \text{ s}^{-1}$, R_2 $6.71 \pm 0.046 \text{ s}^{-1}$ and diffusion $1.92 \pm 0.12 \times 10^{-9} \text{ m}^2/\text{s}$ (Fig. 2). Compared to gold-standard measures, it represents an under-estimation of respectively 10.8 % (R_1), 2.1 % (R_2) and 4.0 % (ADC). Standard deviation values over the slice indicates a limited spatial dependence regardless of B_1^+ inhomogeneity. Associated errors maps on Fig. 2 demonstrate an error inferior to 1 % for M_0 , R_1 and R_2 , 0.2 % for the flip angle and 5 % for the diffusion map.

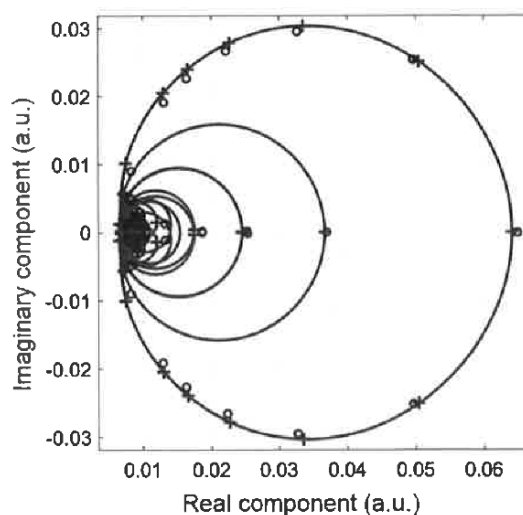


Fig. 1 : Measured signal for each RF increment (blue dots) and fit (red curve) displayed in the complex plane for the central pixel of central slice of the phantom. Maximum real value corresponds to a RF increment of 0° .

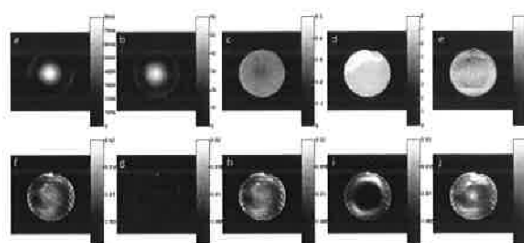


Fig. 2 : First row shows fitted parameters maps for the central slice of the phantom : M_0 (a), flip angle in degrees (b), R_1 and R_2 in s^{-1} (c, d), diffusion map in $10^{-9} \text{ m}^2/\text{s}$ (e). Second row displays their associated errors (f, g, h, i, j). A higher density has been detected in the upper area in (d) and (e), showing the potential of the method to distinguish some heterogeneities of signal.

Discussion/Conclusion: These preliminary results validated the QuICS approach on a phantom at 7 Tesla. For in vivo application on the whole brain at high isotropic resolution, the acquisition strategy can be optimized by selecting the most informative RF and gradient spoiling steps to determine the desired parameters, including diffusion coefficient, without jeopardize the clinical applicability. An

optimization algorithm based on Fisher information and Cramér–Rao lower bound will be used for this purpose [9]. To speed up the acquisition, parallel imaging and k-space acceleration strategies can also be considered.

References:

- [1] D. Ma, et al., “Magnetic resonance fingerprinting,” *Nature*, vol. 495, no. 7440, pp. 187–192, Mar. 2013.
- [2] J. B. M. Warntjes, et al., “Novel method for rapid, simultaneous T1, T2*, and proton density quantification,” *Magn. Reson. Med.*, vol. 57, no. 3, pp. 528–537, Mar. 2007.
- [3] R. Heule, et al., “Triple echo steadystate (TESS) relaxometry,” *Magn. Reson. Med.*, vol. 71, no. 1, pp. 230–237, Jan. 2014.
- [4] J. B. M. Warntjes, et al., “Rapid magnetic resonance quantification on the brain: Optimization for clinical usage,” *Magn. Reson. Med.*, vol. 60, no. 2, pp. 320–329, Aug. 2008.
- [5] P. Schmitt, et al., “Inversion recovery TrueFISP: Quantification of T1, T2, and spin density,” *Magn. Reson. Med.*, vol. 51, no. 4, pp. 661–667, Apr. 2004.
- [6] L. de Rochefort, proceedings at the Intl. Soc. Mag. Reson. Med., 2015, p. 445.
- [7] M. Weigel, “Extended phase graphs: Dephasing, RF pulses, and echoes pure and simple,” *J. Magn. Reson. Imaging*, vol. 41, no. 2, pp. 266–295, Feb. 2015.
- [8] C. L. Lankford, and M. D. Does, “On the inherent precision of mcDESPOT,” *Magn. Reson. Med.*, vol. 69, pp. 127–136, no. 1, Jan 2013.
- [9] R. Valabregue, proceedings at the Intl. Soc. Mag. Reson. Med., 2016, abstract no. 3319.

5627

Simultaneous multi-parametric and quantitative estimation of ^{23}Na physical properties at 7 Tesla using QulCS

Lisa Leroi¹, Arthur Coste¹, Ludovic de Rochefort², Mathieu Santin³, Romain Valabré³, Franck Mauconduit⁴, Marie-France Hang¹, Edouard Chazel¹, Jérémy Bernard¹, Michel Luong⁵, Eric Giacomini¹, Denis Le Bihan¹, Cyril Poupon¹, Fawzi Boumezbeur¹, Cécile Rabrait-Lerman¹, and Alexandre Vignaud¹

¹Neurospin, CEA, Paris-Saclay University, Saclay, France, ²CRMBM, UMR 7339, Aix-Marseille University, Marseille, France, ³Institut Cerveau Moelle - ICM, CENIR, UPMC-Inserm U1127, CNRS 7225, Paris, France, ⁴Siemens Healthineers, Saint-Denis, France, ⁵IRFU, CEA, Paris-Saclay University, Saclay, France

Synopsis

Quantifying physical properties of sodium could be of benefit to assess more specifically changes in cellular homeostasis accompanying neuroinflammatory or neurodegenerative diseases. This work aimed at adapting for ^{23}Na MRI at 7 Tesla the Quantitative Imaging using Configuration States (QulCS) method, primarily developed for ^1H MRI. We demonstrate the possibility to not only estimate accurately the T_1 , T_2 , FA, M_0 and ADC simultaneously for ^{23}Na at physiological concentration at UHF, but to acquire 3D maps for all of them.

Purpose

Quantifying physical properties of sodium could be of benefit to assess more specifically changes in cellular homeostasis accompanying neuroinflammatory or neurodegenerative diseases. Due to its lower in vivo concentration and NMR sensitivity than ^1H , ^{23}Na MRI remains challenging, resulting in images with relatively low SNR and resolution. Thus, ^{23}Na MRI could benefit from the advent of ultra-high field scanners and novel pulse sequences. Lately, quantitative simultaneous multi-parametric approaches have become of high interest¹⁻⁵, primarily for ^1H MRI. In this preliminary study, we aimed at adapting for ^{23}Na MRI at 7 Tesla the Quantitative Imaging using Configuration States (QulCS) method⁶. This approach allows to estimate simultaneously NMR and physical properties such as spin density (M_0), relaxation parameters (R_1 and R_2), and apparent diffusion coefficient (ADC), in addition to the flip angle (FA) and B_0 distributions.

Methods

MRI acquisitions were performed on our 7T Magnetom MRI (Siemens, Erlangen, Germany) with a home-made transceiver ^{23}Na radiofrequency coil (Fig. 1) and a cylindrical phantom (diameter 7cm, 150mM NaCl). A 3D gradient echo sequence was used to acquire 45 different radiofrequency spoiling increments sequentially, leading to a total acquisition time of 5h16min (TR/TE=20ms/3.2ms, Bw: 220Hz/px, resolution: 6mm³ isotropic, FoV: 192x192x160mm³). Spoiling gradients were restricted to the readout direction, equal to 22 times the readout gradient momentum. The data were fitted voxel-wised to Bloch-Torrey equations to estimate M_0 , R_1 , R_2 , ADC, and the flip angle maps using Matlab (The MathWorks, Natick, USA).

Results and Discussion

Given the hemi-cylindrical geometry of the coil (Fig.1.), a region-of-interest (ROI) was defined over the top of the phantom as shown in Fig.2. In this ROI, mean R_1 was $17.3 \pm 1.43 \text{ s}^{-1}$ ($T_1=58\text{ms}$), R_2 $19.9 \pm 2.13 \text{ s}^{-1}$ ($T_2=50\text{ms}$), ADC $1.11 \pm 0.50 \times 10^{-9} \text{ m}^2 \cdot \text{s}^{-1}$ and flip angle $51.5 \pm 10.9^\circ$ (Fig. 2).

For saline solutions of 140-150mM mimicking the physiological CSF, T_1 values of 50-55ms and T_2 values of 55-65ms are reported in the literature^{7,8} for in vivo conditions. Diffusion coefficient were estimated for sodium in the rat brain at 25°C to be $1.15 \times 10^{-9} \text{ m}^2 \cdot \text{s}^{-1}$ ⁹ and in sodium fluorine in aqueous solution at 25°C to be $1.3 \times 10^{-9} \text{ m}^2 \cdot \text{s}^{-1}$ ¹⁰. Overall, our results were in good agreement with these data, with an error of 5% for T_1 , 9% for T_2 and 8% for ADC.

Conclusion

In this preliminary in vitro study, we have demonstrated the possibility to use the QulCS method, not only to estimate accurately the T_1 , T_2 , FA, M_0 and ADC simultaneously for ^{23}Na at physiological concentration at UHF, but to acquire 3D maps for all of them. This is particularly exciting considering the difficulty of conventional approaches to estimate parameters such as the ADC for nuclei with short T_2 relaxation times. To the knowledge of the authors, this is the first time that such multi-parametric extraction is reported in the context of X-nuclei imaging.

Diffusion was the most complicated parameter to estimate and required the full range of RF spoiling increments described above. However, the estimation of M_0 , R_1 and R_2 was achieved with good precision in less than an hour. For now, the long acquisition time remains a significant hurdle to translate this method to clinical or preclinical MRI. We are aiming at accelerating our method by using shorter TE, non-Cartesian sampling trajectories¹¹, a better coil configuration¹² and eventually less FA, RF and gradient spoiling steps. An optimization algorithm based on Fisher information and Cramér-Rao lower bound will be used for this purpose^{13,14}.

Acknowledgements

This project received financial support from France Life Imaging ("qMRI" starter project).

References

1. D. Ma et al., "Magnetic resonance fingerprinting," *Nature*, vol. 495, no. 7440, pp. 187–192, Mar. 2013.
2. J. b. m. Warntjes et al., "Novel method for rapid, simultaneous T_1 , T_2^* , and proton density quantification," *Magn. Reson. Med.*, vol. 57, no. 3, pp. 528–537, Mar. 2007.
3. J. b. m. Warntjes, et al., "Rapid magnetic resonance quantification on the brain: Optimization for clinical usage," *Magn. Reson. Med.*, vol. 60, no. 2, pp. 320–329, Aug. 2008.

Appendix 3

4. R. Heule et al., "Triple echo steady-state (TESS) relaxometry," *Magn. Reson. Med.*, vol. 71, no. 1, pp. 230–237, Jan. 2014.
5. P. Schmitt et al., "Inversion recovery TrueFISP: Quantification of T1, T2, and spin density," *Magn. Reson. Med.*, vol. 51, no. 4, pp. 661–667, Apr. 2004.
6. L. de Rochefort, "Encoding with Radiofrequency Spoiling, Equilibrium States and Inverse Problem for Parametric Mapping," *Proc. Intl. Soc. Mag. Reson. Med.*, 2015, p. 445.
7. G. Madelin and R. R. Regatte, "Biomedical applications of sodium MRI in vivo," *J. Magn. Reson. Imaging*, vol. 38, no. 3, pp. 511–529, Sep. 2013.
8. N. J. Shah et al., "Imaging of sodium in the brain: a brief review," *NMR Biomed.*, vol. 29, no. 2, pp. 162–174, Feb. 2016.
9. J. A. Goodman, C. D. Kroenke, G. L. Bretthorst, J. J. H. Ackerman, and J. J. Neil, "Sodium ion apparent diffusion coefficient in living rat brain," *Magn. Reson. Med.*, vol. 53, no. 5, pp. 1040–1045, May 2005.
10. A. C. F. Ribeiro et al., "Diffusion Coefficients of Sodium Fluoride in Aqueous Solutions at 298.15 K and 310.15 K," *ResearchGate*, vol. 57, no. 2, pp. 410–4, Jun. 2010.
11. A. Coste et al., "Assessment of benefit to use a non-Cartesian trajectory and nonlinear reconstruction method compared to a Cartesian strategy for fast 31P MRI," *Proc. Intl. Soc. Mag. Reson. Med.* 24, 2016, p. 3940.
12. G. Shajan et al., "Three-layered radio frequency coil arrangement for sodium MRI of the human brain at 9.4 Tesla," *Magn. Reson. Med.*, vol. 75, no. 2, pp. 906–916, Feb. 2016.
13. L. de Rochefort et al., "In Vivo Feasibility of Multi-Parametric Mapping Based on Fast Steady-State Sequences," *Proc. Intl. Soc. Mag. Reson. Med.*, 2016, p. 1823.
14. R. Valabrègue and L. de Rochefort, "Fisher Information Matrix for Optimizing the Acquisition Parameters in Multi-Parametric Mapping Based on Fast Steady-State Sequences," *Proc. Intl. Soc. Mag. Reson. Med.*, 2016, p. 1569.

Figures

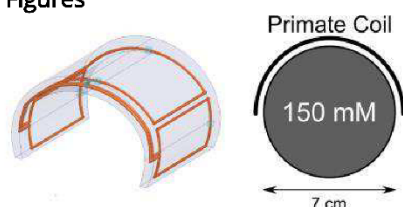


Fig. 1 : Schematic of our hemi-cylindrical non-human primate ^{23}Na RF coil and NaCl phantom positioning



Fig. 2 : Multi-parametric maps: (a) M_0 , (b) FA in degrees, (c, d) R_1 and R_2 in s^{-1} , (e) diffusion map in $10^{-9}\text{m}^2\cdot\text{s}^{-1}$. Average physical parameters detailed in the text were calculated over the ROI (in red)

B1+ homogenization at 7T using an innovative meta-atom

Lisa Leroi¹, Alexandre Vignaud¹, Pierre Sabouroux², Elodie Georget¹, Benoit Larrat¹, Stefan Enoch², Gérard Tayeb², Nicolas Bonod², Alexis Amadon¹, Denis Le Bihan¹, and Redha Abdeddaïm²

¹UNIRS, CEA Saclay - DSV - I2BM - Neurospin - UNIRS, Gif-sur-Yvette, France, ²CNRS, Aix-Marseille Université, Centrale Marseille, Institut Fresnel, UMR 7249, Marseille, France

Synopsis

B₁⁺ heterogeneity at ultra-high field (UHF) can be tackled performing “passive shimming” with High-Dielectric Constant (HDC) pads. Nevertheless, HDC pads have shown structural, manufacturing and composition constraints. Here, we substitute HDC padding with a new meta-atom (MA) structure with a high equivalent dielectric constant, leaving behind the identified limitations. In this work, we compare this MA structure to a classic BaTiO₃ pad used in UHF clinical routine. Results demonstrate this solution to strongly impact local B₁⁺ distribution. Implementing multiple MA structures into the coil design might suggest a good potential for brain global B₁⁺ inhomogeneity mitigation.

Target audience

MR physicist, anyone interested in using high permittivity materials to improve RF coil performance

Purpose

The introduction of relative High-Dielectric Constant (HDC) materials in radiofrequency (RF) coils has been shown to address efficiently the B₁⁺ inhomogeneity in ultra-high field MRI (B₀≥3T) with limited Specific Absorption Ratio (SAR) constraints [1]. HDC materials act as a secondary RF field source modifying the global RF distribution in the transmit coil [2, 3]. Literature reports that they can be made out CaTiO₃ [1] or BaTiO₃ [4] powders mixed with de-ionized or deuterated water, or monolithic blocks of lead zirconium titanate (PZT) [5]. Unfortunately, none of them are really fulfilling the requirements to be used in high field clinical routine. HDC pads represent an important bulk in the coil, they reduce patient's comfort, and they are aging rapidly. Some materials can be expensive and, like BaTiO₃, referenced as highly toxic [6]. To foster the RF transmission and avoid these inconveniences, we came up with an innovative solution based on the use of a new Meta-Atom (MA) structure, acting like a magnetic resonator in the RF coil, which solves all these limitations. To the knowledge of the authors, it is the first time that a MA structure is proposed for “dielectric shimming” purpose.

Materials and methods

The MA structure (pending patent) was designed in order to mimic the effect of a BaTiO₃ pad, currently one of the most efficient solution found in the literature [4, 7]. It was made of four 1mm diameter copper rods with a length of 40cm, separated from each other by 1.5cm, forming a rectangular parallelepiped in order to create magnetic mode [8,9]. The estimation of the equivalent dielectric constant of the MA structure, considered as a homogeneous object including also 2cm of vacuum representing the distance from the patient, has been estimated using CST Software (Darmstadt, Germany) and has been compared to a BaTiO₃ pad placed against the left ear measuring 12x10x1cm³ with a dielectric constant $\epsilon'=225$. The pad permittivity has been determined using Nicolson and Ross protocol [10] associated to a de-embedding operation using an innovating coaxial cell with sample holder [11]. To assess the impact of our MA structure on the B₁⁺ distribution, validation experiments were performed using a birdcage head coil 1Tx/1Rx (Invivo Corp., Gainesville, USA) and a Specific Anthropomorphic Mannequin phantom (SPEAG, Zürich, Switzerland) on a 7T Magnetom MRI (Siemens Healthcare, Erlangen, Germany). B₁⁺ maps were acquired with an AFI sequence [12] with the MA structure or with a BaTiO₃ pad.

Results

Figure 1 shows the dielectric or equivalent dielectric constants of the different solutions. Their respective effects on the B₁⁺ distribution can be observed on Figure 2. Even further away from the object, the MA structure demonstrates a much stronger impact on the B₁⁺ field, spread over a larger volume. This is consistent with its design and its larger equivalent dielectric constant at 297MHz.

Discussion/Conclusion

Besides its clear effect on RF field distribution, our MA structure has the potential to overcome limitations of the dielectric pads currently used: it has a smaller size, and can be set further away from the patient. It is not aging, it is cost effective and very easy to manufacture. Its equivalent dielectric constant is also tunable modifying the length and the distance between the rods. Copper rods embedded in the MA structure are so far very long. A solution to shorten them is currently being developed. If so, it should be possible to integrate MA

Appendix 3

structures directly inside the transmission birdcage design, clearing space inside the coil. Thus, a combination of several MA structures inside the coil might not only restore locally the B_1^+ excitation but also improve the global B_1^+ NRMSE (Normalized Root Mean Square Error) in the whole brain at 7T. But before implementing such a solution in a state of the art routine clinical coil, some questions need to be addressed and will be the topic of later work. First, the interference of this MA structure with a specific receiving phased array must be examined. Furthermore, its impact on the SAR value needs to be evaluated accurately, even though the design of the structure has been elaborated in order to center the magnetic mode at 297MHz, reducing significantly the contribution of the electric mode.

Acknowledgements

This project received financial support from France Life Imaging and from the Institut Carnot STAR ("CMRI" grant).

References

- [1] W. M. Teeuwisse, et al, *Mag. Reson. Med.*, 2012;67(5):1285–1293 [2] W. M. Brink et al., *Mag. Reson. Med.* Jun. 2015, online [3] Q. X. Yang et al., *J. Mag. Reson. Imaging*, 2006 ; 24(1) : 197-202 [4] W. M. Teeuwisse et al., *Mag. Reson. Med.*, 2012;67(4):912–918 [5] Rupprecht et al., *Proceedings ISMRM 2013* p. 5458 [6] Regulation EC 1272/2008 [7] K. R. O'Brien, *J. Mag. Reson. Imaging*, 2014 ; 40(4) : 804–812 [8] B. Kanté, et al., *Phys. Rev. B*, 2009;79(7):075121. [9] R. Abdeddaim, et al., *Phys. Rev. B*, 2011;83(3):033101 [10] L. F. Chen et al., "Electromagnetic Properties of Materials," in *Microwave Electronics*, John Wiley & Sons, 2004. [11] É. Georget et al., *Comptes Rendus Phys.*, 2014;15(5) :448–457 [12] V. L. Yarnykh, *Mag. Reson. Med.*, 2007;57(1):192–200

Figures

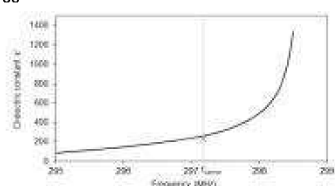


Figure 1: Evolution of the equivalent dielectric constant of the homogeneous object containing the MA structure and 2cm of vacuum (line) and the BaTiO₃ pad ϵ' (cross) as a function of the frequency

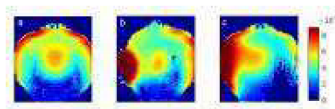


Figure 2: Coronal B_1^+ map distributions (in Tesla) acquired at 7T with AFI using SAM phantom in a birdcage transceiver coil a) without dielectric shimming b) with BaTiO₃ pad located on the SAM phantom left ear c) with our MA structure facing the same SAM ear at a 2cm distance

References

- Abdeddaim, R., Ourir, A., and de Rosny, J. (2011). Realizing a negative index metamaterial by controlling hybridization of trapped modes. *Phys. Rev. B* *83*, 033101.
- Aghaeifar, A., Mirkes, C., Bause, J., Steffen, T., Avdievitch, N., Henning, A., and Scheffler, K. (2018). Dynamic B0 shimming of the human brain at 9.4 T with a 16-channel multi-coil shim setup. *Magn. Reson. Med.* *80*, 1714–1725.
- Ahn, C.B., Kim, J.H., and Cho, Z.H. (1986). High-speed spiral-scan echo planar NMR imaging-I. *IEEE Trans. Med. Imaging* *5*, 2–7.
- Alexander, D.C. (2008). A general framework for experiment design in diffusion MRI and its application in measuring direct tissue-microstructure features. *Magn. Reson. Med.* *60*, 439–448.
- Amadon, A., Boulant, N., Cloos, M.A., Giacomini, E., Wiggins, C.J., Luong, M., Ferrand, G., and Fautz, H.-P. (2010). B1 mapping of an 8-channel TX-array over a human-head-like volume in less than 2 minutes: the XEP sequence. In *Proc. Intl. Soc. Mag. Reson. Med.* *18* (2010), p. 2828.
- Anastasiou, A., and Hall, L.D. (2004). Optimisation of T2 and M0 measurements of bi-exponential systems. *Magn. Reson. Imaging* *22*, 67–80.
- Anderson, C., Wang, C., Gu, Y., Jiang, Y., Ma, D., Griswold, M., Yu, X., and Flask, C.A. (2017). Gradient Moment Dependent T2 Accuracy in FISP Magnetic Resonance Fingerprinting (MRF) at 7T. In *Proc. Intl. Soc. Mag. Reson. Med.* *25*, p. 5211.
- Arnold, J.F.T., Fidler, F., Wang, T., Pracht, E.D., Schmidt, M., and Jakob, P.M. (2004). Imaging lung function using rapid dynamic acquisition of T1-maps during oxygen enhancement. *Magn. Reson. Mater. Phys. Biol. Med.* *16*, 246–253.
- Athey, T.W. (1989). A model of the temperature rise in the head due to magnetic resonance imaging procedures. *Magn. Reson. Med.* *9*, 177–184.
- Athey, T.W., and Czerski, P. (1988). Safety of magnetic resonance in vivo diagnostic examinations. In *Proceedings of the Annual International Conference of the IEEE Engineering in Medicine and Biology Society*, pp. 892–893.
- Babsky, A.M., Topper, S., Zhang, H., Gao, Y., James, J.R., Hekmatyar, S.K., and Bansal, N. (2008). Evaluation of extra- and intracellular apparent diffusion coefficient of sodium in rat skeletal muscle: Effects of prolonged ischemia. *Magn. Reson. Med.* *59*, 485–491.
- Badve, C., Yu, A., Dastmalchian, S., Rogers, M., Ma, D., Jiang, Y., Margevicius, S., Pahwa, S., Lu, Z., Schluchter, M., et al. (2016). MR Fingerprinting of Adult Brain Tumors: Initial Experience. *Am. J. Neuroradiol.*
- Barber, B.J., Schaefer, D.J., Gordon, C.J., Zawieja, D.C., and Hecker, J. (1990). Thermal effects of MR imaging: worst-case studies on sheep. *Am. J. Roentgenol.* *155*, 1105–1110.

- Basser, P.J., Mattiello, J., and LeBihan, D. (1994). MR diffusion tensor spectroscopy and imaging. *Biophys. J.* *66*, 259–267.
- Baudrexel, S., Nürnberger, L., Rüb, U., Seifried, C., Klein, J.C., Deller, T., Steinmetz, H., Deichmann, R., and Hilker, R. (2010). Quantitative mapping of T1 and T2* discloses nigral and brainstem pathology in early Parkinson's disease. *NeuroImage* *51*, 512–520.
- Bernarding, J., Braun, J., Hohmann, J., Mansmann, U., Hoehn-Berlage, M., Stapf, C., Wolf, K.J., and Tolxdorff, T. (2000). Histogram-based characterization of healthy and ischemic brain tissues using multiparametric MR imaging including apparent diffusion coefficient maps and relaxometry. *Magn. Reson. Med.* *43*, 52–61.
- Bernstein, M.A., King, K.F., and Zhou, X.J. (2004). *Handbook of MRI Pulse Sequences* (Elsevier).
- Bertram, H.C., Holdsworth, S.J., Whittaker, A.K., and Andersen, H.J. (2005). Salt diffusion and distribution in meat studied by ²³Na nuclear magnetic resonance imaging and relaxometry. *J. Agric. Food Chem.* *53*, 7814–7818.
- Bieri, O., Ganter, C., and Scheffler, K. (2012). Quantitative in vivo diffusion imaging of cartilage using double echo steady-state free precession. *Magn. Reson. Med.* *68*, 720–729.
- Bloch, F. (1946). Nuclear Induction. *Phys. Rev.* *70*, 460–474.
- Bloembergen, N., Purcell, E.M., and Pound, R.V. (1948). Relaxation Effects in Nuclear Magnetic Resonance Absorption. *Phys. Rev.* *73*, 679–712.
- Blystad, I., Warntjes, J.B.M., Smedby, Ö., Lundberg, P., Larsson, E.-M., and Tisell, A. (2017). Quantitative MRI for analysis of peritumoral edema in malignant gliomas. *PLOS ONE* *12*, e0177135.
- Boesen, L., Chabanova, E., Løgager, V., Balslev, I., and Thomsen, H.S. (2015). Apparent diffusion coefficient ratio correlates significantly with prostate cancer gleason score at final pathology. *J. Magn. Reson. Imaging* *42*, 446–453.
- Bottomley, P.A., and Andrew, E.R. (1978). RF magnetic field penetration, phase shift and power dissipation in biological tissue: implications for NMR imaging. *Phys. Med. Biol.* *23*, 630.
- Bottomley P. A., Hardy C. J., Argersinger R. E., and Allen-Moore G. (1998). A review of 1H nuclear magnetic resonance relaxation in pathology: Are T1 and T2 diagnostic? *Med. Phys.* *14*, 1–37.
- Bradley, W.G. (1993). MR appearance of hemorrhage in the brain. *Radiology* *189*, 15–26.
- Brink, W.M., and Webb, A.G. (2014). High permittivity pads reduce specific absorption rate, improve B1 homogeneity, and increase contrast-to-noise ratio for functional cardiac MRI at 3 T. *Magn. Reson. Med.* *71*, 1632–1640.

- Brink, W.M., Remis, R.F., and Webb, A.G. (2016). A theoretical approach based on electromagnetic scattering for analysing dielectric shimming in high-field MRI. *Magn. Reson. Med.* 75, 2185–2194.
- Brück, W., Bitsch, A., Kolenda, H., Brück, Y., Stiefel, M., and Lassmann, H. (2004). Inflammatory central nervous system demyelination: Correlation of magnetic resonance imaging findings with lesion pathology. *Ann. Neurol.* 42, 783–793.
- Bruder, H., Fischer, H., Graumann, R., and Deimling, M. (1988). A new steady-state imaging sequence for simultaneous acquisition of two MR images with clearly different contrasts. *Magn. Reson. Med.* 7, 35–42.
- Buxton, R.B. (1993). The diffusion sensitivity of fast steady-state free precession imaging. *Magn. Reson. Med.* 29, 235–243.
- Carr, H.Y. (1958). Steady-State Free Precession in Nuclear Magnetic Resonance. *Phys. Rev.* 112, 1693–1701.
- Carr, H.Y., and Purcell, E.M. (1954). Effects of Diffusion on Free Precession in Nuclear Magnetic Resonance Experiments. *Phys. Rev.* 94, 630–638.
- Chavhan, G.B., Babyn, P.S., Thomas, B., Shroff, M.M., and Haacke, E.M. (2009). Principles, Techniques, and Applications of T2*-based MR Imaging and Its Special Applications. *Radiographics* 29, 1433–1449.
- Chen, Y., Jiang, Y., Pahwa, S., Ma, D., Lu, L., Twieg, M.D., Wright, K.L., Seiberlich, N., Griswold, M.A., and Gulani, V. (2016). MR Fingerprinting for Rapid Quantitative Abdominal Imaging. *Radiology* 279, 278–286.
- Cheng, H.-L.M., Stikov, N., Ghugre, N.R., and Wright, G.A. (2012). Practical medical applications of quantitative MR relaxometry. *J. Magn. Reson. Imaging* 36, 805–824.
- Cho, S., Jones, D., Reddick, W.E., Ogg, R.J., and Steen, R.G. (1997). Establishing norms for age-related changes in proton T1 of human brain tissue in vivo. *Magn. Reson. Imaging* 15, 1133–1143.
- Cloos, M.A., Boulant, N., Luong, M., Ferrand, G., Giacomini, E., Hang, M.-F., Wiggins, C.J., Le Bihan, D., and Amadon, A. (2012). Parallel-transmission-enabled magnetization-prepared rapid gradient-echo T1-weighted imaging of the human brain at 7 T. *NeuroImage* 62, 2140–2150.
- Cloos, M.A., Knoll, F., Zhao, T., Block, K.T., Bruno, M., Wiggins, G.C., and Sodickson, D.K. (2016). Multiparametric imaging with heterogeneous radiofrequency fields. *Nat. Commun.* 7, 12445.
- Connell, I.R.O., Gilbert, K.M., Abou-Khousa, M.A., and Menon, R.S. (2015). Design of a parallel transmit head coil at 7T with magnetic wall distributed filters. *IEEE Trans. Med. Imaging* 34, 836–845.
- Coste, A., Chauffert, N., Vignaud, A., Ciuciu, P., Boumezbeur, F., Weiss, P., Romanzetti, S., Le Bihan, D., and Lerman, C. (2016). Assessment of benefit to use a non-Cartesian trajectory

and nonlinear reconstruction method compared to a Cartesian strategy for fast ^{31}P MRI. In *Proc. Intl. Soc. Mag. Reson. Med.* 24, p. 3940.

Crawley, A.P., Wood, M.L., and Henkelman, R.M. (1988). Elimination of transverse coherences in FLASH MRI. *Magn. Reson. Med.* 8, 248–260.

Damadian, R. (1971). Tumor Detection by Nuclear Magnetic Resonance. *Science* 171, 1151–1153.

Darrasse, L., Mao, L., and Saint-James, H. (1986). Steady-State management in fast low-angle imaging. In *Proc. Soc. Mag. Reson. Med.*, p. 944.

Deichmann, R. (2005). Fast high-resolution T1 mapping of the human brain. *Magn. Reson. Med.* 54, 20–27.

Deichmann, R., and Haase, A. (1992). Quantification of T1 values by SNAPSHOT-FLASH NMR imaging. *J. Magn. Reson.* 96, 608–612.

Deniz, C.M., Alon, L., Brown, R., and Zhu, Y. (2016). Subject- and resource-specific monitoring and proactive management of parallel radiofrequency transmission. *Magn. Reson. Med.* 76, 20–31.

Deoni, S.C.L. (2011). Magnetic resonance relaxation and quantitative measurement in the brain. *Methods Mol. Biol.* 711, 65–108.

Deoni, S.C.L., Rutt, B.K., and Peters, T.M. (2003). Rapid combined T1 and T2 mapping using gradient recalled acquisition in the steady state. *Magn. Reson. Med.* 49, 515–526.

Deoni, S.C.L., Peters, T.M., and Rutt, B.K. (2005). High-resolution T1 and T2 mapping of the brain in a clinically acceptable time with DESPOT1 and DESPOT2. *Magn. Reson. Med.* 53, 237–241.

Dobbing, J., and Sands, J. (1973). Quantitative growth and development of human brain. *Arch. Dis. Child.* 48, 757–767.

Dubois, M., Leroi, L., Raolison, Z., Abdeddaim, R., Antonakakis, T., de Rosny, J., Vignaud, A., Sabouroux, P., Georget, É., Larrat, B., et al. (2018). Kerker Effect in Ultra High Field Magnetic Resonance Imaging. *Phys. Rev. X* in press.

Elster, A.D. (2018). MRI Questions: Questions and Answers in MRI, <http://mriquestions.com>.

Erkinjuntti, T., Ketonen, L., Sulkava, R., Sipponen, J., Vuorialho, M., and Iivanainen, M. (1987). Do white matter changes on MRI and CT differentiate vascular dementia from Alzheimer's disease? *J. Neurol. Neurosurg. Psychiatry* 50, 37–42.

Ferrie, J.C., Barantin, L., Saliba, E., Akoka, S., Tranquart, F., Sirinelli, D., and Pourcelot, L. (1999). MR assessment of the brain maturation during the perinatal period: quantitative T2 MR study in premature newborns. *Magn. Reson. Imaging* 17, 1275–1288.

- Foy, B.D., and Burstein, D. (1990). Interstitial sodium nuclear magnetic resonance relaxation times in perfused hearts. *Biophys. J.* *58*, 127–134.
- Frahm, J., Hanicke, W., and Merboldt, K.-D. (1987). Transverse coherence in rapid FLASH NMR imaging. *J. Magn. Reson.* *1969* *72*, 307–314.
- Fram, E.K., Herfkens, R.J., Johnson, G.A., Glover, G.H., Karis, J.P., Shimakawa, A., Perkins, T.G., and Pelc, N.J. (1987). Rapid calculation of T1 using variable flip angle gradient refocused imaging. *Magn. Reson. Imaging* *5*, 201–208.
- Freed, D.E., Scheven, U.M., Zielinski, L.J., Sen, P.N., and Hürlimann, M.D. (2001). Steady-state free precession experiments and exact treatment of diffusion in a uniform gradient. *J. Chem. Phys.* *115*, 4249–4258.
- Freeman, R., and Hill, H.D.W. (1971). Phase and intensity anomalies in fourier transform NMR. *J. Magn. Reson.* *4*, 366–383.
- Freire, M.J., Jelinek, L., Marques, R., and Lapine, M. (2010). On the applications of metamaterial lenses for magnetic resonance imaging. *J. Magn. Reson.* *203*, 81–90.
- Garwood, M., and DelaBarre, L. (2001). The return of the frequency sweep: designing adiabatic pulses for contemporary NMR. *J. Magn. Reson.* *153*, 155–177.
- Ge, Y., Zohrabian, V.M., and Grossman, R.I. (2008). 7T MRI: New Vision of Microvascular Abnormalities in Multiple Sclerosis. *Arch. Neurol.* *65*, 812–816.
- Geffrin, J.M., García-Cámara, B., Gómez-Medina, R., Albella, P., Froufe-Pérez, L.S., Eyraud, C., Litman, A., Vaillon, R., González, F., Nieto-Vesperinas, M., et al. (2012). Magnetic and electric coherence in forward- and back-scattered electromagnetic waves by a single dielectric subwavelength sphere. *Nat. Commun.* *3*, 1171.
- van Gelderen, P., Jiang, X., and Duyn, J.H. (2016). Effects of Magnetization Transfer on T1 Contrast in Human Brain White Matter. *NeuroImage* *128*, 85–95.
- Georget, E., Luong, M., Vignaud, A., Giacomini, E., Chazel, E., Ferrand, G., Amadon, A., Mauconduit, F., Enoch, S., Tayeb, G., et al. (2017). Stacked magnetic resonators for MRI RF coils decoupling. *J. Magn. Reson.* *275*, 11–18.
- Ghugre, N.R., Enriquez, C.M., Gonzalez, I., Nelson, M.D., Coates, T.D., and Wood, J.C. (2006). MRI detects myocardial iron in the human heart. *Magn. Reson. Med.* *56*, 681–686.
- Giri, S., Chung, Y.-C., Merchant, A., Mihai, G., Rajagopalan, S., Raman, S.V., and Simonetti, O.P. (2009). T2 quantification for improved detection of myocardial edema. *J. Cardiovasc. Magn. Reson.* *11*, 56.
- Gnahm, C., and Nagel, A.M. (2015). Anatomically weighted second-order total variation reconstruction of ²³Na MRI using prior information from ¹H MRI. *NeuroImage* *105*, 452–461.

Goodman, J.A., Kroenke, C.D., Bretthorst, G.L., Ackerman, J.J.H., and Neil, J.J. (2005). Sodium ion apparent diffusion coefficient in living rat brain. *Magn. Reson. Med.* 53, 1040–1045.

Gras, V., Vignaud, A., Amadon, A., Le Bihan, D., and Boulant, N. (2017a). Universal pulses: A new concept for calibration-free parallel transmission. *Magn. Reson. Med.* 77, 635–643.

Gras, V., Farrher, E., Grinberg, F., and Shah, N.J. (2017b). Diffusion-weighted DESS protocol optimization for simultaneous mapping of the mean diffusivity, proton density and relaxation times at 3 Tesla. *Magn. Reson. Med.* 78, 130–141.

Gras, V., Bolland, M., Vignaud, A., Ferrand, G., Amadon, A., Mauconduit, F., Bihan, D.L., Stöcker, T., and Boulant, N. (2017c). Homogeneous non-selective and slice-selective parallel-transmit excitations at 7 Tesla with universal pulses: A validation study on two commercial RF coils. *PLOS ONE* 12, e0183562.

Grissom, W., Yip, C., Zhang, Z., Stenger, V.A., Fessler, J.A., and Noll, D.C. (2006). Spatial domain method for the design of RF pulses in multicoil parallel excitation. *Magn. Reson. Med.* 56, 620–629.

Griswold, M.A., Jakob, P.M., Heidemann, R.M., Nittka, M., Jellus, V., Wang, J., Kiefer, B., and Haase, A. (2002). Generalized autocalibrating partially parallel acquisitions (GRAPPA). *Magn. Reson. Med.* 47, 1202–1210.

Guiheneuf, T.M., Gibbs, S.J., and Hall, L.D. (1997). Measurement of the inter-diffusion of sodium ions during pork brining by one-dimensional ^{23}Na Magnetic Resonance Imaging (MRI). *J. Food Eng.* 31, 457–471.

Haacke, E.M., and Frahm, J. (1991). A guide to understanding key aspects of fast gradient-echo imaging. *J. Magn. Reson. Imaging* 1, 621–624.

Haacke, E.M., Brown, R.W., Thompson, M.R., Venkatesan, R., and Cheng, Y.-C.N. (2014). *Magnetic Resonance Imaging: Physical Principles and Sequence Design* (John Wiley & Sons).

Haase, A., Frahm, J., Matthaei, D., Hanicke, W., and Merboldt, K.-D. (1986). FLASH imaging. Rapid NMR imaging using low flip-angle pulses. *J. Magn. Reson.* 67, 258–266.

Hagiwara, A., Hori, M., Yokoyama, K., Takemura, M.Y., Andica, C., Tabata, T., Kamagata, K., Suzuki, M., Kumamaru, K.K., Nakazawa, M., et al. (2017). Synthetic MRI in the Detection of Multiple Sclerosis Plaques. *Am. J. Neuroradiol.* 38, 257–263.

Hahn, E.L. (1950). Spin Echoes. *Phys. Rev.* 80, 580–594.

Hambrock, T., Somford, D.M., Huisman, H.J., van Oort, I.M., Witjes, J.A., Hulsbergen-van de Kaa, C.A., Scheenen, T., and Barentsz, J.O. (2011). Relationship between apparent diffusion coefficients at 3.0-T MR imaging and Gleason grade in peripheral zone prostate cancer. *Radiology* 259, 453–461.

Hammer, M. (2013). MRI Physics: MRI Pulse Sequences - XRayPhysics, <http://xrayphysics.com/sequences.html>.

- Hammond, K.E., Lupo, J.M., Xu, D., Metcalf, M., Kelley, D.A.C., Pelletier, D., Chang, S.M., Mukherjee, P., Vigneron, D.B., and Nelson, S.J. (2008). Development of a robust method for generating 7.0 T multichannel phase images of the brain with application to normal volunteers and patients with neurological diseases. *NeuroImage* 39, 1682–1692.
- Hansen, C.L., van der Berg, F., Ringgaard, S., Stødtkilde-Jørgensen, H., and Karlsson, A.H. (2008). Diffusion of NaCl in meat studied by ^1H and ^{23}Na magnetic resonance imaging. *Meat Sci.* 80, 851–856.
- Hara, M., Kuroda, M., Ohmura, Y., Matsuzaki, H., Kobayashi, T., Murakami, J., Katashima, K., Ashida, M., Ohno, S., and Asaumi, J.-I. (2014). A new phantom and empirical formula for apparent diffusion coefficient measurement by a 3 Tesla magnetic resonance imaging scanner. *Oncol. Lett.* 8, 819–824.
- van der Heide, O., Sbrizzi, A., Kruseman, A., Cloos, M.A., Luijten, P.R., and van den Berg, C.A.T. (2017). In-vivo Validation of MR-STAT: Simultaneous Signal Localization and Quantification of Tissue Parameters on a 3T Clinical MR-System. In *Proc. Intl. Soc. Mag. Reson. Med.* 25, p. 3962.
- Helpert, J.A., Jensen, J., Lee, S.-P., and Falangola, M.F. (2004). Quantitative MRI assessment of Alzheimer's disease. *J. Mol. Neurosci.* 24, 45–48.
- Henderson, E., McKinnon, G., Lee, T.Y., and Rutt, B.K. (1999). A fast 3D look-locker method for volumetric T1 mapping. *Magn. Reson. Imaging* 17, 1163–1171.
- Hennig, J. (1991a). Echoes—how to generate, recognize, use or avoid them in MR-imaging sequences. Part I: Fundamental and not so fundamental properties of spin echoes. *Concepts Magn. Reson.* 3, 125–143.
- Hennig, J. (1991b). Echoes—how to generate, recognize, use or avoid them in MR-imaging sequences. Part II: Echoes in imaging sequences. *Concepts Magn. Reson.* 3, 179–192.
- Heule, R., Ganter, C., and Bieri, O. (2014). Triple echo steady-state (TESS) relaxometry. *Magn. Reson. Med.* 71, 230–237.
- Higer, H.P., and Bielke, G. (2012). *Tissue Characterization in MR Imaging: Clinical and Technical Approaches* (Springer Science & Business Media).
- Hilbert, T., Kober, T., Zhao, T., Block, K.T., Yu, Z., Thiran, J.-P., Krueger, G., Sodickson, D.K., and Cloos, M.A. (2017). Mitigating the Effect of Magnetization Transfer in Magnetic Resonance Fingerprinting. In *Proc. Intl. Soc. Mag. Reson. Med.* 25, p. 74.
- Holloway, C.L., Kuester, E.F., Gordon, J.A., O'Hara, J., Booth, J., and Smith, D.R. (2012). An Overview of the Theory and Applications of Metasurfaces: The Two-Dimensional Equivalents of Metamaterials. *IEEE Antennas Propag. Mag.* 54, 10–35.
- Hoult, D.I. (2000a). Sensitivity and Power Deposition in a High-Field Imaging Experiment. *J. Magn. Reson. Imaging* 12, 46–67.
- Hoult, D.I. (2000b). The principle of reciprocity in signal strength calculations—A mathematical guide. *Concepts Magn. Reson.* 12, 173–187.

- Hoult, D.I., and Lauterbur, P.C. (1979). The sensitivity of the zeugmatographic experiment involving human samples. *J. Magn. Reson.* 1969 *34*, 425–433.
- Hurley, S.A., Yarnykh, V.L., Johnson, K.M., Field, A.S., Alexander, A.L., and Samsonov, A.A. (2012). Simultaneous variable flip angle–actual flip angle imaging method for improved accuracy and precision of three-dimensional T1 and B1 measurements. *Magn. Reson. Med.* 68, 54–64.
- Hurshkainen, A.A., Derzhavskaya, T.A., Glybovski, S.B., Voogt, I.J., Melchakova, I.V., van den Berg, C.A.T., and Raaijmakers, A.J.E. (2016). Element decoupling of 7T dipole body arrays by EBG metasurface structures: Experimental verification. *J. Magn. Reson.* 269, 87–96.
- Hutchison Robert B., and Shapiro Joseph I. (1991). Measurement of intracellular sodium with NMR methods. *Concepts Magn. Reson.* 3, 215–236.
- Jaccard, G., Wimperis, S., and Bodenhausen, G. (1986). Multiple-quantum NMR spectroscopy of $S=3/2$ spins in isotropic phase: A new probe for multiexponential relaxation. *J. Chem. Phys.* 85, 6282–6293.
- Jacobs, M.A., Ouwerkerk, R., Kamel, I., Bottomley, P.A., and Kim, H.S. (2009). Proton, Diffusion-weighted Imaging, and Sodium (^{23}Na) MRI of Uterine Leiomyomata after MR-guided High Intensity Focused Ultrasound: A Preliminary Study. *J. Magn. Reson. Imaging* 29, 649–656.
- Jakob, P.M., Hillenbrand, C.M., Wang, T., Schultz, G., Hahn, D., and Haase, A. (2001). Rapid quantitative lung ^1H T1 mapping. *J. Magn. Reson. Imaging* 14, 795–799.
- Jamin, Y., Tucker, E.R., Poon, E., Popov, S., Vaughan, L., Boulton, J.K.R., Webber, H., Hallsworth, A., Baker, L.C.J., Jones, C., et al. (2013). Evaluation of clinically translatable MR imaging biomarkers of therapeutic response in the TH-MYCN transgenic mouse model of neuroblastoma. *Radiology* 266, 130–140.
- Jiang, Y., Ma, D., Seiberlich, N., Gulani, V., and Griswold, M.A. (2015). MR fingerprinting using fast imaging with steady state precession (FISP) with spiral readout. *Magn. Reson. Med.* 74, 1621–1631.
- Jiang, Y., Ma, D., Jerecic, R., Duerk, J., Seiberlich, N., Gulani, V., and Griswold, M.A. (2017). MR fingerprinting using the quick echo splitting NMR imaging technique. *Magn. Reson. Med.* 77, 979–988.
- Jouvaud, C., Abdeddaim, R., Larrat, B., and de Rosny, J. (2016). Volume coil based on hybridized resonators for magnetic resonance imaging. *Appl. Phys. Lett.* 108, 023503.
- Just, M., and Thelen, M. (1988). Tissue characterization with T1, T2, and proton density values: results in 160 patients with brain tumors. *Radiology* 169, 779–785.
- Kaiser, R., Bartholdi, E., and Ernst, R.R. (1974). Diffusion and field-gradient effects in NMR Fourier spectroscopy. *J. Chem. Phys.* 60, 2966–2979.

- Kanté, B., Burokur, S.N., Sellier, A., de Lustrac, A., and Lourtioz, J.-M. (2009). Controlling plasmon hybridization for negative refraction metamaterials. *Phys. Rev. B* 79, 075121.
- Katscher, U., and Börnert, P. (2006). Parallel RF transmission in MRI. *NMR Biomed.* 19, 393–400.
- Kerker, M., Wang, D.-S., and Giles, C.L. (1983). Electromagnetic scattering by magnetic spheres. *J. Opt. Soc. Am.* 73, 765–767.
- Kim, H.G., Moon, W.-J., Han, J., and Choi, J.W. (2017). Quantification of myelin in children using multiparametric quantitative MRI: a pilot study. *Neuroradiology* 59, 1043–1051.
- Koopmans, P.J., Manniesing, R., Niessen, W.J., Viergever, M.A., and Barth, M. (2008). MR venography of the human brain using susceptibility weighted imaging at very high field strength. *Magma N. Y.* 21, 149–158.
- Larsson, H.B.W., Frederiksen, J., Petersen, J., Nordenbo, A., Zeeberg, I., Henriksen, O., and Olesen, J. (2005). Assessment of demyelination, edema, and gliosis by in vivo determination of T1 and T2 in the brain of patients with acute attack of multiple sclerosis. *Magn. Reson. Med.* 11, 337–348.
- Laubach, H.J., Jakob, P.M., Loevblad, K.O., Baird, A.E., Bovo, M.P., Edelman, R.R., and Warach, S. (1998a). A Phantom for diffusion-weighted imaging of acute stroke. *J. Magn. Reson. Imaging* 8, 1349–1354.
- Laubach, H.J., Jakob, P.M., Loevblad, K.O., Baird, A.E., Bovo, M.P., Edelman, R.R., and Warach, S. (1998b). A Phantom for diffusion-weighted imaging of acute stroke. *J. Magn. Reson. Imaging* 8, 1349–1354.
- Lauterbur, P.C. (1973). Image Formation by Induced Local Interactions: Examples Employing Nuclear Magnetic Resonance. *Nature* 242, 190–191.
- Lazarus, C., Weiss, P., Chauffert, N., Mauconduit, F., Bottlaender, M., Vignaud, A., and Ciuciu, P. (2017). SPARKLING: Novel Non-Cartesian Sampling Schemes for Accelerated 2D Anatomical Imaging at 7T Using Compressed Sensing. In *Proc. Intl. Soc. Mag. Reson. Med.* 25, (Proc. Intl. Soc. Mag. Reson. Med. 25), p. 1529.
- Le Bihan, D., Breton, E., Lallemand, D., Grenier, P., Cabanis, E., and Laval-Jeantet, M. (1986). MR imaging of intravoxel incoherent motions: application to diffusion and perfusion in neurologic disorders. *Radiology* 161, 401–407.
- Lecocq, A., Fur, Y.L., Amadon, A., Vignaud, A., Cozzone, P.J., Guye, M., and Ranjeva, J.-P. (2015). Fast water concentration mapping to normalize ¹H MR spectroscopic imaging. *Magn. Reson. Mater. Phys. Biol. Med.* 28, 87–100.
- Leroi, L., Coste, A., de Rochefort, L., Santin, M.D., Valabrègue, R., Mauconduit, F., Hang, M.-F., Chazel, E., Bernard, J., Luong, M., et al. (2017). Simultaneous multi-parametric and quantitative estimation of ²³Na physical properties at 7 Tesla using QuICS. In *Proc. Intl. Soc. Mag. Reson. Med.* 25, p. 5627.

- Liao, C., Wang, K., Cao, X., Li, Y., Wu, D., Ye, H., Ding, Q., He, H., and Zhong, J. (2018). Detection of Lesions in Mesial Temporal Lobe Epilepsy by Using MR Fingerprinting. *Radiology* 172131.
- Ma, D., Gulani, V., Seiberlich, N., Liu, K., Sunshine, J.L., Duerk, J.L., and Griswold, M.A. (2013). Magnetic resonance fingerprinting. *Nature* 495, 187–192.
- Madelin, G., and Regatte, R.R. (2013). Biomedical applications of sodium MRI in vivo. *J. Magn. Reson. Imaging* 38, 511–529.
- Madelin, G., Chang, G., Otazo, R., Jerschow, A., and Regatte, R.R. (2012). Compressed sensing sodium MRI of cartilage at 7T: Preliminary study. *J. Magn. Reson.* 214, 360–365.
- Marques, J.P., and Norris, D.G. (2018). How to choose the right MR sequence for your research question at 7T and above? *NeuroImage* 168, 119–140.
- Maxwell, J.C. (1865). A Dynamical Theory of the Electromagnetic Field. *Philos. Trans. R. Soc. Lond.* 155, 459–512.
- McAllister, A., Leach, J., West, H., Jones, B., Zhang, B., and Serai, S. (2017). Quantitative Synthetic MRI in Children: Normative Intracranial Tissue Segmentation Values during Development. *Am. J. Neuroradiol.* 38, 2364–2372.
- Meiboom, S., and Gill, D. (1958). Modified Spin-Echo Method for Measuring Nuclear Relaxation Times. *Rev. Sci. Instrum.* 29, 688–691.
- Meinzer, N., Barnes, W.L., and Hooper, I.R. (2014). Plasmonic meta-atoms and metasurfaces. *Nat. Photonics* 8, 889–898.
- Mezer, A., Yeatman, J.D., Stikov, N., Kay, K.N., Cho, N., Dougherty, R.F., Perry, M.L., Parvizi, J., Hua, L.H., Butts-Pauly, K., et al. (2013). Quantifying the local tissue volume and composition in individual brains with MRI. *Nat. Med.* 19, 1667–1672.
- Miller, K.L., Tijssen, R.H.N., Stikov, N., and Okell, T.W. (2011). Steady-state MRI: Methods for neuroimaging. *Imaging Med.* 3, 93–105.
- Moonen, C.T.W., Sobering, G., Van Zijl, P.C.M., Gillen, J., Von Kienlin, M., and Bizzi, A. (1992). Proton spectroscopic imaging of human brain. *J. Magn. Reson.* 98, 556–575.
- Morrell, G., Kaggie, J., Stein, M., parker, S., and Bangerter, N.K. (2016). Rapid high-resolution sodium relaxometry in human breast. In *Proc. Intl. Soc. Mag. Reson. Med.* 24, p. 404.
- Nagel, A.M., Umatham, R., Rösler, M.B., Ladd, M.E., Litvak, I., Gor’kov, P.L., Brey, W.W., and Schepkin, V.D. (2016). ³⁹K and ²³Na relaxation times and MRI of rat head at 21.1 T. *NMR Biomed.* 29, 759–766.
- Neeb, H., Zilles, K., and Shah, N.J. (2006). Fully-automated detection of cerebral water content changes: Study of age- and gender-related H₂O patterns with quantitative MRI. *NeuroImage* 29, 910–922.

- Neeb, H., Ermer, V., Stocker, T., and Shah, N.J. (2008). Fast quantitative mapping of absolute water content with full brain coverage. *NeuroImage* *42*, 1094–1109.
- Nekolla, S., Gneiting, T., Syha, J., Deichmann, R., and Haase, A. (1992). T1 maps by K-space reduced snapshot-FLASH MRI. *J. Comput. Assist. Tomogr.* *16*, 327–332.
- Nelson, T.R., and Tung, S.M. (1987). Temperature dependence of proton relaxation times in vitro. *Magn. Reson. Imaging* *5*, 189–199.
- Neves, A.L., Leroi, L., Raolison, Z., Cochinaire, N., Letertre, T., Abdeddaïm, R., Enoch, S., Wenger, J., Berthelot, J., Adenot-Engelvin, A.-L., et al. (2018). Compressed perovskite aqueous mixtures near their phase transitions show very high permittivities: New prospects for high-field MRI dielectric shimming. *Magn. Reson. Med.* *79*, 1753–1765.
- O'Brien, K.R., Magill, A.W., Delacoste, J., Marques, J.P., Kober, T., Fautz, H.-P., Lazeyras, F., and Krueger, G. (2014). Dielectric pads and low- B1+ adiabatic pulses: Complementary techniques to optimize structural T1w whole-brain MP2RAGE scans at 7 tesla. *J. Magn. Reson. Imaging* *40*, 804–812.
- Ocali, O., and Atalar, E. (1998). Ultimate intrinsic signal-to-noise ratio in MRI. *Magn. Reson. Med.* *39*, 462–473.
- Odrobina, E.E., Lam, T.Y.J., Pun, T., Midha, R., and Stanisz, G.J. (2005). MR properties of excised neural tissue following experimentally induced demyelination. *NMR Biomed.* *18*, 277–284.
- O'Halloran, R., Aksoy, M., Aboussouan, E., Peterson, E., Van, A., and Bammer, R. (2015). Real-Time Correction of Rigid-Body-Motion-Induced Phase Errors for Diffusion-Weighted Steady State Free Precession Imaging. *Magn. Reson. Med. Off. J. Soc. Magn. Reson. Med. Soc. Magn. Reson. Med.* *73*, 565–576.
- Oppelt, A., Graumann, R., and Barfuss, H. (1986). FISP : a new fast MRI sequence. *Electro-medica* *54*, 15–18.
- Padormo, F., Beqiri, A., Hajnal, J.V., and Malik, S.J. (2016). Parallel transmission for ultra-high-field imaging. *NMR Biomed.* *29*, 1145–1161.
- Parker, G.J.M., Barker, G.J., and Tofts, P.S. (2001). Accurate multislice gradient echo T1 measurement in the presence of non-ideal RF pulse shape and RF field nonuniformity. *Magn. Reson. Med.* *45*, 838–845.
- Pauly, J., Roux, P.L., Nishimura, D., and Macovski, A. (1991). Parameter relations for the Shinnar-Le Roux selective excitation pulse design algorithm. *IEEE Trans. Med. Imaging* *10*, 53–65.
- Paus, T., Collins, D.L., Evans, A.C., Leonard, G., Pike, B., and Zijdenbos, A. (2001). Maturation of white matter in the human brain: a review of magnetic resonance studies. *Brain Res. Bull.* *54*, 255–266.

Pendry, J.B., Holden, A.J., Robbins, D.J., and Stewart, W.J. (1999). Magnetism from conductors and enhanced nonlinear phenomena. *IEEE Trans. Microw. Theory Tech.* 47, 2075–2084.

Pipe, J.G. (1999). Motion correction with PROPELLER MRI: Application to head motion and free-breathing cardiac imaging. *Magn. Reson. Med.* 42, 963–969.

Pohmann, Speck, and Scheffler (2015). Signal-to-noise ratio and MR tissue parameters in human brain imaging at 3, 7, and 9.4 tesla using current receive coil arrays. *Magn. Reson. Med.* 75, 801–809.

Polimeni, J.R., and Uludağ, K. (2018). Neuroimaging with ultra-high field MRI: Present and future. *NeuroImage* 168, 1–6.

Preibisch, C., and Deichmann, R. (2009). Influence of RF spoiling on the stability and accuracy of T1 mapping based on spoiled FLASH with varying flip angles. *Magn. Reson. Med.* 61, 125–135.

Press, W.H., Teukolsky, S.A., Vetterling, W.T., and Flannery, B.P. (2007). *Numerical Recipes 3rd Edition: The Art of Scientific Computing* (Cambridge University Press).

Pruessmann, K.P., Weiger, M., Scheidegger, M.B., and Boesiger, P. (1999). SENSE: sensitivity encoding for fast MRI. *Magn. Reson. Med.* 42, 952–962.

Radu, X., Garra, D., and Craeye, C. (2009). Toward a wire medium endoscope for MRI imaging. *Metamaterials* 3, 90–99.

Recht, M.P., and Resnick, D. (1998). Magnetic resonance imaging of articular cartilage: an overview. *Top. Magn. Reson. Imaging* 9, 328–336.

Reese, T.G., Weisskoff, R.M., and Wedeen, V.. J. (1998). Diffusion NMR facilitated by a refocused eddy-current EPI pulse sequence. In *Proc. Intl. Soc. Mag. Reson. Med.* 6, p. 663.

Ribeiro, A.C.F., Lobo, V.M.M., Sobral, A.J.F.N., Soares, H.T.F.C., Estes, A.R.J., and Estes, M.A. (2010). Diffusion coefficients of sodium fluoride in aqueous solutions at 298.15 K and 310.15 K. *Acta Chim. Slov.* 57, 410–414.

Ridgway, J.P. (2010). Cardiovascular magnetic resonance physics for clinicians: part I. *J. Cardiovasc. Magn. Reson.* 12, 71.

Ridley, B., Nagel, A.M., Bydder, M., Maarouf, A., Stellmann, J.-P., Gherib, S., Verneuil, J., Viout, P., Guye, M., Ranjeva, J.-P., et al. (2018). Distribution of brain sodium long and short relaxation times and concentrations: a multi-echo ultra-high field ^{23}Na MRI study. *Sci. Rep.* 8, 4357.

Robinson, S., Grabner, G., Witoszynskyj, S., and Trattnig, S. (2011). Combining phase images from multi-channel RF coils using 3D phase offset maps derived from a dual-echo scan. *Magn. Reson. Med.* 65, 1638–1648.

de Rochefort, L. (2015). Encoding with Radiofrequency Spoiling, Equilibrium States and Inverse Problem for Parametric Mapping. In *Proc. Intl. Soc. Mag. Reson. Med.* 23, p. 445.

- de Rochefort, L. (2016). Method and device for imaging by magnetic resonance (WO 2016/180947 A1).
- de Rochefort, L., Guillot, G., Dubuisson, R.-M., and Valabrégue, R. (2016). In Vivo Feasibility of Multi-Parametric Mapping Based on Fast Steady-State Sequences. In Proc. Intl. Soc. Mag. Reson. Med. 24, p. 1823.
- Roux, P.L., and Hinks, R.S. (1993). Stabilization of echo amplitudes in FSE sequences. Magn. Reson. Med. 30, 183–190.
- Rupprecht, S., Sica, C.T., Sahul, R., Kwon, S., Lanagan, M.T., and Yang, Q.X. (2013). Drastic Enhancement and Manipulation of RF Field with Ultra High Dielectric Constant (uHDC) Material at 3T. In Proc. Intl. Soc. Mag. Reson. Med., p. 396.
- Santin, M.D. (2018). Pending Patent, #1759804/1000427656.
- Saylor, C.A. (2008). High-field mode-stable resonator for magnetic resonance imaging, US7345482 B2.
- Sbrizzi, A., van der Toorn, A., Hoogduin, H., Luijten, P.R., and van den Berg, C.A.T. (2015). Spin TomogrAphy in Time domain: the MR-STAT project. In Proc. Intl. Soc. Mag. Reson. Med. 23, p. 3712.
- Sbrizzi, A., Heide, O. van der, Cloos, M., Toorn, A. van der, Hoogduin, H., Luijten, P.R., and van den Berg, C.A.T. (2018). Fast quantitative MRI as a nonlinear tomography problem. Magn. Reson. Imaging 46, 56–63.
- Scheffler, K. (1999). A pictorial description of steady-states in rapid magnetic resonance imaging. Concepts Magn. Reson. 11, 291–304.
- Scheffler, K., and Hennig, J. (2001). T1 quantification with inversion recovery TrueFISP. Magn. Reson. Med. 45, 720–723.
- Scheffler, K., and Lehnhardt, S. (2003). Principles and applications of balanced SSFP techniques. Eur. Radiol. 13, 2409–2418.
- Schein, A., Enriquez, C., Coates, T.D., and Wood, J.C. (2008). Magnetic resonance detection of kidney iron deposition in sickle cell disease: a marker of chronic hemolysis. J. Magn. Reson. Imaging 28, 698–704.
- Schmitt, P., Griswold, M.A., Jakob, P.M., Kotas, M., Gulani, V., Flentje, M., and Haase, A. (2004). Inversion recovery TrueFISP: Quantification of T1, T2, and spin density. Magn. Reson. Med. 51, 661–667.
- Schwenzer, N.F., Machann, J., Haap, M.M., Martirosian, P., Schraml, C., Liebig, G., Stefan, N., Häring, H.-U., Claussen, C.D., Fritsche, A., et al. (2008). T2* relaxometry in liver, pancreas, and spleen in a healthy cohort of one hundred twenty-nine subjects-correlation with age, gender, and serum ferritin. Invest. Radiol. 43, 854–860.
- Shah, N.J., Zaitsev, M., Steinhoff, S., and Zilles, K. (2001). A New Method for Fast Multislice T1 Mapping. NeuroImage 14, 1175–1185.

- Shajan, G., Mirkes, C., Buckenmaier, K., Hoffmann, J., Pohmann, R., and Scheffler, K. (2016). Three-layered radio frequency coil arrangement for sodium MRI of the human brain at 9.4 Tesla. *Magn. Reson. Med.* *75*, 906–916.
- Shchelokova, A.V., Slobozhanyuk, A.P., de Bruin, P., Zivkovic, I., Kallos, E., Belov, P.A., and Webb, A. (2018). Experimental investigation of a metasurface resonator for in vivo imaging at 1.5 T. *J. Magn. Reson.* *286*, 78–81.
- Slobozhanyuk, A.P., Poddubny, A.N., Raaijmakers, A.J.E., Berg, C.A.T. van den, Kozachenko, A.V., Dubrovina, I.A., Melchakova, I.V., Kivshar, Y.S., and Belov, P.A. (2016). Enhancement of Magnetic Resonance Imaging with Metasurfaces. *Adv. Mater.* *28*, 1832–1838.
- Slotboom, J., Mehlkopf, A.F., and Bovée, W.M.M.J. (1991). A single-shot localization pulse sequence suited for coils with inhomogeneous RF fields using adiabatic slice-selective RF pulses. *J. Magn. Reson.* *95*, 396–404.
- de Sousa, P.L., Vignaud, A., Fleury, S., and Carlier, P.G. (2011). Fast monitoring of T₁, T₂, and relative proton density (M₀) changes in skeletal muscles using an IR-TrueFISP sequence. *J. Magn. Reson. Imaging* *33*, 921–930.
- de Sousa, P.L., Vignaud, A., Caldas de Almeida Araújo, E., and Carlier, P.G. (2012). Factors controlling T₂ mapping from partially spoiled SSFP sequence: Optimization for skeletal muscle characterization. *Magn. Reson. Med.* *67*, 1379–1390.
- Staroswiecki, E., Nnewihe, A., Bangerter, N.K., Daniel, B.L., and Hargreaves, B.A. (2009). In Vivo Sodium Imaging and Relaxometry of the Breast at 3T. (*Proc. Intl. Soc. Mag. Reson. Med.* *17*), p. 2129.
- Staroswiecki, E., Granlund, K.L., Alley, M.T., Gold, G.E., and Hargreaves, B.A. (2012). Simultaneous estimation of T₂ and apparent diffusion coefficient in human articular cartilage in vivo with a modified three-dimensional double echo steady state (DESS) sequence at 3 T. *Magn. Reson. Med.* *67*, 1086–1096.
- Steinhoff, S., Zaitsev, M., Zilles, K., and Shah, N.J. (2001). Fast T₁(1) mapping with volume coverage. *Magn. Reson. Med.* *46*, 131–140.
- Stejskal, E.O., and Tanner, J.E. (1965). Spin Diffusion Measurements: Spin Echoes in the Presence of a Time-Dependent Field Gradient. *J. Chem. Phys.* *42*, 288–292.
- Stüber, C., Morawski, M., Schäfer, A., Labadie, C., Wähnert, M., Leuze, C., Streicher, M., Barapatre, N., Reimann, K., Geyer, S., et al. (2014). Myelin and iron concentration in the human brain: a quantitative study of MRI contrast. *NeuroImage* *93*, 95–106.
- Sullivan, D.C., Obuchowski, N.A., Kessler, L.G., Raunig, D.L., Gatsonis, C., Huang, E.P., Kondratovich, M., McShane, L.M., Reeves, A.P., Barboriak, D.P., et al. (2015). Metrology Standards for Quantitative Imaging Biomarkers. *Radiology* *277*, 813–825.

- Teeuwisse, W.M., Brink, W.M., and Webb, A.G. (2012a). Quantitative assessment of the effects of high-permittivity pads in 7 Tesla MRI of the brain. *Magn. Reson. Med.* 67, 1285–1293.
- Teeuwisse, W.M., Brink, W.M., Haines, K.N., and Webb, A.G. (2012b). Simulations of high permittivity materials for 7 T neuroimaging and evaluation of a new barium titanate-based dielectric. *Magn. Reson. Med.* 67, 912–918.
- Thulborn, K.R. (2018). Quantitative sodium MR imaging: A review of its evolving role in medicine. *NeuroImage* 168, 250–268.
- Tofts, P. (2005). *Quantitative MRI of the Brain: Measuring Changes Caused by Disease* (John Wiley & Sons).
- Torrey, H.C. (1956). Bloch Equations with Diffusion Terms. *Phys. Rev.* 104, 563–565.
- Townsend, T.N., Bernasconi, N., Pike, G.B., and Bernasconi, A. (2004). Quantitative analysis of temporal lobe white matter T2 relaxation time in temporal lobe epilepsy. *NeuroImage* 23, 318–324.
- Trattinig, S., Winalski, C.S., Marlovits, S., Jurvelin, J.S., Welsch, G.H., and Potter, H.G. (2011). Magnetic Resonance Imaging of Cartilage Repair. *Cartilage* 2, 5–26.
- Valabrègue, R., and de Rochefort, L. (2016). Fisher Information Matrix for Optimizing the Acquisition Parameters in Multi-Parametric Mapping Based on Fast Steady-State Sequences. In *Proc. Intl. Soc. Mag. Reson. Med.* 24, p. 1569.
- van Valenberg, W., Vos, F., Klein, S., ven Vliet, L., and Poot, D. (2017). Determining the Time Efficiency of Quantitative MRI Methods using Bloch Simulations. In *Proc. Intl. Soc. Mag. Reson. Med.* 25, p. 1470.
- Van de Moortele, P.-F., Akgun, C., Adriany, G., Moeller, S., Ritter, J., Collins, C.M., Smith, M.B., Vaughan, J.T., and Ugurbil, K. (2005). B1 destructive interferences and spatial phase patterns at 7 T with a head transceiver array coil. *Magn. Reson. Med.* 54, 1503–1518.
- Van de Werf, F., Bax, J., Betriu, A., Blomstrom-Lundqvist, C., Crea, F., Falk, V., Filippatos, G., Fox, K., Huber, K., Kastrati, A., et al. (2008). Management of acute myocardial infarction in patients presenting with persistent ST-segment elevation: the Task Force on the Management of ST-Segment Elevation Acute Myocardial Infarction of the European Society of Cardiology. *Eur. Heart J.* 29, 2909–2945.
- Vannesjo, S.J., Dietrich, B.E., Pavan, M., Brunner, D.O., Wilm, B.J., Barmet, C., and Pruessmann, K.P. (2014). Field camera measurements of gradient and shim impulse responses using frequency sweeps. *Magn. Reson. Med.* 72, 570–583.
- Vasanawala, S.S., Pauly, J.M., and Nishimura, D.G. (2000). Linear combination steady-state free precession MRI. *Magn. Reson. Med.* 43, 82–90.
- Voelker, M.N., Kraff, O., Brenner, D., Wollrab, A., Weinberger, O., Berger, M.C., Robinson, S., Bogner, W., Wiggins, C., Trampel, R., et al. (2016). The traveling heads: multicenter brain imaging at 7 Tesla. *Magn. Reson. Mater. Phys. Biol. Med.* 29, 399–415.

- Volz, S., Nöth, U., Rotarska-Jagiela, A., and Deichmann, R. (2010). A fast B1-mapping method for the correction and normalization of magnetization transfer ratio maps at 3 T. *NeuroImage* *49*, 3015–3026.
- Volz, S., Nöth, U., and Deichmann, R. (2012). Correction of systematic errors in quantitative proton density mapping. *Magn. Reson. Med.* *68*, 74–85.
- Vymazal, J., Righini, A., Brooks, R.A., Canesi, M., Mariani, C., Leonardi, M., and Pezzoli, G. (1999). T1 and T2 in the brain of healthy subjects, patients with Parkinson disease, and patients with multiple system atrophy: relation to iron content. *Radiology* *211*, 489–495.
- Walsh, D.O., Gmitro, A.F., and Marcellin, M.W. (2000). Adaptive reconstruction of phased array MR imagery. *Magn. Reson. Med.* *43*, 682–690.
- Wang, J., Qiu, M., and Constable, R.T. (2005). In vivo method for correcting transmit/receive nonuniformities with phased array coils. *Magn. Reson. Med.* *53*, 666–674.
- Wangsness, R.K., and Bloch, F. (1953). The Dynamical Theory of Nuclear Induction. *Phys. Rev.* *89*, 728–739.
- Warntjes, J. b. m., Dahlqvist, O., and Lundberg, P. (2007). Novel method for rapid, simultaneous T1, T*2, and proton density quantification. *Magn. Reson. Med.* *57*, 528–537.
- Warntjes, J. b. m., Leinhard, O.D., West, J., and Lundberg, P. (2008). Rapid magnetic resonance quantification on the brain: Optimization for clinical usage. *Magn. Reson. Med.* *60*, 320–329.
- Webb, A. g. (2011). Dielectric materials in magnetic resonance. *Concepts Magn. Reson. Part A* *38A*, 148–184.
- Weidensteiner, C., Allegrini, P.R., Sticker-Jantscheff, M., Romanet, V., Ferretti, S., and McSheehy, P.M.J. (2014). Tumour T1 changes in vivo are highly predictive of response to chemotherapy and reflect the number of viable tumour cells—a preclinical MR study in mice. *BMC Cancer* *14*, 88.
- Weigel, M. (2015). Extended phase graphs: Dephasing, RF pulses, and echoes - pure and simple. *J. Magn. Reson. Imaging* *41*, 266–295.
- Welsch, G.H., Scheffler, K., Mamisch, T.C., Hughes, T., Millington, S., Deimling, M., and Trattnig, S. (2009). Rapid estimation of cartilage T2 based on double echo at steady state (DESS) with 3 Tesla. *Magn. Reson. Med.* *62*, 544–549.
- Whittall, K.P., MacKay, A.L., Graeb, D.A., Nugent, R.A., Li, D.K., and Paty, D.W. (1997). In vivo measurement of T2 distributions and water contents in normal human brain. *Magn. Reson. Med.* *37*, 34–43.
- Wiggins, G.C., Polimeni, J.R., Potthast, A., Schmitt, M., Alagappan, V., and Wald, L.L. (2009). 96-Channel Receive-Only Head Coil for 3 Tesla: Design Optimization and Evaluation. *Magn. Reson. Med.* *62*, 754–762.

- Wiltshire, M.C.K., Pendry, J.B., Young, I.R., Larkman, D.J., Gilderdale, D.J., and Hajnal, J.V. (2001). Microstructured Magnetic Materials for RF Flux Guides in Magnetic Resonance Imaging. *Science* 291, 849–851.
- Winfield, J.M., Collins, D.J., Priest, A.N., Quest, R.A., Glover, A., Hunter, S., Morgan, V.A., Freeman, S., Rockall, A., and deSouza, N.M. (2016). A framework for optimization of diffusion-weighted MRI protocols for large field-of-view abdominal-pelvic imaging in multicenter studies. *Med. Phys.* 43, 95–110.
- Xu, Z., Lyu, M., Hui, E., Mei, Y., Chen, Z., Chen, W., Wu, E.X., and Feng, Y. (2017). Motion Correction for Magnetic Resonance Fingerprinting by Using Sliding-Window Reconstruction and Image Registration. In *Proc. Intl. Soc. Mag. Reson. Med.* 25, p. 1273.
- Yang, Q.X., Mao, W., Wang, J., Smith, M.B., Lei, H., Zhang, X., Ugurbil, K., and Chen, W. (2006). Manipulation of image intensity distribution at 7.0 T: Passive RF shimming and focusing with dielectric materials. *J. Magn. Reson. Imaging* 24, 197–202.
- Yarnykh, V.L. (2007). Actual flip-angle imaging in the pulsed steady state: A method for rapid three-dimensional mapping of the transmitted radiofrequency field. *Magn. Reson. Med.* 57, 192–200.
- Yeatman, J.D., Wandell, B.A., and Mezer, A.A. (2014). Lifespan maturation and degeneration of human brain white matter. *Nat. Commun.* 5, 4932.
- Yip, C., Fessler, J.A., and Noll, D.C. (2005). Iterative RF pulse design for multidimensional, small-tip-angle selective excitation. *Magn. Reson. Med.* 54, 908–917.
- Yu, A.C., Badve, C., Ponsky, L.E., Pahwa, S., Dastmalchian, S., Rogers, M., Jiang, Y., Margevicius, S., Schluchter, M., Tabayoyong, W., et al. (2017). Development of a Combined MR Fingerprinting and Diffusion Examination for Prostate Cancer. *Radiology* 283, 729–738.
- Yuan, C., and Kerwin, W.S. (2004). MRI of atherosclerosis. *J. Magn. Reson. Imaging* 19, 710–719.
- Zbyn, S., Juras, V., Bogner, W., Szomolanyi, P., Welsch, G.H., Bittsanky, M., Mlynarik, V., Moser, E., and Trattnig, S. (2009). Sodium in vivo measurement of T1 and T2* relaxation times of articular cartilage at 7 Tesla. In *Proc. Intl. Soc. Mag. Reson. Med.* 17, p. 3997.
- Zelinka, I. (2004). SOMA — Self-Organizing Migrating Algorithm. In *New Optimization Techniques in Engineering*, (Springer, Berlin, Heidelberg), pp. 167–217.
- Zhang, Y., Poirer-Quinot, M., Springer, C.S., and Balschi, J.A. (2010). Discrimination of intra- and extracellular $^{23}\text{Na}^+$ signals in yeast cell suspensions using longitudinal magnetic resonance relaxography. *J. Magn. Reson.* 205, 28–37.
- Zhao, B., Haldar, J.P., Setsompop, K., and Wald, L.L. (2016). Optimal experiment design for magnetic resonance fingerprinting. In *38th Annual International Conference of the IEEE Engineering in Medicine and Biology Society (EMBC)*, pp. 453–456.

van Zijl, P.C., Moonen, C.T., Alger, J.R., Cohen, J.S., and Chesnick, S.A. (1989). High field localized proton spectroscopy in small volumes: greatly improved localization and shimming using shielded strong gradients. *Magn. Reson. Med.* *10*, 256–265.

Zur, Y., Wood, M.L., and Neuringer, L.J. (1991). Spoiling of transverse magnetization in steady-state sequences. *Magn. Reson. Med.* *21*, 251–263.

Zur, Y., Bosak, E., and Kaplan, N. (1997). A new diffusion SSFP imaging technique. *Magn. Reson. Med.* *37*, 716–722.

Titre : IRM de quantification : vers des cartographies T_1 , T_2 , DP rapides et fiables à très hauts champs magnétiques chez l'homme

Mots clés : IRM quantitative, relaxométrie, T_1 , T_2 , densité de protons, Ultra-haut champs

Résumé : L'IRM quantitative recouvre l'ensemble des méthodes permettant de mesurer des paramètres physiques accessibles en Résonance Magnétique Nucléaire. Elle offre un bénéfice par rapport à l'imagerie en pondération classiquement utilisée, notamment pour la détection, la caractérisation physiopathologique mais aussi pour le suivi thérapeutique des pathologies. Malgré ce potentiel avéré connu de longue date, ces méthodes restent peu utilisées dans la routine clinique. La raison principale est la longueur des acquisitions par rapport à l'approche classique. Les paramètres physiques que nous souhaitons étudier plus particulièrement sont le temps de relaxation longitudinal (T_1), transversal (T_2), le coefficient de diffusion apparent (ADC), et la densité de protons (DP).

Malgré la possibilité d'atteindre une meilleure qualité d'images, ces cartographies in vivo sont quasiment inexistantes dans la littérature au-delà de 3T

car leur implémentation nécessite de surmonter un certain nombre de limites spécifiques aux IRM ultra-haut champs (UHF).

Au travers de ce projet de thèse, une méthode d'imagerie quantitative basée sur les états de configurations (QuICS) a été implémentée, pour déterminer ces paramètres quantitatifs de façon simultanée sous fortes contraintes propres aux UHF. L'approche a été optimisée dans le but d'obtenir des cartographies fiables et rapides. Le potentiel de la méthode a été démontré dans un premier temps in vitro sur un noyau tel que le sodium démontrant des propriétés complexes à cartographier. Puis dans un second temps, des acquisitions ont été réalisées sur proton, in vivo, en un temps d'acquisition compatible avec une utilisation en routine clinique à 7T. L'application d'une telle méthode d'IRM quantitative à UHF sur des populations permettra d'ouvrir de nouvelles voies d'études pour le futur.

Title : Quantitative MRI : towards fast and reliable T_1 , T_2 and proton density mapping at ultra-high field

Keywords : Quantitative MRI, relaxometry, T_1 , T_2 , proton density, ultra-high magnetic fields (UHF)

Abstract : Quantitative MRI refers to methods able to measure different physical parameters accessible in Nuclear Magnetic Resonance. It offers benefits compared to weighting imaging commonly used, for the detection, the pathophysiological characterization but also for the therapeutic follow-up of pathologies for example. Despite this long-established potential, these methods remain little used in clinical routine. The main reason is the long acquisition time compared to the classical approach. The physical parameters that we will study more particularly are the longitudinal (T_1), transverse (T_2) relaxation time, the apparent diffusion coefficient (ADC), and the proton density (DP). Despite the possibility to achieve a better image quality, these in vivo mappings are virtually non-existent in the literature

beyond 3T because their implementation requires overcoming a number of specific ultra-high-field (UHF) MRI limits.

Through this thesis project, a Quantitative Imaging method using Configuration States (QuICS) was implemented under strong UHF constraints, to determine these parameters simultaneously. The technique has been optimized to obtain fast and reliable maps. The potential of the method was first demonstrated in vitro on a nucleus such as sodium, exhibiting complex properties. As a second step, acquisitions were performed in proton, in vivo, in an clinically-relevant acquisition time, compatible with a routine use at 7T for population imaging. The application of such a method of quantitative MRI to UHF will open new research possibilities for the future.